# Validation of Non-Destructive Testing methods for reinforced concrete

A practical case study on the Ardeweg viaduct

Zhi Xiang Zhong

Master thesis

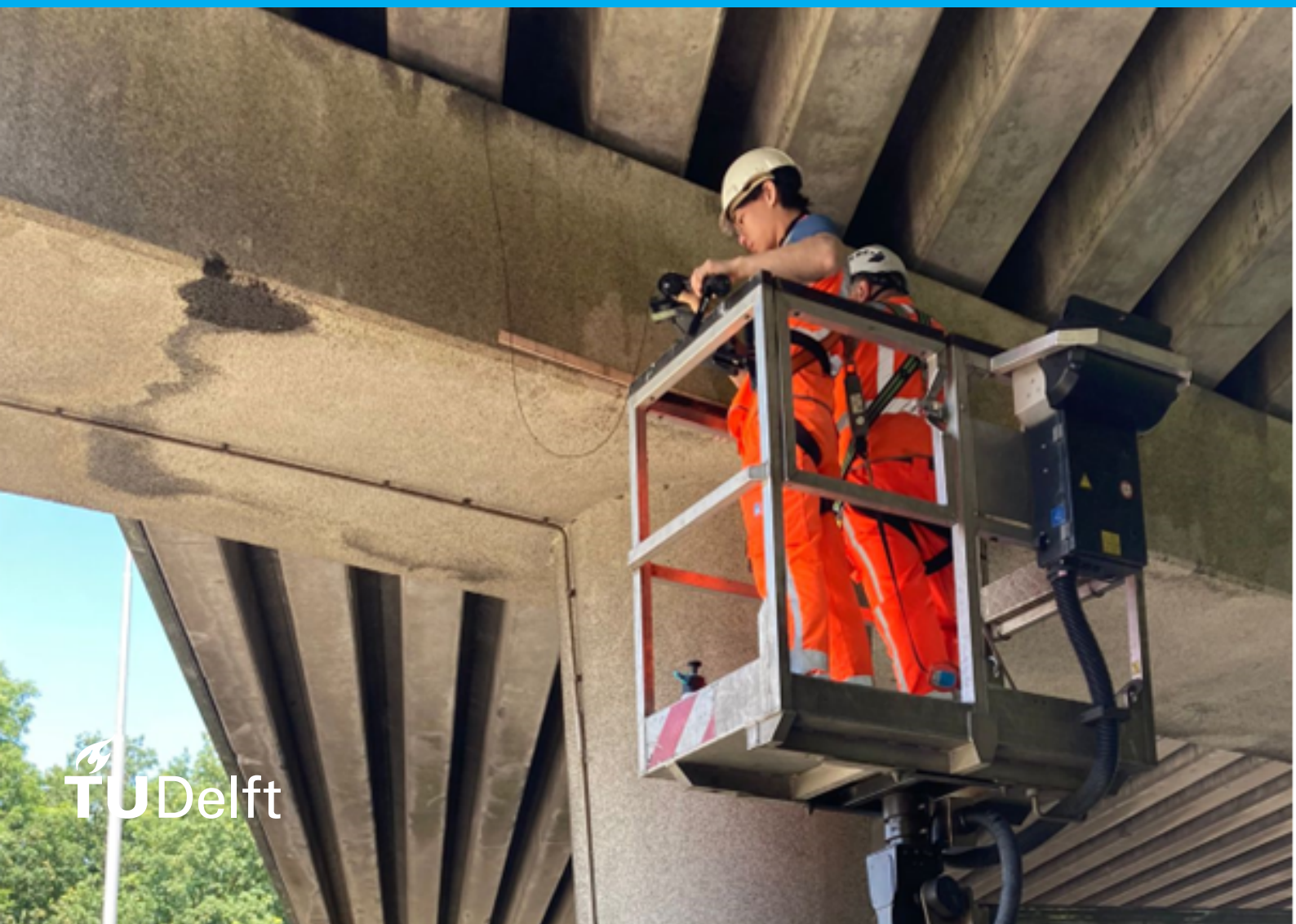

TU Delft

Master thesis

# Validation of Non-Destructive Testing methods for reinforced concrete

## A practical case study on the Ardeweg viaduct

by

Zhi Xiang Zhong

*Comittee*

| | |
|---|---|
| dr. ir. Penny Pipilikaki | Rijkswaterstaat |
| prof. dr. ir. Erik Schlangen | TU Delft |
| dr. ir. Mohammad Fotouhi | TU Delft |
| dr. Branko Šavija | TU Delft |
| dr. Sandra Nunes | TU Delft |

**June 30, 2025**

TU Delft

# Acknowledgments

This thesis marks the final step in my Master's journey at the Delft University of Technology, specializing in Materials and Environment. And what a beautiful journey it has been. It was a long, challenging, but most importantly, rewarding experience, only made possible through the help, knowledge, and encouragement of many individuals and organizations. I would like to take this opportunity to thank everyone who contributed to this project and supported me along the way.

First and foremost, I would like to express my sincere gratitude to my supervisor at Rijkswaterstaat, Penny Pipilikaki. This amazing project would not have been possible without you and the unwavering support you have given me, especially when things did not work out as planned. Your expertise, guidance, enthusiasm, and presence during the measurement days have helped me tremendously to shape myself into a better engineer that I can be proud of today. Thank you so, so much.

I also wish to deeply thank my thesis committee for their support, guidance, and valuable feedback throughout the course of my research. Thank you, Mohammad Fotouhi, Erik Schlangen, Branko Šavija, and Sandra Nunes. I am especially thankful to Mohammad for guiding and supporting me from the beginning until the very end. I am thankful for the bi-weekly meetings with the SHM group, which taught me a lot about other interesting topics, and where I met some amazing people.

Special thanks are due to the laboratory technicians at the Microlab and Stevinlab. Thank you, Maiko van Leeuwen, for helping me create thin sections and preparing my concrete samples; Ton Blom, for sawing and testing my numerous concrete cores; Michel van Aggelen, for supervising me during the polishing; and Arjan Thijssen, for teaching me how to work with the digital microscope. Lastly, a very deep and sincere thank you to John van den Berg for teaching me all about the Gecor-10 and the Volhard titrations in the chemical lab. Your presence since the start of my research has been a tremendous help in everything corrosion-related. You were the one who pushed me toward the finish line, and I will be forever grateful for that.

I would also like to thank the companies involved in this project: Rijkswaterstaat, Newa, Heijmans, Dikkerboom, SGS Intron, and Nebest for their collaboration, shared knowledge, and logistical support during the various testing days. A special thanks to Ivo Verheijen for providing me with the required testing equipment and knowledge on how to operate them. I also want to thank Bryan de Jonge for helping me set up logistics and showing me some cool projects from close up.

I want to thank Gert Wilgenburg as well for his beautiful and comprehensive report on the Sluinerweg, which gave me the perfect starting point for my research. Your help with testing and your feedback were greatly appreciated throughout my journey.

Lastly, to my friends and family: thank you for your patience, motivation, and emotional support throughout this journey. I love you all so much!

*Zhi Xiang Zhong*
*The Hague, 2025*

# Abstract

With much of the Netherlands' concrete infrastructure approaching or surpassing its design life in the coming years, reliable and efficient assessment tools are essential to ensure safety and manage maintenance costs effectively. This thesis investigates the effectiveness and reliability of non-destructive testing (NDT) methods for assessing the material condition of aging reinforced concrete viaducts, with a primary case study on the Ardeweg viaduct.

This study is a direct follow-up to Gert Wilgenburg's 2024 report on the Sluinerweg, which is another viaduct in the "Liggerkoppen Project". The end product of his research was a practical methodology for large-scale NDT and DT inspection. This present research aims to further develop this practical methodology by performing another large-scale inspection on the Ardeweg viaduct using various NDT methods, including: Ground Penetrating Radar (GPR), Rebound Hammer (RH), Ultrasonic Pulse Velocity (UPV), Half-Cell Potential (HCP), resistivity, and corrosion current density. The methodology combined the NDT measurements with destructive validation through core compressive strength testing, chloride profiling, carbonation depth analysis, and thin-section microscopy.

Furthermore, two types of rebound hammers (Q- and R-type) were studied to evaluate their interchangeability and variability. Particular attention was given to the effect of surface coatings. SonReb regression models were developed using RH, UPV, and destructive strength data to evaluate their accuracy for strength estimation.
The Q hammer is preferred over the older R-type hammer due to its improved accuracy and user experience. The Kristal-Cement-Graniet (KCG) coating applied to parts of the viaduct has a significant effect on the RH results, increasing the variability noticeably and decreasing the mean rebound values obtained. Furthermore, results show that RH testing correlates strongly with compressive strength ($R^2 >$ 0.9), while UPV ($R^2 = 0.51$) offers complementary value with lower sensitivity to surface conditions, like carbonation. The SonReb method, while slightly improving accuracy, showed diminishing returns relative to rebound-only models. The implementation of a carbonation correction factor for rebound values shows promise in improving the overall accuracy of the strength estimation models in both RH and SonReb models.

Corrosion risk classification from electrochemical methods aligned well with destructive chloride profiles and visual inspection, particularly in areas identified as high-risk. Half-cell potential and resistivity methods proved consistent and reliable under most field conditions, with HCP showing more consistent readings between devices and locations. The Gecor-10 and Profometer both showed a strong correlation with each other, indicating interchangeability between potential results.
The Gecor-10 A sensor showed inconsistencies and more variability in both resistivity and half-cell potential measurements when compared to the other devices, raising questions about the accuracy of its $i_{corr}$ calculation. The use of both 30s and 100s polarization times during inspection could provide more insight into the true $i_{corr}$ value.
The chloride profiles made with the RCT method in the 2019 report show a very promising correlation with the more accurate lab titrations when they are corrected for cement content. Its usefulness should be studied further as it could save time and costs.

This study concludes that NDT methods can serve as reliable tools for material condition assessment of aging concrete. Both strength- and corrosion-focused methods showed strong correlation with their destructive counterpart. Valuable practical knowledge has been obtained from the Ardeweg research, which could help shape future maintenance strategies for similar concrete structures.

# Contents

# 1

# Introduction

Rijkswaterstaat, also known as the Ministry of Infrastructure and Water Management of the Netherlands, is challenged with an unprecedented increase in the renovation and maintenance of concrete structures in the coming years. The ”Vervanging en Renovatie” (VenR) program is one of the core missions within Rijkswaterstaat, emphasizing the necessity to replace and renovate existing structures that are no longer meeting safety, reliability, and sustainability standards [1].

Many of these structures, such as bridges and tunnels, were constructed in the post-World War II era during the 1950s and 1960s, and they are now approaching the end of their intended service life, as can be seen in Figure 1.1. The yellow bars represent the number of concrete bridges and viaducts constructed, while the black line indicates the VenR challenge in the coming years, given an assumed service life of 80 years [2]. To decide what the best course of action would be for these aging structures, a comprehensive assessment is required.

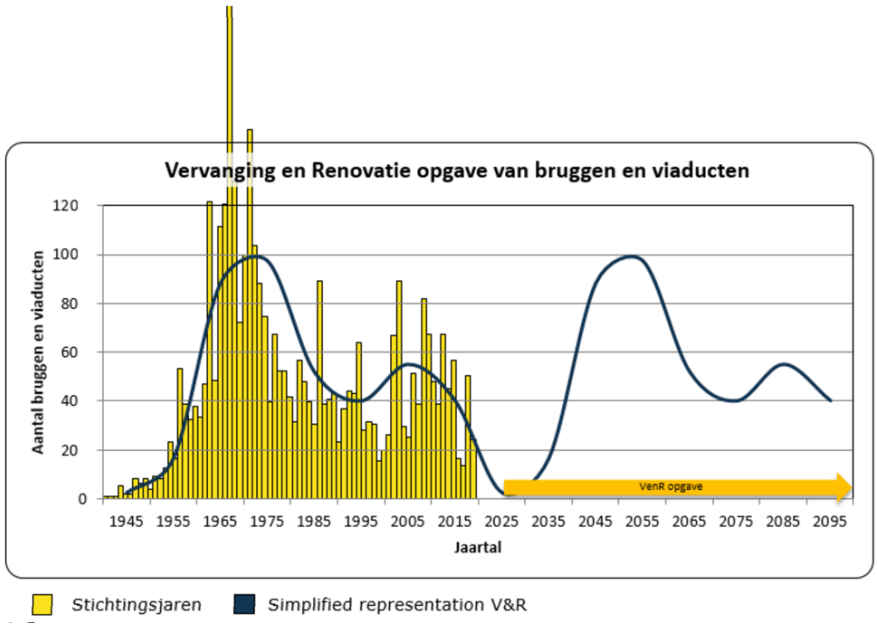


Figure 1.1: Estimation of the upcoming structures to be renovated and the historical building dates of concrete bridges and viaducts. [2]

Traditional methods for assessing the condition and remaining lifespan of concrete structures involve extensive laboratory testing and numerous testing protocols. This is classified as Destructive Testing (DT) due to the inherent damage they cause to structures. On the other hand, Non-Destructive Testing

(NDT) methods have the advantage of doing little to no damage to the structure while performing measurements. The main benefit of using NDTs is thus the fact that it does not significantly weaken the structure that is being assessed. Furthermore, the results of most NDTs can immediately be observed due to them being performed on-site without extensive post-processing. So, NDTs would provide a faster way to determine the underlying condition of the material in comparison to DT's. However, their application in the Netherlands, particularly for concrete structures, remains limited primarily due to a lack of knowledge, trust, and experience compared to their more common use in the steel industry [3].

One of the current VenR projects is the expansion of the A1 highway between Apeldoorn and Twello, which plans to accommodate the growing traffic needs by widening the roads. Two existing viaducts, the Ardeweg and Sluinerweg viaducts, had to be replaced as they were too narrow for the new road design. These two viaducts were also part of the "Liggerkoppen" project, which entails several similarly built viaducts over major highways across the Netherlands. These viaducts all used prefabricated T-beams, which showed similar and consistent damage patterns. The first signs of concern came from inspections performed in 2002, where damage near beam heads was found at several viaducts built in the same time period [4]. Due to the planned deconstruction of the Ardeweg and Sluinerweg viaducts and their similarity to other viaducts in the "Liggerkoppen" project, there was a rare opportunity to test these viaducts in both a destructive and non-destructive manner.

The Sluinerweg viaduct was demolished in February 2024. Rijkswaterstaat initiated an investigation on this particular viaduct, and testing was conducted in November 2023. The research was done by a fellow Master's student, Gert Wilgenburg, and his findings can be found in his report [5]. His recommendations and methodology serve as a basis for this report, as his developed method will be applied to the Ardexweg viaduct as well.
The practical methodology that was developed in the Sluinerweg report followed a very practical, field-oriented approach, which consists of several NDT methods, like ground penetrating radar (GPR), rebound hammer (RH), ultrasonic pulse velocity (UPV), half-cell potential, resistivity, and corrosion current density. The pragmatic strategy offers comprehensive, large-scale assessments by collecting as much data as possible with a set of measurement devices that have been selected to gain more practical experience. However, the approach lacks exhaustive validation that is necessary for accurate material assessment, especially for a novel methodology. Furthermore, the Sluinerweg viaduct did not show any signs of corrosion that could validate the corrosion assessment results, leaving a gap in the dataset and questioning its validity and usability outside of its scope.

## 1.1. Research significance

Accurate assessment of the in-situ condition of aging concrete structures is crucial for making decisions regarding maintenance, repair, or replacement. The Liggerkoppen viaducts need targeted assessments to extend their service life reliably. This study tries to validate the Sluinerweg findings by applying a more in-depth methodology to a comparable viaduct, the Ardeweg. By following the same methodology, the gathered results from the Sluinerweg could be used to build upon and further advance the methodology using a more detailed, research-based approach. This includes the use of destructive test validation, cross-methods correlation reviews, and microstructural analysis to evaluate the reliability of the field assessments. The significance of this research mostly lies in the validation and expansion of the given methodology, ensuring they are efficient and evidence-based. It would help support Rijkswaterstaat's VenR mission by tailoring an effective inspection approach for viaducts within the Liggerkoppen project.

## 1.2. Research objectives

The further development of the practical methodology with the use of NDTs is the main focus of this study. To achieve this objective, the following sub-objectives are formulated:

- Apply and evaluate strength and corrosion-related NDT and DT techniques on the Ardeweg viaduct for validation and method assessment.
- Comparing the Ardeweg measurement results with the available Sluinerweg data.

- Comparing the Ardeweg measurement results with historical measurement data.
- Summarize the gained insights from the similarities and differences in results and practical challenges.
- Refining the existing practical methodology with the gained insights.

Moreover, the Sluinerweg report also recommended specific topics that should be explored. The ones that will be looked at are:

- Finding a quantifiable relation between the R- and Q-hammer rebound values.
- Developing a SonReb model and evaluating its effectiveness in estimating the concrete compressive strength.
- Exploring the resistivity value for the corrosion assessment.
- Looking into the polarization time for the corrosion current density measurements and its influences on the $i_{corr}$ value

## 1.3. Research questions

From the research objective and significance, the following research question is formulated:

> *'To what extent can non-destructive testing (NDT) methods effectively assess the material condition of aging concrete viaducts in the Liggerkoppen project?'*

To answer the main research question, the following four sub-questions have been formulated:

1. To what extent can corrosion and strength-related NDT results be validated with their destructive counterpart?
2. What are the differences in testing results between the Ardeweg and Sluinerweg viaducts, and what insights can be gained from the testing procedure used?
3. How effectively can rebound hammer and ultrasonic pulse velocity measurements estimate the compressive strength of concrete in aging viaducts?
4. How consistent and reliable are half-cell potential and resistivity measurements for identifying and evaluating corrosion risk in aging viaducts?
5. What practical insights can be gained by comparing non-destructive testing results across different viaduct projects to improve assessment methodologies?

## 1.4. Research scope

This report focuses on the application of selected NDT and DT methods to assess the material condition of specific structural elements of the Ardeweg viaduct. The study concentrates on some parts of support beams 4 and 5, as well as selected T-beams near the abutment. These were chosen for reasons of accessibility, cost, and safety.
The research will not go into life cycle analysis, structural evaluation, or repair design. Instead, it aims to provide a comparative analysis of different measurement techniques and their results. These results could be used for similarly constructed concrete viaducts within the Liggerkoppen project, taking into account structural and environmental differences.
To facilitate direct comparison, a range of mostly commercially available NDT methods was selected to be consistent with those applied in the Sluinerweg project. Nevertheless, slight differences in device models or settings might affect comparability, which is acknowledged. The results gathered from these NDTs may not fully represent results gained from other measuring devices that were not considered in this study.
The influence of local environmental factors (e.g., humidity, temperature, wind, traffic load) on the measurements and their interpretation will be acknowledged but not deeply analyzed. The weather conditions will be recorded to inform about the conditions

## 1.5. Report layout

The report is structured as follows:

- **Chapter 1: Introduction** - Provides background, problem statement, and objectives of the study, as well as the research questions and scope.
- **Chapter 2: Literature review** - Summarizes corrosion mechanics, existing research, and standards related to non-destructive testing methods, and their application in structural concrete assessment.
- **Chapter 3: Ardeweg and Sluinerweg viaduct** - Introduces the case study of this research project and its damage history. Furthermore, the comparison and the existing research on the Sluinerweg viaduct are described
- **Chapter 4: Methodology** - Details the approach taken in the on-site and laboratory investigations, including test locations, measurement devices, testing procedures, data acquisition, and data analysis.
- **Chapter 5: Results on-site measurements** - Presents the gathered data from the on-site testing on the Ardeweg viaduct performed in June-July. Visualization of the data is shown, and preliminary observations are performed.
- **Chapter 6: Results harvested T-beams measurements** - Presents the gathered data from the testing on the harvested T-beams performed in October.
- **Chapter 7: Discussion** - Interprets the results, evaluates the performance of the NDT methods, highlights differences between the devices and techniques, and compares the results with historical/Sluinerweg data.
- **Chapter 8: Conclusion and Recommendations** - Summarizes gained insights, answers the research questions, and provides recommendations for future research.
- **Appendices** - Include the raw testing data, additional specifications, testing photos, and historical data.

# 2

# Literature review

## 2.1. Concrete damage

Reinforced concrete (RC) is the most used building material in the world [6]. It is the preferred choice for building material in the construction and infrastructure industries, due to its great structural properties and cost-effectiveness. The steel reinforcement inside RC provides high tensile strength, which offsets the poor tensile strength of concrete alone. In turn, the concrete provides an alkaline environment, enabling the formation of a passive layer on the reinforcement, protecting the steel from corrosion. The synergy between these two properties has unlocked the widespread use of RC in many projects worldwide.

However, despite the advantages, RC is susceptible to different types of damage during its service life. These vulnerabilities stem from environmental conditions, physical load, or chemical attacks. All these factors could characteristically damage the concrete, affecting its structural safety and ultimately reducing its service life. Therefore, it is standard practice to consider these potential damage mechanisms during the design phase to mitigate their effects effectively. The NEN-EN-206 [7] norm has prescribed exposure classes to aid in this phase. Table 2.1 describes these exposure classes.

Table 2.1: Exposure classes and their description

| Exposure class | Ranks | Description |
|---|---|---|
| X0 | - | No risk of corrosion or attack |
| XC | 1-4 | Corrosion induced by carbonation |
| XD | 1-3 | Corrosion induced by chlorides (not from sea water) |
| XS | 1-3 | Corrosion induced by chlorides (from sea water) |
| XF | 1-4 | Freeze/thaw attack with or without de-icing agents |
| XA | 1-3 | Chemical attack |

The selection for the right exposure class depends on the intended use, placement of the concrete, and the aggressiveness of the surrounding environment. A concrete component can be exposed to a combination of different exposure classes. Once the exposure class is decided, it serves as a requirement for the concrete mix design and overall structural considerations.

For exposure classes related to corrosion, specific measures are required, such as using a minimum cement content, a maximum water-to-cement (w/c) ratio, and a minimum concrete cover to protect the reinforcement. For freeze-thaw resistance, air-entraining admixtures are added to the concrete mix to accommodate the expansion of freezing water.

### 2.1.1. Concrete cracking

Cracking of concrete is an undesirable damage type that leads to a reduction of aesthetics, durability, and structural integrity of concrete elements. Cracks form during construction or the service life of the structure, depending on the cause. Varying mechanisms result in the cracking of concrete, with the most common ones being: plastic shrinkage cracks, drying shrinkage cracks, thermal cracks, structural cracks, and corrosion-induced cracks.

Crack width is the critical parameter in assessing the durability and condition of concrete structures. Wider cracks allow aggressive substances like chlorides and carbon dioxide to penetrate the concrete, accelerating deterioration processes such as corrosion and freeze-thaw damage. Standards specify acceptable crack width limits based on the structure's exposure class and intended service life.

### 2.1.2. Concrete corrosion

Corrosion of the steel reinforcement is one of the most common causes of damage in existing RC structures. The process is characterized by the disturbance of the protective passive steel layer inside the concrete. Penetration of chloride ions and carbonation of the concrete cover are the two main mechanisms for corrosion to occur [8]. The result is internal stress buildup due to the corrosion product's larger volume in comparison to the original reinforcement. The stress leads to cracking and spalling of the concrete, reducing its strength and exposing the reinforcement to further deterioration. Due to this feedback loop, if unchecked, active corrosion leads to a severe loss of structural integrity.

The transformation of iron into rust is an electrochemical process that requires the availability of (dissolved) oxygen and water. The oxidation of iron releases free electrons, which are consumed by the reduction of oxygen. The usual oxidation and reduction half-cell reactions can be seen in equations 2.1 and 2.2 respectively. These reactions occur simultaneously.

$$\mathrm{Fe} \longrightarrow \mathrm{Fe}^{2+} + 2\,\mathrm{e}^{-} \tag{2.1}$$

$$\mathrm{O_2} + 2\,\mathrm{H_2O} + 4\,\mathrm{e}^{-} \longrightarrow 4\,\mathrm{OH}^{-} \tag{2.2}$$

Combining the two reactions, the formation of iron(II)hydroxide can be seen in equation 2.3. The $Fe(OH)_2$ is normally further oxidized into other corrosion products like $Fe_3O_4$ or $Fe_2O_3$ under normal conditions [9]. The overall stability of the passive layer can be determined with the Pourbaix diagram for iron, which can be seen in Figure 2.1.

$$\mathrm{Fe} + \frac{1}{2}\,\mathrm{O_2} + \mathrm{H_2O} \longrightarrow \mathrm{Fe(OH)_2} \tag{2.3}$$

The diagram presents the thermodynamic states of iron in water influenced by the potential and pH. Three zones can be observed: Immunity, Passivation, and Corrosion. At low potentials, the iron is considered immune. It will not dissolve in solution in the form of ions, nor form oxide layers. The iron will undergo active corrosion when in a low pH environment to form $Fe^{2+}$ or $Fe^{3+}$ ions by dissolving in solution. Corrosion at high pH and low potential is also possible, as can be seen in the second corrosion zone (formation of $HFeO_2^{-}$).

The two dashed diagonal lines represent the oxygen and hydrogen evolution lines for reduction. Above the oxygen line, oxygen is oxidized from water as a preferred region. Below the hydrogen line, the reduction of hydrogen gas occurs. The zone between the two indicates a stable zone where water is dissolved in $H^{+}$ and $OH^{-}$.

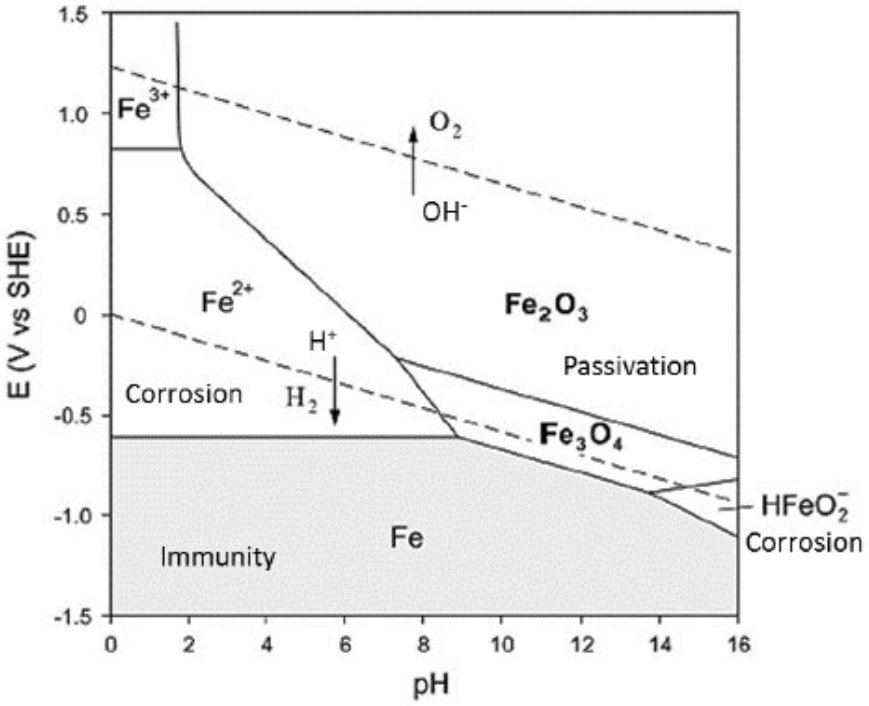


Figure 2.1: Simplified Pourbaix diagram for iron in water under standard conditions (T=25°C, [Fe]= $10^{-}6$ mol/l) [10]

**Carbonation induced corrosion**
Carbonation is a corrosion mechanism that is initiated by the atmospheric carbon dioxide $CO_2$ interacting with the calcium hydroxide ($Ca(OH)_2$) inside the concrete to form calcium carbonate ($CaCO_3$). The process is presented by equation 2.4 to 2.8 [11] [12].

$$Ca(OH)_2 \longrightarrow Ca^{2+}(aq) + 2\,OH^{-}(aq) \tag{2.4}$$

$$Ca^{2+}(aq) + 2\,OH^{-}(aq) + CO_2 \longrightarrow CaCO_3 + H_2 \tag{2.5}$$

$$3\,CaO \cdot 2\,SiO_2 \cdot 3\,H_2O + 3\,CO_2 \longrightarrow 3\,CaCO_3 \cdot 2\,SiO_2 \cdot 3\,H_2O \tag{2.6}$$

$$3\,CaO \cdot SiO_2 + \mu H_2O + 3\,CO_2 \longrightarrow 3\,CaCO_3 + SiO_2 \cdot \mu H_2O \tag{2.7}$$

$$2\,CaO \cdot SiO_2 + \mu H_2O + 3\,CO_2 \longrightarrow 2\,CaCO_3 + SiO_2 \cdot \mu H_2O \tag{2.8}$$

The main mechanism revolves around the reaction with $Ca(OH)_2$ (also known as portlandite) and $CO_2$. This reaction occurs naturally if enough $CO_2$ is present in the atmosphere, which can react inside the pores of the concrete. Furthermore, as can be seen from equations 2.6, 2.7 and 2.8, some calcium silicate hydrate (C-S-H) and unhydrated calcium silicates ($C_3S$, $C_2S$) also interacts with the $CO_2$ to form carbonation products. The reaction of C-S-H and $CO_2$ is slower due to the lower calcium content [11].

Carbonation is mostly a slow process that lowers the pH of the concrete as hydroxyl ($OH^{-}$) ions are slowly being depleted. The carbonation front travels gradually into the concrete pore structure, depositing carbonation products. This deposit of carbonation products is a beneficial side effect due to the reduction of porosity, further slowing the carbonation rate. Furthermore, the carbonation front is generally uniform if the concrete is homogeneous and exhibits no local damage [13].
When the carbonation front reaches the reinforcement, the pH of the concrete lowers, leading to the dissipation of the protective passive layer. Figure 2.2 shows the different stages of carbonation. At $t_0$,

the concrete is unaffected and there is no carbonation front. $t_1$ and $t_2$ show the carbonation front moving into the concrete cover indicated by the different colors. At $t_3$, the carbonation front has reached the reinforcement, and corrosion will likely initiate.

Phenolphthalein indicator solution is used to show the presence of carbonation in concrete. It shows a bright purple color in an alkaline environment with a pH over 10, while becoming colorless at a pH under 8.3. Spraying the indicator on a fresh concrete surface will expose the regions that have carbonated, as can be seen in Figure 2.2.

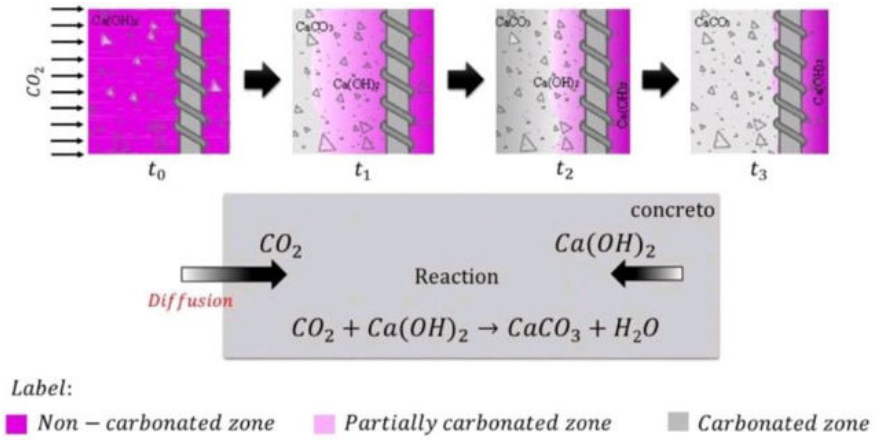


Figure 2.2: Carbonation process with phenolphthalein indicator. [14]

The speed of carbonation is influenced by the condition of the concrete cover. Material factors such as permeability, w/c ratio, use of Supplementary Cementitious Materials (SCM), and overall concrete composition all have their effects on the carbonation depth. Furthermore, environmental effects like $CO_2$ concentration, temperature, relative humidity, wind, and sun exposure have been studied [15–18].Generally, carbonation occurs faster at high temperatures, higher concentrations of $CO_2$, and relative humidity between 50% - 70% [8].

**Chloride induced corrosion**

The other main source of corrosion is chloride penetration. Unlike carbonation-induced corrosion, which uniformly lowers the pH of concrete, chloride-induced corrosion can occur even when the concrete remains alkaline. Chlorides disrupt the protective passive layer on the steel reinforcement. Once the steel reinforcement is exposed to chloride ions, the corrosion process initiates, resulting in the formation of rust. The process is described in the following equations: [9, 19]

$$Fe^{2+} + 2\,H_2O \longrightarrow Fe(OH)_2 + 2\,H^+ \tag{2.9}$$

$$Fe^{2+} + 2\,Cl^- \longrightarrow FeCl_2 \tag{2.10}$$

$$2\,FeCl_2 + 2\,H_2O \longrightarrow 2\,Fe(OH)_2 + 2\,HCl \tag{2.11}$$

The process is initiated by the penetration of chloride ions ($Cl^-$) into the concrete cover through mechanisms like diffusion, capillary action, and permeation. Chloride ions can be found in de-icing salts, marine environments, or contaminated base materials. In this study, the main contributing source of chloride is the use of de-icing salts. In the Netherlands, the use of de-icing salts is very common in wintertime. The most commonly used de-icing salts are NaCl and $CaCl_2$. Polder et al. estimated the average amount of salt strewn on bridge surfaces to be around 250 grams of chloride per square meter per year [20]. This would be classified as an aggressive environment for RC structures, despite various other countries having a higher usage of de-icing salts.

The rate of chloride ingress is influenced by factors like concrete permeability, water-to-cement ratio, and environmental exposure conditions [19]. The XD exposure class accounts for this by setting requirements for the w/c ratio, minimum cement content, and minimum cover distance for the concrete [7].
Over time, enough chloride ions have penetrated the concrete cover and accumulated on the reinforcement. When the concentration of chloride ions at the steel surface reaches a critical threshold, destabilization of the passivation layer occurs. The corrosion that occurs is described as localized pitting corrosion, which is characterized by the formation of deep pits (see Figure 2.3). Pitting corrosion leads to the local breakdown of the passive layer, unlike the more homogeneous carbonation-induced corrosion that affects larger zones of reinforcement.

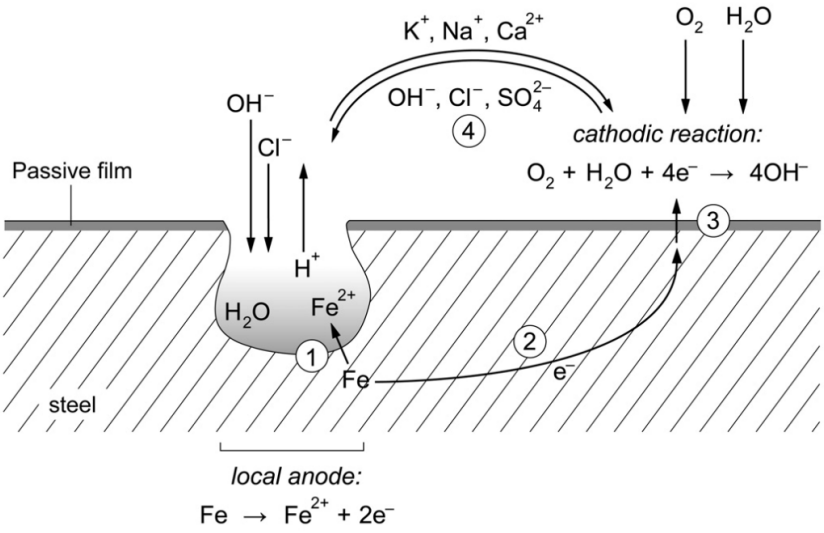


Figure 2.3: Process of chloride induced pitting corrosion with steps: 1. Oxidation of iron in $Fe^{2+}$ ions due to chloride; 2. Electron movement in metal; 3. Reduction of water at the cathode; 4. Free-flowing ions in the electrolyte. [9]

Without a protective passive layer, the anodic dissolution of iron initiates, and acidic byproducts are produced. Equation 2.9 describes the hydrolysis of iron ions, and equations 2.10 and 2.11 describe the interaction of chloride and iron. Both of these initial reactions result in the production of hydrogen ($H^+$) ions, lowering the pH inside the pit. Due to the shape of the corrosion pit, mass transport of oxygen is restricted, resulting in a deficiency of oxygen in the pit. The cathodic reduction is forced to happen at the steel surface adjacent to the pit, marking the pit as a local anode and establishing a macro-cell [9].

The critical chloride threshold necessary to initiate corrosion is influenced by several factors, including the pH of the pore solution, the presence of other aggressive ions, and the characteristics of the concrete matrix. Additionally, the binding capacity of concrete, which refers to its ability to chemically or physically bind chloride ions, plays a significant role in determining the rate of chloride ingress. Concrete can bind chloride ions through chemical reactions with cement hydration products or by adsorption in the pore structure. This binding reduces the concentration of free chlorides available to initiate corrosion. The type of cement and the w/c ratio influence the binding capacity of the concrete, improving overall chloride resistance [21–23].

The critical chloride threshold varies depending on the earlier-mentioned variables. The general consensus is that the value is between 0.4% to 0.6% of the cement weight. The EN-206 uses 0.4% as the threshold for general reinforced concrete [7]. The ACI-318-83 differentiates between acid- and water-soluble chloride content with thresholds of 0.2% and 0.15%, respectively [24]. The water-soluble chloride is measured from the pore solution of the concrete, resulting in the content of chloride that is actively contributing to the corrosion process, while the acid-soluble test extracts all (bound and unbound) chloride available.

Furthermore, Lee et al. showed that the chloride penetration was more pronounced when carbonation was present at the same time as chloride ingress [25]. Despite carbonation leading to lower porosity near the concrete surface, microcracking can occur in advanced carbonation, which increases permeability. This is due to the carbonation of C-S-H and GGBFS leading to porosity increases [26]. The research also highlights that carbonation can lead to the release of chloride ions previously bound within cement hydrates, increasing the chloride content in the pore solution. Ultimately, the chloride threshold is considerably lowered due to the combined effects of carbonation and chloride penetration.

### 2.1.3. Corrosion rate

The Corrosion Rate (CR) is a metric to quantitatively measure the rate of corrosion inside concrete. It describes the material loss over time due to corrosion and is usually expressed in mm/year. It is derived from the corrosion current density ($i_{corr}$), which describes the electrochemical kinetics of corrosion. The most commonly used technique to measure the corrosion rate is by using the linear polarization resistance method developed by Stern-Geary. This method applies a small external voltage or current to the reinforcement while the response is monitored to determine the electrochemical behavior. The corrosion current density is derived from the Polarization resistance (Rp) using the Stern-Geary equation [27]:

$$i_{corr} = \frac{B}{R_p} \tag{2.12}$$

Where:

$$\begin{aligned} i_{corr} &= \text{The corrosion current density } (mA/cm^2) \\ B &= \text{Stern-Geary constant } (mV) \\ R_p &= \text{The polarization resistance } (\Omega \cdot cm^2) \end{aligned}$$

The Stern-Geary constant ($B$) is dependent on temperature, potential, and exchange current densities. The theoretical origin comes from the Tafel Slopes, as can be seen in equation 2.13. $B$ is estimated to be 52 mV for non-corroding reinforcement and 26 mV for actively corroding reinforcement under standard conditions [28]. For unknown conditions, like on-site measurements, it is recommended to use 26 mV [29].

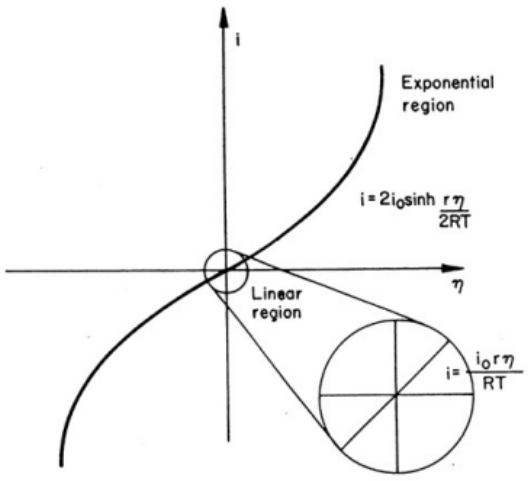


Figure 2.4: The polarization curve for electrochemical processes [30].

The Polarization Resistance ($R_p$) is defined as the slope between the applied voltage and the change in current at the corrosion potential ($E_{corr}$) which comes from Ohm's law, as can be seen in equation 2.14. By using a small polarization potential (20-50 $mV$), it is possible to model the linear part of the

polarization curve, which is shown in Figure 2.4 [29]. $R_p$ is usually displayed as $k\Omega cm^2$ or $k\Omega$ depending on the inclusion of the polarization area.

$$B = \frac{\beta_a \cdot \beta_c}{2.303 \cdot (\beta_a + \beta_c)} \tag{2.13}$$

$$R_p = \left(\frac{\Delta E_p}{\Delta I_p}\right)_{I_p \to 0, \Delta E_p \to E_{corr}} = \left(\frac{\Delta E_p}{I_p}\right)_{\Delta E_p \to E_{corr}} \tag{2.14}$$

Where:

$\beta_a =$ The anodic Tafel slope
$\beta_c =$ The cathodic Tafel slope
$E_p =$ The polarization potential $(mV)$
$E_{corr} =$ The corrosion potential $(mV)$
$I_p =$ The polarization current $(mA)$

The corrosion rate can be calculated using Faraday's law once $i_{corr}$ is known. Deriving the corrosion rate using the polarization resistance is proven to be accurate over the years [31, 32]. Furthermore, the agreement of the gravimetric weight loss of the reinforcement and the weight loss measured electrochemically is well established [27, 33, 34].

$$\text{CR} = \frac{\Delta x}{\Delta t} = \frac{i_{corr}}{\rho} \cdot \frac{M}{zF} \tag{2.15}$$

Where:

CR = Corrosion rate $(cm/s)$
$\Delta x =$ Section loss of steel $(cm)$
$\Delta t =$ Duration of corrosion $(s)$
$i_{corr} =$ The corrosion current density $(A/cm^2)$
$\rho =$ Specific density of iron $(7.8\ g/cm^3)$
$M =$ Molecular mass of iron $(55.845\ g/mol)$
$z =$ Amount of ionic charges for iron = 2 (-)
$F =$ Faraday constant $(96480\ C/mol)$

## 2.2. Non destructive methods

The Sluinerweg report has a comprehensive description of each NDT and DT method used [5, p.24]. The methods described here are complementary to the information available in the Sluinerweg report.

### 2.2.1. Rebound Hammer

The rebound hammer (RH), also called a Schmidt hammer, is a testing device used to estimate the compressive strength of concrete by measuring the rebound of a spring-loaded mass inside the device. The rebound value of the RH indicates the surface hardness of the surface. The surface hardness can be empirically correlated to the compressive strength of concrete [35]. This can be a general curve, but most correlations are used for specific structures and cross-validated with tested cores. The rebound hammer consists of four key parts:

- The hammer
- The spring

- The plunger
- The outer casing

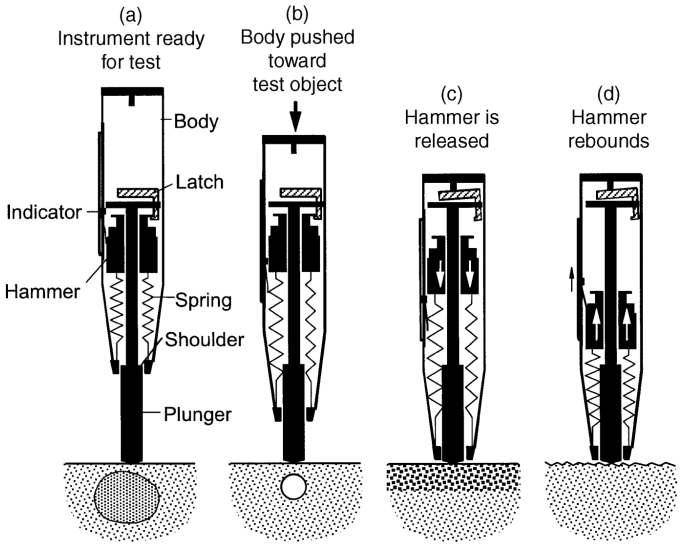


Figure 2.5: Schematic of a mechanical rebound hammer with the internal parts exposed while doing a measurement. [36]

These parts can be seen in Figure 2.5. The plunger is in contact with the surface of the concrete and acts as an interface between the internal mechanism and the concrete. When the rebound hammer is pushed against the concrete, the spring is loaded until the hammer is released at a set distance. The now free-floating hammer is pulled by the spring and bounces against the concrete through the plunger, resulting in movement in the opposite direction. The distance traveled due to the hammer's rebound is linked to a slide on the side of the device where the R-value (rebound value) can be read. The rebound value indicates the kinetic energy absorbed by the concrete. This energy absorption is lower for stiffer, high-strength concrete, resulting in a higher rebound value. Likewise, a less stiff (lower strength) concrete will absorb more energy, resulting in a lower rebound value [36].

The rebound hammer only effectively tests the surface-level concrete close to the plunger. The rebound hammer is thus very sensitive to the heterogeneity of the underlying concrete [37]. An example can be seen in Figure 2.5a, where the rebound hammer is directly positioned near a large aggregate. Here, a higher rebound value is observed as the aggregate, and its properties are mostly measured. Conversely, in Figure 2.5b, the rebound hammer is positioned near an air void, leading to a lower rebound value due to energy dissipation.
Multiple rebounds are needed to account for this scatter of results. For example, the EN12504-2 and ASTM C805 require a minimum of 9 and 10 measurements per test location, respectively [38, 39]. Another limitation of the rebound hammer is the inability to relate the deeper subsurface concrete to the rebound results obtained from the surface.

**Types of rebound hammers**
There are two different strength classifications for rebound hammers. Namely, the type N & L-type rebound hammers (see table 2.2). The L-type rebound hammer differentiates itself from the N-type by having a lighter hammer and thus a lighter impact force. This makes it more suitable for concrete sections that are thin-walled (<100mm) or fresh concrete that is still hardening. In practice, the N-type is most often used for concrete as it is more applicable in testing situations and is also required in several standards like Eurocode 13791 [40].
Everything described above applies to the original mechanical rebound hammer. Currently, an electronic version of the rebound hammer also exists. Also known as the SilverSchmidt. The SilverSchmidt

Table 2.2: Comparison of N- and L-type rebound hammers

| Type | Impact force | Strength range | Application |
|---|---|---|---|
| **N** | 2.207 Nm | 10 - 70 MPa | Hardened concrete >100mm thickness |
| **L** | 0.735 Nm | 5 – 30 MPa | Fresh concrete <100mm thickness |

represents a significant advancement over traditional mechanical rebound hammers in the evaluation of concrete structures. Unlike the conventional rebound hammer, which relies on the mechanical spring mechanism to measure the rebound, the SilverSchmidt uses electronic sensing and processing of the mass just before and after the impact, which is expressed in a new measurement metric: the Q-value. The short time window for the measurement effectively eliminates friction losses as the Q-value is not dependent on the relatively longer mechanical response. Another benefit is the independence of orientation when measuring with the SilverSchmidt. The original hammer has to be corrected for the orientation due to gravity's influence on the mass-spring system.

**R and Q values**

Fundamentally, the R- and Q-values are two different parameters due to the way they are measured. The R-value is a measurement that is obtained by the rebound and mechanical travel of the hammer mass. The Q-value is defined as the ratio between a velocity measurement just before and after an impact. To be more precise, the speed of the hammer is measured and linked to the kinetic energy loss. The equation for the calculation of the Q-value can be seen in equation 2.16.

$$Q = \frac{V_2}{V_1} \cdot 100 \tag{2.16}$$

Where:

$V_2 =$ The speed of the hammer directly after impact
$V_1 =$ The speed of the hammer directly before impact

Equation 2.16 gives values between 1 and 100, which indicate the energy loss on impact. It also highlights the independence of orientation, as both the incoming and returning speeds are measured. This is in contrast to the original hammer, where the returning response is the only measured metric. The longer travel before the measurement also adds another layer of uncertainty to the measurement in the form of inconsistent friction losses.

Due to the difference between the two measuring methods, it raises the question of the interchangeability of these methods. From Winkler and Matthews [41], an established correlation was found between the R and Q values of around +10. However, this study was conducted on varying types of rock and not on aging concrete. It is to be determined if this relation is also applicable to concrete structures. A found correlation would provide a basis for more in-depth analysis, as more historical R-value data can be used to construct strength conversion models. For example, different SonReb models made for the original hammer could be converted and used with Q-value measurements.

**Influencing parameters**

- **Surface finish** of the concrete sample influences the reading from a rebound hammer. A rougher surface would lead to lower overall rebound values due to its inability to distribute the rebound hammer force to the deeper-located concrete [36]. This uneven finish could lead to local crushing of the finishing layer or concrete, resulting in additional energy loss. Maliha et al. found that for higher-strength concrete, the influence of a rougher surface is more significant than that of lower-strength ones [42]. Therefore, any additional surface finish should be grounded to obtain an accurate result in accordance with [36].

- **Carbonation** of the concrete surface will result in higher measured rebound values. Carbon dioxide penetration into the concrete surface will lead to the creation of hardened limestone. This leads to an increase in the surface hardness and thus the rebound value obtained. Consequently, an overestimation of the concrete strength for very carbonated structures is possible. For well-aged structures or structures exposed to a high concentration of carbon dioxide, the influence of carbonation should always be taken into account when reviewing the results.
- **Moisture content** inside the concrete will result in a lower overall rebound value [43]. Excess moisture will enter the concrete and fill the air voids. Severe surface moisture should be monitored before measuring with the rebound hammer.
- **W/C ratio** determines the initial water-to-cement ratio used in the concrete mix design. An increase in w/c ratio decreases the measured rebound value [43]. A high w/c ratio is known to impact the strength of concrete by dilating the cement paste and introducing air voids. This effect is also measurable with the rebound hammer [37].

### 2.2.2. Gecor-10

The Gecor-10 is a linear polarization corrosion rate measurement instrument developed in Spain by Geocisa. It measures the polarization resistance $R_p$ using the modulated current confinement technique. This entails using a guard ring to confine the applied polarization current to a known reinforcement section. The device is capable of measuring all the required parameters for the corrosion rate in one measurement by combining the electrochemical potential, resistivity, and corrosion current density. The Gecor-10 device with its components can be seen in Figure 2.6.


Figure 2.6: The Gecor-10 measurement device with all its components: 1) Gecor-10 main unit, 2) confinement sensor, 3) Potential sensor, 4) 4-tip resistivity sensor, 5) cables, 6) calibration box, and 7) protective housing. [44]

The Gecor-10 is used to measure the $R_p$ value galvanostatically, whereby a constant current is applied while the potential response is monitored as per equation 2.14. It should be noted that the measured $\Delta E_a$ is the total potential drop response and should be corrected for Ohmic drop (see equation 2.17). The Ohmic resistance ($R_\Omega$) must be known before the measurement to accurately calculate the polarization resistance.

$$\Delta E_p = \Delta E_a - \Delta E_\Omega = \Delta E_a - I_p \cdot R_\Omega \tag{2.17}$$

The confinement probe (see Figure2.7) is used to measure the $R_p$ value. A Cu/CuSO4 reference electrode (RE) is located at the center of the probe to measure the corrosion potential $E_{corr}$. Two stainless steel rings surround the middle reference electrode. The smaller one works as a counter-electrode (CE), while the larger one acts as a guard ring (XCE). Two more Cu/CuSO4 reference electrodes are located between the counter-electrodes to aid in the control of the guard ring [45]. This ensures the confinement of a constant area of reinforcement to be used in the calculation of the $R_p$.

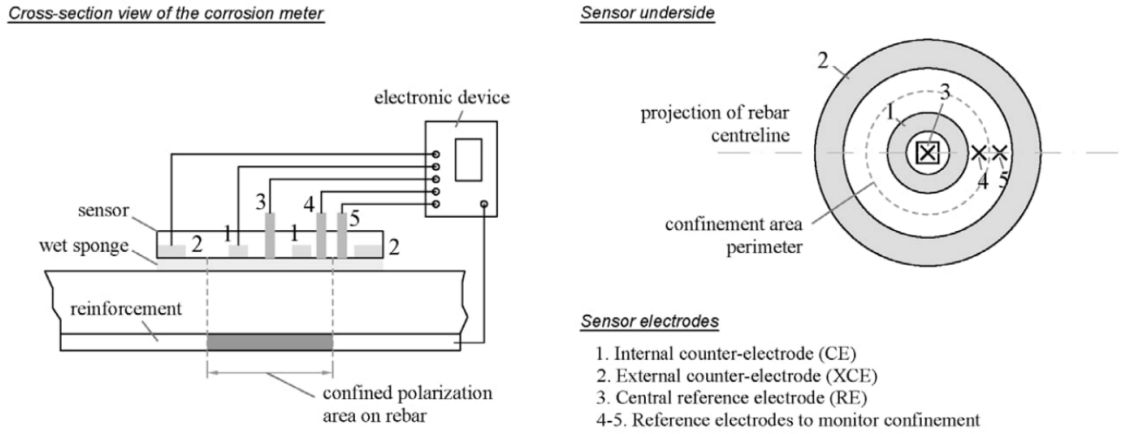


Figure 2.7: Schematic of the Gecor-10 confinement probe [46]

The corrosion rate measurement process can be seen in Figure 2.8 for the similarly operating predecessor: the Gecor-6. The procedure starts with the measurement of the corrosion potential of the reinforcement with the reference electrode. Afterward, a short pulse of current is applied to the CE electrode while the potential is monitored to calibrate the measurement current. During this time, the Ohmic drop is also measured as the current switches off. The $R_p$ measurement now initiates by polarizing the reinforcement with a constant applied current $I_{CE}$ on the inner counter electrode (CE). Another current is applied at the outer counter electrode (XCE) to maintain the same initial conditions for the potential in the two reference electrodes ($E_{Ref2}$ and $E_{Ref3}$). The current is modulated to confine the flow of current inside the predetermined circle with a diameter of 65 mm.

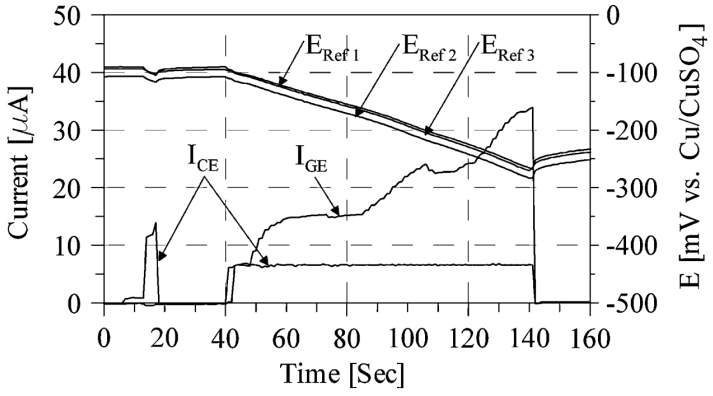


Figure 2.8: Recording of a Gecor-6 measurement on a non-corroding concrete element. The potential is monitored by the three reference electrodes ($E_{Ref1}$ to $E_{Ref3}$), while the applied current is monitored and controlled from the counter electrodes. [45]

The value of $R_p$ is calculated by combining equations 2.13, 2.14, and 2.17, using the measured response of the potential drop $E_a$ corrected for the Ohmic drop. The corrosion current density $i_{corr}$ is then calculated with the value for $R_p$ in a modified version of the Stern-Geary equation that takes polarization area into account (see equation 2.18). A Stern-Geary constant $B$ of 26 mV is used by the Gecor-10, which cannot be changed [44]. After the measurement is completed, the values for the $i_{corr}$, $E_{corr}$, $E_{pol}$, and $R_\Omega$ are displayed.

$$i_{corr} = \frac{B}{R_p A} \tag{2.18}$$

Input parameters for the measurement are reinforcement diameter and the polarization time. The polarization time is normally between 30 to 100 seconds, depending on the assumed corrosion activity [27, 34]. An optimal value of 100 seconds is preferred for low corrosion risk. The time should not be less than 45 seconds in the case of reinforcements without corrosion and 30 seconds for corroded reinforcements. This is because lower polarization times do not allow a steady state to be reached and dissipate the capacitive effect of the electrochemical double layer [44]. Knowledge of the corrosion risk beforehand could help determine the optimal polarization time.
Knowing the diameter of the reinforcement is essential to perform measurements. Construction drawings, visual inspection, or NDTs could be used to ascertain the diameter. Furthermore, other practicalities to consider:

- A connection with the reinforcement is necessary to complete the electrical circuit. If connections with the rebar are limited, the continuity between the different connections must be tested. A stable resistance under 1 Ω is considered to be continuous.
- A wet sponge must be placed under the sensors to have an adequate electrical connection with the concrete below. The concrete surface also must be pre-wetted for the same reason.
- Constant pressure needs to be applied during the full duration of the measurement. Measurements performed on vertical or overhead surfaces will pose a relative challenge, especially using longer polarization times.

# 3

# Liggerkoppen Project

Between 1960 and 1980, dozens of similarly designed viaducts were built over highways across the Netherlands [47]. These viaducts all used post-tensioned prefabricated concrete T-beams in their design. In the early 2000s, inspections on various viaducts showed damage near the beam heads that had not been seen before. These suspicions led to the further inspection of similar viaducts, marking the beginning of the 'Liggerkoppen Project'.

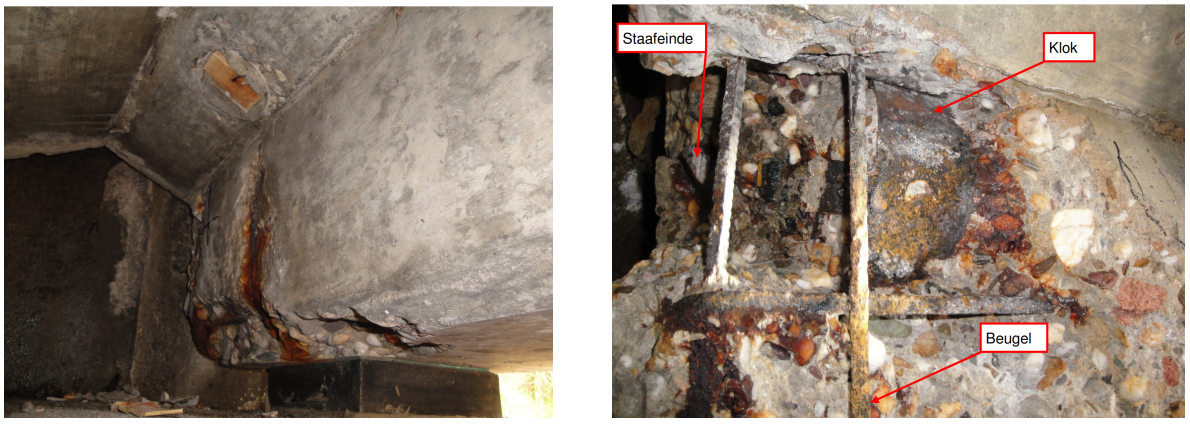


(a) Spalling concrete and corrosion damage to the beam head

(b) Hydroblasted concrete revealing the corroding prestressing anchor an reinforcements

Figure 3.1: Damages present on beam heads of viaducts from the Liggerkoppen Project [48].

The T-beams used in various viaducts from the Liggerkoppen project were designed using Dywidag post-tensioned prestressing bars. Each T-beam had 5 or 6 of these prestressing bars along the length of the beam, with one end being blindly anchored into the concrete, while an anchor was used to tension the other end (see Figure 3.6). After tensioning the bars, the anchors were sealed with mortar, forming the so-called cone at the beam head. Documentation and drawings showed that the prestressing ducts were injected with mortar to protect the bars [49].
Early reports show that the primary damage mechanism was chloride-initiated corrosion of the prestressing anchors. Furthermore, the longitudinal and stirrup reinforcement near the beam heads was also observed to corrode, resulting in visible cracking and spalling of the concrete cover. The T-beams were designed to support the full load of the beam through the prestressing bars, resulting in the minimum longitudinal and stirrup reinforcement being used. Corrosion of the mild steel reinforcement was thus permitted as they were not load-bearing. This would, however, greatly affect the concrete durability, eventually damaging the prestressing over time.
For several structures in the Liggerkoppen Project, it was observed that the cone was cracked and/or spalling, revealing a corroding prestressing anchor (see Figure 3.1b). The corrosion of the prestressing

anchor would pose a serious structural risk, as it is the main load-bearing structure within the T-beam. Calculations performed by Royal-Haskoning revealed that the structural integrity of a beam would still be met if one prestressing bar were to be compromised [4].

The corrosion initiation was attributed to leaking joints between the spans. De-icing salts from the road above would leak into the joints and deposit on the surfaces near the beam heads and support beams, resulting in corrosion initiation shown in Figure 3.1. The damage was most prominent at the abutments, as they used rubber or bituminous joints compared to the flexible concrete joints at the middle supports. These flexible joints were, in theory, immune to leakage of this kind, due to the concrete being continuous and solid. However, later inspections would reveal damage at these flexible joints as well.

In 2011, Rijkswaterstaat commissioned Royal-Haskoning to investigate the damages present within the Liggerkoppen Project with a focus on the structural safety of the affected structures [48]. Risk categories were devised to predict long-term structural safety as a foundation for future repair strategies. The 2011 report proposed several repair strategies listed below and shown in Figure 3.2.

1. Monitoring and replacement of the joints made out of rubber and bitumen. This limits the ingress of additional chloride from de-icing salts and prevents further penetration into the concrete.
2. Repairing the surface damage of the concrete and reinforcement. All loose and cracked concrete was removed, corroded reinforcement was treated and/or replaced, and new mortar was applied to repair the affected locations.
3. Installation of prefab blocks on either side of damaged beams. Thixotropic mortar was used in the beams, and a tension cord was installed on the bottom of the beam. The effective bearing capacity was increased by distributing the forces.
4. Application of passive cathodic protection (CP) on affected beams based on sacrificial anodes to protect the reinforcement. Reference electrodes must be installed to monitor the corrosion activity.
5. Application of active cathodic protection (CP) on affected beams to proactively prevent corrosion from (re)occurring. The continuity of the reinforcement was required before installation. Maintenance and monitoring of the installation must also be performed.
6. The last strategy was replacing the damaged beams with new prefab beams. This strategy would be applied when other repair methods were not feasible or could not be applied.

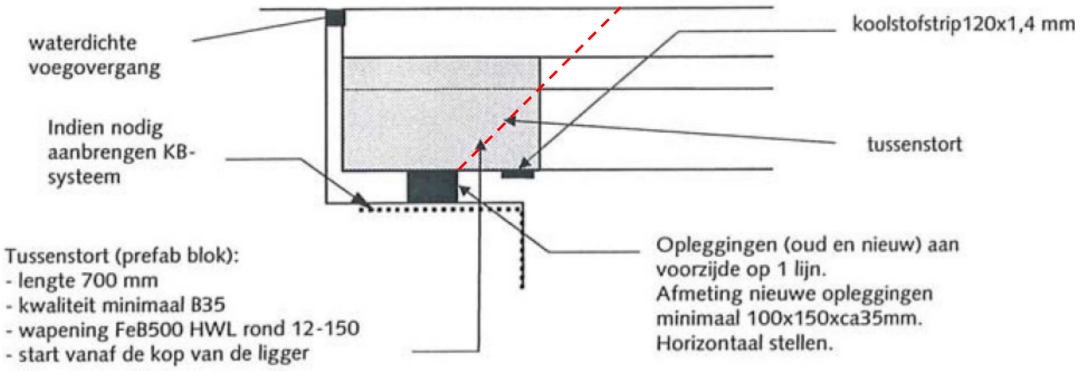


Figure 3.2: Schematic of the proposed repair strategies and where they are applied [4]

.

The 2011 report urged the replacement of all the vulnerable joints for structures within the Liggerkoppen Project. After replacement, they were to be monitored yearly for possible leakage. Secondly, a detailed

damage review was to be performed every 5 years for every structure to monitor damage progression and continually evaluate the risks. Lastly, for structures with a calculated remaining service life of more than 20 years, no intervention was required. All other structures should have active cathodic protection installed to extend the remaining service life. Guidelines were given for the installation of CP. Firstly, when CP was installed on a damaged beam head, the beams on either side of the damaged beam were also fitted with CP. Secondly, all beam heads should have CP installed when more than 50% of the beam heads at the given support need CP.

Rijkswaterstaat awarded the combination of Mourik-Salverda to carry out a 20-year maintenance program using the findings of the 2011 report. The objective of this program was to:

- Install active cathodic protection systems for all the affected beam heads in the Liggerkoppen Project deemed vulnerable.
- Monitor and maintain the installed cathodic protection systems.
- Track and assess new damage to the prefabricated T-beams not equipped with cathodic protection.

For all structures, inspections were scheduled at three fixed dates during the 20-year period. Namely, on the 4th, 9th, and 14th years after installing the CP systems.

The nearly identical Sluinerweg and Ardeweg viaducts were also part of the Liggerkoppen Project. They were located over the A1 Highway between Deventer and Apeldoorn and served regional traffic around Wilp and Twello, as shown in Figure 3.3. As part of the expansion of the A1 highway, the demolition of the two viaducts was necessary to accommodate the widening of the A1. The demolition of these two viaducts was planned for 2024, which prompted the research into these structures as an evaluation of the repair strategy used.

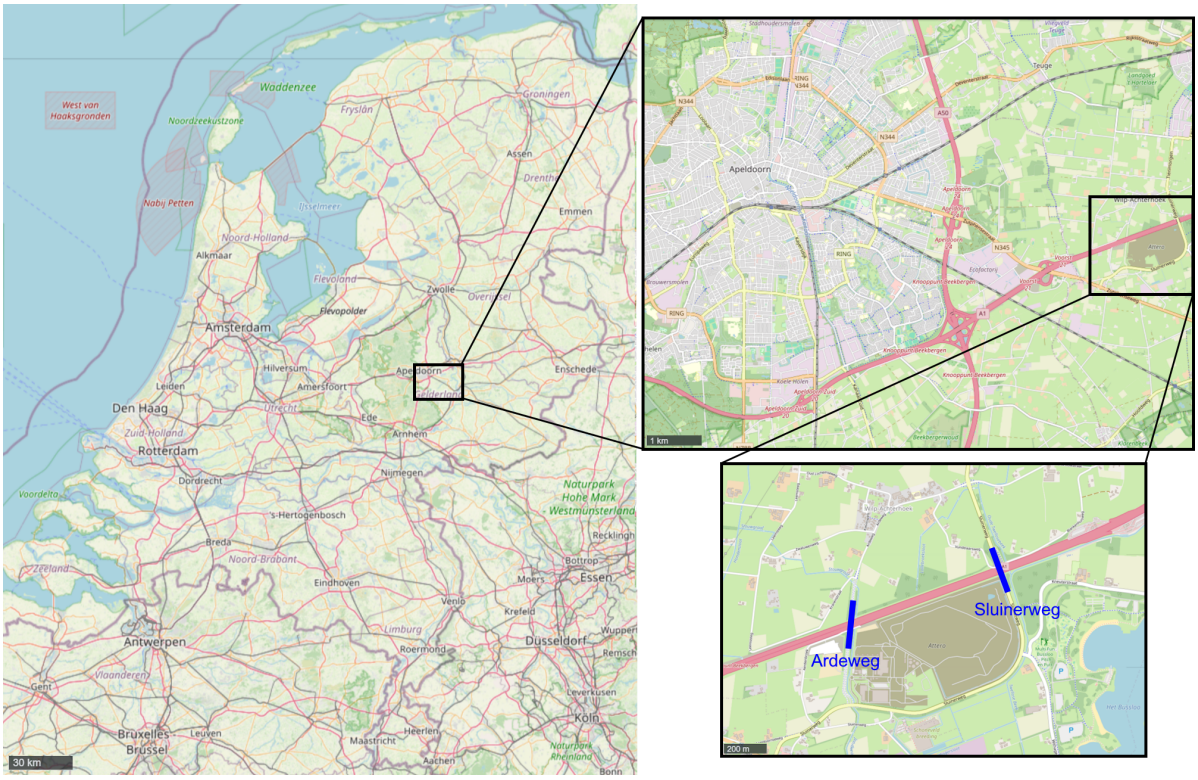


Figure 3.3: Locations of the Sluinerweg and Ardeweg viaducts near Apeldoorn.

## 3.1. Ardeweg viaduct

The Ardeweg viaduct was constructed around 1970 and has 4 spans made with the aforementioned prefab T-beams. Figure 3.4 shows a view of the viaduct. It has a total length of 79.5 meters and a width of 16.25 meters.

Figure 3.4: View of the Ardeweg viaduct as seen from the A1 heading to Deventer. The Aerdenbroek access road can be seen on the right.

The skewed viaduct crosses the A1 highway at an angle of approximately 65°, which can be seen in Figure 3.5. The viaduct serves as a regional road that facilitates mostly local traffic. The road atop the viaduct has a symmetrical design and includes two car lanes, two bike lanes, and sidewalks in both directions. A parallel road (Aerdenbroek) was located adjacent to the south side of the A1 highway, shown in Figure 3.4. This parallel road was transformed into an access road for construction vehicles for the nearby construction depot. The small road gives access to the abutment (STP5) and the southern side of the middle support (STP4).

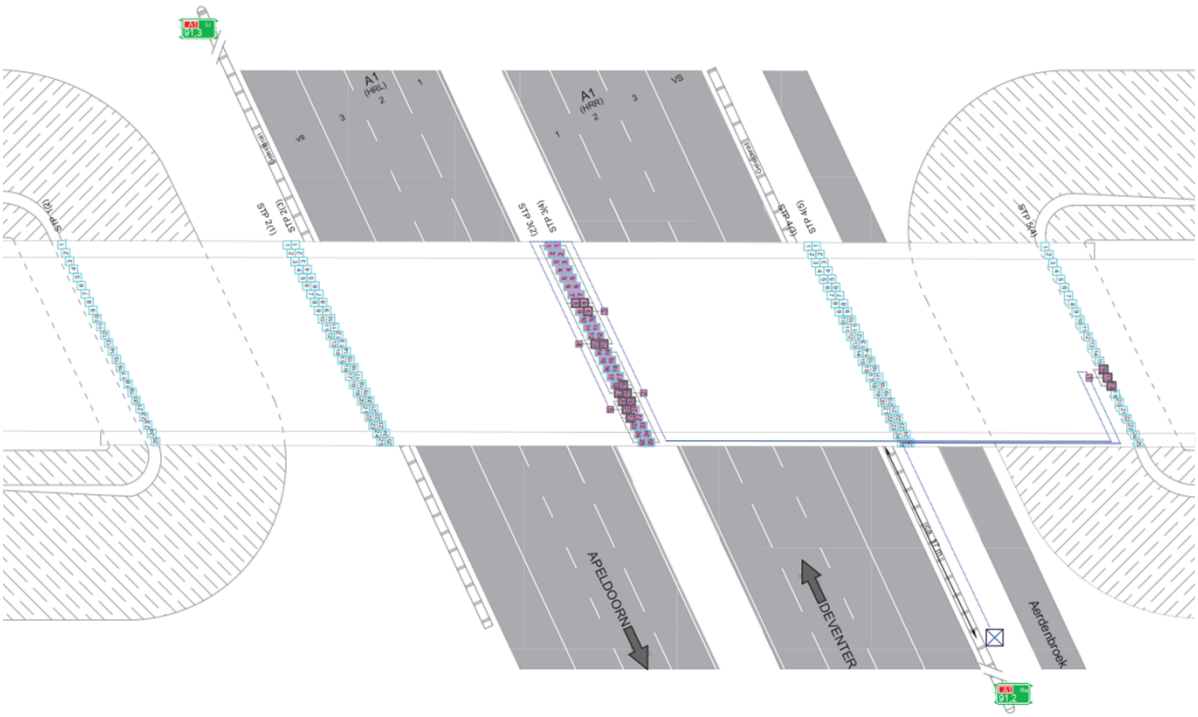


Figure 3.5: Plan of the Ardeweg viaduct. The CP system is visible in purple.

### 3.1.1. Design and structural properties

Three columned middle supports and two abutments at the ends support the four spans, each consisting of 25 T-beams fixed to each other with transverse tensioning bars. The two inner spans (and T-beams) are slightly longer than the outer ones, with a length of 20.95 meters and 18.95 meters, respectively. The abutments and middle supports are labeled consecutively from north to south as STP1 to STP5.

All the support beams and columns were coated with a Kristal Cement Graniet (KCG) coating, which consists of a layer of mortar that adheres granite granules to the concrete subsurface. This was a commonly applied finishing coating for aesthetic purposes at the time. It results in a very rough and uneven surface finish. The prefabricated T-beams did not have this coating.

Figure 3.5 shows the location of the installed active CP systems. All the beam heads at the support beam STP3 were protected using CP. At the southern abutment STP5, three more beam heads were protected (beam L16, L17, and L18). These CP systems were installed in stages around 2013 and 2019 as part of the 20-year repair strategy [49]. The CP system used was the cast$^{3+}$ composite anode system. This system uses a conductive coating that serves as an additional anode. The same CP system was also installed in the Sluinerweg viaduct and other Liggerkoppen projects. A more in-depth description of the system can be found in Section 3.3.5 of the Sluinerweg report [5, p.58].

The T-beams used in the Ardeweg viaduct were designed using Dywidag post-tensioned prestressing bars with tendon diameters of 32mm and 26mm. In the shorter outer spans, five bars were used per beam (4⌀32mm and 1⌀26mm), while the two longer inner spans used six prestressing bars (6⌀32mm). An overview of the cross-sections of the prefab T-beams is shown in Figure 3.6. The cross-section dimensions of the two T-beams are identical, with the only difference being the length of the beams and the number of prestressing bars.

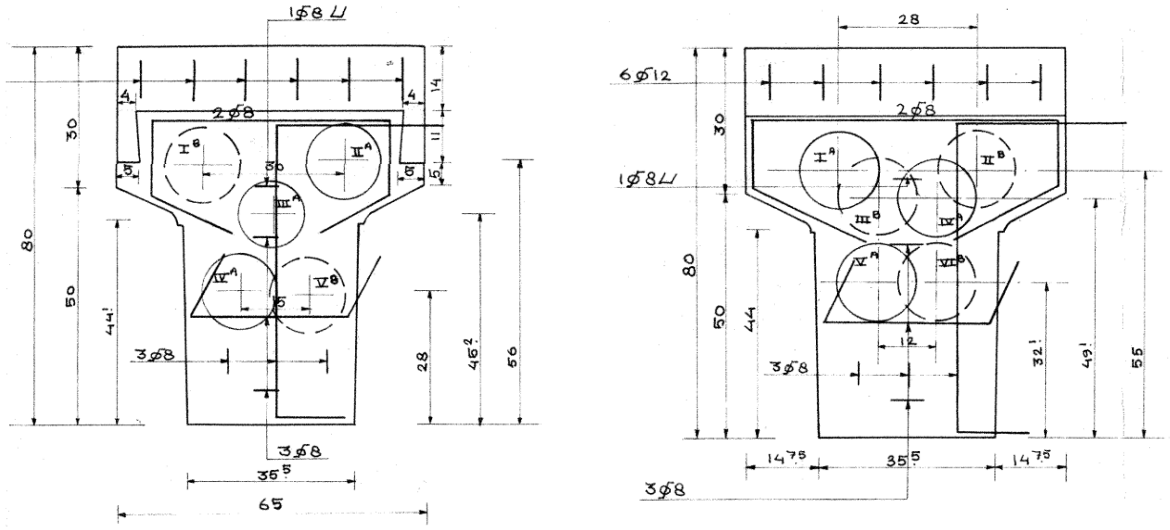


(a) Cross-section for the 18.95m beam with 5 bars

(b) Cross-section for the 20.95m beam with 6 bars

Figure 3.6: Cross sections of the T-beams with multiple prestressing bars. (a) shows the shorter T-beam used in the outer span, while (b) shows the longer beams used in the inner span. The cross-sectional view is from the north side [49].

### 3.1.2. Past Ardeweg inspections

The Ardeweg viaduct, like other structures in the Liggerkoppen Project, has had a history of damage near the beam heads. Inspections were performed in 2011, 2017, 2019, and 2022. The anchors of the prestressing bars, located at the beam heads, were the main concern for damage. Additional issues included joint leakage, insufficient concrete cover, visible corrosion products, and high chloride exposure in the support beams, indicating potential corrosion risks.

The 2017 and 2022 reports were part of a 20-year monitoring program, focusing on visual inspection of the prestressing anchors at the beam heads. All reports used the same five-level damage classification system introduced in 2011, with class one indicating minor damage and class five the most severe. An explanation of the damage classes and the history of the damages across the different reports can be found in Appendix A.

**2017 inspections**
The first known inspection report came in 2017, 4 years after the installation of the first set of CP in 2013. The performed actions are summarized below:

- Monitor the condition of the joints for possible leakage.
- Inspection of the beam heads up to 1 meter from the end of the beam.
- Report the positioning of the beams on the supports
- Visual inspection of the prestressing anchor using a mirror.
- Structural assessment of the prestressing bars.
- Registration of the damages in accordance with the risk classifications.

The 2017 inspection revealed more severe damage than expected. Significant moisture was observed on concrete surfaces beneath the joints, with more leakage observed along the longitudinal joints between the T-beams. These leaks damaged both the beam heads and the support beams, leading to cracking, delamination, and spalling at several locations. Examples are shown in Figure 3.7. Corrosion of the mild-steel reinforcement was present throughout the structure.

(a) Damaged concrete corner at support beam 4 (STP4) with signs of corrosion

(b) Visible leakage between the beam heads of beam 5 and 6 at STP5

Figure 3.7: Pictures taken of damage at the Ardeweg viaduct from the 2017 report [49].

From the damage report shown in Figure 3.8, it is revealed that only 9 beams were equipped with CP at the time. These were: L20-L22 from STP3(2), L18-L20 from STP3(4), and L16-L18 from STP5. These were not observed during this inspection.

Furthermore, an increase in damage was observed between 2011 and 2017. Damaged cones rose from 7 to 18, including two with the C5 damage classification. Concrete damage at the beam heads increased from 3 to 12 locations. At STP4, a large section of the support beam was visibly damaged and corroded (Figure 3.7a), with moisture and calcium deposits present. This location at STP4 is also highlighted by Figure 3.8, which shows damage to the cones of beams L6-L9 in the beam heads of both spans. STP3 showed the most widespread damage, with numerous damage observations spread across the beams. Lastly, some miscellaneous observations seen during the 2017 inspections are listed below.

| Steunpunt | Soort voeg | inspectie-datum | Staven per ligger | 1 | 2 | 3 | 4 | 5 | 6 | 7 | 8 | 9 | 10 | 11 | 12 | 13 | 14 | 15 | 16 | 17 | 18 | 19 | 20 | 21 | 22 | 23 | 24 | 25 |
|---|---|---|---|---|---|---|---|---|---|---|---|---|---|---|---|---|---|---|---|---|---|---|---|---|---|---|---|---|
| Rijbaanindeling | | | | SK | | VP | | | | RB | | | | | | | | | | | | | VP | | | | SK | |
| STP 1 | Voeg | 3-7-2017 | 5 | 0 | 0 | 0 | 0 | 0 | 0 | 0 | 0 | 0 | 0 | 0 | 0 | 0 | 0 | 0 | 0 | 0 | 0 | 0 | 0 | 0 | 0 | 0 | 0 | 0 |
| | | | | | | | | | | | | | | | | | | | | C2 | | | | | | | | |
| | | | | | | | | | | | | | | | | | | | | R1 | | | | | | | | |
| STP 2 [1] | Bituum | 3-7-2017 | 5 | 0 | 0 | 0 | 0 | 0 | 0 | 0 | 0 | 0 | 0 | 0 | 0 | 0 | 0 | 0 | 0 | 0 | 0 | 0 | 0 | 0 | 0 | 0 | 0 | 0 |
| | | | | | | | | C3 | | | | | | | | | | | | | | | | | | | | |
| | | | | | | | | R1 | | | | | | | | | | | | | | | | | | | | |
| STP 2 [3] | Bituum | 3-7-2017 | 6 | 0 | 0 | 0 | 0 | 0 | 5 | 0 | 0 | 0 | 0 | 0 | 0 | 0 | 0 | 0 | 0 | 0 | 0 | 0 | 1 | 0 | 0 | 2 | 0 | 0 |
| | | | | | | | C2 | | | | | | | | | | | | | | | | | | | | | |
| | | | | | | | R1 | | R2 | | | | | | | | | | | | | | | | | | | |
| STP 3 [2] | Bituum | 3-7-2017 | 6 | 0 | 0 | 4 | 0 | 0 | 4 | 0 | 0 | 0 | 0 | 0 | 0 | 0 | 0 | 0 | 0 | 0 | 4 | 0 | 0 | KB | KB | KB | 0 | 4 | 0 |
| | | | | | | | | | | | C2 | | | | | C1 | | | | | | | C2 | KB | KB | KB | | | |
| | | | | | | R1 | | | R1 | | R1 | | | | | R1 | | | | | R1 | | R1 | KB | KB | KB | | R1 | |
| STP 3 [4] | Bituum | 3-7-2017 | 6 | 0 | 0 | 0 | 0 | 0 | 0 | 0 | 0 | 4 | 0 | 0 | 0 | 0 | 0 | 0 | 0 | 0 | 0 | KB | KB | KB | 0 | 4 | 0 | 0 | 2 |
| | | | | | | | | | | | C5 | | | | | C1 | | | | | KB | KB | KB | C2 | | | | |
| | | | | | | | | | | | R2 | R1 | | | | R1 | | | | | KB | KB | KB | R1 | R1 | | | |
| STP 4 [3] | Bituum | 3-7-2017 | 6 | 0 | 0 | 0 | 0 | 0 | 0 | 0 | 0 | 0 | 0 | 0 | 0 | 0 | 0 | 0 | 0 | 0 | 0 | 0 | 0 | 0 | 0 | 5 | 0 | 0 | 0 |
| | | | | | | | | | C2 | C2 | | C5 | | | | | | | | | | | | | | | | | |
| | | | | | | | | | R1 | R1 | | R2 | | | | | | | | | | | | | | R2 | | | |
| STP 4 [5] | Bituum | 3-7-2017 | 5 | 0 | 0 | 2 | 0 | 0 | 0 | 0 | 0 | 0 | 0 | 0 | 0 | 3 | 0 | 0 | 0 | 0 | 0 | 0 | 0 | 0 | 0 | 0 | 0 | 0 | 0 |
| | | | | | | | | | C2 | C1 | C2 | | | | | | | | | | | | | | | | C2 | | |
| | | | | | | | | | R1 | R1 | R1 | | | | | R1 | | | | | | | | | | | R1 | | |
| STP 5 | Voeg | 3-7-2017 | 5 | 0 | 0 | 0 | 0 | 0 | 0 | 0 | 0 | 0 | 0 | 0 | 0 | 0 | 0 | 0 | KB | KB | KB | 0 | 0 | 0 | 0 | 0 | 0 | 0 |
| | | | | | C2 | | | | | | | C2 | | | | | | | KB | KB | KB | | | | | | | |
| | | | | | R1 | | | | | | | R1 | | | | | | | KB | KB | KB | | | | | | | |

Figure 3.8: Damage analysis of the Ardeweg viaduct from the 2017 report [49]

- The existing CP system was not operational during the inspection due to the theft of the solar and power supply.
- At STP5, the stainless steel tubes for the CP system's cabling had noticeable corrosion damage.
- Visual inspection of the beam heads with mirrors was proven hard due to several factors:
  - The support beams were very wide. Getting to the end of the beam head was a distance of approximately 1-1.5 meters.
  - The angle of the beams gave way to a preferred side for inspection.
  - EPS foam plates were placed between the beam heads and abutments, which prevented visual clearance.
  - Some shearing blocks were installed between beams to resist horizontal forces. These prevented inspections at certain locations.
- Three of the five shearing blocks showed signs of mechanical damage.

The report proposed the installation of CP for all beam heads with risk class R1 and above (function loss expected within 10 years or less). As shown in Table 3.1, 65 beam heads were identified using the adjacency guideline. Since CP coverage exceeded 50% at STP3(2) and STP3(4), the final proposal was to install CP on all beam heads of this middle support.
Of the proposed measures, only the CP systems for STP3(2) and STP3(4) were implemented. The CP installation for STP1 and STP2 was financially not worth it due to the limited damage observed. Instead, these beams were to be closely monitored in the follow-up inspections. The CP systems for STP4 and STP5 were not installed due to uncertainty in the health of the support beams.

**2019 inspections**
The 2019 report was not part of the periodic maintenance inspections, but focused solely on the support beams. Specifically, the two abutments (STP1, STP5) and the middle support (STP3) were inspected.

Table 3.1: Proposed number of beams for CP installation after the 2017 inspection (50% ruling not yet applied).

| Support beam | Existing CP | Proposed CP | Total CP | Percentage |
|---|---|---|---|---|
| STP1 | 0 | 3 | 3 | 12% |
| STP2(1) | 0 | 3 | 3 | 12% |
| STP2(3) | 0 | 5 | 5 | 20% |
| STP3(2) | 3 | 18 | 21 | 84% |
| STP3(4) | 3 | 10 | 13 | 52% |
| STP4(3) | 0 | 9 | 9 | 36% |
| STP4(5) | 0 | 11 | 11 | 44% |
| STP5 | 3 | 6 | 9 | 36% |
| **Total** | **9** | **65** | **74** | - |

The inspection of the support beams was commissioned by Rijkswaterstaat due to the concerning moisture damage observed in 2017.
The report's objective was to monitor the amount of damage present and review the need for the proposed CP expansion. The inspection focused on corrosion, as the main damage mechanism was excess moisture. Several (semi-)NDT methods were used to monitor the support beams quantitatively. The used methods are listed below.

- Visual inspection
- Concrete cover
- Carbonation depth
- Chloride content
- Half-cell potential mapping

Only support beams STP1, STP3, and STP5 were observed during the inspection, which focused on the vertical front face and the horizontal top face of the support beams. Damage outside the scope was not considered in the corrosion assessment, although they were noted. The general scope of the investigated areas is shown in Figure 3.9, while Figure 3.10 details the measurement locations performed on STP5.

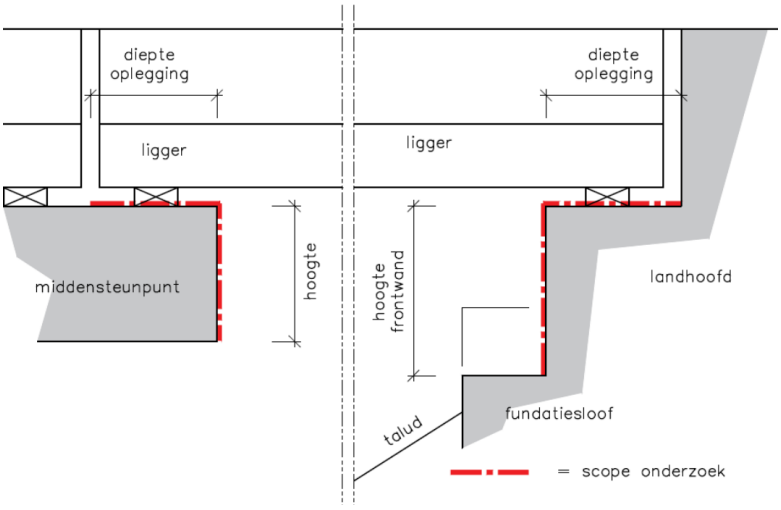


Figure 3.9: Overview of the scope where measurements were taken marked in red. Middle supports are on the left (STP3), and abutment support beams are on the right (STP1, STP5). The height of the middle support face is 0.8m, while the abutment height is between 0.3m and 0.4m [50].

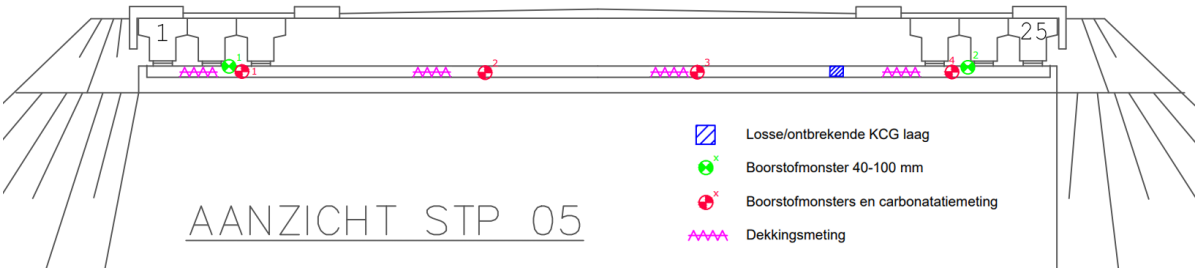


Figure 3.10: Overview of measurement locations on the STP5 support beam.

Concrete cover measurements were conducted on the vertical face of the three support beams using a rebar detector. Exposure classes XC4, XD3, and XF2, were determined to apply to the concrete elements in the Ardeweg viaduct, as defined by the EN-206-1. A minimum concrete cover of 40 mm is required in these conditions to ensure adequate protection of the reinforcement. Table 3.2 shows the results for support beam 5 at four locations (see Figure 3.10). Numerous measurements were performed at these locations, and the minimum and average cover was noted. The average cover met the requirement, while the minimum cover was lower than the required 40mm in some places.

Table 3.2: Concrete cover results from the 2019 measurements at STP5 [50].

| Location | Minimum cover [mm] | Average cover [mm] |
|---|---|---|
| STP5 1 | 35 | 44 |
| STP5 2 | 38 | 47 |
| STP5 3 | 41 | 46 |
| STP5 4 | 54 | 57 |

Carbonation depth measurements of the concrete cover were performed using phenolphthalein indicator. Fresh and cleaned boreholes were sprayed with the phenolphthalein solution according to NEN-EN 14630:2006. The observed color transition was linked to the carbonation front, which was measured at four locations for each support beam. The maximum carbonation depth of each support beam is shown in Table 3.3.

Table 3.3: Concrete carbonation front results from the 2019 measurements [50].

| Location | Max Carbonation depth [mm] |
|---|---|
| STP1 | 0 |
| STP3(2) | 3 |
| STP3(4) | 4 |
| STP5 | 0 |

Carbonation was not present in STP1 and STP5 of the viaduct. Middle support 3 had a maximum carbonation depth of 3-4mm. This was not concerning, given the depth of reinforcement and within expectations for a structure of this age.

Chloride concentrations were measured using the Rapid Chloride Test (RCT) method. The RCT method is a portable test kit used to determine the chloride content of gathered concrete powder. The powder is mixed with an extraction fluid that dissolves the chloride ions, which is later measured using a calibrated electrode to determine the amount of chloride ions present. An average cement content of 14% was assumed for the chloride percentage to be expressed in cement weight. Boreholes were drilled at four locations for each support beam (see Figure 3.10). Concrete samples were gathered from the vertical front face at three depths: 0-20mm, 20-40mm, and 40-60mm. Two additional samples per support

beam were taken from the horizontal face at a depth of 20mm from the top and 40-100mm from the front face.
The results for STP5 are summarized in Table 3.4. An elevated surface (0-20mm) chloride content was seen in all four locations, with the highest being at STP5-4, with a value of 0.4733, just below the critical threshold. The chloride content gradually lowered further into the concrete, except for STP5-1. The critical threshold of 0.5% was reached three times, indicated in red. These samples were taken between beams L2 and L3 at both the top and front faces.

Table 3.4: Chloride content for STP5 from the 2019 measurements [50]. The locations with an asterisk were gathered from the top face

| Location | Depth [mm] | Chloride [wt.%] |
|---|---|---|
| STP5-1 | 0-20 | 0,2940 |
| STP5-1 | 20-40 | 0,8615 |
| STP5-1 | 40-60 | 0,8022 |
| STP5-1* | 40-100 | 1,5620 |
| STP5-2 | 0-20 | 0,2490 |
| STP5-2 | 20-40 | 0,0031 |
| STP5-2 | 40-60 | 0,0000 |
| STP5-3 | 0-20 | 0,4039 |
| STP5-3 | 20-40 | 0,2751 |
| STP5-3 | 40-60 | 0,0045 |
| STP5-4 | 0-20 | 0,4733 |
| STP5-4 | 20-40 | 0,3504 |
| STP5-4 | 40-60 | 0,0047 |
| STP5-2*[1] | 40-100 | 0,3374 |

The half-cell potential was mapped for the vertical front faces of STP1, STP3(2), STP3(4), and STP5, as shown in Figure 3.9. The values were measured using a multimeter and a Cu/CuSO4 reference electrode, which were then mapped. The continuity of the rebar was confirmed before measurements started to be below 1 Ω. The produced potential map of STP5 is shown in Figure 3.11.
The potential map shows two rows of measurements on the front face of the support beam and a measurement between each beam on the top face. On the left side of the support (beam L1-L3), a zone with lower potentials is seen with values under -250 mV. The rest of the support shows varying potentials with some lower values around the CP beam (L17). Except for the left zone, the potential values of STP5 do not exceed -200 mV.

Based on the performed measurements, several conclusions for STP5 were drawn.

- Carbonation at STP5 was not observed. This, together with the measured minimum concrete cover of 35mm and average cover of 44mm, made it unlikely that the carbonation front would reach the reinforcement in the coming decades.
- An increased surface chloride content at all four locations was measured with a maximum value of 0.47% at location STP5-4. At three of the four locations, increased chloride content was measured at the reinforcement (depth 20-40mm). The maximum value was at STP5-1 with 0.86%, well over the critical threshold. When observing the 40-100mm sample, the chloride content increases to an even higher value of 1.5%.
- The half-cell potential map shows a low potential zone near the left side of the support beam. The low potential values in combination with the sudden change in potential indicate potential corrosion here. This location coincides with the increased chloride content observed earlier, consolidating the possibility of corrosion.

[1] Although the top face RCT test result is named STP5-2*, it is more closely located to the STP5-4 as shown in Figure 3.10. The STP5-2* concrete sample was gathered from the top face of the support beam between beams L23 and L24.

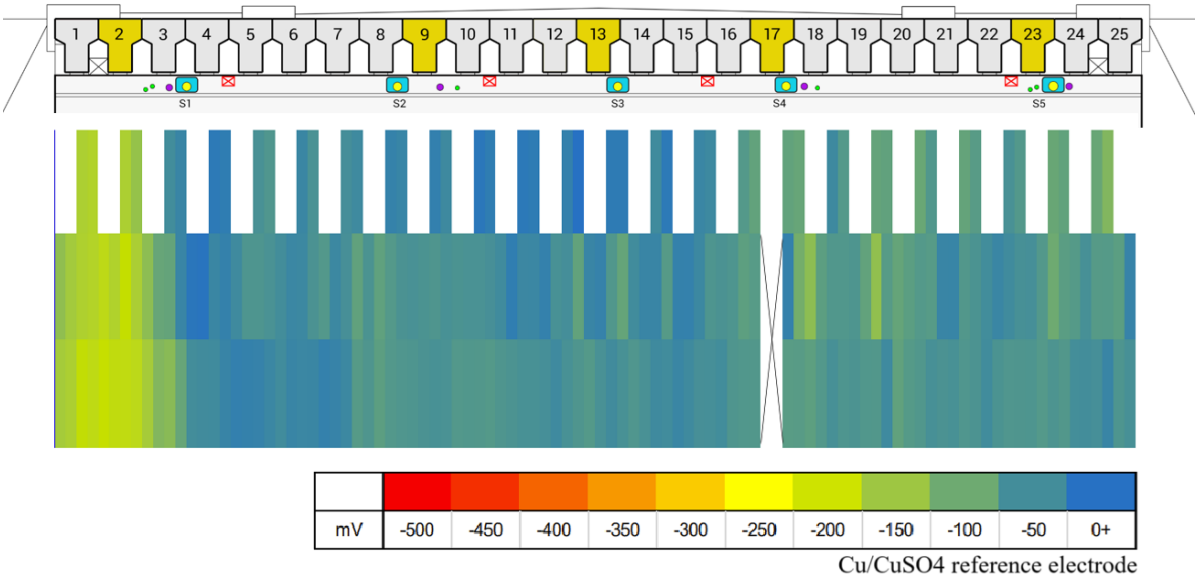


Figure 3.11: Potential map of the STP5 support beam from the 2019 measurements [50].

Due to the elevated chloride levels and the measured potential values at STP5, it was proposed to seal the expansion joints to protect the beams from further chloride ingress. Also, applying a polymer-based protective coating was advised to protect the support beam further. Lastly, periodic inspections and monitoring of the support were to be performed.

### 2022 inspections

The last reported inspection of the Ardeweg viaduct was performed in 2022. This was the second periodic inspection, as part of the 20-year maintenance program, with 2017 being the first one. The objectives and methodology of the inspection are similar to the 2017 report.
Figure 3.12 shows an overview of the observed damages and classifications. No discernible increase in concrete damage to the beam heads was observed. However, some new damaged cones were seen. The number of damaged beam heads has decreased compared to the 2017 report. This was in part due to the performed repairs on the damaged beams and the installation of CP along STP3.

| Steunpunt | Inspectiedatum | Voeg | per ligger | 1 | 2 | 3 | 4 | 5 | 6 | 7 | 8 | 9 | 10 | 11 | 12 | 13 | 14 | 15 | 16 | 17 | 18 | 19 | 20 | 21 | 22 | 23 | 24 | 25 |
|---|---|---|---|---|---|---|---|---|---|---|---|---|---|---|---|---|---|---|---|---|---|---|---|---|---|---|---|---|
| STP 1(2) | 23 juni 2022 | Voeg | Liggerkop | | | | | | | | | | | | | | | | | 1 | | | | | | | | |
| | | | Conusvulling | | | | | | | | | | | | | | | | | C2 | | | | | | | | |
| | | | Risicoklasse | | | | | | | | | | | | | | | | | R1 | | | | | | | | |
| STP 2(1) | 10 mei 2022 | Bituum | Liggerkop | | | | | | | | | | | | | | | | | | | | | | | | | |
| | | | Conusvulling | | C2 | | | | | | | | | | | | | | | | | | | | | | | C2 |
| | | | Risicoklasse | | R1 | | | | | | | | | | | | | | | | | | | | | | | R1 |
| STP 2(3) | 10 mei 2022 | Bituum | Liggerkop | | | | | | 4 | | | | | | | | | | | | | | | | | 2 | | |
| | | | Conusvulling | C2 | C2 | | | | C5 | | | | | | | | | | | | | | | | | | | C2 |
| | | | Risicoklasse | R1 | R1 | | | | R2 | | | | | | | | | | | | | | | | | | | R1 |
| STP 3(2) | n.v.t. | Bituum | Liggerkop | KB | KB | KB | KB | KB | KB | KB | KB | KB | KB | KB | KB | KB | KB | KB | KB | KB | KB | KB | KB | KB | KB | KB | KB | KB |
| | | | Conusvulling | KB | KB | KB | KB | KB | KB | KB | KB | KB | KB | KB | KB | KB | KB | KB | KB | KB | KB | KB | KB | KB | KB | KB | KB | KB |
| | | | Risicoklasse | | | | | | | | | | | | | | | | | | | | | | | | | |
| STP 3(4) | n.v.t. | Bituum | Liggerkop | KB | KB | KB | KB | KB | KB | KB | KB | KB | KB | KB | KB | KB | KB | KB | KB | KB | KB | KB | KB | KB | KB | KB | KB | KB |
| | | | Conusvulling | KB | KB | KB | KB | KB | KB | KB | KB | KB | KB | KB | KB | KB | KB | KB | KB | KB | KB | KB | KB | KB | KB | KB | KB | KB |
| | | | Risicoklasse | | | | | | | | | | | | | | | | | | | | | | | | | |
| STP 4(3) | 8 maart 2022 | Bituum | Liggerkop | | | | | | | | | | | | | | | 2 | | | | | 2 | 2 | 3 | | | |
| | | | Conusvulling | | | | | | C3 | | | | | | | | | | | | | | | | | | | |
| | | | Risicoklasse | | | | | | R1 | | | | | | | | | | | | | | | | R1 | | | |
| STP 4(5) | 8 maart 2022 | Bituum | Liggerkop | 2 | | 2 | | | | | | | | | | 2 | | | | | | | | | | | | |
| | | | Conusvulling | | | | | | | | | | | | | | | | | | | C3 | | | | | C2 | |
| | | | Risicoklasse | | | | | | | | | | | | | | | | | | | R1 | | | | | R1 | |
| STP 5(4) | 19 januari 2022 | Voeg | Liggerkop | | | | | | | | | 1 | | | | | | | KB | KB | KB | | | | | 1 | | |
| | | | Conusvulling | | C2 | | | | | | | | | | | | | | KB | KB | KB | | | | | | | |
| | | | Risicoklasse | | R1 | | | | | | | | | | | | | | | | | | | | | | | |

Figure 3.12: Damage overview of the Ardeweg viaduct from the 2022 report [51].

Figure 3.12 shows that 11 beam heads were expected to experience long-term function loss (within 10 years). It was advised to install CP for all the damaged (and their adjacent) beam heads, which is shown in Table 3.5. A total of 31 beam heads were proposed to be equipped with CP. The 50% ruling was not reached for any support beam.

Table 3.5: Proposed number of beams for CP installation after the 2022 inspection (50% ruling not yet applied).

| Support beam | Existing CP | Proposed CP | Total CP | Percentage |
|---|---|---|---|---|
| STP1 | 0 | 3 | 3 | 12% |
| STP2(1) | 0 | 5 | 5 | 20% |
| STP2(3) | 0 | 8 | 8 | 32% |
| STP3(2) | 25 | 0 | 25 | 100% |
| STP3(4) | 25 | 0 | 25 | 100% |
| STP4(3) | 0 | 6 | 6 | 24% |
| STP4(5) | 0 | 6 | 6 | 24% |
| STP5 | 3 | 3 | 6 | 24% |
| **Total** | **53** | **31** | **84** | - |

The plans for further installation of the CP system were never carried out due to the planned expansion of the A1. The planned 2024 demolition ended the need for further inspections, making this the last inspection of the Ardeweg viaduct.

## 3.2. Sluinerweg viaduct

The closely located Sluinerweg viaduct was constructed in the same period as the Ardeweg viaduct and uses the same prefab T-beams. The Sluinerweg viaduct crosses the A1 perpendicularly, making it slightly smaller than the Ardeweg. It measures 76m in length and 14.95m in width, with 23 T-beams per span. All four spans use the shorter 18.95m prefab T-beams, each with 5 prestressing bars. An overview of the two viaducts and their properties is shown in Table 3.6. The main differences between the two viaducts are the larger size, orientation, applied CP, and observed damages.

Table 3.6: Overview of the technical specification for the Ardeweg and Sluinerweg viaducts.

| | Ardeweg | Sluinerweg |
|---|---|---|
| Construction year | 1970 | 1970 |
| Length | 79.5 m | 76 m |
| Spans | 2x20.95 m, 2x18.95 m | 4x18.95 m |
| Width | 16.25 m | 14.95 m |
| T-Beams | 25 per span | 23 per span |
| Prestressing | 5-6 tendons per beam | 5 tendons per beam |
| Orientation | Skewed (65°) | Perpendicular (90°) |
| CP | 50 beam heads (STP3)<br>3 beam heads (STP5) | 3 beam heads (STP1) |
| Inspections | 2011, 2017, 2019, 2022 | 2002, 2011, 2017, 2020, 2022 |

A comparison of inspection reports shows that, of the two viaducts, more extensive damage was found at the Ardeweg at both the beam heads and support beams. The Sluinerweg's support beams were inspected in 2020 using the same methodology as the 2019 Ardeweg report. The potential and chloride content results showed an unlikely chance of corrosion for all locations. Values for chlorides did not exceed the critical threshold for all locations, while the half-cell potential values did not fall below -200 mV [5].

The latest inspection report from 2022 identified 16 beam heads with expected long-term function loss, 13 of which were at the middle support (STP3). Although CP was recommended for the south side of the middle support (STP3(4)), installation was not carried out due to the viaduct's planned demolition.

### 3.2.1. Wilgenburg Report

The Sluinerweg viaduct is extensively covered in Wilgenburg's 2024 report [5], which includes detailed design specifications and further background information. The report developed a practical methodology for assessing concrete conditions using non-destructive tests while addressing practical challenges. The selected NDTs were: GPR, UPE, rebound hammer, UPV, half-cell potential, resistivity, and corrosion current density.

**Inspection results**

Measurements were conducted over three days in November 2023. The scope was constrained to measure only the northern abutment (STP1). Tendon ducts in the T-beams were also examined using the GPR and UPE. A total of 28 cores were taken for analysis of chloride content, carbonation, and compressive strength. Further details about the measurement procedures are provided in Chapter 4 and Appendix D of [5, p.65]. The inspection results are summarized below.

**Visual inspection**

The visual inspection revealed minor defects throughout the viaduct. At the support and T-beams, observed damages include minor corrosion, superficial cracking, efflorescence, and sulfur-rich black crusts. No inspection of the cones was performed.

**GPR and UPE**

The GPR successfully identified reinforcement layouts and the prestressing bars. Vertical line scans revealed the concrete cover depths to be approximately 9.7cm, matching prior measurements and outperforming standard cover meters in precision. A fitted dielectric constant of 6.1 was used for general measurements. GPR was also able to detect anchorage zones in the beam heads. Lastly, 3D scans were made using the area scan measurement data, which helped visualize the reinforcements and prestressing bars. However, measurements on CP-coated areas (beam L13) were unsuccessful due to interference with the conductive coating. No problems were encountered when using the GPR on the rough KCG coating.

The UPE was used to inspect the tendon ducts for faults in the injected mortar. It provided 3D imaging of the tendon ducts, indicating two main reflections which were linked to the prestressing ducts. No grouting defects were identified across 11 scans on six T-beams, although the interpretation of results was a challenge. The combined use of GPR and UPE would be an effective measurement tool as they complement each other's weaknesses.

Overall, the GPR was proven to be a capable and effective tool for the localization of reinforcement. It is especially useful for structures without drawings of the rebar layout. The application of the GPR is, however, hindered by conductive coatings and is less effective for deeper investigations behind reinforcements. The combination of GPR and UPE methods was useful in detecting grouting defects. The on-site visualization capabilities allowed for quick localization and analysis. However, the visual verification of the suspicious locations did not yield any noticeable defects, raising the question of the true effectiveness.

**Rebound hammer and UPV**

The rebound hammer tests show an increased spread for the support beam measurements compared to the T-beams. The results of the RH measurements are visualized with a boxplot in Figure 3.13. The median Q-value for the T-beams is noticeably higher than the support beam, with ranges between 69-73 and 42-46, respectively. Additionally, UPV measurements were performed at the same locations. These also yielded different transmission speeds, with a mean value of 4972 m/s for the T-beams and 3650 m/s for the support beam.

The results suggest a better concrete quality and higher compressive strength for the T-beams, as both RH and UPV results showed higher values. However, discrepancies between the two methods were seen in the results, as an increase in the Q-value did not directly translate to an increase in transmission speed. The influence of the small dataset, moisture, and different measurement placements was considered as a plausible explanation.

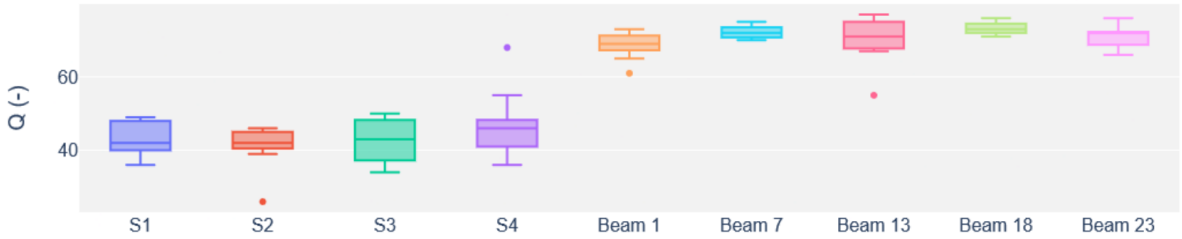


Figure 3.13: Boxplots for the rebound hammer Q-values of the Sluinerweg viaduct [5].

Existing Sonic Rebound (SonReb) models were also compared to the measurement results. However, this was proven difficult due to the use of mainly R-values in literature models as opposed to the Q-values gathered from the measurements. Conversion of these Q-values was required, which introduced additional uncertainty that was not worth pursuing by the author. Furthermore, the sole reliance on the UPV data was not preferred due to the sensitivity to moisture content. The compressive strength determination was thus based on the Q-value data and two conversion curves, which gave a mean cube compressive strength of 49.5 MPa and 28.0 MPa for the support beam and 94.5 MPa and 104.8 MPa for the T-beams.

The differing results from the conversion models raise questions about the usability of the RH on-site. The limited availability of Q-type hammer conversion models also presents challenges for the accurate estimation of concrete strength. The sensitivity for moisture content in concrete was the main challenge for using UPV. The literature shows consistently higher transmission speeds in lab environments compared to on-site measurements. Using the rebound hammer is simple and does not require extensive prior training for effective use. This, while the UPV is relatively harder to use. The author advises using UPV as a supplementary method next to the rebound hammer for strength evaluation.

**Half-cell potential**
Support beam potentials ranged mostly from -100 to 0 mV with both the Profometer and Gecor-10 measurement devices, indicating a low probability of corrosion. The spread and mean potentials of both devices were in agreement with each other, even with the Profometer having roughly ten times more measurements. This also resulted in the Profometer having more observed outliers. T-beams showed mostly positive potentials, often exceeding +200 mV, which was likely due to dense concrete or carbonation. No signs of corrosion were expected for both the support beam and T-beams.
Half-cell potential measurements proved stable and consistent between the different measurement devices. The use of the Profometer wheel electrode was effective in mapping large concrete areas. However, for smaller, tighter spaces, the wheel electrode was not as practical due to its size. The Profometer app helped allow for quick analysis during measurements on-site.

**Resistivity**
The T-beams measured with the Resipod reported high resistivity (3.36–4.49 $k\Omega m$), consistent with low corrosion risk. The support beam was measured with the Resipod and the two Gecor-10 sensors, which also reported high resistivity for all locations (0.98–4.82 $k\Omega m$). Discrepancies between the Resipod and Gecor-10 sensors were observed, with the former showing conservative but more stable values. The standard deviations of both Gecor-10 sensors were twice that of the Resipod. Furthermore, the mean resistivity of the Gecor-10 C-sensor is consistently around 1 $k\Omega m$ higher than the Resipod values. No corrosion risk was expected as almost all resistivity values exceed 1 $k\Omega m$.
The Resistivity results were less consistent between the Gecor and Resipod. A subsequent lab investigation was conducted by the author, resulting in a comparison between the two devices in a controlled environment. The moisture content was ruled out as a possible cause for the differences in resistivity. The use of the Resipod is preferred due to its better stability and conservative measurements. Due to its inconsistency and instability, the author does not recommend solely relying on the resistivity despite it being the fastest corrosion assessment tool.

**Corrosion current density**
Corrosion current density measurements confirmed negligible corrosion activity, with values between 0.02-0.13 $A/cm^2$. A clear trend showed higher $i_{corr}$ values at locations with lower potential and resistivity, validating the combined use of NDT analysis.
The corrosion current density was the only method able to calculate the rate of corrosion, which makes it an important corrosion assessment tool. However, on-site assessment is difficult due to the lengthy measurements and the expertise required. The Gecor-10 used is one of the limited corrosion rate measurement devices and requires analog logging of results, further impeding on-site assessment.

**Compressive strength**
Four cores were extracted from the support beam to be tested in compression. Three of them yielded representative strengths with a mean cylinder strength of 44.8 MPa and a standard deviation of 6.0 MPa. At the T-beams, six more cores were tested in the same manner. The resulting mean compressive strength and standard deviation were 82.2 MPa and 9.1 MPa, respectively. Both RH strength estimations were overestimated when compared to the true mean concrete strength.

**Carbonation**
Sixteen cores were analyzed for carbonation depth. For the support beam, the carbonation depth varied between 1.5–5 mm, while T-beams mostly had depths under 2.5 mm, with some deeper pits up to 18 mm. Pairs of cores showed noticeable variability, supporting the recommendations for paired sampling. The carbonation did not reach the reinforcement and was thus not considered a corrosion risk. Compared to the 2020 carbonation results, discrepancies were observed. The east side of the support beam showed a slight natural increase, while the west side showed a decrease in depth. These differences were likely due to the different test methods used.

**Chloride content**
The Chloride content determination proved very time-consuming. Only the first two slices (0-10 mm, 10-20 mm) of each core were investigated. However, the full profile of CL3 has been mapped, as it had the highest initial chloride content. Figure 3.14 shows the chloride profiles of the support beams and T-beams. The support beam showed overall higher chloride content.

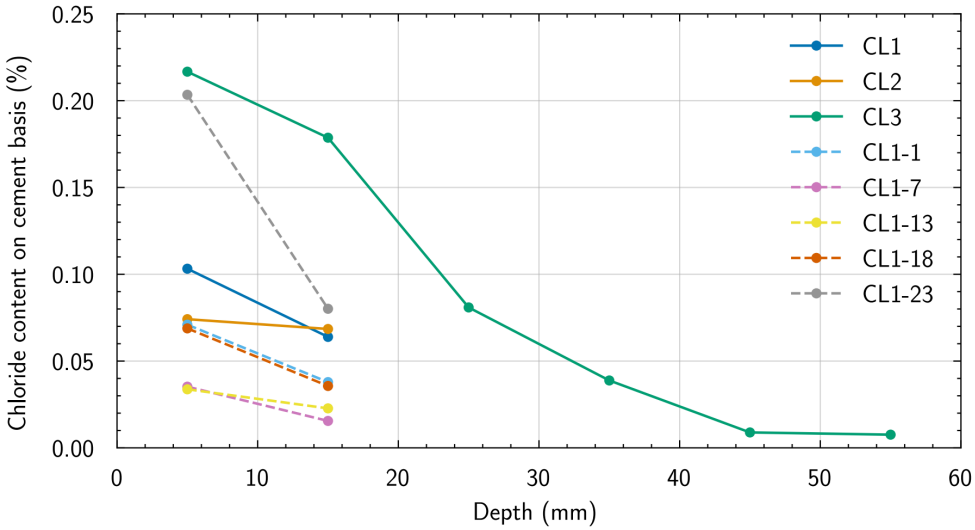


Figure 3.14: Chloride profiles of the Sluinerweg viaduct, with solid lines for support beam cores and dotted lines for T-beam cores [5].

The CL3 curve showed a good fit with Fick's second law for diffusion. All chloride content values did not exceed the critical value of 0.5%, indicating a low corrosion risk. These findings support earlier NDT results. Compared to the 2020 report, the newfound chloride values were consistently lower, likely due to the different methods used and the estimation of the cement content.

**Review earlier inspections**
The results of the inspections showed no indication of corrosion risk. The destructive verification also supports the results from the non-destructive tests. It is therefore concluded that the previous application of CP on the Sluinerweg viaduct was not necessary.
Previous inspections assessed chloride content only in the support beam and generalized findings to the T-beams, despite differences in concrete strength and chloride exposure. Limitations in coring led to sub-optimal sampling as cores could not be extracted close to the beam head. Chloride levels in the support beam were generally higher, supporting the idea that it could serve as an indirect indicator for the beam heads. The past inspection program was not ideal for its given objective, yet reasonable given the circumstances.

**Conclusions and recommendations**
The conclusions from the study can be found in chapter 7 of the Wilgenburg report [5, p.113]. A summary of the main conclusions is given below.

Several NDT methods proved to be reliable and correlated well with destructive results, supporting their usefulness in future inspections. No risk of corrosion was seen during the inspection, which raises questions about the inspection regimes used in the past and the necessity of the CP installations. Although suboptimal, the methods used were deemed reasonable given the complexity and accessibility of the project.

- The GPR was preferred over the cover meter due to its increased accuracy and user-friendly visualization capabilities. Cases where GPR cannot be applied are when measuring on conductive CP coatings and estimating rebar diameter.
- The KCG-layer did not pose any problems during measurement for all measurement devices.
- SonReb models should not be applied due to the need for structure-specific calibration.
- There is a lack of Q-value conversion models for the estimation of concrete compressive strength with the rebound hammer. The conservative model of EN 13791 would be acceptable to use as a lower bound.
- The Resipod was the most stable resistivity measurement device, but provided consistently lower values compared to the Gecor-10 Wenner probe. Subsequent lab tests revealed that the difference was less pronounced with active corrosion. The influence of moisture content was furthermore ruled out.

A practical methodology for viaduct inspection was proposed in [5, p.219], emphasizing the importance of trained personnel, environmental control during testing, and proper calibration settings. Key recommendations include starting GPR with a dielectric constant of 6–7, combining GPR and UPE, monitoring moisture content, and tiered application of corrosion methods depending on the severity of the observed corrosion.

For future research, the report suggests the following recommendations:

- Performing similar studies to improve the developed methodology and validate its efficacy.
- Performing a detailed cost-benefit analysis concerning the testing methods to encourage widespread use in the industry.
- Linking the R- and Q-values for the rebound hammer. A comparative study between these two hammers does not exist yet for ageing concrete.
- Investigate the resistivity parameter more in depth to improve corrosion assessment.
- Using the Giatec ICOR to test its ability to measure the corrosion rate without connection to the reinforcement.
- Investigate the influence of pulse duration on corrosion current density measurements.

## 3.3. Demolition

The Sluinerweg viaduct was demolished on February 26, 2024, and the Ardeweg viaduct followed on July 29, 2024. Both demolitions were carried out similarly due to their nearly identical designs. The key requirement was for the demolition to be completed overnight to minimize disruptions over this crucial international highway.

The process began with milling and removal of the asphalt road for recycling, exposing the underlying concrete structure. The outer spans were dismantled first, leaving the two inner spans over the A1 highway. These were removed using a specialized SPMT truck to transport them to a nearby demolition site (see Figure 3.15). Finally, the columns and support beams were demolished on site, completing the demolition within one night [52].


Figure 3.15: A SPMT truck lifting one of two inner spans to be transported for later research. Photo by Hans Broekhuizen [53]

.

The motivation to transport the whole inner span intact stemmed from the discovery of asbestos in the transverse prestressing anchors. To minimize health risks, these were to be dismantled by specialists at a later time. Another reason for preservation was to investigate the possible reuse of the T-beams.

### 3.3.1. Harvested Beam heads

During the demolition of the Ardeweg, five beam heads were harvested from the viaduct for further research. The five beam heads came from the southern outer span between STP4 and STP5, where the NDT measurements were performed. Specifically, beam heads L2, L13, L17, and L23 from STP5 and L3 from STP4 were harvested. The beams were cut to a length of approximately 2.5 meters and transported to an empty parking lot next to the Rijkswaterstaat office in Wolfheze for further investigation (see Figure 3.16).

Figure 3.16: The harvested beam heads from the Ardeweg Viaduct at the Rijkswaterstaat location in Wolfheze.

# 4

# Methodology

The methodology for the various measurement techniques is described in this chapter. This chapter outlines the choice of measurement devices, experimental procedures, data collection, and analysis strategies used.

## 4.1. Data acquisition

As a continuation of the previous Sluinerweg study, the use of the same measurement techniques was expected to review the overall practical methodology. The Ardeweg measurement plan is thus similar to the one utilized in the Sluinerweg inspection, with numerous NDT and DT techniques. Large amounts of quantitative data were gathered to ensure that the cross-validation between NDT devices and their destructive counterpart was possible.

Tables 4.1 and 4.2 outline the measurement devices and techniques used for both NDT's and DT's, respectively. Table 4.1 mentions the models of the devices used and their application in the overall measurement plan. Table 4.2 describes the methods, their application, and the general workflow.

Table 4.1: Overview of the used non-destructive tests and their application

| **Method** | **Device** | **Application** |
|---|---|---|
| Visual inspection | - | Localizing surface defects (presence cracks, corrosion) |
| GPR | Proceq GP8800 | localizing reinforcement<br>Cover depth<br>3D mapping |
| UPV | Proceq Pundit 200 | Compressive strength |
| Rebound hammer (Q&R) | Proceq Silver Schmidt OS8200<br>Proceq Original Schmidt | Compressive strength |
| Resistivity | Proceq Resipod<br>Gecor-10 | Corrosion risk |
| Half-cell potential[1] | Proceq Profometer PM8500<br>Gecor-10 | Corrosion risk |
| Corrosion current density[1] | Gecor-10 | Corrosion risk |

[1] Semi-destructive method. The concrete cover needs to be removed locally for a direct connection with the reinforcement.

Table 4.2: Overview of the destructive tests and their application

| Method | Application | Workflow |
|---|---|---|
| Standard compression test | Compressive Strength | Coring<br>Cutting to length<br>End polishing<br>Compression failure test |
| Carbonation | Corrosion risk | Coring<br>Splitting<br>Phenolphthalein testing |
| Chloride content | Corrosion risk | Coring<br>Slicing<br>Cement determination<br>Volhard titration |
| Thin section analysis | Microstructure Assessment | Coring<br>Sample preparation<br>Visual analysis microscope<br>Point counting |

The test methods were divided into two categories: strength assessment and corrosion risk. Strength assessment mainly focused on the use of the rebound hammer and UPV to predict the compressive strength of the concrete, while corrosion risk entailed the use of resistivity, half-cell potential, and corrosion rate measurements to map the corrosion risk for certain areas. Each NDT method had a destructive counterpart: compression tests for strength, and carbonation depth and chloride profiling for corrosion risk validation.

Compared to the Sluinerweg's testing program, the Ardeweg study included R-type rebound hammer measurements and thin-section analysis, while handheld XRF and UPE testing of tendon ducts were not included [1].
The R-type hammer was added to compare the Q and R hammer types for aging concrete, based on recommendations from the Sluinerweg study. The Thin-section analysis was conducted to study the concrete microstructure of the support beam at select locations. This was prompted by earlier reports, which showed a significant chloride content in the leftmost part of support beam 5. The microscopic analysis also aided in identifying defects in the concrete, like cracks, excessive air voids, and the overall soundness of the concrete.

In addition to the newfound data from the Ardeweg, historical data from the Ardeweg was also gathered from past reports. Especially the support beams analysis from the 2019 report provided quantitative data, which was used to develop the measurement plan and to compare with the newfound data [50]. Furthermore, the Sluinerweg viaduct, which was examined in November of 2023, was also used for further comparison [5]. The data from these reports was extracted for further comparative analysis. Raw datasets from the Sluinerweg measurements were provided by their author for the analysis of the (combined) results.

### 4.1.1. Data storage

Some devices were capable of logging the measured data internally or electronically. Most Proceq devices required connection to an iPad, which served as the user interface and uploaded data to the cloud. The GP8800 (GPR), Q-type rebound hammer, and Profometer (HCP) all required the use of the iPad, while the Resipod (resistivity) and Pundit 200 (UPV) were to be used as standalone devices. Lastly, the R-type rebound hammer was the only mechanical device. The Resipod and R-hammer

[1] Tests with the UPE were tried by a third party during the on-site inspections in June, but were not conclusive enough to report any valuable insights.

results were logged manually on paper. The Pundit 200 used its own user interface, which stored the data internally. The data from the other Proceq devices was gathered from the online environment. The Gecor-10 also stored the measured data internally, but due to its counterintuitive user interface, this functionality was not used. Manual logging in combination with photos of the result screen was used to store the data from the corrosion current density measurements.

### 4.1.2. Measurement locations

The measurement locations were chosen to be in line with the earlier inspections performed on both the Sluinerweg and Ardeweg viaducts for an optimal comparative analysis. Other factors, such as time, accessibility, and safety, also contributed to the determination of these locations.

The two southernmost support beams (STP4 and STP5) were chosen for the main measurement locations. Accessibility, costs, and safety were the most important considerations. The highway could not be closed off for the inspection due to its vital role as an international transport road. The costs would be unfeasibly high to guarantee safety when performing measurements in the middle supports (STP3) just above the highway.
This led to the abutments as the only potential choice for the inspection, with STP5 being the more interesting option given its damage history. The access road under the outer southern span (Aerdenbroek, see Figures 3.4 and 3.3) was closed during the inspections to guarantee the safety of the inspection crew. Furthermore, the same safety procedures as the Sluinerweg inspection were taken into account for the on-site measurements of the Ardeweg, which can be found in [5, p.65]. For example, a walking platform and physical barriers were installed to improve work conditions and safety.

Both the support beams and select T-beams were chosen to be inspected using the measurement techniques to align with the Sluinerweg measurements. An overview of the measurement locations for support beams 5 and 4 is shown in Figure 4.1.

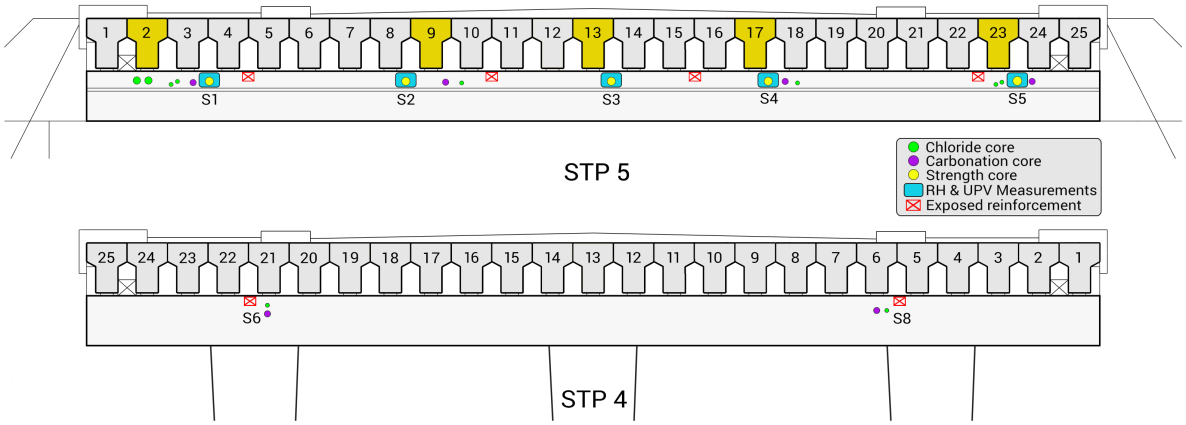


Figure 4.1: Schematic of the measurement locations for support beam 5. The colored circles indicate the different types of extracted cores. The investigated beam heads of the T-beams are highlighted in yellow.

**Support beams 4 and 5**

Five (mostly) evenly spaced locations at STP5 (S1-S5) were selected for strength testing. RH and UPV measurements were taken at these locations, after which cores were extracted to validate the concrete strength. For the corrosion measurements, the top half of the vertical face of STP5 was measured in its entirety with the resistivity, half-cell potential, and corrosion current density. In this manner, a direct comparison between the Sluinerweg and the 2019 Ardeweg data could be performed. At the four locations: S1, S2, S4, and S5, additional cores were extracted to be analyzed for chloride content and carbonation depth.
At STP4, no strength testing was performed to focus on the corrosion assessment with carbonation and chloride cores taken at two locations (S6 and S8).

**T-beams**
At T-beams L2, L13, L17, and L23, similar chloride and carbonation cores were taken, which roughly aligned with the locations of S1-S5 of the support beam. Additionally, the reinforcement was exposed at four locations as attachment points for potential and corrosion rate measurements, which are indicated with red crosses. The length of the Gecor-10 cable determined the spacing of these holes, as a connection with the reinforcement was necessary.
The choice to inspect T-beams L2, L9, L13, L17, and L23 was due to the damage history at the beam heads of these specific beams, as shown in Appendix B. L17 was already fitted with CP, while L2, L9, and L23 had existing damages at the cones or the beam itself. L13 was not previously damaged and served as a reference for further comparison. These different known damage classes provided insights into the damage history and will be linked to the obtained results to compare the influences.

**Harvested beams**
After the demolition of the Ardeweg viaduct, the four beam heads at STP5 (L2, L13, L17, L23) were harvested and further studied for corrosion risk assessment. This additional research was performed due to the inconclusive results obtained from the on-site measurements on the T-beam, as later described in Section 5.1. The harvesting of the beams also provided an opportunity to conduct measurements at locations closer to the beam heads that were not accessible on-site. The main focus of this set of measurements was the corrosion risk assessment of the T-beams, as well as the influence of distance from the beam head on corrosion measurements. The distance to the beam head was still an unknown variable that had not been quantified in previous literature and could provide valuable information for future inspection programs.

### 4.1.3. Measurement plans
Measurement plans were formulated for the on-site inspection in preparation for the measurements. These can be found in appendix B. The plans describe the general day-to-day planning with the performed activities, along with the location of each measurement and extracted core. An overview of all the measurement techniques used for both the Ardeweg and Sluinerweg viaducts can be seen in Figure 4.2. It shows all the measurement techniques utilized for the Sluinerweg and the two Ardeweg inspections. The overview shows the different categories for strength and corrosion, with other miscellaneous tests seen in the bottom row. A red marking indicates a destructive test that required an extracted concrete core.

Direct comparison of the results between different inspections was possible for almost all cases due to the acknowledgement of the prior inspections when developing the new measurement plan. The only exceptions are the carbonation and chloride measurements from the 2019 inspection, which used different on-site techniques described in Section 3.1.2.

## 4.2. Methods per measurement technique
This section details the measurement techniques and the procedures used for data collection and processing. For each NDT and DT method, the field or laboratory testing procedure is described.

### 4.2.1. Ground penetrating radar
The GPR was used to locate the reinforcement bars beneath the concrete. This is a critical step, as most subsequent measurements depend on accurate knowledge of the rebar positioning. For example, resistivity measurements must avoid direct placement over the rebar due to electrical interference. This is contrary to HCP and CR measurements, where the sensors need to be directly above the rebar for optimal accuracy. Furthermore, the extraction of the cores is also reliant on avoiding the rebar, especially for the compressive strength tests. The other uses of the GPR include the determination of the cover depth, as well as developing 3D imaging of the reinforcement nets.

At the support beam, horizontal line scans on the front face were performed to locate the vertical stirrups, while vertical scans located longitudinal reinforcement. These were then marked with concrete chalk for later measurements. The same procedure was used for the T-beam.

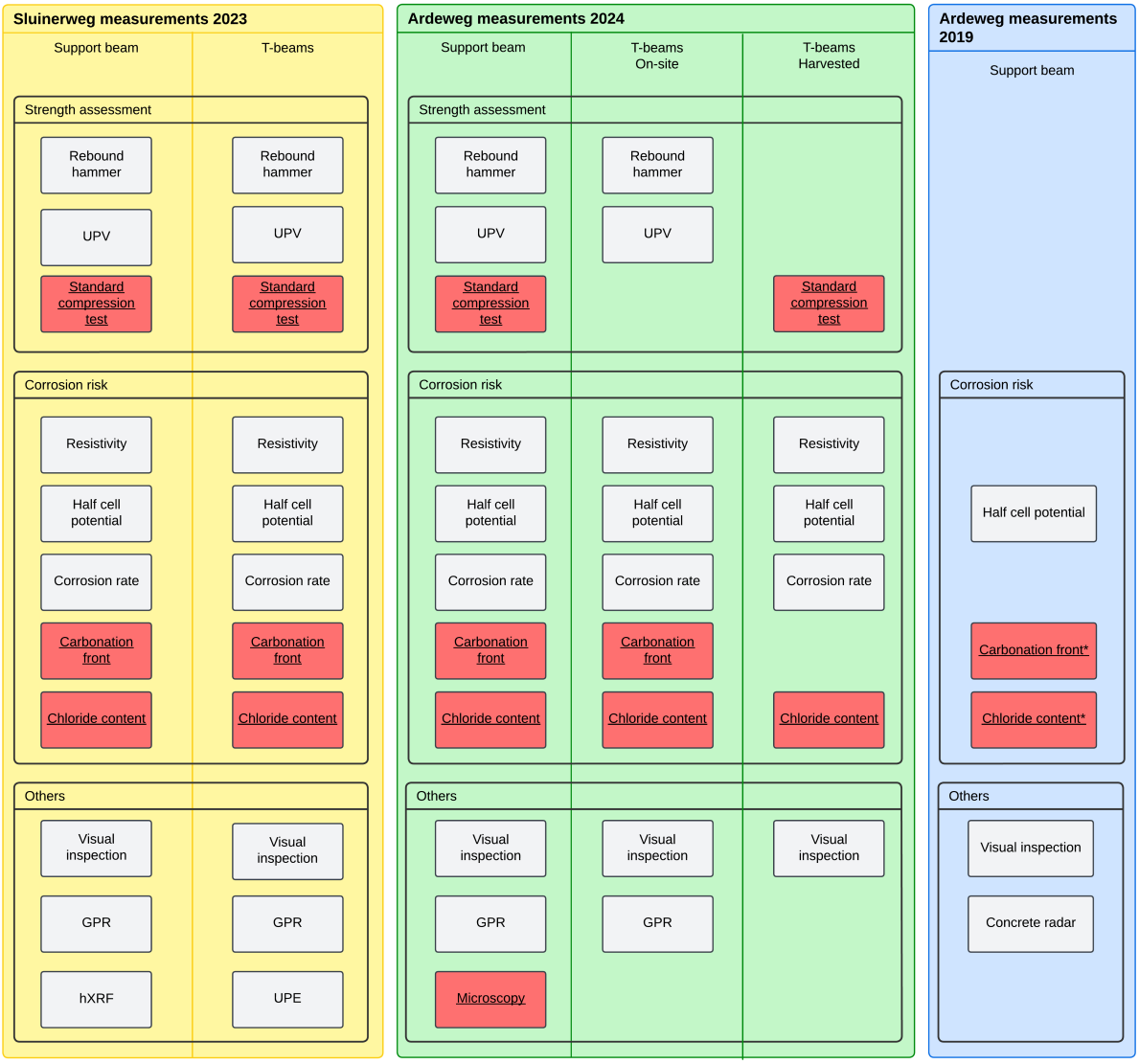


Figure 4.2: Overview of all the used measurement techniques for both the Ardeweg and Sluinerweg viaduct. The 2019 Ardeweg inspection is also included. Red indicates a destructive method, while gray indicates an NDT method.

Area scans were also performed for the T-beams and parts of the support beam to map the reinforcement for cover depth analysis. From the Sluinerweg report [5, p.69], a dielectric constant of 6 was used as a starting value for imaging. After exposure of the reinforcement, the dielectric constant was determined by comparing GPR-derived and visually confirmed cover depths. Care was taken to apply the GPR device as close as possible to the concrete surface to ensure consistent depth readings. The uneven surface coating of the support beam did hinder this process slightly.

All of the GPR scans were saved in Proceq's online environment. The scans were able to be edited afterwards to improve the results. This was done for the cover depth analysis, whereby the dielectric constant was refined with the measured cover depths. 3D scans were also altered to differentiate between the mild steel reinforcement and the prestressing bars.

### 4.2.2. Rebound hammer

Rebound hammer measurements were performed on the measurement locations using both R- and Q-type hammers. Both hammers were calibrated with a reference anvil before use, as instructed in the manual. To study the influence of the KCG coating, measurements were taken with and without the

coating for both hammers. After the first round of measurements with both hammers, the coating was removed with a normal steel hammer to expose the bare concrete surface. Another round of tests was then performed at the same locations.

At each location, at least 12 measurements were taken in an area of 15x15cm. A 3×4 grid with at least 25mm spacing was used for consistency, following NEN-EN 12504-2 [39]. Measurement results for the mechanical R-type hammer were written down, while measurements with the Q-type hammer were digitally saved and stored online. The support beam measurements were performed on the vertical front face, while the T-beam measurements were performed on the bottom surface of the beams. The orientation of the hammers was kept at a constant angle between measurements to prevent any bias. The orientation of the used hammer was noted for all measurements. Non-valid measurements far from the mean measured values were noted and repeated.
All rebound values were stored in Excel to perform preliminary statistical analysis. The median, average, and standard deviation were calculated for each measurement location after identification of outliers.

### 4.2.3. Ultrasonic pulse velocity

UPV measurements were performed to assess the internal quality and uniformity of the concrete. A Proceq Pundit 200 was used with the 54 kHz transducers following NEN-EN 12504-4 [54]. Measurements were taken at the same locations as the RH measurements. For STP5, a semi-direct transmission method was used with transducers placed on the front and top face of the support beam, with a distance of 150mm from the corner. For the T-beams, the direct transmission method was applied to the beam web. The width of the T-beam was measured after the measurements. Coupling gel was required for the transducers to measure the signal through the KCG coating accurately. Furthermore, multiple measurements were taken at each location.

The measurement data was locally stored on the Pundit 200 device, which was transferred to a computer after the measurements were completed. The proprietary ”PL-Link” software was used to extract this data and transfer it to an Excel database.

### 4.2.4. Corrosion assessment

The corrosion assessment included the use of resistivity, half-cell potential, and corrosion current density measurements to estimate the corrosion risk. The used equipment included the Proceq Resipod for resistivity measurements, the Proceq Profometer PM8500 for half-cell potential mapping, and the Gecor-10 for corrosion current density measurements. Furthermore, the Gecor-10 also measured half-cell potential and resistivity when a corrosion current density measurement was performed.
Half-cell potential measurements were conducted following NEN-EN 1504-10 to identify areas with a high probability of active corrosion. For the resistivity measurements, the recommendations from the RILEM TC 154-EMC were followed [55]. For the potential and corrosion current density measurements, an electrical connection with the reinforcement was required as mentioned in section 4.2. The general workflow is described by Wilgenburg [5] and summarized in Figure 4.3.

1. Verify electrical continuity along the rebar.
2. Measure concrete resistivity using both Resipod and Gecor-10 Wenner probes on moist concrete.
3. Perform half-cell potential measurements with the clamp connected to the rebar.
4. Assess the corrosion risk and use that to determine the polarization time for the CR measurement
    - Low corrosion risk → Set polarization time to 100 seconds
    - Moderate/high corrosion risk → Set polarization time to 30 seconds
5. Perform CR measurement with the determined polarization time
6. Note results and reflect on alignment with resistivity and half-cell potential

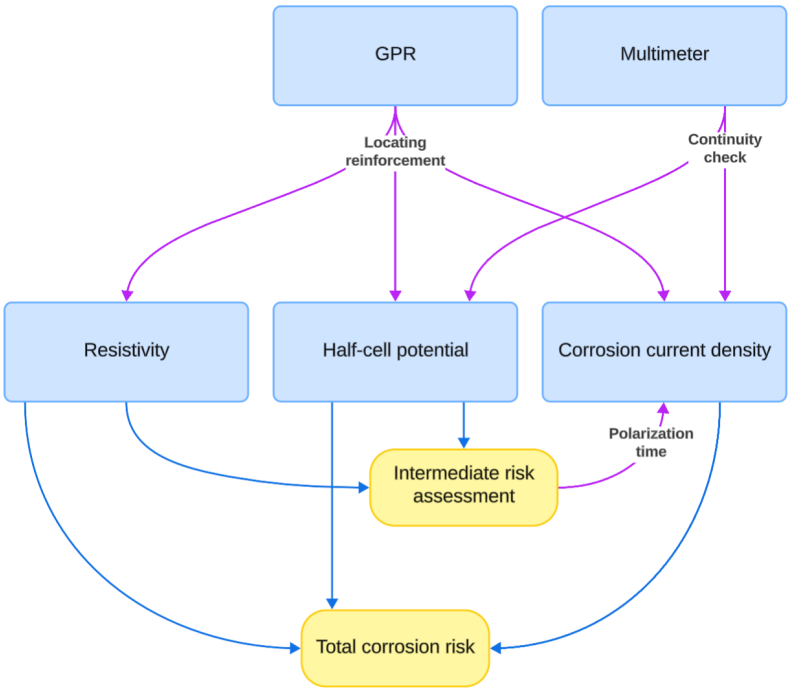


Figure 4.3: Overview of the workflow for the corrosion risk assessment.

An intermediate assessment is necessary to determine the polarization time for the corrosion rate measurement. This setup for CR measurement was chosen as the polarization duration affects the CR value measured. Care was taken to compare the corrosion risk classes of the values gathered with different techniques before and after the CR measurements were taken.

The workflow for the harvested beams was similar to the one used in the field tests. The resistivity and half-cell potential were both measured before any CR measurements were performed. For all harvested beams, both 30s and 100s polarization times measurements were performed to investigate the influence of polarization time. Care was taken to prevent measurements from being taken directly after each other. Otherwise, the polarization current in the reinforcement cannot dissipate and will affect subsequent measurements.

### 4.2.5. Concrete coring

A total of 39 cores were extracted from the Ardeweg viaduct (see Table 4.3). The cores for compressive strength had a diameter of around 100mm and a minimum length of 140mm. The requirement for a 1:1 core indicates a length of 100mm, but the additional thin-section analysis from the same core samples and some overhead for grinding was calculated in the required length.

Table 4.3: Overview of the extracted concrete cores for the Ardeweg viaduct

| Location | Strength | Chloride | Carbonation | Total |
|---|---|---|---|---|
| STP5 Support beam | 5 | 8 | 4 | **17** |
| STP5 Beam heads | - | 4 | 4 | **8** |
| STP4 Support beam | - | 2 | 2 | **4** |
| STP5 Harvested beam head | 4 | 6 | - | **10** |
| **Total** | **9** | **20** | **10** | **39** |

The carbonation and chloride cores had a diameter of 60mm and 40mm, respectively. The core length for chloride and carbonation was chosen to be at least 100mm to reach behind the cover and examine

the effects on the reinforcements. Due to structural safety concerns, cores for strength testing could not be extracted from the T-beams during the July (on-site) measurements. However, due to the harvesting of the beam heads, these cores were still able to be extracted successfully.

The cores for strength testing were taken from STP5 and the 4 harvested T-beams. The STP5 cores were drilled horizontally from the support beam, while the cores from the harvested beams were extracted vertically. The locations coincide with the Rh and UPV measurement locations and are shown in Figure 4.1. The chloride and carbonation cores were also extracted using the same orientations. It should be noted that the harvested beams were flipped to expose the bottom of the beam for easier core extraction.

The cores were extracted using the guidelines stated in NEN-EN 12504-1[56] and NEN-EN 13791[40]. This entails the use of a rigid and perpendicularly applied drill with a water source. Drilling in reinforcements was avoided as much as possible with the markings from GPR measurements. After extraction, cores were labeled with a name, the time of extraction, and the orientation. Lastly, cores were packed in watertight foil for transport and storage to facilitate further research.

### 4.2.6. Compressive strength

Nine 100mm cores were taken from STP5 (S1-S5) and the four harvested beams (L2, L13, L17, L23). Care was taken to extract the cores at the same location as where the RH and UPV measurements were taken. Core preparation followed NEN-EN 12504-1[56] and EN 12390-3[57], as detailed below.

- Unpacking the cores from their foil for measuring/visual inspection
- Trimming the cores with a saw to a length of ∼100mm to create a 1:1 core sample
- Grinding the ends with a polishing machine
- Final dimensions were measured and logged
- Samples were stored in a wet chamber for at least 48 hours before testing
- Samples were tested with a loading speed of $0.6\ Mpa/s$
- Test results were noted, and photos were taken of the failure mode and evaluated

### 4.2.7. Carbonation depth

Carbonation depth measurements were conducted to assess the extent of carbonation in the concrete, following NEN-EN 14630[58]. The cores were split along the longitudinal axis to expose a freshly broken surface. The fresh surface was cleared of dust and then sprayed with a 1% phenolphthalein solution. The indicator reacts with the pH of the concrete, turning pink in non-carbonated areas while remaining colorless in carbonated regions. The maximum carbonation depth is then measured and documented. Pictures of the cores are made for later evaluation.

### 4.2.8. Chloride content distribution

The chloride content distribution was gathered from chemical analysis using samples from the extracted cores. Firstly, the cores were cut into slices of 10mm or 20mm thickness, depending on the diameter and required resolution. The slicing was done using a wet sawing machine due to safety protocols and equipment availability. The slices were then hammered to obtain smaller and more workable granulates. The chloride content was determined using the Volhard titration method following NEN 5921 and NEN 3104, which are extensively described in the Sluinerweg report [5, p.79]. All titrations were performed in duplicate to ensure accuracy.

### 4.2.9. Thin-section analysis

Fluorescent epoxy-impregnated thin sections were prepared from the strength cores extracted from S1, S3, and S5. The thin sections were cut approximately 2–3 cm below the surface of each core to

ensure a representative concrete microstructure without surface deviations. Samples were vacuum-impregnated with a fluorescent epoxy resin and ground to an approximate thickness of 30 $\mu m$. The preparations were performed under the supervision of the lab technician and according to ASTM C856/C856m standards.
High-resolution scans of the thin sections were made using the Keyence VHX-7100 Digital Microscope, using the 20x and 50x magnifications to scan the entirety of the thin section. Image analysis was performed in JMicroVision, where point counting with a recursive grid was done to classify the area distribution of cement matrix, fine aggregate, coarse aggregate, and air voids. As the air voids were the main variable to be studied, no further distinction was made for the other components. At least 500 points were identified to ensure the statistical relevance of the analysis. The UV scans were enhanced and masked using binary thresholding to highlight the pores for better porosity distribution evaluation.

## 4.3. Data analysis

Most of the data analysis was performed within the Excel datasheet with the stored results. Descriptive statistics for each test method are described when relevant. Outlier removal and averaging of results at one sampling location are also performed for most methods. Descriptive statistics were computed to assess overall trends and variability. Mean, median, and standard deviation values were calculated for each measurement type and test location. This helped identify patterns across the viaduct.

Correlation analysis formed a key part of the interpretation of the results. Scatterplots were used to compare the different variables for the identification of possible trends. Regression fits were then implemented with the inclusion of the coefficient of determination ($R^2$).

### 4.3.1. Strength estimation

With the strength-oriented testing methods, several correlation studies have been performed. The performed correlation analyses are highlighted below:

- RH vs UPV
- RH vs tested core strength
- UPV vs tested core strength
- SonReb (RH and UPV) vs tested core strength
- Ardeweg RH vs Sluinerweg RH
- Ardeweg UPV vs Sluinerweg UPV

The correlations with the strength cores were performed using least squares regression techniques to obtain usable models for strength estimations. The single-method models (either RH or UPV) used linear regression fits, whereas the combined SonReb method utilized a power-law regression. Different models were developed based on outlier inclusion and carbonation corrections. The models are then visualized in a scatterplot to compare the estimated model strength with the true tested compressive strength.

### 4.3.2. Corrosion assessment

Cross-validation between the different corrosion devices was performed. Half-cell potential results from the Profometer and Gecor-10 were compared using paired scatterplots and correlation matrices. Similarly, resistivity values from the Resipod and Gecor-10 were compared to assess consistency across devices. The corrosion current density was also paired with both half-cell potential and concrete resistivity to study the impact and consistency of either metric.

Spatial trends were analyzed by mapping corrosion-related measurements across the support beam. Potential maps, chloride profiles, and resistivity heatmaps were compared to identify areas of high corrosion risk. Furthermore, historical data from 2019 were evaluated to assess changes over time.

Finally, the NDT results were validated using destructive testing data. Chloride content and carbonation depth were used to validate the NDT readings. Microstructural analysis from thin sections helped explain unexpected results, such as areas with low strength or increased porosity. Throughout the analysis, uncertainties and limitations due to equipment, measurement environment, or human error were acknowledged and considered in the interpretation of findings.

# 5

# Results on site Ardeweg measurements

This chapter presents the results of the measurements performed on the Ardeweg viaduct during the on-site inspection from June to July 2024. This includes both the NDT's performed on-site and the subsequent DT's performed in the lab.
The first set of measurements took place on June 24, 25, and 26, 2024, focusing on strength tests, some corrosion tests, and preparation of the inspection areas for the (semi-)DT's. On the 11th of July 2024, another round of tests was performed, focusing on corrosion assessment and extracting the remaining cores. An overview of the activities is provided in Table 5.1, with detailed measurement plans available in Appendix B.

Table 5.1: Summary of measurements performed

| **Date** | **Activities** |
|---|---|
| 24-06-2024 | Visual inspection<br>GPR scanning and rebar marking<br>RH tests on columns and STP5<br>UPV on columns |
| 25-06-2024 | GPR scanning and rebar marking<br>RH tests on STP5 and the T-beams<br>UPV on the T-beams<br>Exposing rebar at select locations<br>Extraction of cores STP5<br>Potential mapping of STP 4 and 5 |
| 26-06-2024 | Resistivity on T-beams<br>RH tests on STP5<br>UPV on STP5<br>Extraction of cores STP5 |
| 11-07-2024 | Resistivity on STP4, STP5 and T-beams<br>Gecor measurements on STP5 and T-beams (resistivity, potential and CR)<br>Extraction of cores STP4 and the T-beams |

## 5.1. Non destructive tests

### 5.1.1. Visual inspection and weather conditions

The first three days of measurements were sunny, with an ambient temperature of 23-26 °C. On the 11th of July, the ambient temperature was noticeably lower, at 19-21 °C. On all four days, no rain occurred, resulting in dry concrete surfaces. Due to the measurement areas' location under the viaduct, no direct sunlight came into contact with the concrete. The concrete surface temperature was not measured.
The visual state of the viaduct was assessed on the first day of measurements. The observed damage was mostly in accordance with the earlier reports. Some unreported corrosion damage was present, especially in the beams. Figure 5.1 shows several examples of the damage. Corrosion at several beams was noticed due to the lack of concrete cover (see Figure 5.1ab). When comparing the beams to the Sluinerweg, the surface finishing was subpar. At some locations on STP5 (mainly S1, S5, and under beam L17), existing boreholes were seen. These were remnants of previous inspections that had not been treated. The damaged location of S5 is shown in Figure 5.1. Lastly, corrosion damage was found on support beam 4, near the rightmost column (see Figure 5.1d). The exposed rebar indicates an active corrosion case. This case of damage was not reported in the earlier reports.

(a) **Minor corrosion damage on the side of beam 21**

(b) **Minor corrosion damage on the bottom of beam 14**

(c) **Existing boreholes from previous experiments at location S5**

(d) **Exposed reinforcement at the right side of support beam 4**

Figure 5.1: Spotted visual damage at the Ardeweg viaduct during the June inspections.

### 5.1.2. Concrete cover and GPR

The concrete cover at support beam 5 has been directly measured with a tape measure and with GPR scans at the four locations where the rebar was exposed, indicated by the red markings in Figure 4.1. These exposed locations only revealed the deeper longitudinal reinforcement, which was measured directly with a tape measure. The results of these measurements are shown in Table 5.2. The cover for the stirrups could not be measured directly as they were not exposed at these locations. The measured longitudinal cover distance was used to calibrate the GPR measurements, which were then used to calculate the stirrup cover distances. The cover distances of the four locations differ noticeably by quite a margin, with the highest distance being 132mm at location 1 between beams L4 and L5 and the shortest distance being 86mm at location 3 between beams L15 and L16.

The GPR scans estimate the stirrup cover to be between 33mm and 55mm in the leftmost half of the support beam. Numerous measurements were performed at each location, with the mean cover depth listed in Table 5.2

Table 5.2: Concrete cover measured at select locations for support beam 5. Longitudinal rebar depth was measured directly, while the stirrup cover was measured using the GPR.

| Location | Longitudinal rebar depth[mm] | Stirrup rebar depth [mm] |
|---|---|---|
| 1 | 132 | 46 |
| 2 | 113 | 34 |
| 3 | 86 | 34 |
| 4 | 111 | 40 |

The GPR was an integral part of the measurement plan as the location of the reinforcements was necessary for determining the measurement locations for other measurement techniques. Care was taken to calibrate the measurement settings when available.

### 5.1.3. Rebound hammer

The results from the rebound hammer were measured at five locations at the vertical face of support beam 5 (S1, S2, S3, S4, S5) and at the soffits of five T-beams (L2, L9, L13, L17, L23). The raw measurement data can be found in Appendix D.

#### Support beam 5

The results for the support beam with both R- and Q-type hammers are summarized in Tables 5.3 and 5.4. In Figure 5.2, the results are also visually represented with boxplots for each location.

Table 5.3: Summary of the R-type Rebound hammer results on support beam 5 with and without coating.

| R | With Coating | | | No Coating | | |
|---|---|---|---|---|---|---|
| **Location** | **Median** | **Average** | **Std. Dev** | **Median** | **Average** | **Std. Dev** |
| S1[1] | - | - | - | 45.0 | 45.6 | 4.89 |
| S2 | 48.0 | 44.2 | 7.94 | 47.5 | 49.1 | 5.68 |
| S3 | 51.5 | 47.7 | 7.82 | 53.5 | 53.8 | 4.85 |
| S4 | 37.5 | 39.3 | 7.39 | 55.0 | 53.9 | 4.94 |
| S5 | 54.0 | 53.6 | 3.91 | 45.5 | 49.7 | 7.96 |
| **Total** | **48.0** | **46.0** | **8.54** | **50.5** | **50.4** | **6.42** |

Table 5.4: Summary of the Q-type Rebound hammer results on support beam 5 with and without coating.

| Q | With Coating | | | No Coating | | |
|---|---|---|---|---|---|---|
| **Location** | **Median** | **Average** | **Std. Dev** | **Median** | **Average** | **Std. Dev** |
| S1 | 52.0 | 48.5 | 12.15 | 63.0 | 63.3 | 4.14 |
| S2 | 43.0 | 44.4 | 8.89 | 60.0 | 61.4 | 5.81 |
| S3 | 51.0 | 53.2 | 10.08 | 67.0 | 67.6 | 4.42 |
| S4 | 48.0 | 51.0 | 13.51 | 72.0 | 71.4 | 3.50 |
| S5 | 48.0 | 50.2 | 11.72 | 62.0 | 62.5 | 5.14 |
| **Total** | **47.0** | **49.3** | **11.35** | **65.5** | **65.0** | **5.87** |

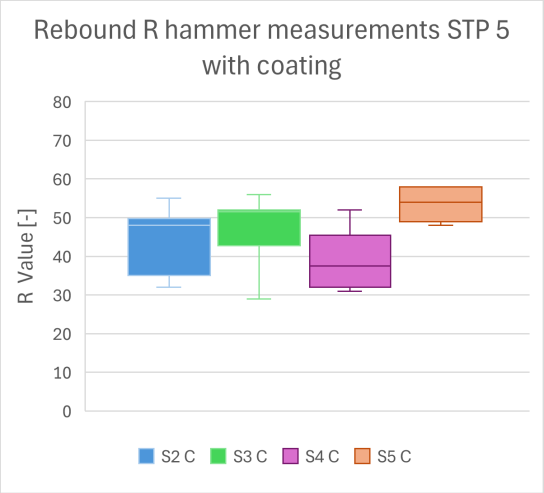


(a) **R hammer, with coating**[1]

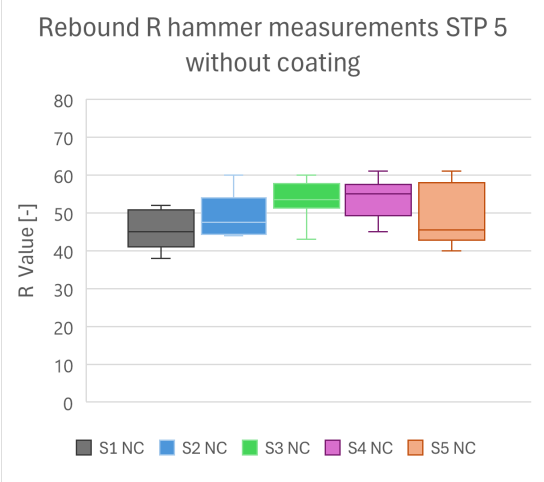


(b) **R hammer, without coating**

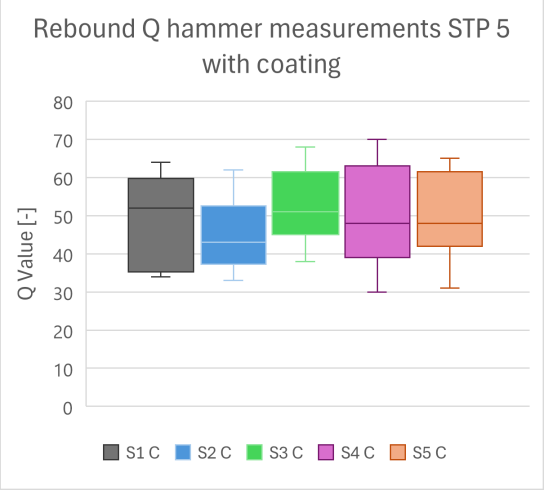


(c) **Q hammer, with coating**

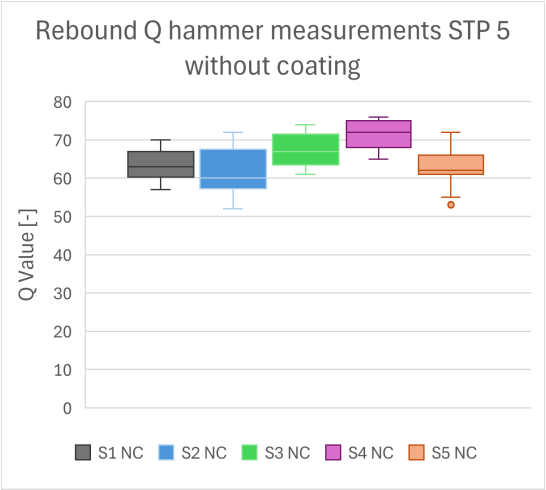


(d) **Q hammer, without coating**

Figure 5.2: Boxplots of the rebound hammer results at STP 5 using R and Q-type hammers, with (C) and without (NC) coating.

The results show a bigger variance in the measurements with the presence of the KCG coating, while the measurements without the coating show a lower standard deviation. When comparing results with and without coating, the standard deviation of the R-type hammer is decreased from 8.54 to 6.42. The Q-type hammer is more sensitive to the coating, with a decrease in standard deviation from 11.35 to 5.87. The effect of the coating is more pronounced with the Q-type hammer, which was also used in the Sluinerweg measurements.

Comparing the Q and R values, the results show consistently higher Q values. The increase in rebound value is more noticeable without the coating, with a difference of 15 in median and 14.6 in mean values. With the coating present, the differences are 1.0 and 3.3 for median and mean, respectively. When looking at Figure 5.2a and c, the measurements' variance with coating can be observed by the larger boxplot in comparison to those of Figure 5.2b and d.

**T-Beams**

Table 5.5 and Figure 5.3 summarize the rebound hammer results on the T-beams with both R- and Q-type hammers. The T-beams were not coated with a KCG layer and had a smooth finish. Measurements on the T-beams were performed on the bottom of the T-beams.

Furthermore, the results show consistently higher Q values with a mean rebound value of 73.9 and 63.1 for Q and R, respectively. The standard deviation is slightly smaller for the Q-type hammer, with a value of 2.98 compared to 3.50 for the R-type hammer. With this in mind, the Q-hammer produces the most reproducible measurements with the least variance.

Table 5.5: Results of the R- and Q-type Rebound hammers on the T-beams

| | R | | | Q | | |
|---|---|---|---|---|---|---|
| **Location** | **Median** | **Average** | **Std. Dev** | **Median** | **Average** | **Std. Dev** |
| L2 | 64 | 63,3 | 3,50 | 76 | 74,8 | 4,16 |
| L9 | 65 | 64,1 | 2,14 | 73 | 73,3 | 1,91 |
| L13 | 61 | 60,3 | 2,80 | 72,5 | 72,4 | 2,96 |
| L17 | 63 | 62,5 | 2,33 | 74 | 73,5 | 2,10 |
| L23 | 66 | 65,2 | 4,06 | 76 | 75,5 | 1,76 |
| **Total** | **63** | **63,1** | **3,50** | **74** | **73,9** | **2,98** |

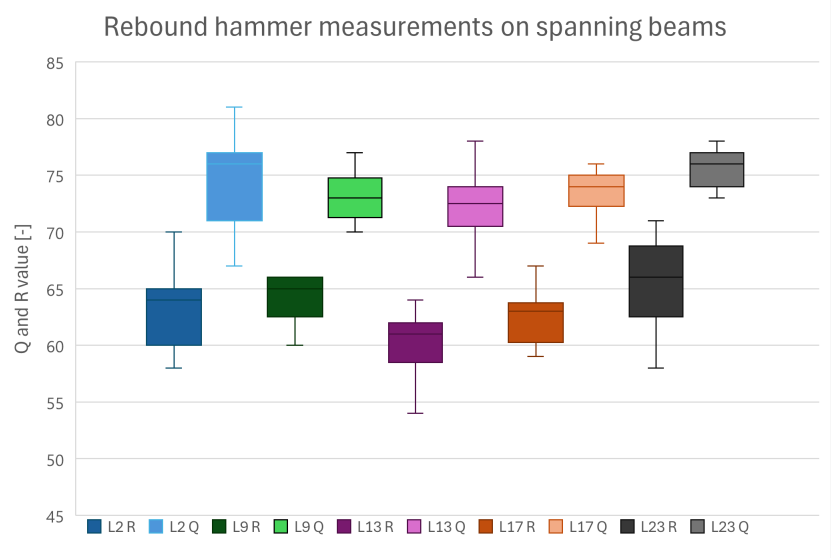


Figure 5.3: Rebound hammer result on the five T-beams using R- and Q-type hammers visualized with boxplots. Each primary color represents a T-beam. The darker color represents the R-type hammer, while the lighter color represents the Q-type.

[1]S1 has not been measured due to user error during the procedure.

### 5.1.4. Ultrasonic Pulse Velocity

The UPV measurements performed on the support beam and T-beams are shown in Table 5.6. Multiple measurements were taken at each location to get a stable mean value. The raw measurement data can be found in Appendix D.

Table 5.6: Mean ultrasonic pulse velocity speeds measured at support beam 5 and the beams

| Location | Name | Time [µs] | Distance [mm] | Transmission speed [m/s] |
|---|---|---|---|---|
| STP5 | S1 | 60.89 | 212 | 3483.9 |
| | S2 | 56.17 | 212 | 3776.8 |
| | S3 | 55.08 | 212 | 3851.7 |
| | S4 | 58.80 | 212 | 3607.7 |
| | S5 | 57.50 | 212 | 3689.3 |
| **Mean** | | **57.32** | **212** | **3700,8** |
| Beams | L2 | 79.30 | 365 | 4602.8 |
| | L9 | 76.40 | 364 | 4764.4 |
| | L13 | 81.00 | 363 | 4481.5 |
| | L17 | 86.90 | 365 | 4200.2 |
| | L23 | 76.00 | 360 | 4736.8 |
| **Mean** | | **79,8** | **363** | **4553,9** |

Compared to the support beam, the T-beams show noticeably higher values for transmission speed, with mean values of 3701 m/s and 4554 m/s, respectively. This aligns with the rebound hammer results, which also show higher rebound values in the T-beams. Some variation in the transmission speeds is observed among the T-beams, with beam L17 showing a speed that is 354 m/s lower than the mean, which could indicate an outlier, localized damage, or a less sound concrete quality.
The difference between the support beam and T-beams also suggests possible differences in concrete mix design or environmental exposure conditions. These values fall within the range indicating good to excellent concrete quality (> 3500 m/s) [59], suggesting the structural integrity of the T-beams.

### 5.1.5. Half-cell potential

Potential tests have been performed on both support beams (STP 4 & 5) and at the soffits of the five T-beams.

**Support beam 5**

The vertical face of STP5 was fully mapped with the Gecor-10 and the Profometer equipped with the wheel electrode. With the Gecor-10, 25 evenly spaced measurements were performed on the support beam, with the spacing of the measurements aligning with the width of one beam. With the Profometer, the full width of the support beam was continuously measured every 5cm with three rows of measurements, producing 915 data points. Before the potential measurements, the electrical continuity of the reinforcement was confirmed to be below 1 $\Omega$. Figure 5.4 shows the comparison between the two devices. Both the Gecor-10 sensors A and B were included in the comparison. All the curves are very much in agreement with each other, with the first 2 meters on the left of the support beam showing lower values. This trend is captured by all measurement techniques and is most pronounced with the Gecor-10 sensor A, giving a value of -360 mV.

**T-beams**

For the five T-beams (L2, L9, L13, L17, and L23), the bottom surfaces were mapped using the Profometer equipped with the wheel electrode. Only the soffits of the beams, approximately 2–3 meters away from the support beam, were measured. Holes at the same distance were made in the T-beams for the electrical connection to the reinforcement as shown in Figure 5.5b. The results of these measurements can be found in Appendix C. The measured potential values were mostly positive or close

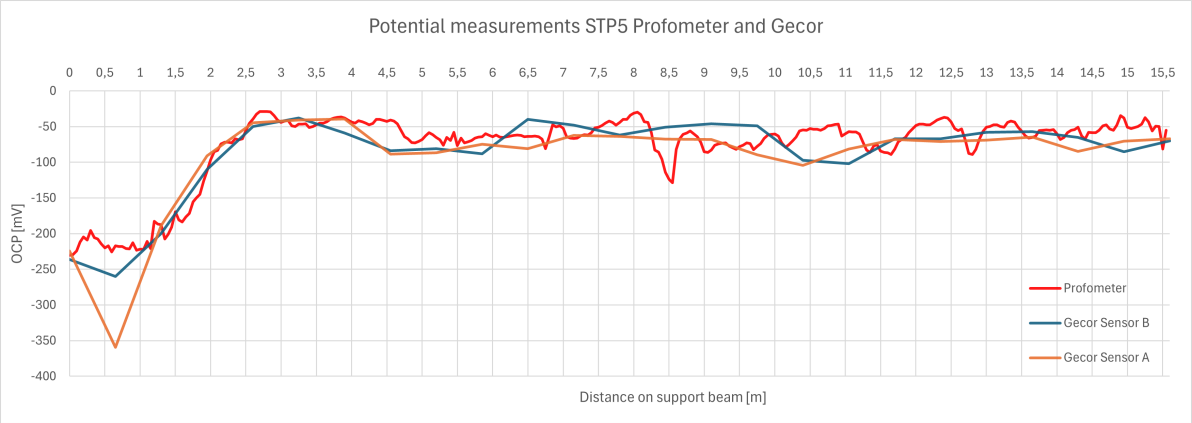


Figure 5.4: The potential measurements with Gecor-10 and Profometer mapped on support beam 5.

to zero, suggesting no corrosion risk. These values were consistent across all beams except for beam L17.

(a) The inspected area of the T-beam marked in red

(b) Hole made in the T-beam for the connection to the rebar

Figure 5.5: Location of the T-beam potential measurements, showing the soffit of beam L17 to be measured. Distance to the anchor hole was approximately 2-3 meters

The CP-protected L17 showed a decrease in potential near the beam head, shown in Figure C.7. At the start of the CP-coated section, a drop in values was observed and continued toward the end of the measurable beam. This trend was not observed in the other beams, which remained mostly stable throughout their length. Deeper measurements closer to the beam head were attempted, but these were unsuccessful due to limited access. The confined space, combined with the length of the Profometer setup, made maneuvering and maintaining sufficient contact pressure difficult.

### Support beam 4

Support beam 4 was also measured using the Profometer with the wheel electrode. The surface area of STP4 was larger than that of STP5 due to the full height of the beam being accessible. Vertical strokes with the wheel electrode were taken with a spacing of 100mm. The resulting potential map of STP4 can be seen in Figure 5.6. The measurements on the right half of STP4 came out with uniform values around +0 mV. The anchor electrode was likely not connected properly to the rebar, resulting in these unusual values. The region between beams L21 and L22 has a considerably lower potential than the surrounding surface.

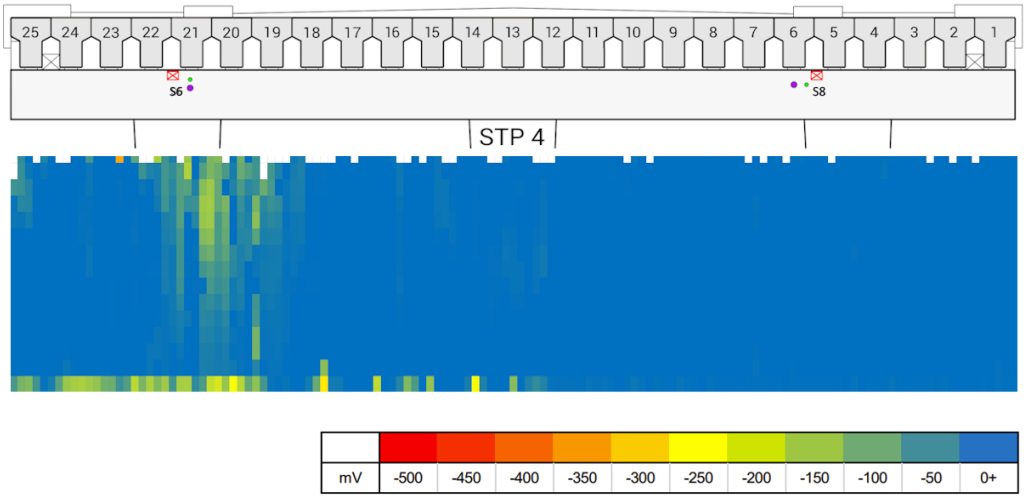


Figure 5.6: Potential map of the vertical face of support beam 4.

### 5.1.6. Resistivity

The resistivity was measured at support beam 5 and four T-beams, during the on-site measurements. The Resipod and the Gecor-10 were used to perform standalone resistivity measurements, both of which used the Wenner style probe. The resistivity was also estimated using the concrete resistivity obtained during CR measurements with the A sensor of the Gecor-10. The procedure is described in the Gecor-10 manual, which uses Equation 5.1, whereby $R_\Omega$ is the Ohmic resistance that is outputted alongside the $i_{corr}$ value [44].

$$\rho = 0.06 \cdot R_\Omega \tag{5.1}$$

**Support beam 5**

The support beam has been measured at the vertical face with 25 evenly spaced measurements. The measurement points correspond with the earlier performed half-cell potential measurements. These points were measured three to five times to average the results. The results for the two Gecor-10 sensors and the Resipod can be seen in Figure 5.7.

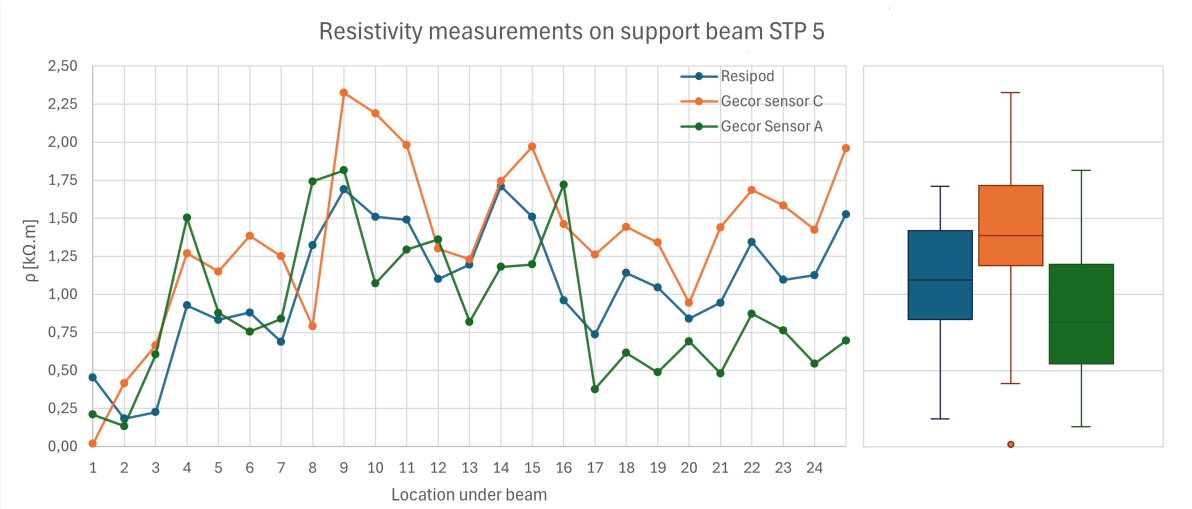


Figure 5.7: The resistivity values distribution measured across support beam 5 with boxplots.

The left side of the support beam shows a region (L1 to around L6) with lower resistivity values reported by all three methods. This location overlaps with the low-value region observed with half-cell potential measurements.

The resistivity measurements on STP5 show a trend of lower resistivity values concentrated at the leftmost positions (L1–L6). The Resipod gives values as low as 0.18–0.45 $k\Omega m$, and the Gecor-10 Sensor C reports a minimum of just 0.02 $k\Omega m$ at L1. These lower resistivity values were reported by all three methods. This location overlaps with the low-value region observed with half-cell potential measurements.

From L7 onward, all sensors show an increase in resistivity, reaching values above 1.0 $k\Omega m$ for most locations. Furthermore, sensor A reports more conservative values, especially in the region of L17–L23. Curiously, Sensor C reports higher values in the same region, with the Resipod values being in the middle of the Gecor-10 sensors. This is also seen in the boxplot of the measurement results (5.7), showing the spread of the devices with median values of $\rho_{Resipod} = 1.10$, $\rho_{Gecor,C} = 1.39$, and $\rho_{Gecor,A} = 0.82\ k\Omega m$, respectively.

#### T-beams

For beams L2, L13, L17, and L23, the soffits of the beams close to the support beam were measured for resistivity using the same methods as before. The measurement results are shown in Table 5.7.

Table 5.7: Resistivity results for the T-beams

| Location | Resipod ρ [kΩ.m] | Sensor C ρ [kΩ.m] | Sensor A ρ [kΩ.m] |
|---|---|---|---|
| L2 | 0.91 | 0.73 | 2.63 |
| L13 | 1.35 | 1.20 | 0.46 |
| L17 | 1.05 | 1.57 | 0.51 |
| L23 | 2.34 | 1.51 | 0.29 |

The resistivity values of A sensor are noticeably lower than those of the other methods, with three of them being under 0.5 $k\Omega m$. The Resipod and sensor C report values more than twice as high as these values. Furthermore, sensor A reported a relatively high value of $\rho = 2.63\ k\Omega m$ at L2, while the Resipod and C sensor showed significantly lower values of $\rho = 0.91$ and $\rho = 0.73\ k\Omega m$, indicating inconsistencies between the measurement devices.

### 5.1.7. Corrosion current density

#### Support beam 5

The corrosion current density measurements were performed at the same locations on STP5 as the resistivity and half-cell potential measurements. A polarization time of 100 seconds was chosen as the base for low corrosion risk zones. At locations with a suspected higher corrosion risk (moderate to high), a 30-second polarization time was used. The leftmost zone under beams L1-L3 was chosen to be measured using the shorter polarization time based on the risk classifications. Additionally, Beam L17 was also analyzed with the shorter 30s polarization time, due to the historical damages seen and the fact that it is now protected with CP. A detailed overview of all the measurements performed with the Gecor-10 can be found in Appendix E.

The results of the corrosion current density measurements are shown in Figure 5.8. 23 measurements were taken with a polarization time of 100s, and 4 measurements were taken with 30s. Most $i_{corr}$ values stay under $0.2\ \mu A/cm^2$, indicating a low corrosion rate.

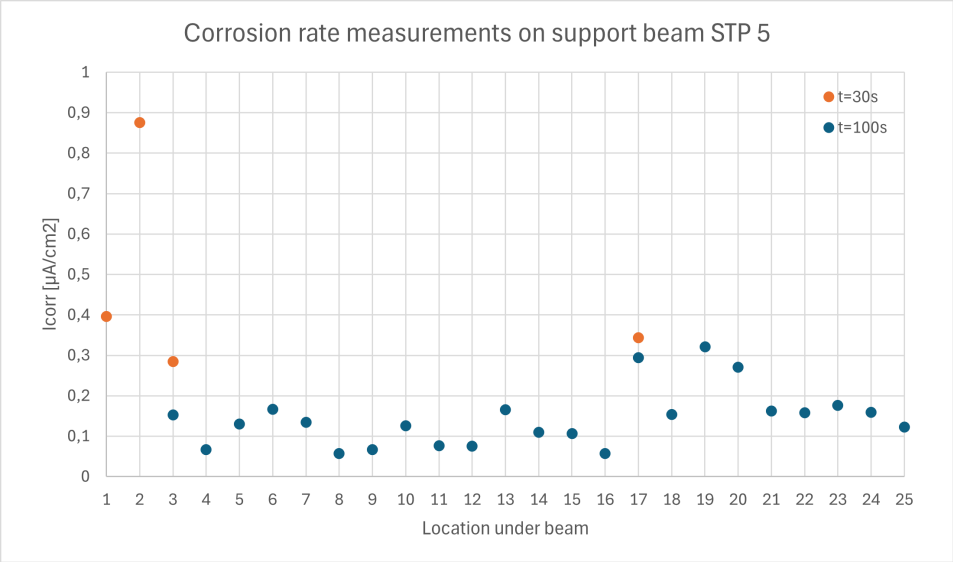


Figure 5.8: The corrosion current density values for support beam 5 under each beam with 2 polarization times. [1]

Higher values for $i_{corr}$ have been found at the leftmost beams (L1-L3) and a beam group around L17-L20. The highest value came from under L2 with an $i_{corr}$ value of $0.876\ \mu A/cm^2$, indicating a moderate to almost high corrosion rate. This is in line with the earlier performed potential and resistivity measurements. Higher values for the $i_{corr}$ were also found for the locations L1 and L3, with values of $0.396\ \mu A/cm^2$ and $0.285\ \mu A/cm^2$, respectively. The measurements with a polarization time of 30s showed overall higher $i_{corr}$ values compared to the 100s measurements, which is to be expected due to the pre-selection based on corrosion risks.
At the location under L17, $i_{corr}$ values of $0.344\ \mu A/cm^2$ and $0.294\ \mu A/cm^2$ were measured using the 30 and 100 second polarization times, respectively. The difference between these values ($0.050\ \mu A/cm^2$) is significantly smaller than at the location of L3 ($0.132\ \mu A/cm^2$).

**T-beams**
The results of the T-beam measurements are shown in Table 5.8. The same T-beams and measurement location were used as with the resistivity measurements. All of the corrosion current density measurements on the T-beams were performed with a 100-second polarization time, as no indication of active corrosion was observed.

Table 5.8: Corrosion current density values for the T-beams

| Location | Polarization time [s] | $i_{corr}$ [µA/cm2] | $E_{corr}$ [mV] | $\rho$ [kΩ.m] | $E_{pol}$ [mV] |
|---|---|---|---|---|---|
| L2 | 100 | 0.039 | 54.6 | 2.63 | 202.4 |
| L13 | 100 | 0.395 | 47.4 | 0.46 | 24.3 |
| L17 | 100 | 0.315 | -16.3 | 0.51 | 35.5 |
| L23 | 100 | 0.694 | 35.4 | 0.29 | 13.8 |

The results show a significantly high $i_{corr}$ value at beam L23 of ($0.694\ \mu A/cm^2$), which would classify as a moderate corrosion rate. This value is not in agreement with earlier observed potential and resistivity results, which were generally higher at this location. On the contrary, L2 shows a very low $i_{corr}$ value of ($0.039\ \mu A/cm^2$), which is noteworthy as the measured resistivity values at L2 were among the lowest for the T-beams. The polarization potential $E_{pol}$ is also remarkably high (202.4 mV), suggesting a low corrosion activity, dry surface, or poor electrical contact. The inconsistent results from these beams raise questions about their validity.

[1] Measurement under L1 and L2 with a polarization time of 100 seconds was unfortunately not performed due to time constraints.

# 5.2. Destructive tests

## 5.2.1. Compressive strength

The extracted cores from the support beam have been tested in the lab to determine the compressive strength of the in-situ concrete. The tests were performed according to the standards described in NEN-EN 12504-1[56] and EN 12390-3[57]. The cores were cut to an approximate length of 100 mm to produce 1:1 cores. The ends were ground, and the finished cores were then cured in a wet chamber for at least 48 hours. The final dimensions of the cores were measured just before loading. The A loading speed of 0.6 Mps/s was used until the failure of the core was registered. The failure mechanism was checked for each core after loading. The compression test results for the cores taken from support beam 5 and the T-beams are shown in Table 5.9.

Table 5.9: Results of the compression strength tests on the extracted cores.

| Location | Length [mm] | Diameter [mm] | Area [mm$^2$] | Max force [kN] | $f_{c,1:1core}$ [MPa] |
|---|---|---|---|---|---|
| S1 | 103 | 95.2 | 7118.1 | 333.3 | 46.8 |
| S2 | 103 | 95.2 | 7118.1 | 480.5 | 67.5 |
| S3 | 104 | 95.2 | 7118.1 | 574.5 | 80.7 |
| S4 | 106 | 95.2 | 7118.1 | 579.6 | 81.4 |
| S5 | 102 | 95.2 | 7118.1 | 514.3 | 72.3 |
| L2 | 101 | 98.0 | 7543.0 | 677.4 | 89.8 |
| L13 | 100 | 98.0 | 7543.0 | 621.7 | 82.4 |
| L17 | 99 | 98.0 | 7543.0 | 656.4 | 87.0 |
| L23 | 98 | 98.0 | 7543.0 | 575.2 | 76.3 |

The length and the diameters of the cores remain within the specified tolerances given in EN 12390-3. Although the diameter size of 100mm was commissioned for both extractions, the delivered size was slightly smaller for both the support beam and T-beams. The extracted support beam cores had a diameter of 95.2 mm, while the T-beam cores all had a diameter of 98 mm. The maximum force at which failure was measured is seen in the fifth column of Table 5.9. The corresponding maximum stress is calculated by dividing the maximum force by the area.

**Support beam 5**

The mean compressive strength of the support beam is 69.74 MPa with a standard deviation of 14.08. For the T-beams, values of 83.9 MPa and 5.92 are seen for strength and standard deviation, respectively. The mean T-beam compressive strength is higher than that of the support beam, which is in line with the NDT analysis performed with the RH and UPV. The spread of the support beam results is also much higher than that of the T-beams, which is due to the lower value of S1. It can be observed that the strength test for S1 (and, to a lesser extent, S2) is much lower than the other values for the support beam. This is reflected in a compressive strength that is approximately 40% lower than the values from S3-S5, indicating a poor local concrete quality.

The $f_{c,1;1core}$ represents the compressive strength of a core with equal diameter and length and is comparable to the cube compressive strength. To obtain the in-situ compressive strength $f_{c,is}$, the mean value of the core strength is multiplied by a correction factor $CLF$. Before the calculation of the in-situ strength, outlier tests will be performed, given the large spread in the support beam core strengths.

When performing the Grubb outlier test on the support beams, the following equations are obtained. The Grubb's value for n=5 is 1.764, which indicates an outlier if exceeded

$$\frac{f_{c,is,highest} - f_{c,m(n),is,stp}}{s} = \frac{81.43 - 69.74}{14.08} = 0.83 < 1.76 \tag{5.2}$$

$$\frac{f_{c,m(n),is,stp} - f_{c,is,lowest}}{s} = \frac{69.74 - 46.82}{14.08} = 1.63 < 1.76 \tag{5.3}$$

Where:

$$s = \max(s_c\ ;\ 0.08 f_{c,m(n)is})$$
$$f_{c,is,highest} = \text{Highest core strength value [MPa]}$$
$$f_{c,is,lowest} = \text{Lowest core strength value [MPa]}$$
$$f_{c,m(n),is} = \text{Mean strength of all cores [MPa]}$$

It can be seen that the support beam values pass the Grubb test, and the minimum and maximum values are acceptable. Nevertheless, the minimum core strength value of S1 is close to the Grubb value of 1.63, raising concerns about the inclusion of this test result. Another test for the spread is to be performed, as the support beam is considered a 'small test region'. The spread must be smaller than 15% of the mean strength to be able to calculate the in situ strength. This 15% range is seen in Equation 5.4. Both the highest (81.43 MPa) and lowest (46.82 MPa) strength cores exceed these limits, which means that the selection of cores should be reconsidered.

$$59.23 < f_{c,m(n),is,stp} < 80.2 \tag{5.4}$$

Due to the resulting spread test, S1 could be seen as a separate location with a lower local concrete strength. S1 is thus not considered for the analysis of the in-situ concrete strength of the whole support beam. A new 15% spread test is performed using the S2-S5 cores, resulting in the limits shown in Equation 5.5

$$64.15 < f_{c,m(n),is,stp} < 86.79 \tag{5.5}$$

This time, the highest (81.43 MPa) and lowest (67.5 MPa) values are within the limits. The support beam locations of S2-S5 can thus be considered as a single area with a mean compressive cube strength of $f_{c,m(n),is,stp}$ = 75.47 MPa. The corresponding cylinder strength is calculated in Equation 5.6.

$$f_{c,is,stp} = CLF \cdot f_{c,m(n),is,stp} = 0.82 \cdot 75.47 = 61.89 \text{ MPa} \tag{5.6}$$

**T-beams**

For the T-beams, the Grubb limit for four cores is 1.496, which was not exceeded by the T-beam values as shown in Equations 5.8 and 5.8, indicating no apparent outlier. The 15% limits are also calculated and shown in Equation 5.9. These limits are also not exceeded, indicating that the T-beams could be identified as having the same strength. The mean compressive cube strength of the T-beams is thus $f_{c,m(n),is,tbeam}$ = 83.88 MPa, with a corresponding cylinder strengths of 68.78 MPa.

$$\frac{f_{c,is,highest} - f_{c,m(n),is,tbeam}}{s} = \frac{89.81 - 83.88}{6.71} = 0.884 < 1.496 \tag{5.7}$$

$$\frac{f_{c,m(n),is,tbeam} - f_{c,is,lowest}}{s} = \frac{83.88 - 76.26}{6.71} = 1.136 < 1.496 \tag{5.8}$$

$$71.29 < f_{c,m(n),is,tbeam} < 96.46 \tag{5.9}$$

The final compressive strengths for both support beam 5 (without S1) and the T-beams are presented in Table 5.10. The T-beams still maintain a higher compressive strength even after the removal of the (lower) S1 measurement for the support beam.

Table 5.10: Mean compressive strength of support beam 5 and the T-beams.

| **Location** | $f_{c,m,cube}$ [MPa] | $f_{c,m,cyl}$ [MPa] |
|---|---|---|
| STP5 | 75.47 | 61.89 |
| T-beams | 83.88 | 68.78 |

### 5.2.2. Carbonation front

The carbonation front has been identified for 10 cores taken from the vertical face of the support beam and the bottom of the T-beams. The maximum depths of the carbonation can be seen in Table 5.11. Photos of the cores taken directly after application of the phenolphthalein indicator solution can be found in Appendix F.

Table 5.11: carbonation depth of the concrete cores

| Location | Max depth [mm] |
|---|---|
| S1-CL1 | 24 |
| S2-CL1 | 16 |
| S4-CL1 | 5 |
| S5-CL1 | 8 |
| L2-CL1 | 0 |
| L13-CL1 | 11 |
| L17-CL1 | 5 |
| L23-CL1 | 11 |
| S6-CL1 | 9 |
| S8-CL1 | 8 |

The highest value for the carbonation depth is observed at S1 of STP5 (24mm), with the second highest value at S2, with 16mm. These results show an agreement at S1 for the risk of corrosion measured with the NDT methods and the carbonation level. The maximum carbonation front has not reached the rebar, as the STP5 cover is at least 30mm, making corrosion initiated by carbonation unlikely.

### 5.2.3. Chloride profiles

The chloride content of both the support beams and the T-beams can be seen in Figure 5.9, illustrating the chloride content as a function of concrete depth. At location S1, an additional core (S1*) was extracted and analyzed due to the increased risk of corrosion identified from the NDT measurements. All cores were sliced into 20mm sections except for S1*, which was cut into 10mm sections for a better curve resolution. An overview of the results and the raw data gathered can be found in Appendix G.

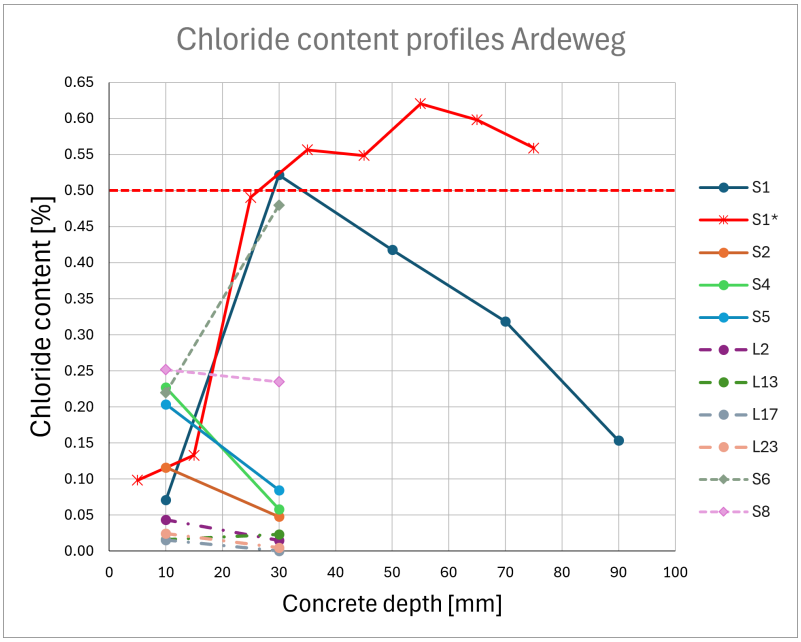


Figure 5.9: The plotted chloride content profiles in weight% of cement. Cores taken from STP5: S1-S5, T-beams: L2-L23, and STP4: S6-S8.

**Support beam 5**

The data shows a general trend of decreasing chloride content with increasing depth, which is to be expected due to the ingress of chlorides at the surface. The two profiles at S1 show significant chloride content, exceeding the critical value of 0.5% at depths of around 30mm, suggesting severe chloride penetration at this location. The other locations of support beam 5 (S2-S5) show noticeably less chlorides content, staying mostly below 0.25% with a steep decrease between 10mm and 30mm.

The chloride profile of S1 shows a peak-shaped distribution, with the maxima deeper in the concrete cover. The concentrations are relatively low near the surface and peak at a depth of around 30mm with 0.52%. After the peak, the trend gradually decreases with depth. The peak of S1* is not as easily identified as S1, as the chloride content continues to increase after 30mm. Subsequent values at depths beyond 30mm remain above the critical value of 0.5%, suggesting critical chloride exposure at the reinforcement (cover depth was 40mm at S1*). The presence of corrosion at S1* was visually validated after core extraction. The drill hit the stirrup reinforcement during extraction, which marked the end of the chloride core. Figure 5.10 shows the location of S1* and the extracted core with corrosion signs both inside the borehole and on the core.

Figure 5.10: Location of S1* showing signs of corrosion products.

**T-beams**

The values for the T-beams show noticeably small chloride concentrations, with maximum values not exceeding 0.05%. The low values are an effect of the change in locations for the extracted cores. The extraction of the chloride cores according to the original measurement plan could not be performed due to the size of the drilling equipment. The actual location of the chloride core was moved back approximately 2 meters from the original location, as seen in Figure 5.11. The moving of the core resulted in the evaluation of the T-beam at a location where chloride exposure was not probable, as the highest concentrations were expected at the dilation joint just above the beam head. The distance of the extracted cores to the beam head was more than 3 meters, indicating a disconnect between the chloride exposure conditions at the beam head and the measured chloride content.

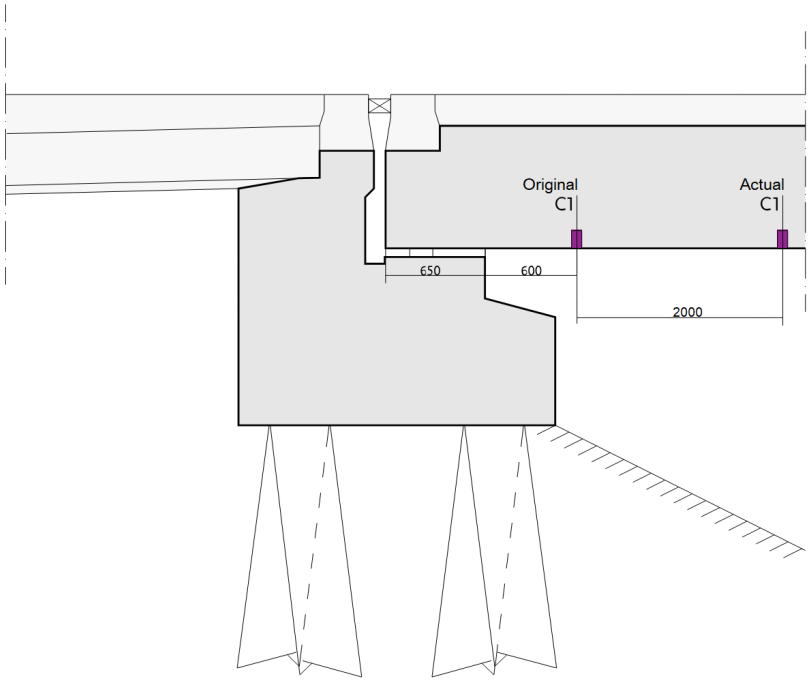


Figure 5.11: The change in location of the chloride cores for the T-beams.

**Support beam 4**
The cores S6 and S8, extracted from support beam 4, show chloride content values between 0.25% and 0.5%, which is generally higher than the STP5 cores (excluding S1 and S1*). S6 almost reaches the critical limit with a value of 0.48% at the depth of 30mm. The curve of the S6 core also follows the same shape as the two S1 cores, with a lower surface concentration and a higher peak chloride content deeper inside the concrete cover.

### 5.2.4. Thin-section analysis

Three fluorescent epoxy-impregnated thin sections were prepared from the strength cores S1, S3, and S5. These sections were taken approximately 2 to 3 cm below the top surface of each core. The fluorescent epoxy highlights the pore structure and air voids, enabling both visual and quantitative analysis. Point counting was performed to determine the area fractions of the major concrete components. The results are presented in Figure 5.12, showing the three thin sections under normal and UV lighting, as well as a filtered mask highlighting the porosity.

The area fractions obtained from the point counting analysis are shown in Table 5.12, which shows S1 having the highest air void content with 5.0%. The voids present in S1 are much larger than the other two thin sections, as seen in the UV scan of Figure 5.12. The fluorescence of the cement matrix for S1 and S5 is also notably brighter compared to S3. At S5, porosity within the coarse aggregates is also seen.

Table 5.12: Point count composition analysis for each thin-section.

| Location | # of points | Cement Matrix | Fine Aggregate | Coarse Aggregate | Air Voids |
|---|---|---|---|---|---|
| S1 | 726 | 29.6% | 42.1% | 23.3% | 5.0% |
| S3 | 542 | 32.8% | 43.5% | 22.7% | 0.9% |
| S5 | 542 | 32.5% | 36.9% | 27.5% | 3.1% |

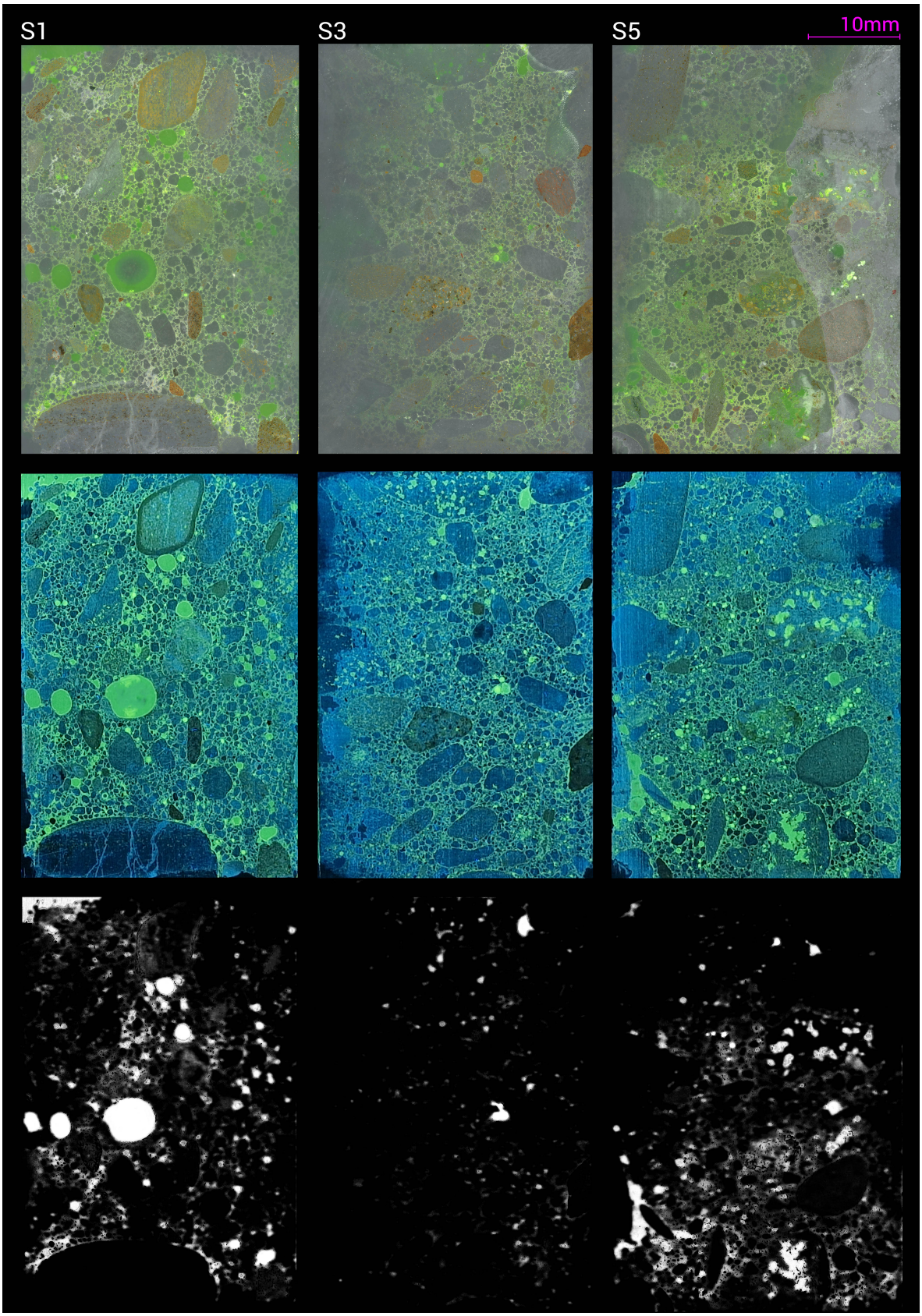


Figure 5.12: Overview of the 3 fluorescence impregnated thin-sections under normal lighting, UV lighting, and highlighted porosity.

# 6

# Results harvested beams

This chapter presents the results of the measurements performed on the harvested beams from the Ardeweg viaduct on 29 October 2024, in Wolfheze. The testing program was focused on the corrosion assessment near the beam heads that could not be performed on-site. The test results are further divided into NDTs and DTs.

## 6.1. Non destructive tests

### 6.1.1. Visual inspection and weather conditions

The isolated beam heads were approximately 2.5 meters in length, being slightly damaged by the demolition process. Beam head L3 from STP4 was found to be in significantly bad condition, with most of its top surface missing. Measurements on this beam were ruled out due to the missing concrete cover. Measurements were performed on the other four beam heads from STP5.

The surface where the beams were cut revealed protruding reinforcement and prestressing bars as shown in Figure 6.1a. Minor surface damage was seen on all beams, likely due to the demolition process. The beam head ends were also damaged to varying degrees. At beams L13, L17, and L23, the concrete cover at the beam heads was missing, exposing the mild steel reinforcement underneath. At beam L2, the cover was mostly intact, except for the location of the prestressing anchor (the cone). Here, the concrete was missing, and corrosion was spotted. Furthermore, at beam L23, larger damages were present on the top surface with broken-off corners. The missing cover made measurements at this location (x=75cm) impossible for the corrosion current density as seen in Figure 6.1b. Furthermore, all the exposed reinforcement and prestressing bars were covered with a layer of superficial rust. It cannot be confirmed whether this corrosion was initially present or appeared after the harvesting.

Beam L17 has had a cathodic protection coating applied to the first 100cm of the beam head. The conductive coating was not applied evenly across the surface of the beam. At the location of x=25cm, the beam used to be connected with a bearing pad to the support beam. At this location, the coating is noticeably thinner. At the location where the coating was thicker, namely x=50cm and x=75cm, the conductivity of the coating had a noticeable impact on the measurements.

On the day of the measurements, it was cloudy with an ambient temperature of around 12-15 °C. Constant light rainfall was present throughout the day, resulting in a wet concrete surface. Watering of the concrete surface for corrosion measurements was not performed.

(a) **Absent concrete cover at the end of the beam head of L13 with exposed reinforcements. Resistivity test is being performed.**

(b) **Broken edges and surface damage at the top surface of beam L23, making measurements at this location difficult.**

(c) **Minor surface defects on beam L2. Markings for the measurement grid can be seen in yellow.**

(d) **Resistivity measurement being performed with the Gecor-10 on the cathodic protection coating on beam L17.**

Figure 6.1: Inspection of the harvested beams of the Ardeweg viaduct with various observed damages. The centerline of the beam is marked in the middle of the beam.

A constant measurement grid was used for all corrosion measurements. Starting from the end of the beam head, measurements were taken every 25cm up to a length of 150cm. This increment was chosen as it aligns with the spacing of stirrups inside the T-beam. The Resistivity and potential measurements were taken on the left and right sides of the center line to be averaged during the analysis. The corrosion current density measurements were only taken once per 25cm along the centerline of the beam. Measurements were taken with the reinforcement grid in mind, e.g., measuring between rebars for the resistivity and directly above the connected rebar for the potential measurement.

### 6.1.2. Resistivity

Resistivity measurements were taken along four isolated beams (L2, L13, L17, and L23) using the Resipod and Gecor-10 (sensors A and C). Each data point is based on at least six measurements, avoiding areas directly above the reinforcement. The results are shown in Figure 6.2.

Most resistivity values fall between 0.1 and 2 $k\Omega m$. Beam L7 measured the lowest values at x=50cm

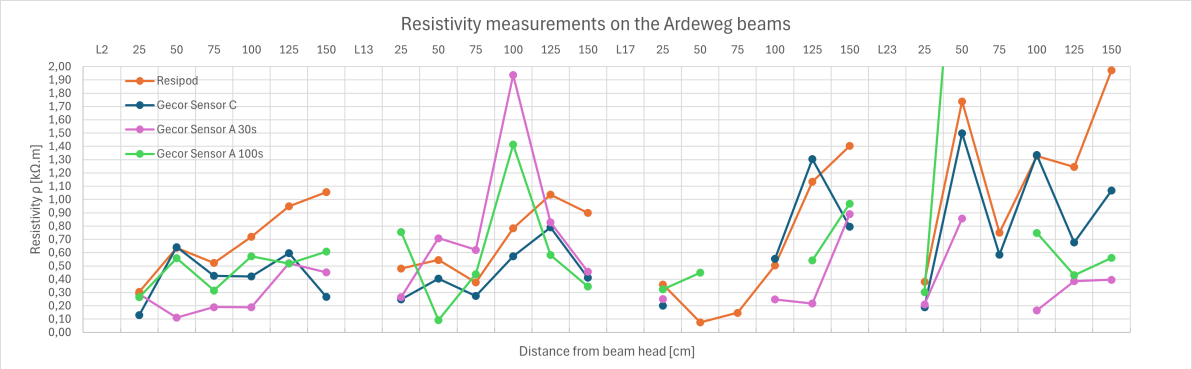


Figure 6.2: Resistivity of all 4 isolated beams (L2, L13, L17, L23) with distances from the beam head. Measured with both Resipod and Gecor-10. The resistivity values from the corrosion rate measurements (sensor A) are also included with their corresponding polarization times.

and x=75cm ($0.08$ and $0.15$ $k\Omega m$, respectively), corresponding with the CP-coated area. The highest measured value of $3.75$ $k\Omega m$, was observed at beam L23 x=50cm.
Lower resistivity values were observed near the beam heads, except for beam L23, which shows alternating high and low values along its length. Furthermore, measurements taken with Sensor A show a larger spread, especially at L23, where high and low values are measured at the same location (x=50cm). Conversely, measurements from x=100cm to x=150cm show more conservative values compared to the Resipod and Sensor C data.
Certain locations could not be measured due to the earlier described local damage or the presence of the conductive CP coating. The Gecor-10 was especially sensitive to these surface flaws, reporting errors at beam L17 x=50cm and x=75cm, as the surface was too conductive for both sensors A and C. In these areas, the Resipod still functioned well, although reporting noticeably lower values. Overall, the Resipod and Gecor-10 Sensor C provided consistent results, with sensor C generally reporting conservative values.

### 6.1.3. Half-cell potential

For potential measurements, both the Profometer and the Gecor-10 were used. The Profometer was equipped with the point electrode attachment. The Gecor-10 measured the half-cell potential using both the point electrode (Sensor B) and the built-in reference electrode of Sensor A, which recorded the potential during CR measurements. The measurements were taken at the same locations as the resistivity measurements while ensuring their placement directly above the steel rebar. The connection with the rebar was made with the exposed mild steel reinforcement as seen in Figure 6.1a.

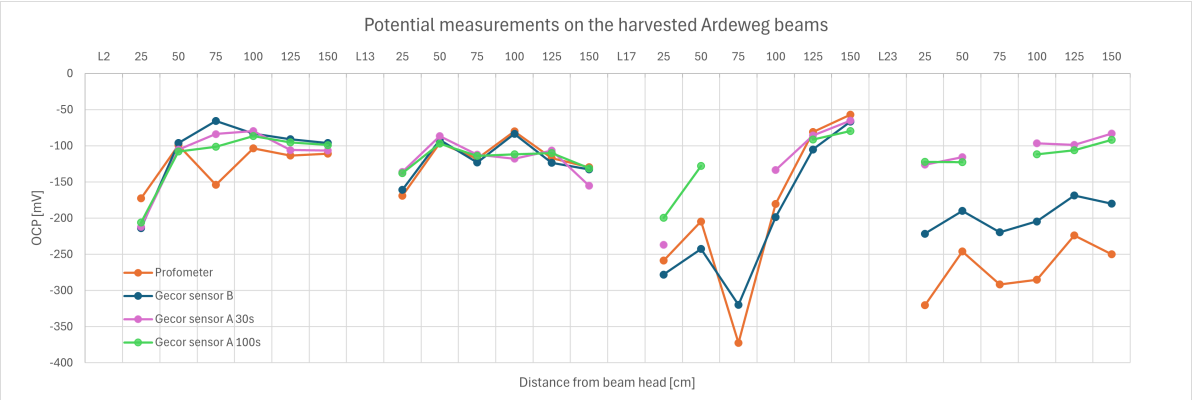


Figure 6.3: Potential of all 4 isolated beams (L2, L13, L17, L23) with distances from the beam head. Measured with both Profometer and Gecor-10. The potential values from the corrosion rate measurements (sensor A) are also included with their corresponding polarization times.

The half-cell potentials for the beams are plotted in Figure 6.3 along with their distance to the beam

head. In beam L23, the Profometer recorded consistently lower potentials than the Gecor-10, though both followed a similar trend. Conversely, the Gecor-10 A sensor recorded significantly more positive values than sensor B, a pattern not observed in the other beams. In beam L17, a sudden potential drop to -372 mV was recorded at x=75cm from the beam head, corresponding to the region near the CP coating.

### 6.1.4. Corrosion current density

The $i_{corr}$ values for the four harvested beams are shown in Figure 6.4. Measurements were taken with 30s and 100s polarization times, with six measurements per beam, starting from x=25cm. Some measurements were not possible due to local concrete damage (beam L23) or the CP coating (beam L17)[1]. A detailed overview of the Gecor-10 results can be found in Appendix E.

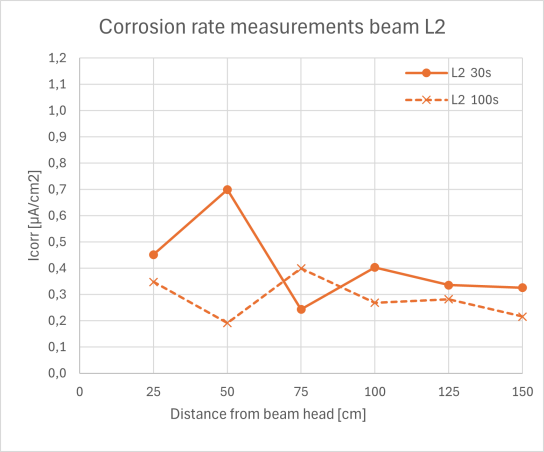


(a) **L2**

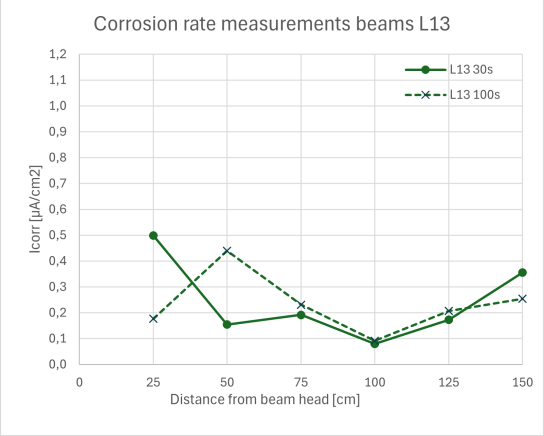


(b) **L13**

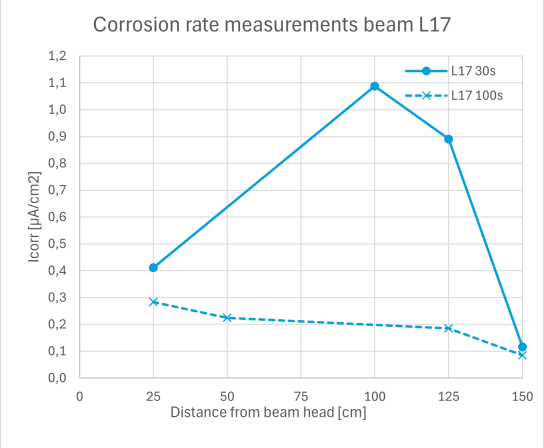


(c) **L17**

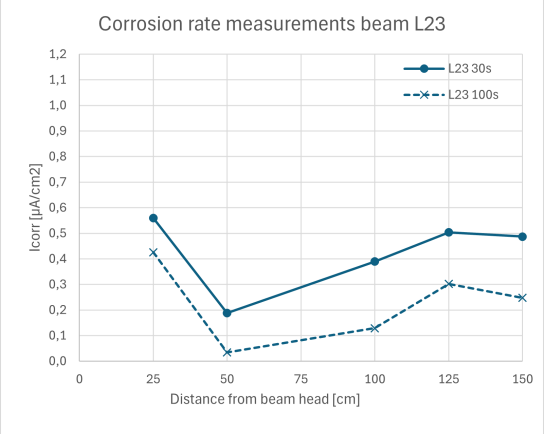


(d) **L23**

Figure 6.4: The corrosion current density values for the beams with both 30s and 100s polarization times.

[1] For beam L17, measurements at 50cm and 75cm (30s) and 75cm and 100cm (100s) were invalid due to excessive conductivity, causing errors using the Gecor-10.

The $i_{corr}$ values generally vary along the beam length, with notable differences between the two polarization durations.

- Beam L2 shows mostly consistent $i_{corr}$ values between the two polarization durations, with a sharp peak around 50cm for the 30s polarization time. At this location, the disconnect in $i_{corr}$ is the most significant, with a difference of approximately 0.5 $\mu A/cm^2$ between the two durations. A $R_\Omega$ of 1,84 and 9,30 $k\Omega m$ was measured for the 30s and 100s values, respectively. The 30s values are consistently higher than the 100s values, except at the location of x=75cm where a value of 0.24 $\mu A/cm^2$ was observed for the 30s measurement.
- Beam L13 shows stable values for both polarization times, showing similar values, except for the first two measurements. The 30s measurement at x=25cm increases noticeably compared to the other measurements. The $i_{corr}$ values for this beam all stay under 0.5 $\mu A/cm^2$, indicating a low corrosion rate.
- CP beam L17 exhibits significant 30s peak values of 1.09 and 0.89 $\mu A/cm^2$ at 100cm and 125cm, respectively. This, while the 100s results show consistently lower values below 0.3 $\mu A/cm^2$. This leads to the largest differences between values for all the beams. The missing values of beam L17 are seen in the locations of 50, 75, and 100cm.
- At beam L23, the 30s measurements show consistently higher $i_{corr}$ values compared to the 100s measurements, while still following the same trend. The Value at x=25cm is notably higher for both polarization times.

## 6.2. Destructive tests

### 6.2.1. Compressive strength

One core was extracted from each harvested beam to be tested for compressive strength. The location of the cores was at a distance of approximately 1500mm from the beam head, roughly corresponding with the location of RH and UPV tests performed in the June inspections. The results of the strength tests were already combined with the support beam measurements, which are shown in Chapter 5.2.1,

### 6.2.2. Chloride content

The chloride content of the harvested beams was measured for two beams (L2 and L17) at varying distances from the end of the beam head. The locations chosen were 200mm, 700mm, and 1200mm from the center as shown in Figure 6.5.

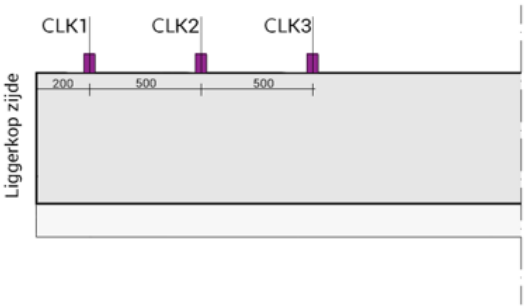


Figure 6.5: The location of the extracted cores for the harvested beams. Distance is in relation to the end of the beam head. The depicted beam is flipped vertically with the flange on the bottom.

The locations were not accessible on-site due to the overlap with the support beam. The previously extracted cores from the July measurements were approximately 2-3 meters from the beam head. The distance to the beam head and the low chloride content observed prevented the identification of the conditions of any of the beam heads, which resulted in this secondary study into the influence of distance from the beam head.

Just like the previous chloride analysis, only the first two slices were analyzed in the lab using the same methods. The resulting chloride content curves obtained are shown in Figure 6.6. A detailed overview of all individual titrations measurements performed is found in Appendix G.

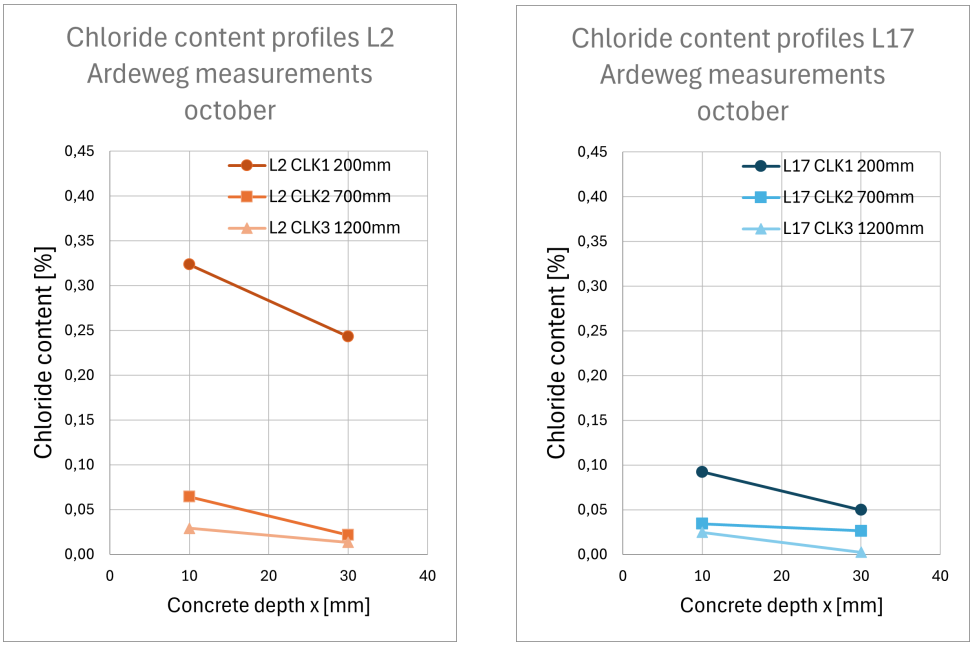


(a) L2 (b) L17

Figure 6.6: The chloride content curves for L2 and L17 at different distances from the beam head. The chloride content % is compared against the cement weight.

The chloride content near the beam head is significantly higher for beam L2 compared to L17, with a maximum of 0.32% and 0.09%, respectively. Furthermore, all core samples had a higher chloride concentration at the surface (x=10mm) compared to the second slice (x=30mm). Lastly, none of the analyzed samples exceeded the critical limit of 0.5%, indicating a low risk of mild steel corrosion.
The results are also visualized in Figure 6.7, where the maximum chloride content value of each core is plotted against the beam head distance on the x-axis. The decreasing chloride content further from the beam head can be observed, with a significant decrease of ~90% between 200mm and 1200mm for beam L2.

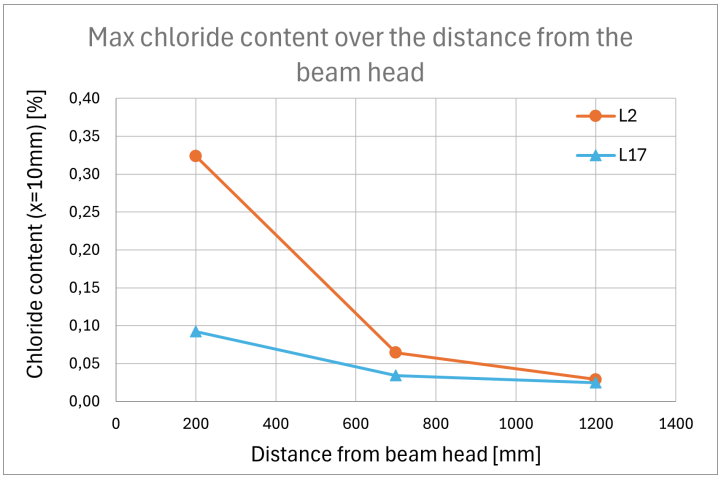


Figure 6.7: The maximum chloride content of the harvested beam plotted over the length of the beam. Distance is measured from the end of the beam head.

# 7

# Discussion

## 7.1. Strength estimation and validation with RH and UPV

The rebound hammer results from the on-site measurements showed influences from the KCG coating and the type of hammer used. Differences will be highlighted in this section, as well as the comparison with the UPV and the past Sluinerweg results. Lastly, the compressive strength estimations will also be looked into.

### 7.1.1. KCG coating

The results from Section 5.1.3 showed pronounced differences in results depending on the presence of the KCG coating. The measurements before removal of the coating show a greater variance, as shown in Tables 5.3 and 5.4. The uneven striking surface was the cause of the spread, as a good transfer of energy is not guaranteed.
An interesting effect was seen when striking the coating at the same location multiple times. At a column under the middle support STP4, multiple tests were performed to analyze the influence of the KCG coating. Three strikes were performed at one location before moving to another location. The results are shown in Figure 7.1, where the same 4 locations have been measured with and without coating.

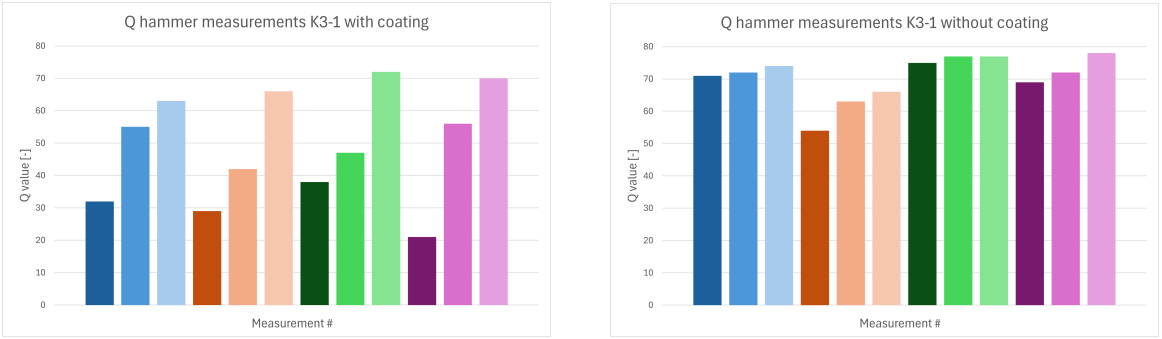


(a) RH measurements with the KCG coating.

(b) RH measurements without the KCG coating.

Figure 7.1: RH measurements performed with a Q-type hammer on column K3-1 with and without the KCG coating. A set of strikes performed at the same location is depicted with the same base color.

In the case with the KCG coating, the rebound value was initially lower, increasing with each strike, as seen in Figure 7.1a. The first hit was approximately 50-70% lower than the value measured from the third hit. When the coating was removed, it was observed that this 'growing' effect was significantly lessened (see Figure 7.1b). The measurement results stabilized with only slight changes in rebound value. The coating thus prevents the rebound hammer from measuring stable rebound values. This would explain the lower mean values observed in the measurements with coating from Tables 5.3 and 5.4.

It was observed that small granules would detach from the KCG layer and fly off violently during the measurements. The lower values obtained from the first few measurements were likely due to the energy loss sustained from this local crushing of the KCG layer, which prevented the true subsurface concrete from being evaluated properly. With each subsequent strike, the surface finish would even out due to the force of the RH, stabilizing over time and resulting in the 'growing' values observed. One measurement affecting another one should never occur for accurate measurement gathering.
These findings reinforce the known sensitivity of rebound hammer tests to surface roughness. Similar effects have been noted in literature, like Maliha et al., which presents a mean difference in rebound value of 15-20 between smooth and rough surfaced concrete samples [42]. This coincides with the found difference in mean Q-value (49.3 with coating and 64.8 without) as shown in Table 5.4. Further studies about KCG layers were not found in the literature.

The ACI 228.1R-03 [36] and other codes require a smooth, even surface before measuring with the rebound hammer. The EN 12504-2 [39] recommends checking each surface impression after a strike for local crushing of (sub)surface voids, which could invalidate the reading. The advice of these codes is to be followed, given the observations made in this study.
Within the Liggerkoppen project, the KCG coating was commonly applied to support beams and columns, while the T-beams remained uncoated. Care should thus be taken when performing a strength assessment with the RH on coated elements. However, support strength has not been a primary structural concern, especially given the history of the damages from the Sluinerweg and Ardeweg viaducts. If the strength of the supports were ever to be questioned, then removing the KCG layer at the measurement location is necessary. This surface preparation, however, reduces one of the RH's main advantages: its ease of use as an NDT.

### 7.1.2. R vs Q rebound hammer

The results also show a significant difference in rebound values between the R- and Q-type hammers. This is best visualized at the T-beams shown in Figure 5.3, where the mean differs by 10.8. The support beam shows a larger difference of 14.4 for the Q hammer without coating. This aligns with expectations from previous literature, which shows a higher Q-value than the corresponding R-value.

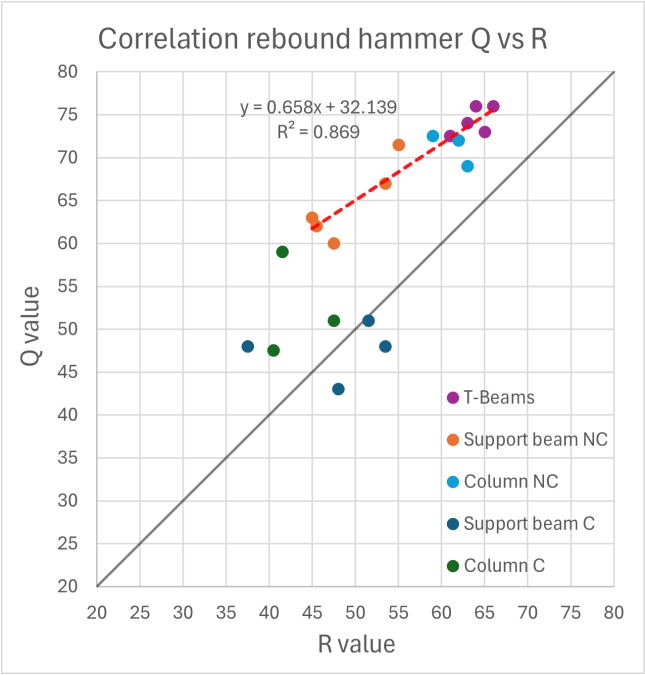


Figure 7.2: Correlation between the R- and Q-type hammer test results. A linear interpolation curve is shown in red. Presence of the KCG coating is labeled with a 'C', with 'NC' indicating no coating.

A scatter plot with the R- and Q-type hammer pairings is shown in Figure 7.2. The x-axis indicates the rebound values from the R-type hammer, while the y-axis represents the Q-type hammer. The

rebound values were gathered at locations where both types of RH measurements were taken. These include the T-beams, support beam 5, and the columns supporting STP4. The latter two also include measurement with and without the KCG coating, which is labeled with a 'C' and 'NC', respectively. A dot represents the mean rebound value at a location, with ∼12 measurements using each RH.
It could be observed that the Q-values are consistently higher for a given R-value, with almost all measurements being above the equality line. This discrepancy is attributed to the differing ways of measuring the rebound value. The Q-type hammer calculates the rebound velocity, whereas the R-type measures rebound distance. Furthermore, the measurements with the KCG coating show overall lower rebound values with a greater spread, while the no-coating pairs are more tightly grouped. This is expected given the earlier-mentioned effects of the KCG coating. The variance in rebound values is the smallest for the T-beams, as they had a smooth testing surface.

A linear correlation curve is fitted for the measurements without coating, which is shown in red. With an R-squared of 0.869, the fit shows a strong correlation between the two hammers, despite the offset. The slope of the best fit is shallower than the equality line, which suggests a flattening response at higher strength ranges, or the Q-hammer's diminishing sensitivity relative to the R-hammer at higher values. However, this is hard to determine given the sample size of this study.
If the extremes of the NC measurements (R=45-65) were to define the applicable region for this correlation, then a difference of 10-16.7 is observed between the rebound values. The lower bound of the difference range aligns with the results from Winkler et al., which found that a general +10 conversion could be used between R- and Q-type hammers (see figure 7.3a) [41]. However, for lower rebound values, the increasing difference between the R and Q hammers does not agree with a general conversion model as seen in Winkler et al. Further research should be conducted with more data to establish a model that spans a larger range of rebound values.

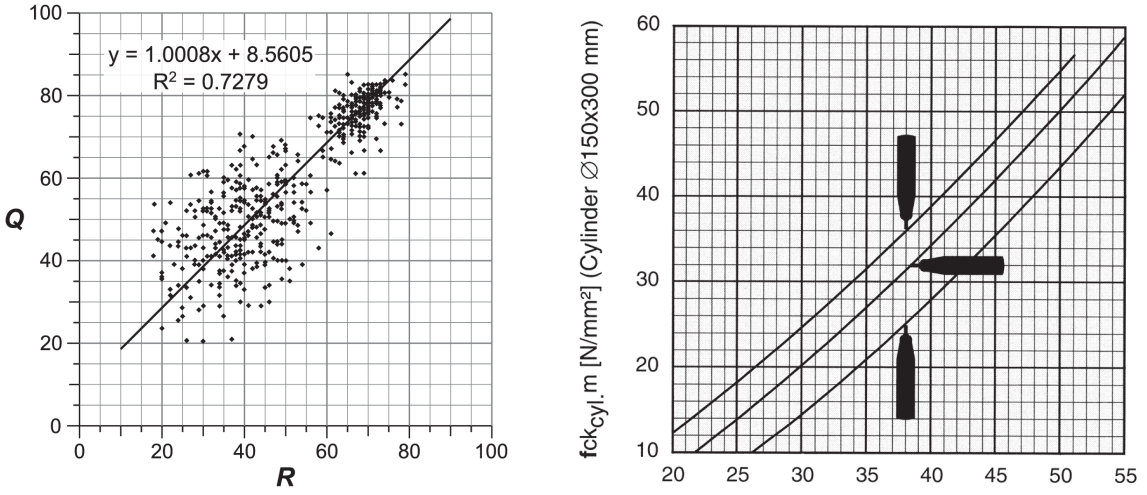


(a) Scatter plot of Q- and R-hammer pairings for stone samples [41]

(b) The Proceq SA curve for young concrete [60]

Figure 7.3: Winkler et al.'s correlation curve with Q- and R-type hammer pairings on the left, with the Proceq SA curve on the right.

It should be noted that the orientation of the RH was not consistent for all measurements. The measurement direction for the T-beam was upwards, striking the bottom of the beam. This, while the support beam and columns were hit horizontally. This is a key variable, as the R-type hammer is sensitive to the orientation. An upward measurement opposes the rebound and yields lower values due to the influence of gravity on the internal mass. Conversely, measurements from a Q-type hammer are independent of the orientation due to its electronic measurement method. The T-beam R-values have to be increased slightly if they were to be corrected for their orientation to align with a horizontal orientation. From the Proceq SA curves (see Figure 7.3b), an increase of +4 to +6 is seen between an upward and horizontal measurement [60]. These are, however, used for the strength determination of younger concrete (14-56 days). The measurement range encountered during this study also exceeds

the manual's maximum acknowledged R-value of 55. All in all, this highlights the uncertainties involved with using the rebound hammer for aging concrete. Further research should be performed on aging concrete to establish a better insight into the relationship between the two values.
When the corrections were to be applied to the R-values, the fit would become even more shallow, as the T-beam grouping would translate further along the x-axis. This further dismisses the use of a simple constant conversion between the two types of hammers.

**Practical experience**
The results gathered from the rebound hammer tests show an overall close relationship in usability and variability between the two devices. However, the Q-type hammer should be preferred, as it performs marginally better with lower spread in all testing scenarios.
Another improvement over the R-type hammer is the improved user experience, as more user-friendly features are available. The electronic recording of the measurements removes the need to manually read the values after each strike, which saves time and another source of bias. The ability to do on-site analysis is also a great feature, as conversions could be applied on the spot for different standards and automatic outlier detection.

### 7.1.3. Rebound hammer vs UPV

Figure 7.4 compares the Q- and R-type rebound hammer results with UPV measurements at corresponding locations. A positive linear trend is observed in both cases, with a moderate correlation between the two variables. This aligns with the literature as both methods reflect the surface hardness and internal material quality.
The T-beam measurements are grouped in a higher Q-value and UPV range, while STP5 locations are generally lower in both parameters, suggesting that the T-beams are of higher overall quality. The R-hammer has a higher R-squared value of 0.814 compared to the 0.631 of the Q-hammer, which indicates a better correlation between the R-hammer and the UPV results. However, no statistically relevant conclusion could be formulated as differences could be caused by noise and the limited number of tests performed. The beams had water applied to them for the corrosion measurements, but this applied moisture was not quantitatively measured, making it difficult to determine the effect on the measurements between locations.
Although the rebound hammer and UPV reflect different physical properties, their agreement supports the reliability of using both for strength assessment. However, the moderate R-squared also highlights the importance of not relying solely on either test, especially in aged structures, where many influencing variables for both RH and UPV are present. More data, preferably with environmental control, is required for a more comprehensive correlation analysis.

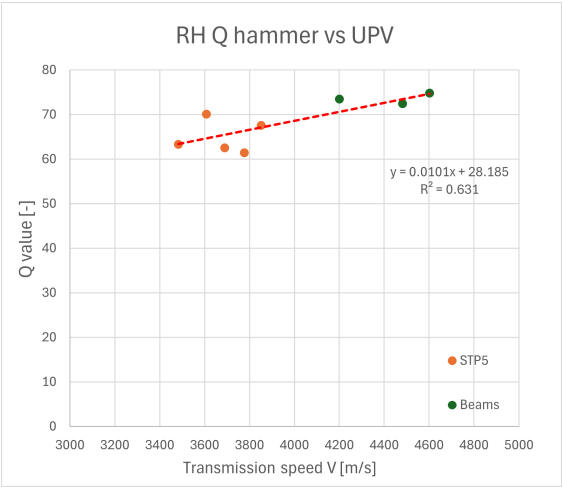


(a) UPV vs the Q-hammer results

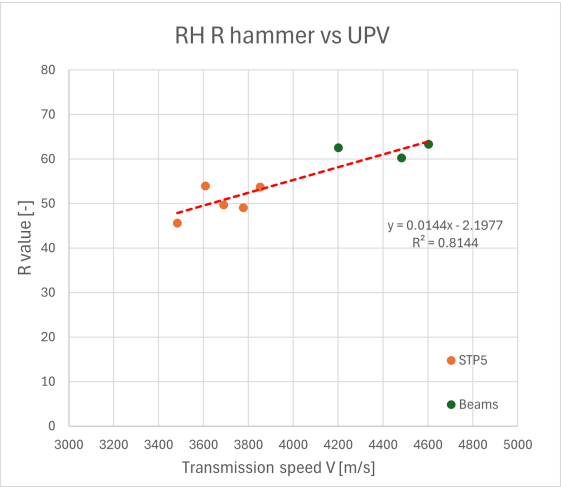


(b) UPV vs the R-hammer results

Figure 7.4: Scatterplot for the UPV and rebound hammer measurements performed on support beam 5 and the T-beams. A linear interpolation curve is shown in red.

### 7.1.4. Compressive strength estimation

The rebound values and UPV measurements were used to estimate the concrete compressive strength using separate and combined conversion models. This section will compare the estimated strength values with the concrete compressive strengths obtained from lab tests.

**Rebound hammer**

The combined results from the rebound hammer tests and the obtained cube compressive strengths $f_{c,cube}$ are shown in Figure 7.5. No strength conversion has been applied to the rebound values thus far. Figure 7.5a shows both the cube compressive strengths and raw R- and Q-values plotted for both support beam 5 and the T-beam locations. A slight increasing trend in the strength can be seen with increasing rebound values for a higher strength. Figure 7.5b visualizes this trend more clearly with a scatterplot, showing the increasing positive trend between the two values.

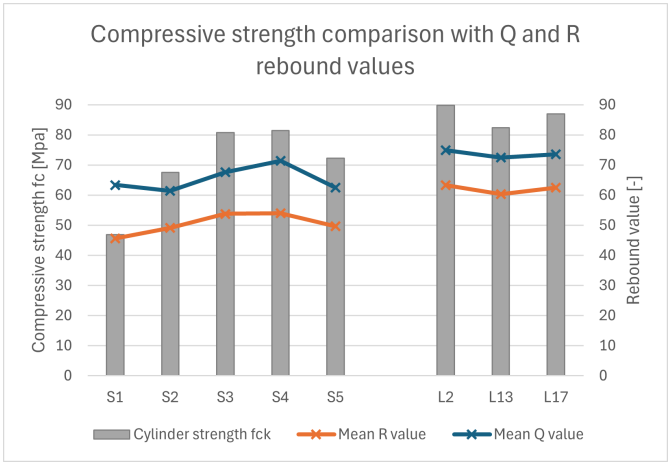


(a) Combined plot with rebound values and compressive strength $f_{c,cube}$

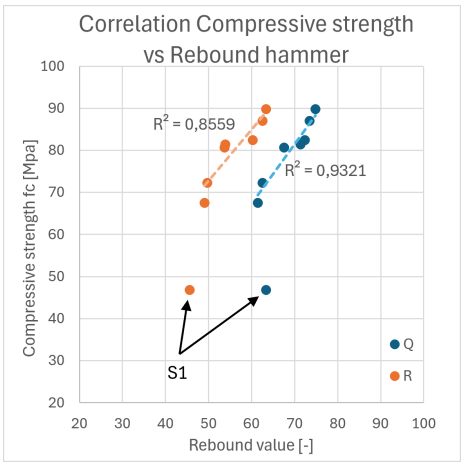


(b) Scatterplot of the rebound values and compressive strength $f_{c,cube}$

Figure 7.5: Correlation of the R- and Q-values with the compressive strength $f_{c,cube}$ before conversion.

One outlier that does not follow this trend is the location of S1 at STP5. It was seen in the results that the strength measured at this location is significantly lower compared to the other locations of the support beam. The rebound hammer was not able to measure the lower-strength concrete with the performed measurements. The Q-hammer even observed higher rebound values at S1 compared to S2. This is also visualized in 7.5b, where the pairings of S1 are highlighted and separated from the main cluster. A linear interpolation curve was fitted for the R- and Q-hammer, which is seen in Figure 7.5b. The outlier S1 was not included in the calculation of these fits. The linear curves show a great correlation for both R- and Q-hammers, with R-squared values of 0.856 and 0.932, respectively. The high values for the coefficient of determination indicate a great alignment of the two variables and the reliability of using both hammers for strength assessment.

The inability of the RH to detect the difference in concrete quality at S1 is noteworthy, especially as the other locations aligned well with the data. A likely cause of this discrepancy is the influence of carbonation, as it is known to increase the rebound value depending on the depth of the carbonation front. The measured depth of the carbonation front was the highest at S1 with a maximum depth of 24 mm and a mean depth of 16 mm. Carbonation reduction curves are provided in the Proceq manual, which could be applied to correct the higher rebound value. The curves are based on the JGJ/T 23-2011 Chinese code, which proposes a rebound value reduction of 40%[1] for a carbonation depth of 6 mm and deeper [60]. When this correction is applied for the rebound values of S1, a corrected scatterplot could be made, shown in Figure 7.6. The R-squared values of both hammers improved significantly and showed great alignment with the other pairs.

[1]The reduction curve described in the Proceq user manual describes the use of the curve to be exclusively used for the R-type original Schmidt hammer. The application of the reduction factor on the rebound values of the Q-hammer is purely illustrative.

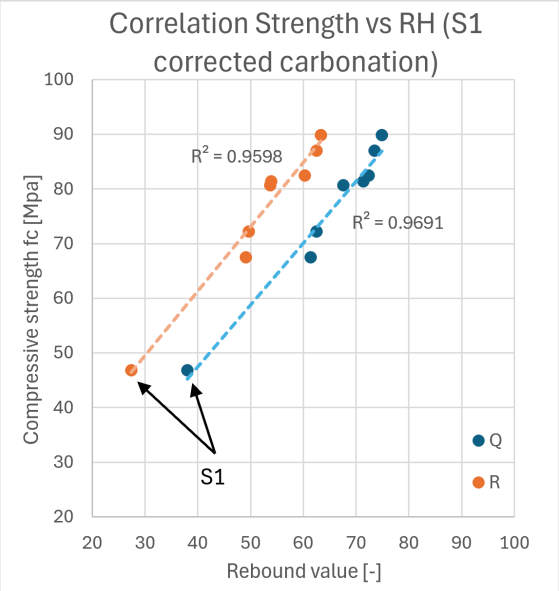


Figure 7.6: New scatterplot of the rebound values and compressive strength $f_{c,cube}$ with the reduced rebound values at S1.

The results highlight the importance of interpreting RH data in carbonated structures. While the application of the carbonation correction factor appears to improve the correlation, this factor is still based on generalized empirical relationships derived from other concrete mixes in differing environments. Its applicability can thus be questioned for this specific structure, as other correction methods exist with different correction factors [61–63]. Nevertheless, the carbonation reduction for the rebound values could serve as a useful tool to improve material assessment, although it would require additional carbonation measurements to be taken.

Another cause for the discrepancy could be a faulty test of the S1 concrete core. While care was taken to follow the norms and guidelines for extracting and testing the concrete cores, several external factors could have influenced the measured strength, which were not foreseen within the testing procedure. The lack of additional cores at this location does raise suspicions about the true compressive strength at S1.

**UPV**

Similarly to the rebound hammer, the UPV transmission speeds have also been plotted against the compressive strength in Figure 7.7. The combined graph in Figure 7.7a displays both the cube compressive strength and the corresponding UPV transmission speed. A slight increasing trend can be observed: The general increase of compressive strength at STP5 is somewhat reflected in the transmission speeds, except for S4, where the speed is lower than expected. At L17, the transmission speed also does not follow the higher compressive strength when compared to the other two T-beam pairings.

The correlation is more clearly visualized in the scatterplot shown in Figure 7.7b. A linear interpolation was fitted to the dataset indicated in red. The resulting trendline shows a positive correlation between UPV and compressive strength, with an R-squared value of 0.514. Although the correlation is not as strong as the one observed with the rebound hammer, it still suggests that UPV can serve as an (complementary) indicator for internal concrete quality, especially deeper into the concrete.
At S1, the UPV speed aligns with the lower compressive strength, which the rebound hammer failed to identify. This supports the earlier observations for a lower quality concrete region. In contrast to the rebound hammer, where carbonation may have masked this lower strength zone, UPV measures the material's internal density and homogeneity, and is thus less sensitive to surface conditions such as carbonation or finishing. Additionally, the agreement of the low UPV speed and low compressive strength at S1 adds trust to the core test result.

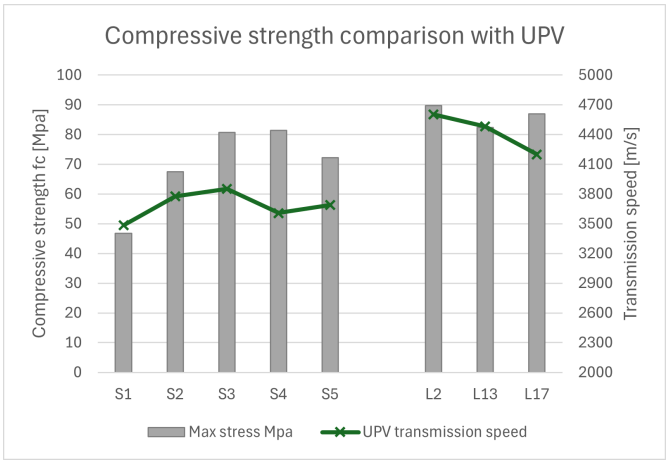


(a) Combined plot with UPV values and compressive strength $f_{c,cube}$

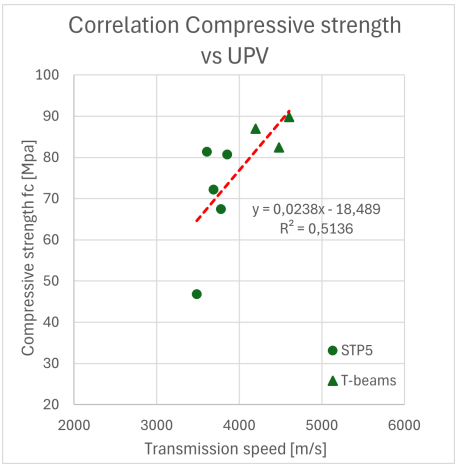


(b) Scatterplot of the UPV values and compressive strength $f_{c,cube}$

Figure 7.7: Correlation of the UPV values with the compressive strength $f_{c,cube}$ before conversion.

So, while the UPV method shows worse alignment with the tested cores than the rebound hammer, it compensates by being less sensitive to surface effects and influences of carbonation. As a result, it plays a great complementary role in strength estimation, particularly in heterogeneous or aged concrete where surface properties no longer represent the internal condition accurately.

**SonReb model**

The SonReb method was used to increase the accuracy of the concrete strength assessment by combining Q-hammer values and UPV speeds. A power-law regression model to estimate the cube compressive strength was made using Equation 7.1. The least squares method was used to fit the model constants. The calculation method to develop the regression model was adopted from Screening Eagles [64].

$$f_{ck} = a \cdot V^b \cdot Q^c \tag{7.1}$$

Where:

$a,\ b,\ c$ = Regression model constants [-]
$V$ = UPV transmission speed [m/s]
$Q$ = Rebound hammer (Q-value) [MPa]

Three SonReb models were developed using the measurement data. The SonReb model fitting constants and corresponding statistical data are described in Table 7.1, along with the regression models for only the RH and UPV. From these models, a scatterplot of the estimated and true strength is visualized and compared in Figure 7.8. The first model (Figure 7.8a) used all measurement pairs, including the outlier at location S1, which had previously shown low compressive strength values despite relatively high NDT measurements. This model has a coefficient of determination of $R^2 = 0.578$, suggesting a moderate correlation. The inclusion of S1 introduced bias into the fit, resulting in a skewed fit, which underestimates compressive strength at higher strengths as seen in Figure 7.8a.

Table 7.1: Overview of the strength estimation models with their regression parameters and coefficient of determination.

| Model | Type | a | b | c | $R^2$ |
|---|---|---|---|---|---|
| RH R | Linear | 1.224 | 11.551 | - | 0.856 |
| RH R (S1 carb. corrected) | Linear | 1,175 | 14,332 | - | 0,960 |
| RH Q | Linear | 1.410 | -17.261 | - | 0.921 |
| RH Q (S1 carb. corrected) | Linear | 1.132 | 2.322 | - | 0.969 |
| UPV | Linear | 0.0238 | -18.489 | - | 0.514 |
| SonReb 1 (incl. S1) | Power | 0.00164 | 0.7724 | 1.0256 | 0.578 |
| SonReb 2 (excl. S1) | Power | 0.7189 | 0.0376 | 1.0393 | 0.939 |
| SonReb 3 (S1 carb. corrected) | Power | 0.7291 | 0.1180 | 0,8787 | 0.985 |

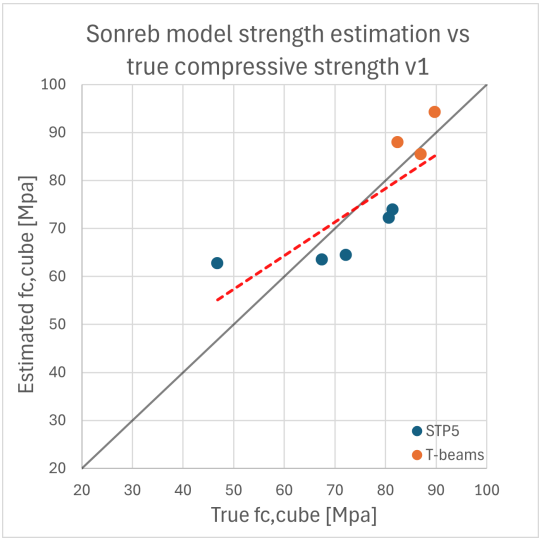


(a) SonReb model 1 including the S1 measurements

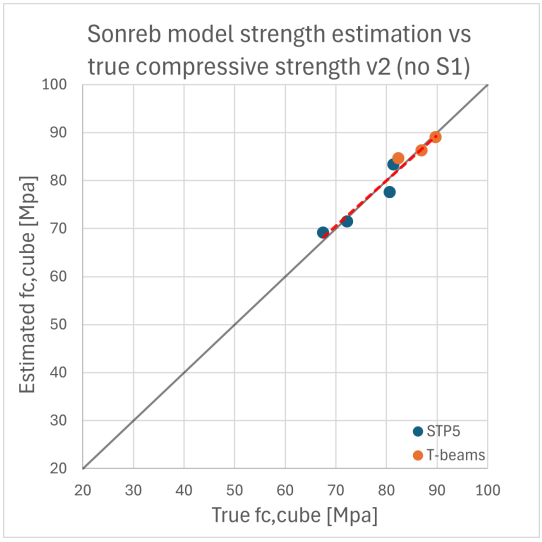


(b) SonReb model 2 excluding the S1 measurements

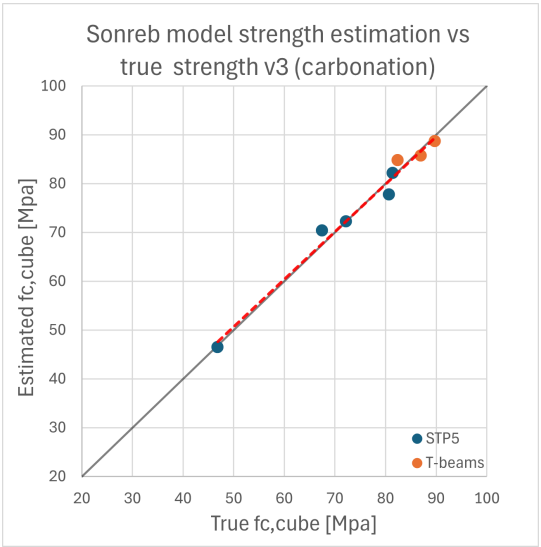


(c) SonReb model 3 including the S1 measurements corrected for carbonation

Figure 7.8: SonReb models fitted with the combined test data of the compressive strength, Q rebound value, and UPV measurements. A scatter plot is made with the model's estimated strength on the y-axis and the true strength on the x-axis.

A second model was fitted without the S1 measurements, as shown in Figure 7.8b. The resulting fit shows a greatly improved correlation, with an R-squared of 0.939 and a tightly grouped set of points

along the equality line. The removal of S1 in the dataset resulted in a more accurate SonReb model, which could estimate the compressive strength with less error. The improved accuracy of the second model highlights the sensitivity of combined NDT strength estimations to outliers. It furthermore highlights the necessity of verifying outlier data through repeat testing or additional investigation, particularly when developing regression models.
The third and last model was fitted using the corrected carbonation value for S1 with a 40% reduction in rebound value. This model showed the highest coefficient of determination with an R-squared of 0.985. The grouping of the estimates is similar to the second model without S1, but with the addition of the extra data pair, as shown in Figure 7.8c. The trend showed a perfect alignment with the equality line, just like the second model. The addition of the extra data pair resulted in a slight increase over the second model and a significant improvement over the first one. This highlights the possibilities for carbonation-corrected rebound values when developing strength estimation models, as both standalone RH and SonReb models show a better fit with this correction.

**Comparison to single models**
Comparing the SonReb method to the single variable methods using only the RH or UPV yielded interesting observations. The strength estimation using only UPV measurements showed a mild correlation with a coefficient of determination of $R^2 = 0.514$. On the other hand, the RH model (Q-hammer without the S1 measurements) showed a great correlation with a high coefficient of determination of $R^2 = 0.9321$. The second SonReb model, which uses the same dataset as the above RH model, only slightly improves the RH model with a coefficient of determination of $R^2 = 0.9393$. This slight increase shows an added benefit of including UPV data in the regression. However, the effect is so small that it could be questioned if the added costs of the additional measurements would be worth the effort.

Apart from the minimal statistical improvement in $R^2$, UPV does still provide valuable information about the concrete condition, which could be useful in a diagnostic setting. Deeper internal flaws, air voids, or delaminations are some examples of damage types that are not easily detectable with the RH. So, even if the UPV contributes less to the strength estimation, its inclusion in a broader structural assessment can still be justified.

The fitted regression parameters in Table 7.1 also indicate the relative influence of each method. In model 2, the RH coefficient $c = 1.039$ is significantly higher than the UPV coefficient $b = 0.038$, indicating that the rebound value has a far greater influence on the estimated compressive strength. This is also seen in the contour plot of the second model shown in Figure 7.9. whereby the contour lines are mostly horizontal, indicating a strong dependence on the rebound value. It supports the earlier observation that the RH correlates more strongly with strength than UPV, while also confirming the similarity of the second SonReb model to the standalone RH model, as they both have similar R-squared values.

It is important to note that the dataset used for fitting the SonReb models is relatively small. Only 8 data points (7 in Model 2) were used, making the regression vulnerable to overfitting and may not generalize well to other structures or concrete types. Larger and more diverse datasets are required to develop a more robust model for use in other Liggerkoppen structures. The same could be said about the carbonation corrected value for S1 in model 3. Here, only one anecdotal location was chosen to represent the reduced rebound value and is therefore not indicative of an overall greater correlation in all cases where carbonation is present. Especially carbonation fronts, which are not as deep as at S1, require more research to map their influence on the rebound values obtained.

**Comparison to the literature**
It's known that the SonReb method's effectiveness varies across studies, influenced by factors such as concrete composition, age, and testing conditions. The correlation found in the second model aligns well with the upper range of values reported in various studies, indicating a strong correlation between predicted and actual compressive strengths.
For instance, a study by Chandak and Kumavat reported that the SonReb method yielded results more accurate and reliable than individual tests for both lab and in-situ measurements [65]. Another study by Abbaszadeh showed an increase in $R^2$ when using a SonReb model compared to standalone RH and UPV models[66]. The coefficient of determination of $\sim$0.50 (RH) and $\sim$0.49 (UPV) was improved

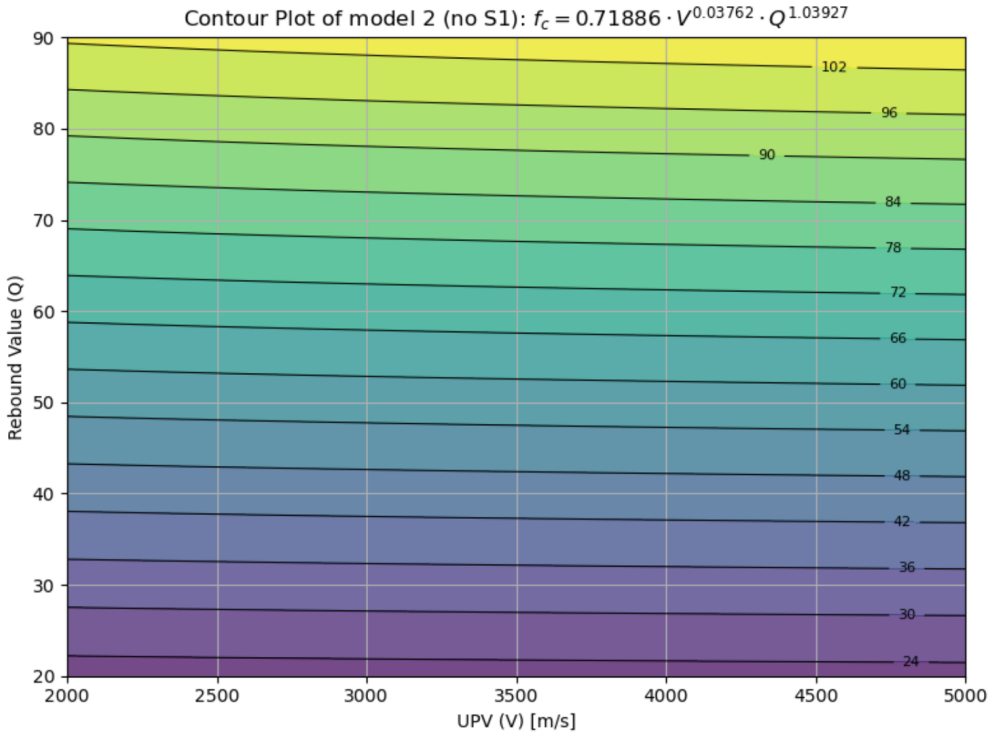


Figure 7.9: Contour plot of the second SonReb model showing the influences of UPV transmission speeds and rebound values on the strength estimation.

to 0.57 when combined, showing the usefulness of the SonReb method even with lower initial correlations. However, the SonReb model in this study used a second-degree polynomial correlation, instead of a power correlation. Another study performed by Mantegazza et al. showed close agreement with the findings of this study [67]. This large-scale study was performed at an abandoned building site with a wide range of identified concrete mixes. It was observed that the RH performed the best in terms of correlation out of all the single variable methods tested (RH, UPV, Windsor probe), while the UPV performed the worst with an $R^2 < 10\%$ for 10/12 cases [67]. Comparing the single RH model to the SonReb model showed a minimal improvement in correlation with only a slight increase in $R^2$, aligning perfectly with the results of this study.

### 7.1.5. Comparison Sluinerweg

**Rebound hammer**

The Sluinerweg only used the Q-hammer to perform RH measurements. This section will thus only compare the Q-hammer measurements. The Q-values for the Ardeweg and Sluinerweg are compared in Table 7.2, Figure 7.10, and Figure 7.11. The KCG coating was not an investigated variable during the study on the Sluinerweg. It was assumed that its influence did not pose any issues for the RH measurements [5, p.70]. This assumption can be questioned as the results of the Ardeweg show a significant effect on the RH measurements, whether the coating is present or not.

Table 7.2: Comparison of the Ardeweg and Sluinerweg mean RH measurements for the support beams and the T-beams. Presence of the KCG coating is indicated with 'C', while no coating is indicated with 'NC'.

| | | Ardeweg C | | Ardeweg NC | | Sluinerweg |
|---|---|---|---|---|---|---|
| **Location** | **Name** | **Rebound value Q [-]** | **Name** | **Rebound value Q [-]** | **Name** | **Rebound value Q [-]** |
| Support beam | S1 | 48.5 | S1 | 63.3 | S1 | 43.0 |
| | S2 | 44.4 | S2 | 61.4 | S2 | 42.8 |
| | S3 | 53.2 | S3 | 67.6 | S3 | 42.7 |
| | S4 | 51.0 | S4 | 71.4 | S4 | 44.3 |
| | S5 | 50.2 | S5 | 62.5 | | |
| | **Mean** | **49.3** | **Mean** | **65.0** | **Mean** | **43.2** |
| | **Std.dev.** | **11.35** | **Std.dev.** | **5.87** | **Std.dev.** | **4.77** |
| T-Beam | | | L2 | 74,8 | L1 | 68.6 |
| | | | L9 | 73,3 | L7 | 72,3 |
| | | | L13 | 72,4 | L13 | 70,3 |
| | | | L17 | 73,5 | L18 | 73,4 |
| | | | L23 | 75,5 | L23 | 70,8 |
| | | | **Mean** | **73.9** | **Mean** | **71.1** |
| | | | **Std.dev.** | **2.98** | **Std.dev.** | **3.99** |

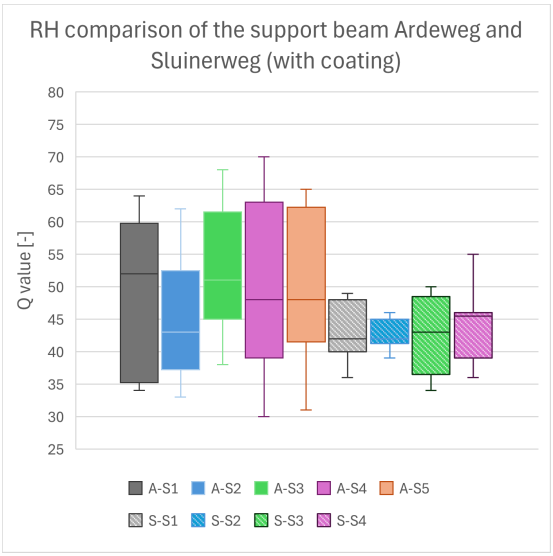


(a) Q-values with the Ardeweg KCG coating

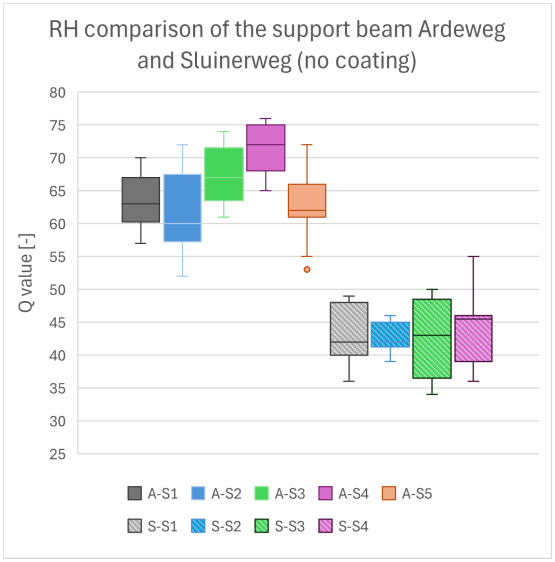


(b) Q-values without the Ardeweg KCG coating

Figure 7.10: Boxplots of the Ardeweg (A) and Sluinerweg (S) Q-values at the support beam. The measurements with and without coating for the Ardeweg measurements are shown in the two graphs.

It is observed that the overall rebound values are lower for the Sluinerweg measurements for both the support beam and T-beams, with differences being more significant at the support beam. At the

T-beams, the difference between the means is 2.8 MPa, while the support beam shows a difference in mean values of 6.1 MPa and 21.8 MPa with and without the coating, respectively.
Interestingly, the Sluinerweg RH measurements on the support beam show a lower standard deviation (4.77) than the Ardeweg values with the coating removed (5.87). Especially as the coating was not influenced during the testing, according to the report. This is unexpected, as the presence of was linked to a greater variance. A possible explanation could be differences in the number of measurements, impact technique, data processing, or the condition of the coating itself. If during the Sluinerweg testing, fewer impact locations, consistent user technique, or less degraded coating surfaces were present, then this may have artificially influenced the variability. Regardless, this result highlights the importance of surface preparation and standardization to ensure consistent RH measurement results within and across structures.
Nine measurements were taken for each location, at the Sluinerweg, compared to the 12 measurements at the Ardeweg. Furthermore, the condition of the KCG coating for both viaducts was not reported, nor taken into account during the measurements. It could, however, be assumed that the coating was evenly applied, as no surface discrepancies were observed at the measurement locations.

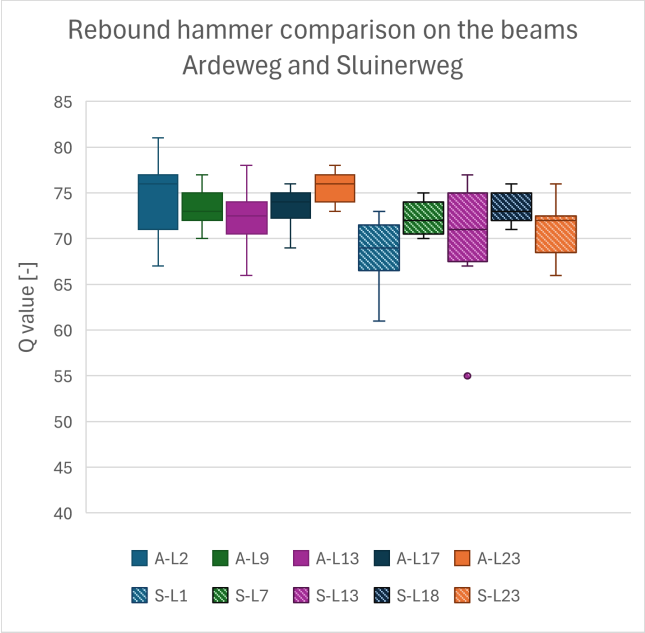


Figure 7.11: Rebound hammer test results on the T-beams using the Q-type hammer.

The T-beams of both viaducts show similar rebound values and spread, which is in line with the expectations, as both T-beams were prefabricated in the same factory. The consistent values can also be explained by the lack of surface coating on the T-beams, which removes another influencing variable during RH measurements. The T-beam results show that under controlled surface conditions, the Q-hammer yields consistent results.
Just like the Sluinerweg report, the established compressive strength values are compared against existing Q value conversion models of Nedeljkovic et al. and CEN/TR 17086 [68, 69]. The results for both the Ardeweg and Sluinerweg viaducts are shown in Table 7.3.

Table 7.3: The RH Q values of the Ardeweg and Sluinerweg viaducts with the two strength conversion models.

| | **Location** | **Median Q** | $f_{c,cube}$ **[68]** | $f_{c,cube}$ **[69]** | $f_{c,m,cube}$ |
|---|---|---|---|---|---|
| Ardeweg | Support beam | 65.5 | 85.1 | 79.2 | 75.5 |
| | T-beams | 74.0 | 98.7 | 118.2 | 83.9 |
| Sluinerweg | Support beam | 42.5 | 49.5 | 28.0 | 44.8 |
| | T-beams | 72.0 | 94.5 | 104.8 | 82.2 |

**UPV**

An overview of the UPV results for both the Ardeweg and Sluinerweg viaducts is shown in Table 7.4, which displays consistently higher transmission speeds for the T-beams compared to the support beam. It should be noted that the Ardeweg has five evenly spaced measurement locations along the support beam, while the Sluinerweg only has four. The location of S4 at the Sluinerweg is thus more comparable to S5 at the Ardeweg.

Table 7.4: Comparison of the Ardeweg and Sluinerweg UPV measurements

| | Ardeweg | | Sluinerweg | |
|---|---|---|---|---|
| **Location** | **Name** | **Transmission speed [m/s]** | **Name** | **Transmission speed [m/s]** |
| Support beam | S1 | 3484 | S1 | 3792 |
| | S2 | 3777 | S2 | 3532 |
| | S3 | 3852 | S3 | 3798 |
| | S4 | 3608 | S4 | 3477 |
| | S5 | 3689 | | |
| | **Mean** | **3700** | **Mean** | **3650** |
| | **Std.dev.** | **143,7** | **Std.dev.** | **169,2** |
| T-Beam | L2 | 4603 | L1 | 4370 |
| | L9 | 4764 | L7 | 4486 |
| | L13 | 4482 | L13 | 4383 |
| | L17 | 4200 | L18 | 4266 |
| | L23 | 4737 | L23 | 4333 |
| | **Mean** | **4554** | **Mean** | **4368** |
| | **Std.dev.** | **229,4** | **Std.dev.** | **80,3** |

The mean transmission speeds for the Ardeweg are slightly higher than the Sluinerweg speeds, although not significantly. The support beams differ by 50 m/s, while the T-beam measurements differ by 186 m/s. This would indicate that the Ardeweg beams are of similar (or slightly better) quality. This is expected due to the beams being produced by the same manufacturer as well as in the same time period. The T-beams of the Sluinerweg also seem to have a tighter spread when compared to the Ardeweg beams. Due to the limited measurements taken, no statistical explanation could be formulated about this difference. It should also be noted that the Sluinerweg report does not mention T-beam width measurements being taken, as the Ardeweg T-beams show a spread in width for the different beams.

## 7.2. Half-cell Potential

### 7.2.1. Support beam 5

Correlation curves to compare the Gecor-10 and Profometer results at STP5 are plotted in Figure 7.12. Both Sensor A & B are plotted on the y-axis against the values of the Profometer on the x-axis. The two resulting trend lines show a positive correlation with an $R^2$ of 0.754 and 0.774 for sensors A & B, respectively. The trend lines also follow the equality line, indicating a great unbiased correlation between the Gecor-10 sensors and the Profometer measurements.

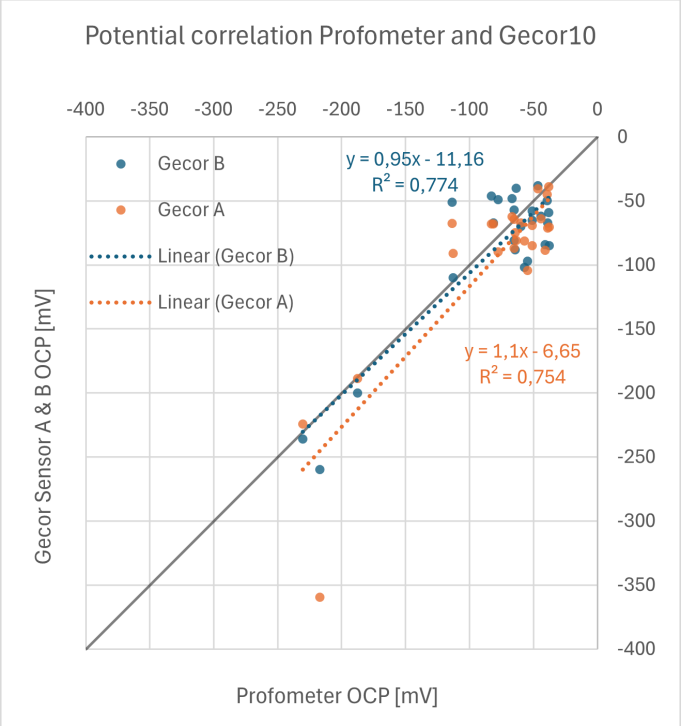


Figure 7.12: Scatter plot showing the correlation between the Gecor-10 sensors and the Profometer measurements for half-cell potential on support beam 5. Linear interpolation curves are fitted for both Gecor-10 sensors.

Most of the pairings are grouped in the lower value region between -50 mV and -100 mV, corresponding with the measurement locations under beams L5-L25. The higher potentials at the more negative end of the trend are from the left region under beams L1-L4, where active corrosion was expected. Despite the great correlation, it must be acknowledged that the high concentration of data points in the lower potential region introduces a bias that may artificially inflate the correlation. The correlation strength in areas of active corrosion remains less certain, which calls for additional data collection for validation.

Nevertheless, the great correlation of both sensors shows the consistency of half-cell potential measurements even with differing measurement devices. The results indicate that external factors like surface finish, contact area, and user experience do not influence the results for a given measurement device more than the other, highlighting the half-cell potential's usefulness as a corrosion identification technique. It also allows users to confidently use either device in similar field conditions, particularly where equipment availability or cost may influence the choice of instrument. Moreover, this cross-device validation supports the use of long-term monitoring strategies where equipment and conditions may change over time.
Most potential values fell between the -50 mV to -100 mV range, indicating a low probability of corrosion based on ASTM C876 criteria [70]. Only one point was classified with a high corrosion risk (< -350 mV), which was the location under beam L2 using the Gecor-10 A sensor. Four additional data points fell in the uncertain region (-350 < x < -200), where the corrosion risk is debatable. These data points were also located on the left side of the support beam. Despite the uncertain classification based on the ASTM C876 criteria, a moderate to high likelihood of corrosion is still expected, as this location aligns with prior visual assessments and high chloride content findings.

### Comparison 2019 report

The potential measurements from the 2019 report are compared to the new potential map in Figure 7.13. The Profometer with the wheel electrode was used to create the displayed potential map, while the 2019 measurements were performed using a simple point electrode. Both measurements used a copper–copper(II) sulfate reference electrode. The 2024 measurements focused on the vertical face of the support beam with three rows, while the 2019 measurements also included 24 spots on the top horizontal face between the T-beams. Additionally, the 2024 potential map shows a higher resolution due to more data being measured.

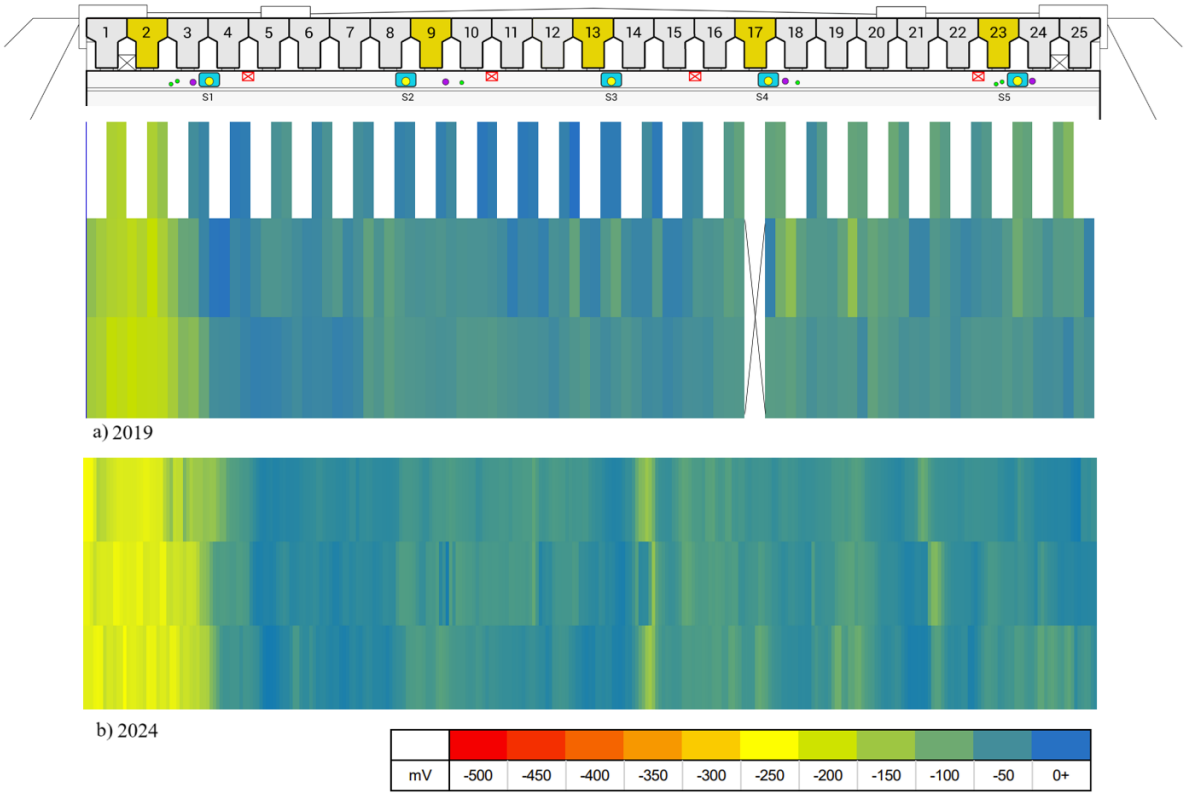


Figure 7.13: Potential map of support beam 5 comparing values from 2019 and 2024

In both potential maps, the previously mentioned low-potential region can be seen on the left side of the support beam. This region has expanded by approximately one beam width over time. Additionally, this region has developed a lower potential over time, indicated by the increased intensity of the color. The growth of this region is within expectations for a time period of five years. Moreover, the fact that this region can be visualized with similar values using different devices signifies the consistency of the overall method and validates the usefulness for long-term monitoring.

The rest of the results mainly show stable values for potential, except for a location under beam L14, where a small peak in potential appears with a minimum value of around -130 mV. This peak would still be classified as a low risk for corrosion, but the sudden change in potential raises suspicion for potential corrosion. To confirm the corrosion activity in these uncertain regions, complementary techniques such as resistivity measurements or chloride content analysis are recommended.

The wheel electrode used by the Profometer proved very useful in mapping large concrete areas, due to its faster gathering of measurements. Its ease of use, along with the ability to monitor potentials in real-time during measurements, showed great potential for on-site inspections. The measurement results can be visualized and reviewed in the field, which could help identify potential corrosion zones and prepare for subsequent investigations.

### 7.2.2. T-Beams

The positive to neutral half-cell potentials measured on the T-beam soffits strongly suggest passive steel reinforcements with low corrosion risk. The values were consistent across all beams except for beam L17. The drop in values near the beam head of L17 was likely caused by the conductive CP coating, misrepresenting the true potential of the underlying concrete.

### 7.2.3. Harvested beams

The half-cell potential values measured from the harvested beams showed great alignment with each other, which was also seen in the results of the support beam. The consistency and reliability of the measurement devices are confirmed by the overall alignment of the measurements across the length of the beams under similar conditions. A correlation heatmap is plotted for the used devices, which is shown in Figure 7.14. The $R^2$ is shown for each pair of measurement devices.

| | Profometer | Gecor B | Gecor A 30s | Gecor A 100s |
|---|---|---|---|---|
| Profometer | 1,000 | | | |
| Gecor B | 0,878 | 1,000 | | |
| Gecor A 30s | 0,223 | 0,595 | 1,000 | |
| Gecor A 100s | 0,301 | 0,639 | 0,968 | 1,000 |

Figure 7.14: Correlation heatmap of the four half-cell potential devices showing the coefficient of determination between the methods. Green shows a better correlation, while red indicates a poor correlation.

**Correlation of potential measurement techniques**

The correlation matrix reinforces the reliability of the Profometer and the Gecor-10 B sensor, which shows strong agreement across the tested beams with a $R^2 = 0.878$. In contrast, the Gecor-10 A sensor shows poor correlation with both devices when recorded at both 30s and 100s. These findings support the use of the Profometer or Gecor-10 B sensor as more stable baselines for field assessments when the half-cell potential is of interest. And while the Gecor-10 A sensor remains consistent between the 30s and 100s measurement (r = 0.968), its differing values with other methods do raise questions about its accuracy for the $icorr$ measurements. Since the linear polarization resistance $R_p$ is measured around this potential, any inaccuracies or bias in Sensor A could skew the resulting slope and misrepresent $icorr$. Using $E_{corr}$ values closer to those recorded by the Profometer or Gecor-10 B sensor would likely yield a more stable and representative assessment of the material's corrosion condition.

Despite the promising correlations, significant deviations were observed in beam L23, where the Profometer recorded consistently more negative values than both Gecor-10 sensors. While the trend remained similar, the shifting potential may point to differences in electrode calibration, contact resistance, or measurement timing. Conversely, Gecor-10 Sensor A showed significantly more positive potentials compared to Sensor B, which would indicate an inherent difference in the sensor

**Influence of CP coating**

In beam L17, a distinct potential drop to –372 mV at x=75cm from the beam head was observed, aligning with the location where the conductive CP coating was the thickest. It remains unclear how much the low potential values are influenced by the actual material condition, and how much is influenced by the CP coating. As a result, an objective assessment of corrosion risk can not be conducted for this beam. The influence highlights the limitation of the half-cell method in environments influenced by CP systems, where electrical potentials do not represent the true corrosion risk. The interpretation of half-cell measurements on structures with an (in)active CP-system should thus be performed with care. Although the assumption could be made that beams protected with CP are not capable of degrading and do not need to be inspected.

**Influence of distance**

A downward trend in potential values toward the beam head is prominently visible in beams L2, L13, and L17. At the location x=25cm, these beams show noticeably more negative potentials compared to the measurements taken further along the beam. While beam L17 shows a local peak at x=75cm, this

discrepancy can be attributed to interference from the CP coating and does not detract from the global trend of decreasing potential toward the beam end.
This downward trend is consistent with expected chloride exposure patterns. The beam heads are located directly below a dilation joint, which would cause a higher exposure to chlorides from de-icing salts and moisture. As a result, the concentration gradient of chlorides is highest near the beam ends, which is seen in Figure 6.7, where the highest chloride concentrations are found near the head of the beam. Given the electrochemical nature of steel corrosion, areas with high chloride concentrations and moisture presence result in more negative half-cell potentials.
What strengthens this interpretation is that the trend is observed across all measurement devices, as the Profometer, Gecor-10 sensor B, and both Gecor-10 A sensors all show a similar downward shift in potential near the beam head (excluding L23 results). All of which negates the likelihood that the observed trend is a measurement error or device inconsistency.

**Accessibility**
Although the observed drop in potential near the beam heads indicates higher corrosion risk, it must be noted that these areas are not typically accessible in the original structure. The beam ends are largely covered by the support beam, with only small gaps on the side allowing access for potential measurements. As a result, the detailed mapping conducted in this study cannot be replicated in practice. Nevertheless, the results highlight a critical vulnerability in these inaccessible regions, especially near the dilation joints. In field applications, targeted strategies such as probe-based electrodes or selective core sampling may be needed to assess these areas.

## 7.3. Resistivity

### 7.3.1. Support beam 5

The resistivity results on Support Beam 5 show a clear trend, with all three measurement devices showing significantly lower values at the left side of the support beam (L1–L6). This region also corresponded with earlier measured low half-cell potential values, strengthening the interpretation that this region is actively corroding. The consistency across techniques highlights the use of multiple corrosion assessment techniques for identifying corrosion.

Despite this trend, the spread in values between sensors is significant. For example, the Gecor-10 C Sensor reports an extremely low resistivity of 0.02 $k\Omega m$ at L1, while the Resipod and Gecor-10 A sensor recorded values of 0.45 $k\Omega m$ and 0.21 $k\Omega m$, respectively. Furthermore, sensor A shows more conservative resistivity values, especially between L17 and L23, which indicates a systematic difference between the measurement devices. This systematic noise makes the interpretation of the resistivity results relatively difficult. Especially when compared to the half-cell potential results, where the measurements across the beam are more in line with one another.
Despite the inconsistencies between methods, the identification of the high-risk zone was still possible, as the methods converged for the high corrosion risk region. This supports the effectiveness of these techniques in detecting active corrosion areas, even when sensor readings differ in scale.

From L7 onward, all sensors report values generally above 1.0 $k\Omega m$, suggesting reduced corrosion risk in that region. This sudden shift in values at L7 may indicate a boundary where environmental exposure has influenced the concrete, like leakage of moisture and chloride ingress.

Overall, these findings highlight the importance of proper interpretation when using resistivity techniques for corrosion assessment. The spread between measurement devices and within the support beam shows a lack of stability that may hinder result interpretation. Despite this, the resistivity measurements converged at the earlier observed active corrosion zone, which was also identified with the half-cell potential. This proves its usefulness as a complementary tool next to other corrosion assessment tools, like the half-cell potential and corrosion current density, for the validation of corrosion risk locations.

### 7.3.2. Harvested beams

#### Correlation and trends between devices

The general trend of lower resistivity near the beam head is consistent for all measurement techniques, which is in agreement with the half-cell potential results described earlier. However, wider spread in resistivity values and inconsistent Sensor A values indicate overall instability of the sensors used.

The trends between the Resipod and Gecor-10 C sensor values show close alignment, even for L23, where the values alternate throughout the beam. Furthermore, the Resipod shows consistently higher resistivity values than the Gecor-10 C sensor. However, the A sensor does not follow the trend seen with the other devices, measuring both significantly lower and higher values at some locations. Figure 7.15 plots the correlation heatmap for the resistivity devices, showing the $R^2$ for each pair of measurement devices.

| | Resipod | Gecor C | Gecor A 30s | Gecor A 100s |
|---|---|---|---|---|
| Resipod | 1,000 | | | |
| Gecor C | 0,852 | 1,000 | | |
| Gecor A 30s | 0,185 | 0,134 | 1,000 | |
| Gecor A 100s | 0,557 | 0,620 | 0,448 | 1,000 |

Figure 7.15: Correlation heatmap of the resistivity devices showing the coefficient of determination between the methods. Green shows a better correlation, while red indicates a poor correlation.

The best correlation was observed between the two surface methods: Resipod and Gecor-10 C sensor with a $R^2 = 0.852$, indicating that both Wenner probe measurements yield comparable results. In contrast, the correlations between Resipod and Sensor C with Sensor A are significantly weaker. For example, the correlation between the Resipod and Sensor A (30s) is low ($R^2 = 0.185$), and similarly weak between Sensor C and Sensor A (30s) at $R^2 = 0.134$. These low values suggest that short polarization durations in embedded probes, like the one used in the A sensor, do not reflect the surface resistivity values well. Local internal conditions, which are not captured with the surface methods, like moisture, steel depth, and rebar placement, may have influenced the estimated resistivity.

#### Influence of polarization time for resistivity

Interestingly, the resistivity values from the longer 100s polarization time measurements show better correlations (Resipod $R^2 = 0.557$, C sensor $R^2 = 0.620$), suggesting that longer polarization times may improve the stability of the concrete resistivity estimation. Furthermore, the moderate correlation between the 30s and 100s A sensor values $R^2 = 0.448$ implies that even with the same sensor, resistivity values can vary significantly depending on the polarization time. The polarization time is thus a key variable for the stable estimation of the concrete resistivity, which may have implications for the corrosion current density results.

These findings indicate that the Resipod and Gecor-10 C sensor are generally consistent and suitable for mapping resistivity, while the Gecor-10 A sensor introduces additional variability. Therefore, careful consideration of sensor type and measurement protocol is of importance when interpreting resistivity data, especially when comparing results across different techniques.

#### Influence of CP coating

For the harvested beams, the lowest values were observed at the CP beam L17, which aligns with expectations that the conductive coating reduces measured resistivity. Conventional interpretation for these low values($< 0.1\ k\Omega m$ would suggest a high probability of corrosion. However, with the influence of the conductive coating, no conclusive statement could be made about the true corrosion condition of the beam, which was also a concern with the half-cell potential measurements. From the chloride content tests shown in Figures 6.6 and 6.7, it was concluded that the chloride content of beam L2 was more than twice that of L17, indicating a significant difference in material condition and corrosion risk. This difference was, however, not found with the resistivity or the potential measurements, highlighting the masking effect of the CP coating on non-destructive corrosion techniques.

# 7.4. Corrosion current density

## 7.4.1. Support beam 5

The measured values for the corrosion current densities $i_{corr}$ are compared against the corrosion potential and resistivity in Figure 7.16a and 7.16b, respectively. Both figures include the risk classification as colored zones mapping the limits of each risk class. The green zone represents low corrosion probability for both $i_{corr}$ and resistivity or potential, while orange and red represent a moderate and high risk for corrosion, respectively. The white areas represent a discord between the risk classifications.

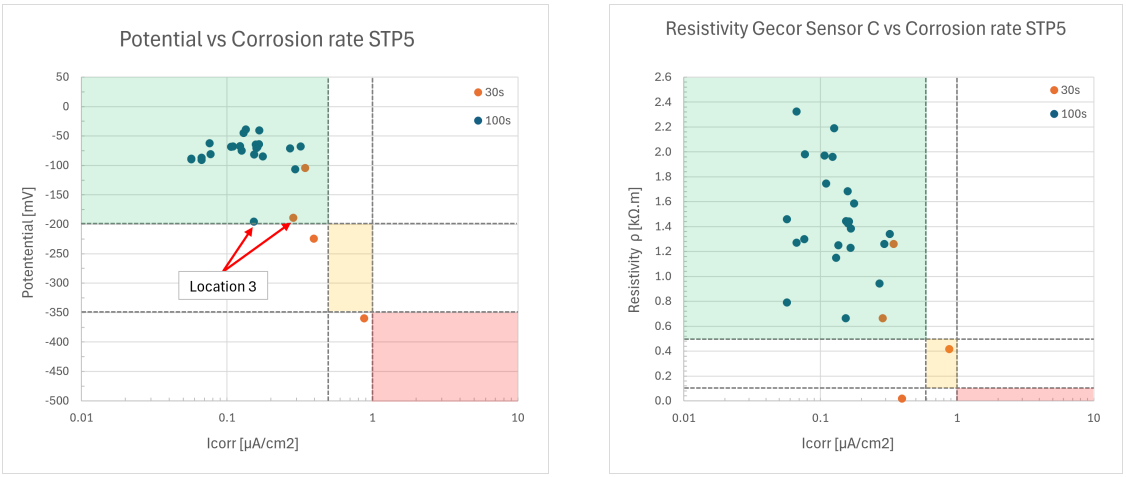


(a) Potential (b) Resistivity

Figure 7.16: Scatterplot of the corrosion current density $i_{corr}$ and the corrosion potential $E_{corr}$ on the left (a) and concrete resistivity $\rho$ on the right (b). Corrosion potential was measured with the Gecor-10 confinement sensor (A), while the 4-tip resistivity sensor (C) was used for the resistivity measurement.

It can be noted that all of the 100 second support beam measurements are located in the low-risk zone for corrosion. The locations chosen for the 30s measurements show more corrosion activity, as they near the orange and red area, especially the location under L2 is concerning with a minimum value for resistivity and potential of 0.42 $k\Omega m$ and -360 $mV$ respectively. A trend can be observed whereby the $i_{corr}$ increases with lowering of the potential. The relation between the $i_{corr}$ and resistivity is less pronounced with more spread, but still follows the same trend. The points at L3 are highlighted in Figure 7.16a, where a shift in $i_{corr}$ can be seen towards the orange zone.
It is important to note that the chosen locations for the 30s corrosion rate measurements were to be expected. An increased risk seen with standalone potential and resistivity measurements was ultimately the reason for the choice of the 30s polarization time. This effect is also enhanced as the values for $i_{corr}$ are generally higher with shorter polarization times. It would have been optimal if the values were measured with both the 30s and the longer 100s durations to compare the differences, but this was unfortunately not possible due to time constraints.

## 7.4.2. Harvested beams

The corrosion rate for the harvested beams shows differences as the measurements performed used both 30s and 100s polarization times. These differences were expected as the polarization time has a known effect on the measurements. Under normal circumstances, only one CR measurement is performed using the methodology described in Section 4.2.4, whereby a shorter or longer polarization time is chosen based on the estimated corrosion risk.
Despite only requiring a single reading to measure the representative $i_{corr}$ value, both 30s and 100s measurements were performed to evaluate the influence of polarization time. Based on corrosion risk indicators, the 100s value was chosen in areas with low or negligible risk, while the 30s value was applied in zones with moderate to high risk. Half-cell potential and resistivity data at corresponding locations determined the classification.
However, determining the corrosion risk was not always straightforward, as up to eight measurements were available per location, including readings from the Resipod, Profometer, Gecor-10 sensors (B

and C), and Sensor A (30s and 100s) for both resistivity and potential. In cases where results were inconsistent, multiple risk classes were assigned to a single location, as shown in Appendix E. The final $i_{corr}$ values chosen are shown in Table 7.5 and Figure 7.17.

Table 7.5: The combined $i_{corr}$ values measured at the harvested beams. The 30s values that were chosen are indicated in bold. Non-bold values are measured with the 100s polarization times. Units are in $\mu A/cm^2$.

| Distance [mm] | L2 | L13 | L17 | L23 |
|---|---|---|---|---|
| 25 | **0.452** | **0.499** | **0.411** | **0.560** |
| 50 | 0.192 | 0.440 | 0.225 | **0.188** |
| 75 | **0.243** | **0,192** | – | – |
| 100 | 0.269 | 0.092 | – | **0.390** |
| 125 | 0.282 | 0.207 | 0.185 | **0.504** |
| 150 | 0.216 | 0.254 | 0.085 | **0.487** |

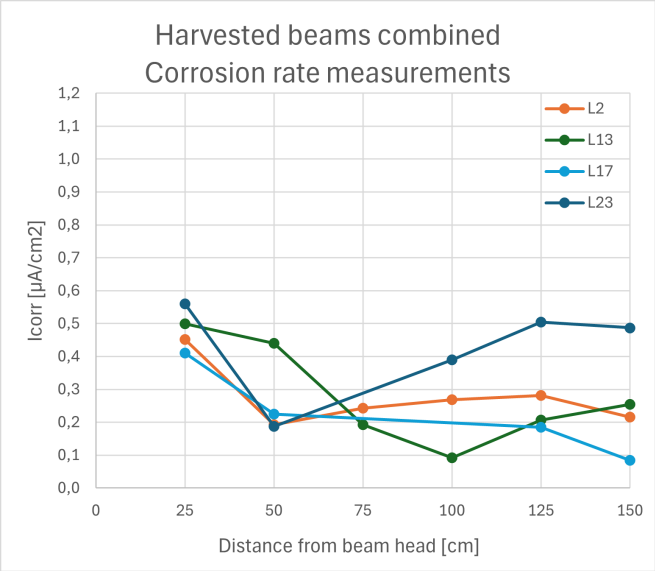


Figure 7.17: The true values for corrosion current density based on the risk classifications for both resistivity and half-cell potential.

The decision-making was based on the criteria for resistivity and potential measurements as seen below. These steps have been put in a flowchart shown in Figure 7.18.

1. Gecor-10 A sensor resistivity and potential measurements were not considered.
2. Shorter 30s polarization time is chosen for:
   - Half-cell potential values indicating a moderate or higher risk with **any** method (< -200 mV).
   - Resistivity values indicating a moderate or higher risk with **both** methods (< 0.5 $k\Omega m$).
3. Longer 100s polarization time is chosen for all other cases.

The exclusion of Gecor-10 Sensor A data was based on its observed instability compared to standalone half-cell potential and resistivity measurements. Its inconsistent readings were the main source of discrepancies in corrosion risk classes. For example, the resistivity at beam L13 (50cm) ranged across three risk classes: 0.40 $k\Omega m$ (Sensor C), 0.71 $k\Omega m$ (Sensor A, 30s), and 0.09 $k\Omega m$ (Sensor A, 100s). Half-cell potential was prioritized as the primary indicator due to its observed stability and consistency across both devices and locations. The Profometer and Gecor-10 B sensor demonstrated excellent agreement, making them interchangeable for corrosion risk assessment. The resistivity was chosen as

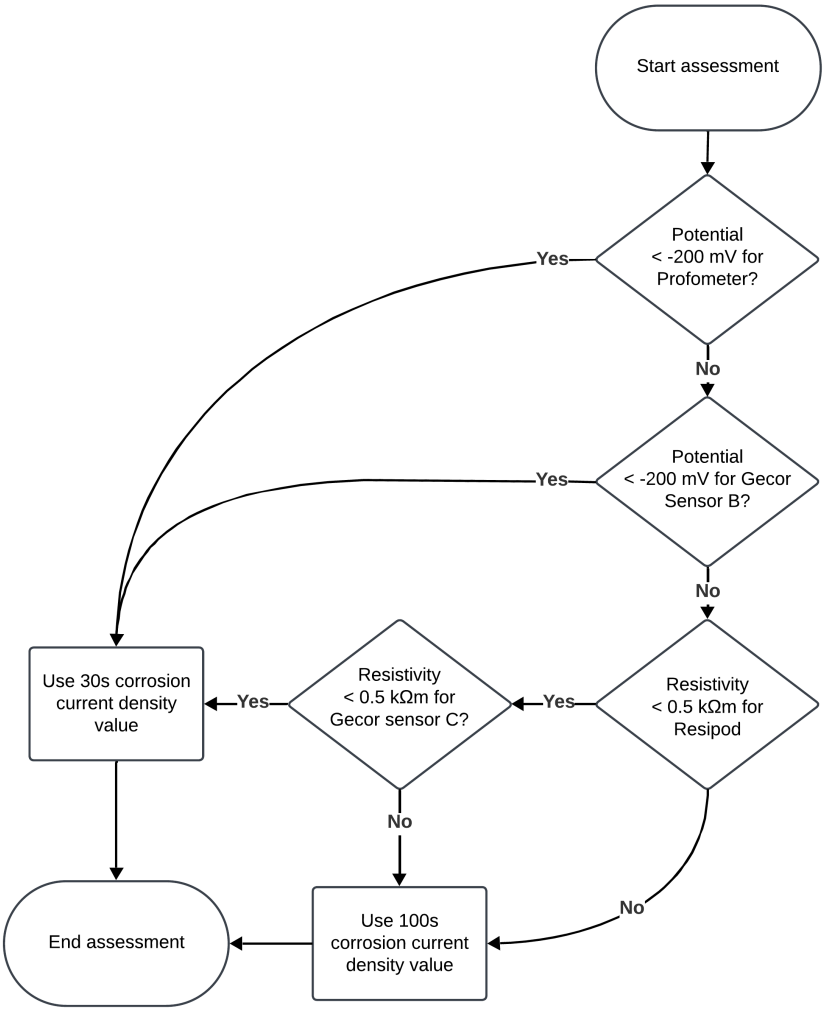


Figure 7.18: Flowchart for the determination of the representative $i_{corr}$ value using the resistivity and potential measurements.

a second indicator as it showed more spread across the beam. It identified more moderate-to-high-risk areas than the potential measurements alone, reinforcing its value in refining the corrosion assessment.

The combined curves shown in Figure 7.17 show a more consistent trend along the length of the beam, with an increased $i_{corr}$ value at the beam head (x=25cm). The value for the $i_{corr}$ gradually decreases slightly with the length of the beam, except for beam L23, where the value increases over the length after an initial drop.

### 7.4.3. Combined results

All the corrosion data from the Ardeweg and Sluinerweg are combined in Figure 7.19. Here $i_{corr}$ is plotted against the half-cell potential and resistivity. For the Ardeweg, Gecor-10 sensors A and C were used for potential and resistivity, respectively, while the Sluinerweg data used Sensor A and the Resipod. Corrosion risk zones are indicated by shaded regions corresponding to the standard risk classifications.

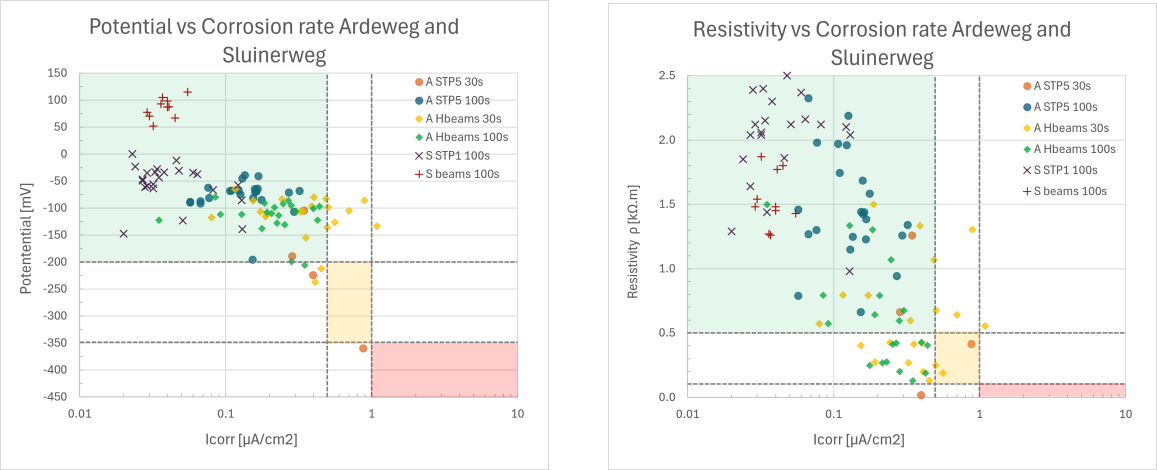


(a) Potential

(b) Resistivity

Figure 7.19: Scatterplots for the corrosion current density $i_{corr}$ with potential and resistivity, comparing all the gathered values, including the Sluinerweg results.

While the majority of results cluster in the low-risk corrosion zone, slight variability is observed among 30s polarization results, especially when compared to the more stable 100s data. The 30s values for both the harvested beams and the support beam seem to be the most likely to have corrosion, as they are mainly present in the uncertain corrosion risk region. Furthermore, a global trend can be observed in both potential and resistivity data, indicating a higher corrosion rate when a higher risk of corrosion is seen. The grouping of half-cell and resistivity data with $i_{corr}$ in passive zones affirms their reliability for routine corrosion risk screening. However, scatter and elevated $i_{corr}$ in uncertain regions raise questions about the corrosion state of these locations.

Overall, the agreement between $i_{corr}$, potential, and resistivity supports the use of combined NDT methods for more robust corrosion assessment in aging concrete structures. The agreement with each other signifies a deeper connection between the three corrosion risk metrics.

## 7.5. Chloride content

### 7.5.1. Comparison 2019 report

The 2019 results for chloride content determinations are compared to the Ardeweg results in Figure 7.20. The locations of S1, S2, S4, and S5 for both measurements are comparable, as can be seen in Figure 7.21. The locations of the 2019 results are renamed to correspond with the Ardeweg naming convention. Only the location at S4 does not align properly, with the S4 core being taken 2 beam widths to the right of the 2019 measurement. The 2019 measurements were performed on-site with the RCT method, instead of the more accurate Volhard titrations performed in the lab for the 2024 values.

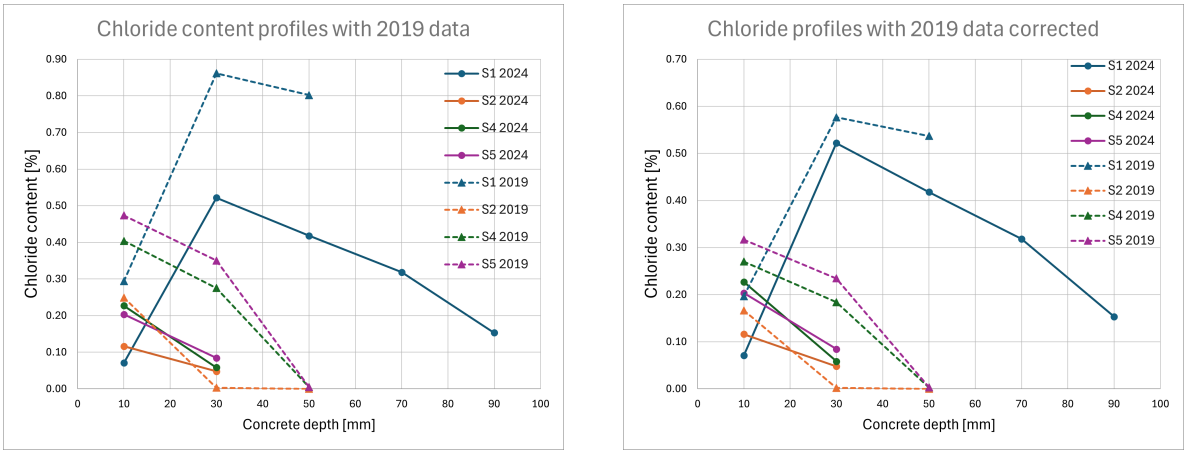


(a) Uncorrected

(b) Corrected

Figure 7.20: The 2024 chloride content profiles compared to the 2019 measurements with uncorrected and corrected values for the Ardeweg viaduct.

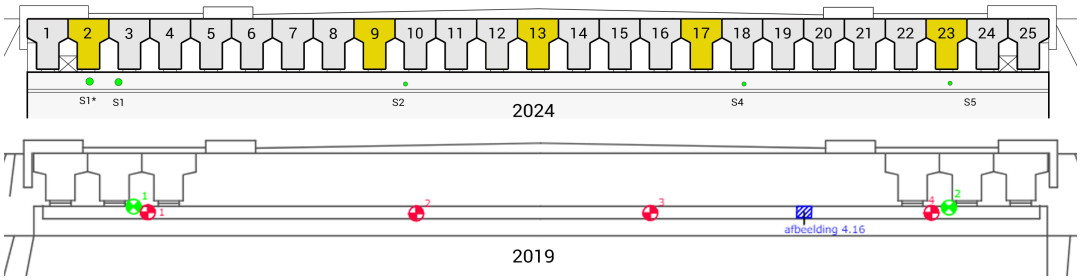


Figure 7.21: Test locations of both 2019 and 2024 chloride measurements. The 2019 measurements on the vertical face of the support beam are indicated with red markers.

**Correction of 2019 data**

Figure 7.20a shows a comparison between the raw data of the 2019 and 2024 measurements. The 2019 results show consistently higher chloride content values for all locations, with the highest concentration of 0.86% at S1 with a depth of 30mm. The overestimation of the chloride values is likely due to the assumed cement content used for the 2019 RCT method, as the method itself does not calculate the cement content. The assumed 14% cement weight was conservative, as the average cement content of all the support beam samples came out to be 20.9%. This calculated average could be used to correct the original 2019 values, which are shown in Figure 7.20b.

After the correction, the 2019 values showed a better alignment with the 2024 chloride profiles. Despite still overestimating the values slightly, the trends of the profiles aligned extremely well, especially at S1. The low initial surface concentration at 10mm, the peak at 30mm, and the gradual decrease at 50mm are all captured with both profiles, showing great consistency between the two methods. A scatterplot was made to visualize the correlation of the two methods, which is shown in Figure 7.22. A linear regression curve was fitted using the corrected data.

**Correlation of corrected data**

The plot shows a great correlation between the two methods with a $R^2 = 0.885$. Furthermore, the slope of the linear regression is similar to the equality line, indicating a strong positive correlation for the whole range of measurements. The consistent overestimation of the RCT results is also seen in the plot with the intercept, which shows a shift of approximately 8%.

The need for an assumption for the cement content highlights the limitation of on-site analysis with the RCT method, as the assumption could lead to systematic deviations. Although the conservative estimations may lean more towards safety during assessments, they may misrepresent actual chloride risks when not corrected. When corrected, the RCT method shows great potential for on-site chloride

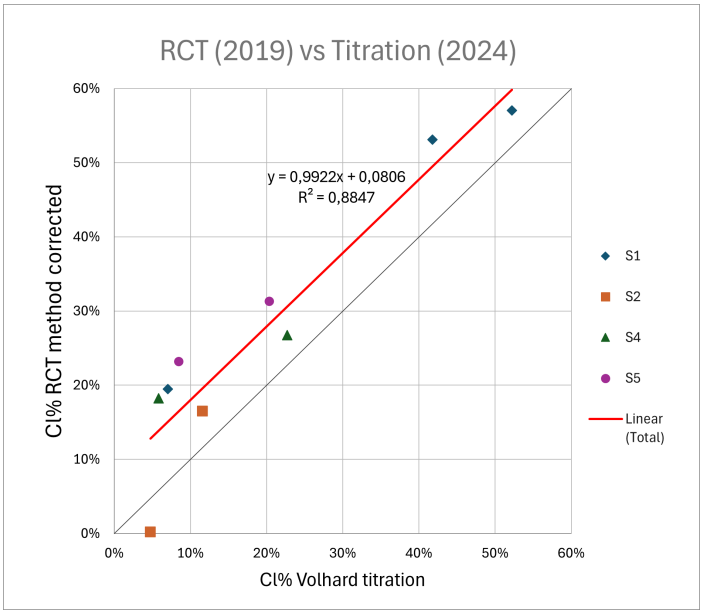


Figure 7.22: Correlation curve for the Volhard-titration and the RCT method

determination, given the high correlation with the more accurate lab results. This is a promising result, especially given the long preparation and processing costs for the Volhard titrations. The introduction of concrete dust sampling during the RCT procedure for later cement determination could improve the reliability and accuracy of this method.

**Time influence**
Despite the 5-year time gap, the trend of the chloride profiles remained consistent, indicating limited chloride ingress between 2019 and 2024. It is also unknown how much of the consistent 8% difference can be attributed to time influences or the difference in measuring techniques. However, the similarity in profile shape suggests that chloride penetration has likely been stabilized, indicating a lack of ongoing exposure.

### 7.5.2. Comparison Sluinerweg

For the Sluinerweg viaduct, chloride content determinations were also performed for the abutment support beam (STP1) and the beam heads. Three cores were extracted from STP1 of the Sluinerweg, in contrast to the four cores taken from the Ardeweg. Two cores (S1, S3) were located at either end of the support beam (under beams L23 and L1, respectively), while the S2 core of the support beam was located between beams L12 and L13. The chloride cores of the T-beams were extracted from the bottom of the T-beams, right next to the support beam. An overview of the Sluinerweg core locations can be found in [5, p.76]. The results of the support beams for both Sluinerweg and Ardeweg are compared in Figure 7.23, while the T-beam values are plotted in Figure 7.24.

The maximum chloride content observed at the Sluinerweg is significantly lower compared to the measured chloride at S1 and S1* of the Ardeweg. The highest chloride concentration was found at the surface of S3, with a value of 0.23 %, far below the critical limit of 0.5%. The chloride contents of the Sluinerweg are similar to the Ardeweg values, excluding the S1 cores, which suggests a consistent chloride exposure for both viaducts under normal circumstances. This reinforces the similarity of the two viaducts in design and external environmental exposure, whereby S1 could be seen as an outlier with a larger observed chloride load.
Furthermore, no active corrosion was expected at the Sluinerweg, given the chloride concentrations and the measured NDT results. This, while the S1 location of the Ardeweg had multiple testing methods (destructive and non-destructive), indicating an active corrosion environment. This highlights the ability of the NDT methodology to correctly identify likely corrosion hotspots within a structure.

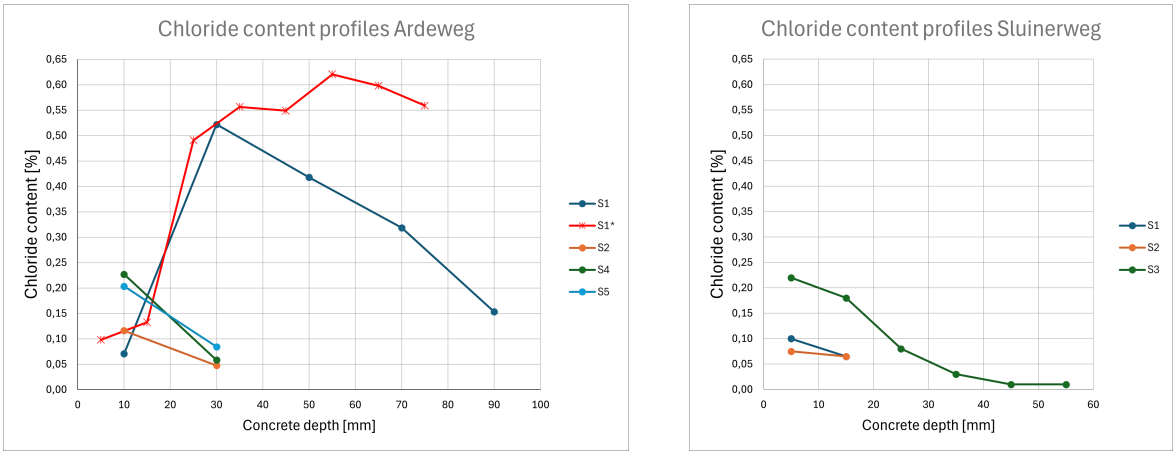


(a) Ardeweg: Support beam 5

(b) Sluinerweg: Support beam 1

Figure 7.23: The chloride content profiles for both the Ardeweg and Sluinerweg viaducts at the support beam.

The shape of Sluinerweg's S3 curve showed a good fit with Fick's second law for diffusion, indicating an expected ingress of environmental chloride. Conversely, the profiles of S1 and S1* show very different trends with low surface concentrations and higher peak concentrations deeper into the concrete cover. This was also noticed for the chloride profile of S6 from STP4, which also exhibited the same trend. This reinforces the trend only being seen in locations with higher peak chloride concentrations.

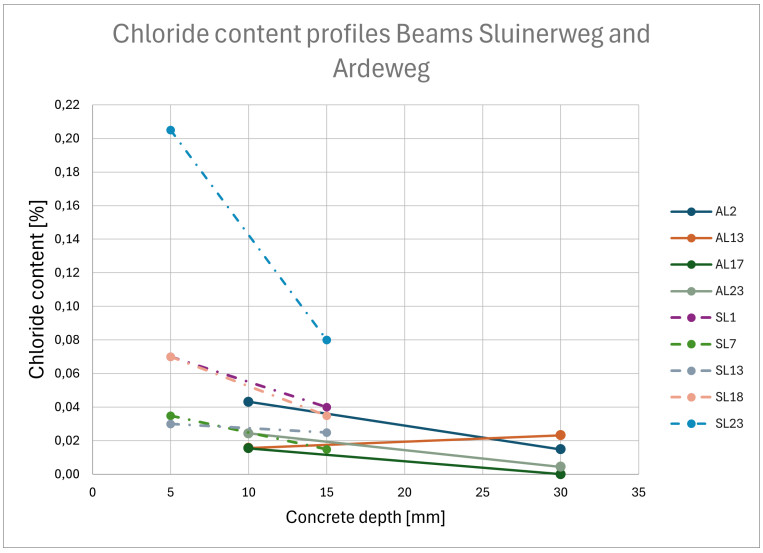


Figure 7.24: The chloride content profiles of the T-beams.

The Sluinerweg shows higher peak concentrations in their samples at the T-beams as shown in Figure 7.24. It should be noted that the core slice thickness of the Sluinerweg samples was 10mm, while that of the Ardeweg was 20mm. Despite this, the difference in peak values still stands. Most of the cores are grouped in the region below 0.07 %, indicating a low exposure to chloride. The core at SL23 was an exception, with peak values of 0.21%, which is significantly higher than the rest of the analyzed cores.

**Influence of location and distance**

The locations of the extracted cores may explain the range of values seen for both the Sluinerweg and Ardeweg results. Firstly, the Ardeweg cores were extracted at a far greater distance from the beam heads than initially planned. In Figure 5.11, the planned location of the cores can be seen, corresponding with the Sluinerweg core locations. The eventual location of the cores was moved to a

distance of approximately 3250mm from the beam heads, while the Sluinerweg cores were extracted at a distance of only 1250mm. These extra 2 meters do raise questions about the influence of distance on the exposure locations for the chloride content. However, the observed differences in the chloride values seem negligible when comparing the Ardeweg and Sluinerweg results, especially given the 160% increase in distance. This may suggest an already unrepresentative measurement for chloride at the initial location of 1250mm, as the concentration has already bottomed out. The true chloride content at the beam head is likely significantly higher as seen in the harvested beam results.
The author mentioned the T-beams having a generally lower chloride content than the support beam, despite the T-beams being the first to make contact with the leaking chloride. This notion is likely explained by the geometry of the structure and the distance of the chloride cores taken. From the chloride analysis on the harvested beams, it was seen that the measurable chloride content drops significantly over the length of the beam, resulting in chloride values at a distance of 1200mm to decrease by 70-90% from the true value right at the beam head. The accessibility and structural safety prevent the extraction of cores from being taken closer to the beam head, resulting in a skewed representation of the beam head condition. The measured chloride content at 1200mm could serve as an indirect indicator for the lower chloride limit, but its efficacy could be questioned. The use of an NDT method near the beam head may serve as a more effective indicator of the true beam head condition.
The Sluinerweg cores SL1 and SL23 were located at the outermost T-beams of the span, which may explain the higher values for chloride, especially compared to SL7 and SL13, which were located in the middle of the span. The higher chloride content at SL23 was also accompanied by a higher corrosion current density measurement [5, p.104], indicating agreement in increased corrosion risk. The drainage system was the likely cause of the higher values, as noted by Wilgenburg.

### 7.5.3. Harvested beams

The chloride measurements from beams L2 and L17 confirm a decrease in chloride concentration with increasing distance from the beam head. Beam L2 showed the highest concentration near the head (0.32%), which dropped by ∼90% at 1200 mm. This suggests that the beam head, located beneath a dilation joint, is more exposed to chloride ingress and likely the first element that comes into contact with chloride-rich moisture when leakage occurs. Although none of the values exceed the critical corrosion threshold of 0.5%, the chloride presence near the surface may still contribute to durability risks. This is especially true for the cones of the beam heads, as these are historically much weaker and more prone to damage, risking structural safety.
Conversely, beam L17 showed lower chloride levels (max. 0.09%), likely due to the presence of the CP coating or differences in chloride exposure. A difference in concrete quality is improbable due to the prefabricated nature of the T-beams and the consistent strength assessment performed in this study.

#### Necessity CP for L17

The higher values at L2 indicate the greater amount of exposure to chlorides at this location, which would explain the corrosion initiation observed here. Curiously, the CP-equipped beam L17 was likely fine without the installation of CP when looking at the chloride concentrations. The low values of the chloride content show no risk for corrosion, even close to the beam head. The choice of the CP installation at L17 could therefore be questioned with the present knowledge. Interestingly, the likelihood of this hypothesis being proven on-site is improbable. Once a CP coating is installed, it will influence all corrosion assessment techniques to show a higher risk of corrosion or prevent measurements entirely, as is seen in the results of this study. This makes it difficult to evaluate the true necessity of a CP installation after the installation. Thus, it is advised to install CP only when a quantifiable corrosion risk is observed to save on costs and resources.

#### Influence of distance

The results support the hypothesis that the core samples taken at ∼1200mm from the beam head heavily underestimate the chloride concentration at the beam head. This implies the need for more structured and closer measurements if the beam head condition is of importance. The accessibility hinders the closer extraction of cores from the soffit of the beam, which would leave the sides of the beam as the only option to assess the beam head condition accurately. The use of a compact NDT method would be the preferred choice given the great alignment of the NDT methods for the assessment of corrosion risk.

It should be acknowledged that the sample size remains limited, with only two beams and three locations each analyzed. This restricts the ability to generalize findings across the entire structure, even if the T-beams are all similarly built. Nonetheless, a clear trend and agreement with earlier corrosion assessment techniques (e.g., potential mapping and current densities) is seen, which provides evidence that chloride-induced corrosion is the main form of deterioration.

## 7.6. Thin-section analysis

The thin-section analysis revealed differences in air void content and concrete microstructure between the samples. Notably, S1 showed the highest air void content at 5.0%, with the presence of large, irregular entrapped air voids, as seen in both the UV and masked images in Figure 5.12. Six entrapped air voids were identified from the S1 thin-section, with the largest one having a diameter of 3.5mm. These large voids differ from the small spherical entrained air voids, which protect the concrete from freeze-thaw cycles. Entrapped air results from poor compaction or excess mix water and reduces the overall concrete strength, while increasing permeability. The higher permeability is also visualized in the UV scan of Figure 5.12, showing brighter fluorescence in the voids and the cement matrix when compared to S3.

Conversely, S3 shows very little air content (0.9%), suggesting a denser microstructure. The observed voids were small but irregularly shaped, indicating the absence of (properly) entrained air. The lack of entrained air could reduce freeze-thaw resistance and lower the overall durability of the concrete structure. S5 displays moderate air content (3.1%) with a more uniform void distribution. The UV scan shows that a large part of the voids are located within the aggregates. These internal aggregate porosities do not contribute to the air voids in the context of concrete microstructure analysis and were accounted for during the point counting procedure.

The high air void content and irregularity observed in S1 are particularly relevant given the elevated chloride concentrations detected at this location. The larger entrapped voids can serve as reservoirs for chloride-induced moisture, accelerating the ingress of chlorides. Furthermore, the higher permeability also increased the ion transport into the concrete matrix. These vulnerabilities likely contributed to the significant chloride penetration seen at S1.

An evolution plot of the point counting fractions from S5 is shown in Figure 7.25. This plot shows the gradual stabilization of the volume fractions over time, indicating a consistent distribution after the examined 542 points. A similar plot was seen for the other two thin sections, confirming the consistency of the point counting technique after approximately 400 points.

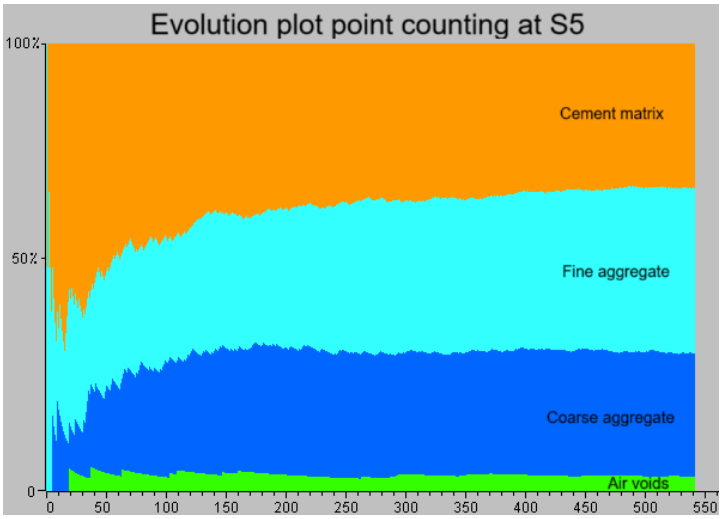


Figure 7.25: Evolution plot of the four point counting categories and their fractions after 542 points examined.

It is important to acknowledge that the sample size of the analysis was limited, with only one section per core at three locations. The inherent heterogeneity of concrete does limit the representativeness of the analysis, especially for the air void and aggregate distribution. The analysis results should be interpreted as indicative, despite the satisfactory results and trends observed. Furthermore, the analysis of thin sections is sensitive to both sample preparation and user interpretation. The thin sections would ideally be consistent in thickness across the surface and across samples, which was challenging to achieve in this study. The prepared samples do show a variation in thickness, which is best seen in S5, where the epoxy did not impregnate the rightmost surface due to the uneven thickness. Furthermore, multiple cores with additional thin sections are required to achieve statistical relevance. The relevance of thin-section analysis in the Liggerkoppen project is also limited. A forensic analysis of the damages seen in the Liggerkoppen project is not needed, as the cause of the leakage is already established to be caused by the leaking joints. The analysis was initiated due to the observed suspicion of differing concrete quality throughout the support beam. This difference in the concrete quality within the support beam was not noted or studied in earlier inspection reports.

Nevertheless, the results gathered from the thin-section analysis were meaningful, confirming the variability in concrete quality across the support beam and reinforcing the suspicion from the performed corrosion assessment. It also gave insights into a possible link between poor compaction, porosity, chloride ingress, and an increased corrosion risk, which was identified and validated with both NDTs and destructive tests. All in all, thin-section analysis is a powerful tool for identifying durability properties that could help explain and deepen the material assessments. Its implementation into the practical methodology could serve as an extra validation step, which could be combined with the other methods if cores are already extracted.

## 7.7. Review of practical methodology

A critical evaluation of the applied practical methodology was conducted to assess the effectiveness of the existing testing program and to compare it with the earlier Sluinerweg viaduct inspections. The validation of the results is discussed, alongside the evaluation of practical challenges and limitations when applying the practical methodology.

### 7.7.1. NDT program and validation

The Ardeweg testing program was mostly similar to the Sluinerweg program, with the exception of the R-type rebound hammer and thin section analysis being included, and the UPE and hXRF being excluded. The focus on rebound hammer types and coating influence made for interesting findings in an academic sense, but does not contribute to the testing program as a practical addition. The same could be said about the CR measurements on the harvested beams, whereby both short and long polarization times were used.

**Strength estimation**

One of the primary objectives of the study was to evaluate the validity of NDT results by comparing them with their destructive counterparts. For strength estimation, RH and UPV results showed clear correlation trends when compared to compressive strength measurements from concrete cores. The combined SonReb models demonstrated strong potential, particularly when outliers like location S1 were excluded and carbonation is corrected for. The use of these methods is justified for the estimation of the concrete strength, given the great correlation between the NDT and DT results.

Current standards emphasize structure-specific strength models, which have proved highly effective for the Ardeweg viaduct. The rebound hammer showed strong correlation with core strength ($R^2 > 0.9$), confirming its value as a strength estimation tool. The UPV showed a lower correlation with the strength and is thus better suited to be a complementary method next to the rebound hammer. The SonReb method only showed slight improvements over the single RH model in accuracy, which was also seen in the literature.

A direct comparison with existing SonReb models was not made due to the wide variability in model parameters. The found models are mostly only applicable for the particular structure they were fitted

for, as described by Kouddane et al. [71]. Their study suggests applying existing conversion models to other structures using calibration methods. The calibrated Ardeweg model could be adapted for similar viaducts within the Liggerkoppen project using limited core data, reducing the required number of extracted cores. This calibration-based approach aligns with RILEM recommendation 249-ISC [72].

**Corrosion assessment**

In the corrosion-related assessments, half-cell potential, resistivity, and corrosion current density readings generally aligned well with chloride content and visual corrosion observations. The left side of STP5 (under beams L1 to L6) consistently displayed low potential and low resistivity values across multiple devices, corresponding with the historically identified high-risk zone. These results supported the use of these NDT methods in practical settings, like on the Ardeweg and Sluinerweg viaduct.

Furthermore, half-cell potential and resistivity methods proved consistent and reliable under most field conditions. The strong correlation between Profometer and Gecor-10 B sensor results confirmed the reproducibility of potential measurements. Similarly, resistivity data from the Resipod and Sensor C showed similar correlations, especially in identifying higher corrosion risk areas near the beam heads. The Gecor-10 A sensor readings for potential and resistivity showed a greater variability, particularly at different polarization times. The correlation with the other resistivity sensors is significantly worse, especially when comparing the results on the harvested beams. This discrepancy in resistivity results is mentioned in the literature, but is still not well understood [27].

The corrosion current density results obtained using the Gecor-10 were also more varied. For the support beam, the higher corrosion rate was easily identified. However, the harvested beam results show a more nuanced view of the true value for $i_{corr}$ and its implications. Using both 30s and 100s polarization times provides more insight into the contextual corrosion state, but increases the difficulty of achieving an accurate value for $i_{corr}$.
Overall, the half-cell potential shows the greatest promise for identifying high corrosion risk areas. This is mainly due to its consistency across devices and surface conditions, along with the more user-friendly way of data gathering. For example, at STP5, a high corrosion risk zone is more easily recognized with the potential map than with the resistivity measurements due to the limited spread. The potential measurements do require a connection with the reinforcements, which officially classifies it as a semi-destructive method.

# 8

# Conclusions and recommendations

This section summarizes the most important findings from the extensive testing and analysis performed on the Ardeweg viaduct, including the comparison with the historical data and the measurements from the Sluinerweg viaduct.

## 8.1. Conclusions

The main conclusions of this report are as follows:

- The analysis of the Ardeweg viaduct using the Practical Methodology developed by Gert Wilgenburg showed great potential in determining the overall concrete condition accurately and comprehensively. The method, along with the choice of NDT's and destructive verifications, works well to improve overall measurement reliability.

- The Ardeweg saw more signs of corrosion when compared to the Sluinerweg viaduct, manifesting itself in an active corrosion region at the left side of the support beam.

- The non-destructive corrosion assessment techniques showed great agreement with each other and were all able to confirm the location of the active corrosion region, demonstrating the effectiveness of individual and combined use of NDT's for corrosion assessment.

The use of numerous NDT's generated several method-specific conclusions, which are listed below:

- The KCG coating significantly reduces and destabilizes RH measurements, introducing unwanted spread in measurements when not accounted for. This highlights the importance of surface preparation for accurate RH measurements. This finding is contrary to the claims made in the Sluinerweg report [5, pg.70].

- The Q-type hammer consistently reports higher rebound values compared to the R-type hammer, showing a strong linear correlation of ($R^2 = 0.869$). Despite this correlation, the small range of gathered values shows an unknown effect of lower rebound values outside this range. Additionally, the relation does not follow the equality line (slope=0.658), which complicates the use of a simple conversion system as seen in [41].

- The Q-hammer showed a strong correlation with the compressive strength ($R^2 = 0.932$), while the UPV measurements showed a weaker correlation ($R^2 = 0.514$). The combined SonReb method yielded the highest correlation ($R^2 = 0.939$), although the improvement over the RH alone was marginal. The findings emphasize the reliability of RH for strength estimations.

- The inclusion of the outlier at S1 for the SonReb regression model resulted in a significantly worse model correlation ($R^2 = 0.939 \rightarrow 0.514$), signifying the model's sensitivity and highlighting the statistical data preparation.

- When correcting the RH values at S1 for carbonation depth, an exceptional correlation is seen with the compressive strength ($R^2 = 0.960$), indicating the importance of carbonation for RH results.
- The Profometer and Gecor-10 B Sensor showed great correlation ($R^2 > 0.75$) for all measurements performed, confirming the reliability across devices and locations. Additionally, the Profometer aligns well with the 2019 data, signifying its usefulness for long-term monitoring.
- The half-cell potential from the Gecor A Sensor deviated significantly from the other methods for the harvested beams, raising concerns about the accuracy of their $i_{corr}$ measurements.
- The conductive CP coating hindered the measurements for all corrosion assessment techniques, reporting values indicating high corrosion risks. This makes monitoring of beams equipped with CP extremely difficult using the methods tested, as the true condition will be masked by conservative measurements.
- The Wenner style resistivity devices, Resipod and Gecor C sensor, showed great alignment, while sensor A showed lower correlations and higher variability.
- After correction for cement content, the 2019 RCT results showed great correlation with the 2024 lab data ($R^2 = 0.885$), validating the consistency of the RCT method for chloride determination.
- Chloride content decreased significantly with distance from the beam heads (90% decrease over 1000mm distance), indicating the importance of measurements close to the exposure source for representative analysis of the damage severity.
- Thin section analysis showed high (entrapped) air void content at S1, indicating a weaker microstructure, which explains the increased chloride ingress and reduced durability at this location.

## 8.2. Recommendations

Based on the findings of this study, several practical and methodological insights have been identified. While the results provide valuable correlations and reveal the influence of various testing limitations, they also point to topics that require further investigation. The following recommendations are proposed:

- Expand the rebound value dataset for both R- and Q-type hammers across a wider range of strengths to improve understanding of their relationship, especially for lower strengths.
- Conduct a larger SonReb model study using a broader and more diverse concrete dataset to assess model robustness and sensitivity. Especially situations where the UPV and Rh are more comparable in correlation should be studied. Special attention should be given to outliers and the role of surface and environmental effects.
- Perform further research into the validation of carbonation correction curves for rebound hammers. The validation should be based on a wide range of carbonation depths and concrete strengths for the development of a model, which could help improve the RH accuracy for aging structures.
- Further investigate the resistivity measurements in a more controlled environment to study the effects of external variables. The resistivity measurements using the Gecor A sensor should also be studied, given the discrepancies with the other methods.
- Investigate further into the potential measurements using Gecor Sensor A, especially its effect on $i_{corr}$ accuracy. Experiments should be performed using potential values of other methods to investigate their effect on the $i_{corr}$ measurements.
- Investigate the applicability and accuracy of the RCT chloride test in field conditions, with the addition of cement content determination. A new combined method could be developed to improve the RCT method's reliability.

- Investigate the practicality of corrosion measurements close to the beam heads. With the given influence of distance on the measurement results, the use of (preferably) NDT's close to the beam head should be studied for the future of the Liggerkoppen project.

# Bibliography


[1] TNO. (2023). *Vernieuwing oudere infrastructuur essentieel en urgent*. TNO. https://www.tno.nl/nl/newsroom/2023/11/vernieuwing-infrastructuur-essentieel/

[2] de Boon, J. (2024). Workshop CRAC: Lecture 1.1: Renovation and Replacement of Bridges in the Netherlands Possible replacement strategies: bridges demolished and amounts of concrete waste.

[3] Postema, F., & van Beek, A. (2003). Ndt used in the netherlands from a principal point of view. *International Symposium (NDT-CE 2003): Non-Destructive Testing in Civil Engineering 2003*. https://www.ndt.net/article/ndtce03/papers/v058/v058.htm

[4] Vergoossen, R. (2011). *Overkoepelende rapportage liggerkoppen* (tech. rep.). Royal Haskoning.

[5] Wilgenburg, G. (2024). *Non-destructive material evaluation of areinforced concrete viaduct: A practicalmethodology* (Master's thesis). TU Delft. https://repository.tudelft.nl/islandora/object/uuid:5cd2d5be-0472-4814-a334-73ac95ae0de2

[6] Gagg, C. R. (2014). Cement and concrete as an engineering material: An historic appraisal and case study analysis. *Engineering Failure Analysis*, *40*, 114–140. https://doi.org/https://doi.org/10.1016/j.engfailanal.2014.02.004

[7] EUROPEAN COMMITTEE FOR STANDARDIZATION. (2021a). NEN-EN 206+A2 Concrete - Specification, performance, production and conformity.

[8] Winter, N. (2012). *Understanding cement: An introduction to cement production, cement hydration and deleterious processes in concrete*. Microanalysis Consultants. https://books.google.nl/books?id=b8qznQEACAAJ

[9] Angst, U. (2011). Chloride induced reinforcement corrosion in concrete: Concept of critical chloride content methods and mechanisms. *Norwegian University of Science and Technology*. https://ntnuopen.ntnu.no/ntnu-xmlui/handle/11250/236720

[10] Nyokana, A. (2019, September). *Effect of concrete quality and cover depth on the efficiency of impressed anodic current to induce corrosion of steel in concrete*=. https://doi.org/10.13140/RG.2.2.29397.99044

[11] Papadakis, V. G., Vayenas, C. G., & Fardis, M. N. (1989). A reaction engineering approach to the problem of concrete carbonation. *AIChE Journal*, *35*(10), 1639–1650. https://doi.org/https://doi.org/10.1002/aic.690351008

[12] Leber, I., & Blakely, F. A. (1956). Some effects of carbon dioxide on mortars and concrete. *ACI Journal Proceedings*, *53*(9). https://doi.org/10.14359/11515

[13] Laurens, S., & Deby, F. (2018). 5 - electrochemical methods. In J.-P. Balayssac & V. Garnier (Eds.), *Non-destructive testing and evaluation of civil engineering structures* (pp. 173–197). Elsevier. https://doi.org/https://doi.org/10.1016/B978-1-78548-229-8.50005-4

[14] Alnahhas, F. (2023). *Carbonation in concrete: Diagram of carbonation in concrete* [Image]. Prontubeam. https://www.prontubeam.com/Detailed-civil-engineering-in-the-network/Carbonation-in-concrete

[15] Chen, Y., Liu, P., & Yu, Z. (2018). Effects of environmental factors on concrete carbonation depth and compressive strength. *Materials*, *11*(11). https://doi.org/10.3390/ma11112167

[16] Chang, C.-F., & Chen, J.-W. (2006). The experimental investigation of concrete carbonation depth. *Cement and Concrete Research*, *36*(9), 1760–1767. https://doi.org/https://doi.org/10.1016/j.cemconres.2004.07.025

[17] Talukdar, S., Banthia, N., & Grace, J. (2012). Carbonation in concrete infrastructure in the context of global climate change part 1: Experimental results and model development. *Cement and Concrete Composites*, *34*(8), 924–930. https://doi.org/https://doi.org/10.1016/j.cemconcomp.2012.04.011

[18] Medeiros-Junior, R., Lima, M., Yazigi, R., & Medeiros, M. (2015). Carbonation depth in 57 years old concrete structures. *Steel and Composite Structures*, *19*, 953–966. https://doi.org/10.12989/scs.2015.19.4.953

[19] Bentur, A., Berke, N., & Diamond, S. (1997). *Steel corrosion in concrete: Fundamentals and civil engineering practice*. CRC press.

[20] Polder, R., & Hug, A. (2000). Penetration of chloride from de-icing salt into concrete from a 30 year old bridge. *Heron*, *45*, 109–124.

[21] Oh, B., Jang, S., & Shin, Y. (2003). Experimental investigation of the threshold chloride concentration for corrosion initiation in reinforced concrete structures. *Magazine of Concrete Research - MAG CONCR RES*, *55*, 117–124. https://doi.org/10.1680/macr.55.2.117.37558

[22] Xu, Q., Liu, B., Dai, L., Yao, M., & Pang, X. (2024). Factors influencing chloride ion diffusion in reinforced concrete structures. *Materials*, *17*(13). https://doi.org/10.3390/ma17133296

[23] John S. Lawler, S. M. G., Jonah C. Kurth, & Krauss, P. D. (2021). Statistical distributions for chloride thresholds of reinforcing bars. *ACI Materials Journal*, *118*(2). https://doi.org/10.14359/51730411

[24] ACI Committee, 3. (1995). *ACI 318: Building code requirements for structural concrete ; and commentary (ACI 318R-95)*. Farmington Hills, MI : American Concrete Institute, [1995] ©1995. https://search.library.wisc.edu/catalog/999777001402121

[25] Lee, M., Jung, S., & Oh, B. (2013). Effects of carbonation on chloride penetration in concrete. *ACI Materials Journal*, *110*, 559–566.

[26] SAEKI, T. (2002). Effect of carbonation on chloridepenetration in concrete (D. of Civil Engineering & N. U. Architecture Faculty of Engineering, Eds.). *RILEM Workshop*. https://www.rilem.net/images/publis/pro038-025.pdf

[27] Andrade, C., Alonso, C., Gulikers, J., Polder, R., Cigna, R., Vennesland, Ø., Salta, M., Raharinaivo, A., & Elsener, B. (2004). Test methods for on-site corrosion rate measurement of steel reinforcement in concrete by means of the polarization resistance method. *Materials and Structures/Materiaux et Constructions*, *37*, 623–643. https://doi.org/10.1617/13952

[28] González, J. A., Albéniz, J., & Feliu, S. (1996). Polarization resistance constant b values for 20 different metal-environment systems. *Revista de Metalurgia*, *32*(1), 10–17. https://doi.org/10.3989/revmetalm.1996.v32.i1.926

[29] Andrade, C., & Martinez, I. (2010). 14 - techniques for measuring the corrosion rate (polarization resistance) and the corrosion potential of reinforced concrete structures. In C. Maierhofer, H.-W. Reinhardt, & G. Dobmann (Eds.), *Non-destructive evaluation of reinforced concrete structures* (pp. 284–316). Woodhead Publishing. https://doi.org/https://doi.org/10.1533/9781845699604.2.284

[30] Cox, R., Vennesland, Ø., & Cigna, R. (1997). *Cost 509 – corrosion and protection of metals in contact with concrete* (E. Commission, D.-G. for Research, & Innovation, Eds.). Publications Office. https://op.europa.eu/en/publication-detail/-/publication/b150ec52-1f5e-4ed3-a65a-c11d09417c20

[31] Stern, M., & Geary, A. L. (1957). Electrochemical polarization: I. a theoretical analysis of the shape of polarization curves. *Journal of the electrochemical society*, *104*(1), 56.

[32] Gabrielli, C., Keddam, M., Takenouti, H., Kinh, V. Q., & Bourelier, F. (1979). The relationship between the impedance of corroding electrode and its polarization resistance determined by a linear voltage sweep technique. *Electrochimica Acta*, *24*(1), 61–65.

[33] Andrade, C., & González, J. (1978). Quantitative measurements of corrosion rate of reinforcing steels embedded in concrete using polarization resistance measurements. *Materials and corrosion*, *29*(8), 515–519. https://onlinelibrary.wiley.com/doi/abs/10.1002/maco.19780290804

[34] Andrade, C., & Rebolledo, N. (2009). Corrosion of reinforced concrete made with different binders and exposed for 20 years in natural sea water. https://digital.csic.es/handle/10261/234317

[35] Aydın, F., & Saribiyik, M. (2010). Correlation between schmidt hammer and destructive compressions testing for concretes in existing buildings. *Scientific research and essays*, *5*.

[36] ACI Committee 228. (2003). *In-place methods to estimate concrete strength: Chapter 2—review of methods* [ACI 228.1R-03]. http://dl.mycivil.ir/dozanani/ACI/ACI%20228.1R-03%20In-Place%20Methods%20to%20Estimate%20Concrete%20Strength_MyCivil.ir.pdf

[37] Szilágyi, K., Borosnyoi-Crawley, D., & Mikó, T. (2013). Comparison of the inherent variability in rebound hammer tests performed with different testing instruments. *Építőanyag-Journal of Silicate Based and Composite Materials*, *65*, 68–75. https://doi.org/10.14382/epitoanyag-jsbcm.2013.14

[38] ACI. (2019). *ASTMC805: Standard Test Method for Rebound Number of Hardened Concrete* (Standard). American Society for Testing and Materials. US.
[39] EUROPEAN COMMITTEE FOR STANDARDIZATION. (2021b). NEN-EN12504-2 Testing concrete in structures - Part 2: Nondestructive testing - Determination of rebound number.
[40] EUROPEAN COMMITTEE FOR STANDARDIZATION. (2019a). NEN-EN 13791 Assessment of in-situ compressive strength instructions and precast concrete components.
[41] Winkler, S., & Matthews, J. A. (2014). Comparison of electronic and mechanical schmidt hammers in the context of exposure-age dating: Are q- and r-values interconvertible? *Earth Surface Processes and Landforms*, *39*(8), 1128–1136. https://doi.org/https://doi.org/10.1002/esp.3584
[42] Maliha, M., Chu, H., Nishiwaki, T., & Amin, A. (2021). Effect of surface roughness on nondestructive tests for screening of low-strength concrete. https://www.researchgate.net/publication/354996296
[43] Szilágyi, K., & Borosnyoi-Crawley, D. (2009). 50 years of experience with the schmidt rebound hammer. *Concrete Structures*, *10*, 46–56.
[44] Geosica. (2016). Gecor-10 instruction manual.
[45] Nygaard, P., Geiker, M., & Elsener, B. (2009). Corrosion rate of steel in concrete: Evaluation of confinement techniques for on-site corrosion rate measurements. *Materials and Structures*, *42*, 1059–1076. https://doi.org/10.1617/s11527-008-9443-1
[46] Ramón, J. E., Castillo, Á., & Martínez, I. (2021). On-site corrosion monitoring experience in concrete structures: Potential improvements on the current-controlled polarization resistance method. *Materiales de Construcción*, *71*(344), e265. https://doi.org/10.3989/mc.2021.11221
[47] Vogel. (2023). *Liggerkoppen / rijkswaterstaat*. Vogel. https://vogel-bv.nl/project/liggerkoppen-rijkswaterstaat/
[48] R.P.H. Vergoossen. (2011). Overkoepelende rapportage liggerkoppen.
[49] Ir. A.W.M. van den Hondel, I. R. t. M. (2017). *Kunstwerk 04: 33e-106-01ardeweginspectie liggerkoppen oost-nederland: Inspectie liggerkoppen oost-nederland 2017* (tech. rep.). Mourik-Salverda.
[50] de Mooij, L. (2019). 19pv0188-15 inspectie en onderzoek object 33e-106-01: Ardeweg. *Solid Services B.V.*
[51] J.J.J. de Bruijn, I. R. t. M., Ir. A.W.M. van den Hondel. (2022). *KW04: 33E-106-01 ARDEWEG LIGGERKOPPEN MJO - INSPECTIE JAAR 9 (2022): Liggerkoppen mjo - inspectie jaar 9 (2022)* (tech. rep.). Mourik-Salverda.
[52] Rijkswaterstaat. (2024). A1oost: Terugblik op de sloop van viaduct ardeweg. https://www.a1oost.nl/nieuws/2885025.aspx?t=Terugblik-op-de-sloop-van-viaduct-Ardeweg
[53] Hans Broekhuizen. (2024). *Sloop van de ardeweg viaduct* [Image]. https://www.a1oost.nl/communities/common/images/2c54f41a-3110-49d3-b17b-689b3d72618e/image-20240912083104-13.jpeg
[54] EUROPEAN COMMITTEE FOR STANDARDIZATION. (2023). NEN-EN 12504-4 Testing concrete in structures - Part 4: Determination of ultrasonic pulse velocity.
[55] Vennesland, Ø., Raupach, M., & Andrade, C. (2007). Recommendation of rilem tc 154-emc: “electrochemical techniques for measuring corrosion in concrete”—measurements with embedded probes. *Materials and Structures*. https://doi.org/10.1617/s11527-006-9219-4
[56] EUROPEAN COMMITTEE FOR STANDARDIZATION. (2021c). NEN-EN 12504-1 Testing concrete in structures - Part 1: Cored specimens - Taking, examining and testing in compression.
[57] EUROPEAN COMMITTEE FOR STANDARDIZATION. (2019b). NEN-EN 12390-3 Testing hardened concrete - Part 3: Compressive strength of test specimens.
[58] EUROPEAN COMMITTEE FOR STANDARDIZATION. (2006). NEN-EN 14630 Products and systems for the protection and repair of concrete structures - Test methods - Determination of carbonation depth in hardened concrete by the phenolphthalein method.
[59] *Is 13311 (part 1): 1992 – non-destructive testing of concrete: Method of test – ultrasonic pulse velocity* [Indian Standard, reaffirmed 2004]. (1992).
[60] SA, P. (2006). *Concrete test hammer: Original schmidt operating instructions*. https://www.metesco.nl/media/m2edm52d/proceq-original-schmidt-type-n-l-manual.pdf
[61] Yasuo Tanigawa, K. B., & Mori, H. (1988). Estimation of concrete strength by combined nondestructive testing method. *ACI SP 82*. https://doi.org/10.14359/6549

[62] JGJ. (2001). Jgj/t 23-2001 : Technical specification for inspection of concrete compressive strength by rebound method: □□□□□□□□□□□□□□□□□. https : / / www . codeofchina . com / standard / JGJT23-2001.html

[63] Kim, J.-K., Kim, C.-Y., Yi, S.-T., & Lee, Y. (2009). Effect of carbonation on the rebound number and compressive strength of concrete. *Cement and Concrete Composites*, *31*(2), 139–144. https: //doi.org/https://doi.org/10.1016/j.cemconcomp.2008.10.001

[64] EAGLES, S. (2014). *Using excel to determine sonreb curve coefficients*. https://media.screeningeagle.com/asset/Downloads/Using%20EXCEL%20to%20determine%20SONREB%20coefficients.pdf

[65] Chandak, N., & Kumavat, H. (2020). Sonreb method for evaluation of compressive strength of concrete. *IOP Conference Series: Materials Science and Engineering*, *810*, 012071. https://doi.org/10.1088/1757-899X/810/1/012071

[66] Abbaszadeh, H. (2018). The effect of different equations and methods on r-square values of ndt correlations. https://doi.org/10.33422/icarest.2018.09.41

[67] Mantegazza, D., Naldi, C., & Sgambati, S. (2011). In situ concrete strength testing by non-destructive combined methods with one, two and three variables (rebound number, ultrasonic pulse velocity, windsor probe). https://www.researchgate.net/publication/321850127_In_situ_concrete_strength_testing_by_non-destructive_combined_methods_with_one_two_and_three_variables_rebound_number_ultrasonic_pulse_velocity_Windsor_probe

[68] Nedeljković, M., Kamat, A., Holthuizen, P., Tošić, N., Schlangen, E., & Fennis, S. (2023). Energy consumption of a laboratory jaw crusher during normal and high strength concrete recycling. *Minerals Engineering*, *204*, 108421. https://doi.org/https://doi.org/10.1016/j.mineng.2023.108421

[69] EUROPEAN COMMITTEE FOR STANDARDIZATION. (2020). NPR-CEN/TR 17086: Further guidance on the application of EN 13791:2019 and background to the provisions.

[70] ASTM International. (2015). *Standard test method for corrosion potentials of uncoated reinforcing steel in concrete* [DOI: 10.1520/C0876-15]. https://store.astm.org/c0876-22b.html

[71] Kouddane, B., Sbartaï, Z. M., Alwash, M., Ali Benyahia, K., Elachachi, S. M., Lamdouar, N., & Kenai, S. (2022). Assessment of concrete strength using the combination of ndt—review and performance analysis. *Applied Sciences*, *12*, 12190. https://doi.org/10.3390/app122312190

[72] Denys, B., & Balayssac, J. P. (2021). Recommendation of rilem tc249-isc on non destructive in situ strength assessment of concrete. *32*. https://doi.org/10.1007/978-3-030-64900-5

# A

# Damage history Ardeweg

This chapter details the damage history of the beam head of the T-beams at the Ardeweg viaduct. An overview of the recorded damage classes from 2011, 2017, and 2022 is shown below.

| Steunpunt | inspectie-datum | Staven per ligger | 1 | 2 | 3 | 4 | 5 | 6 | 7 | 8 | 9 | 10 | 11 | 12 | 13 | 14 | 15 | 16 | 17 | 18 | 19 | 20 | 21 | 22 | 23 | 24 | 25 |
|---|---|---|---|---|---|---|---|---|---|---|---|---|---|---|---|---|---|---|---|---|---|---|---|---|---|---|---|
| Rijbaanindeling | | | SK | | VP | | | | RB | | | | | | | | | | | | | VP | | | | SK | |
| STP 1 | 2011 | 5 | 0 | 0 | 0 | 0 | 0 | 0 | 0 | 0 | 0 | 0 | 0 | 0 | 0 | 0 | 0 | 0 | 0 | 0 | 0 | 0 | 0 | 0 | 0 | 0 | 0 |
| | | | | | | | | | | | | | | | | | | | C2 | | | | | | | | |
| STP 2 [1] | 2011 | 5 | 0 | 0 | 0 | 0 | 0 | 0 | 0 | 0 | 0 | 0 | 0 | 0 | 0 | 0 | 0 | 0 | 0 | 0 | 0 | 0 | 0 | 0 | 0 | 0 | 0 |
| | | | | | | | C3 | | | | | | | | | | | | | | | | | | | | |
| STP 2 [3] | 2011 | 6 | 0 | 0 | 0 | 0 | 0 | 0 | 0 | 0 | 0 | 0 | 0 | 0 | 0 | 0 | 0 | 0 | 0 | 0 | 0 | 0 | 0 | 0 | 2 | 0 | 0 |
| STP 3 [2] | 2011 | 6 | 0 | 0 | 0 | 0 | 0 | 0 | 0 | 0 | 0 | 0 | 0 | 0 | 0 | 0 | 0 | 0 | 0 | 0 | 0 | KB | KB | KB | 0 | 0 | 0 |
| | | | | | | | | | | C2 | | | | | | | | | | | C2 | KB | KB | KB | | | |
| | | | | | | | | | | | | | | | | | | | | | | KB | KB | KB | | | |
| STP 3 [4] | 2011 | 6 | 0 | 0 | 0 | 0 | 0 | 0 | 0 | 0 | 0 | 0 | 0 | 0 | 0 | 0 | 0 | 0 | 0 | KB | KB | KB | 0 | 0 | 0 | 0 | 2 |
| | | | | | | | | | | | | | | | | | | | | KB | KB | KB | | | | | |
| | | | | | | | | | | | | | | | | | | | | KB | KB | KB | | | | | |
| STP 4 [3] | 2011 | 6 | 0 | 0 | 0 | 0 | 0 | 0 | 0 | 0 | 0 | 0 | 0 | 0 | 0 | 0 | 0 | 0 | 0 | 0 | 0 | 0 | 0 | 0 | 0 | 0 | 0 |
| | | | | | | | | | C2 | | | | | | | | | | | | | | | | | | |
| STP 4 [5] | 2011 | 5 | 0 | 0 | 2 | 0 | 0 | 0 | 0 | 0 | 0 | 0 | 0 | 0 | 0 | 0 | 0 | 0 | 0 | 0 | 0 | 0 | 0 | 0 | 0 | 0 | 0 |
| | | | | | | | | C2 | | | | | | | | | | | | | | | | | C2 | |
| STP 5 | 2011 | 5 | 0 | 0 | 0 | 0 | 0 | 0 | 0 | 0 | 0 | 0 | 0 | 0 | 0 | 0 | 0 | KB | KB | KB | 0 | 0 | 0 | 0 | 0 | 0 | 0 |
| | | | | | | | | | | | C2 | | | | | | | KB | KB | KB | | | | | | | |
| | | | | | | | | | | | | | | | | | | KB | KB | KB | | | | | | | |

Figure A.1: Damage overview of the 2011 inspection report [4].

The damage levels to the beams and cones were visually observed and categorized into 5 classes. Separate damage classes were made for the beams and the cones, as shown in Figure A.4 and A.5. A risk class was also associated with the observed damages and is shown in Figure A.6.
A visual guide is included from [49] to help identify the different damage classes. Figure A.7 shows examples for each damage class.

| Steunpunt | Soort voeg | inspectie-datum | Staven per ligger | 1 | 2 | 3 | 4 | 5 | 6 | 7 | 8 | 9 | 10 | 11 | 12 | 13 | 14 | 15 | 16 | 17 | 18 | 19 | 20 | 21 | 22 | 23 | 24 | 25 |
|---|---|---|---|---|---|---|---|---|---|---|---|---|---|---|---|---|---|---|---|---|---|---|---|---|---|---|---|---|
| Rijbaanindeling | | | | SK | | VP | | | | RB | | | | | | | | | | | | | VP | | | | SK | |
| STP 1 | Voeg | 3-7-2017 | 5 | | | | | | | | | | | | | | | | | C2<br>R1 | | | | | | | | |
| STP 2 [1] | Bituum | 3-7-2017 | 5 | | | | | C3<br>R1 | | | | | | | | | | | | | | | | | | | | |
| STP 2 [3] | Bituum | 3-7-2017 | 6 | | | | C2<br>R1 | | R2 | | | | | | | | | | | | | | 1 | | | 2 | | |
| STP 3 [2] | Bituum | 3-7-2017 | 6 | | | 4<br>R1 | | | 4<br>R1 | | C2<br>R1 | | | | | C1<br>R1 | | | | 4<br>R1 | | C2<br>R1 | KB<br>KB<br>KB | KB<br>KB<br>KB | KB<br>KB<br>KB | | 4<br>R1 | |
| STP 3 [4] | Bituum | 3-7-2017 | 6 | | | | | | | | C5<br>R2 | 4<br>R1 | | | | C1<br>R1 | | | | | KB<br>KB<br>KB | KB<br>KB<br>KB | KB<br>KB<br>KB | 0<br>C2<br>R1 | 4<br>R1 | | | 2 |
| STP 4 [3] | Bituum | 3-7-2017 | 6 | | | | | | C2<br>R1 | C2<br>R1 | | C5<br>R2 | | | | | | | | | | | | | 5<br>R2 | | | |
| STP 4 [5] | Bituum | 3-7-2017 | 5 | | | 2 | | | C2<br>R1 | C1<br>R1 | C2<br>R1 | | | | | 3<br>R1 | | | | | | | | | | | C2<br>R1 | |
| STP 5 | Voeg | 3-7-2017 | 5 | | C2<br>R1 | | | | | | | C2<br>R1 | | | | | | | KB<br>KB<br>KB | KB<br>KB<br>KB | KB<br>KB<br>KB | | | | | | | |

Figure A.2: Damage overview of the 2017 inspection report [49].

| Steunpunt | Inspectiedatum | Voeg | per ligger | 1 | 2 | 3 | 4 | 5 | 6 | 7 | 8 | 9 | 10 | 11 | 12 | 13 | 14 | 15 | 16 | 17 | 18 | 19 | 20 | 21 | 22 | 23 | 24 | 25 |
|---|---|---|---|---|---|---|---|---|---|---|---|---|---|---|---|---|---|---|---|---|---|---|---|---|---|---|---|---|
| STP 1(2) | 23 juni 2022 | Voeg | Liggerkop | | | | | | | | | | | | | | | | | 1 | | | | | | | | |
| | | | Conusvulling | | | | | | | | | | | | | | | | | C2 | | | | | | | | |
| | | | Risicoklasse | | | | | | | | | | | | | | | | | R1 | | | | | | | | |
| STP 2(1) | 10 mei 2022 | Bituum | Liggerkop | | | | | | | | | | | | | | | | | | | | | | | | | |
| | | | Conusvulling | | C2 | | | | | | | | | | | | | | | | | | | | | | | C2 |
| | | | Risicoklasse | | R1 | | | | | | | | | | | | | | | | | | | | | | | R1 |
| STP 2(3) | 10 mei 2022 | Bituum | Liggerkop | | | | | | 4 | | | | | | | | | | | | | | | | | 2 | | |
| | | | Conusvulling | C2 | C2 | | | | C5 | | | | | | | | | | | | | | | | | | | C2 |
| | | | Risicoklasse | R1 | R1 | | | | R2 | | | | | | | | | | | | | | | | | | | R1 |
| STP 3(2) | n.v.t. | Bituum | Liggerkop | KB | KB | KB | KB | KB | KB | KB | KB | KB | KB | KB | KB | KB | KB | KB | KB | KB | KB | KB | KB | KB | KB | KB | KB | KB |
| | | | Conusvulling | KB | KB | KB | KB | KB | KB | KB | KB | KB | KB | KB | KB | KB | KB | KB | KB | KB | KB | KB | KB | KB | KB | KB | KB | KB |
| | | | Risicoklasse | | | | | | | | | | | | | | | | | | | | | | | | | |
| STP 3(4) | n.v.t. | Bituum | Liggerkop | KB | KB | KB | KB | KB | KB | KB | KB | KB | KB | KB | KB | KB | KB | KB | KB | KB | KB | KB | KB | KB | KB | KB | KB | KB |
| | | | Conusvulling | KB | KB | KB | KB | KB | KB | KB | KB | KB | KB | KB | KB | KB | KB | KB | KB | KB | KB | KB | KB | KB | KB | KB | KB | KB |
| | | | Risicoklasse | | | | | | | | | | | | | | | | | | | | | | | | | |
| STP 4(3) | 8 maart 2022 | Bituum | Liggerkop | | | | | | | | | | | | | | | 2 | | | | | 2 | 2 | 3 | | | |
| | | | Conusvulling | | | | | | C3 | | | | | | | | | | | | | | | | | | | |
| | | | Risicoklasse | | | | | | R1 | | | | | | | | | | | | | | | | R1 | | | |
| STP 4(5) | 8 maart 2022 | Bituum | Liggerkop | 2 | | 2 | | | | | | | | | | 2 | | | | | | | | | | | | |
| | | | Conusvulling | | | | | | | | | | | | | | | | | | | C3 | | | | | C2 | |
| | | | Risicoklasse | | | | | | | | | | | | | | | | | | | R1 | | | | | R1 | |
| STP 5(4) | 19 januari 2022 | Voeg | Liggerkop | | | | | | | | | 1 | | | | | | | KB | KB | KB | | | | | 1 | | |
| | | | Conusvulling | | C2 | | | | | | | | | | | | | | KB | KB | KB | | | | | | | |
| | | | Risicoklasse | | R1 | | | | | | | | | | | | | | | | | | | | | | | |

Figure A.3: Damage overview of the 2022 inspection report [51].

**Damage levels for beam heads**

| | |
|---|---|
| 1 | Cracks in the corners. |
| 2 | Spalling of (parts of) the corners. |
| 3 | Cracks in the corners and vertical cracks in the beam web. |
| 4 | Spalling of (parts of) the corners and beam web. |
| 5 | Spalling and or cracks beyond the support. |

Figure A.4: Damage classes for the beam heads [5]

| Damage levels for cones | |
|---|---|
| 1 | Cone has cracks. |
| 2 | Cone is loose or pushed out. |
| 3 | Cone is (partially) missing. |
| 4 | Cone with corrosion damage. |
| 5 | Cone with corrosion damage and a visible tendon. |

Figure A.5: Damage classes for the cones [5]

| Risk of prestressing function loss. | |
|---|---|
| R1 | Long term function loss to be expected (within 10 years). |
| R2 | Short term function loss to be expected (within 5 years). |
| R3 | Immediate function loss to be expected (within 1 year). |

Figure A.6: Risk classes for the service life of the beam [5]

| Schadeklasse Liggerkoppen | Schadeklasse Conusvullingen |
|---|---|
|  |  |
| 1: Gescheurde hoeken van de ligger | C1: Conus gescheurd |
|  |  |
| 2: Afgesprongen delen van de hoeken van de ligger | C2: Conus los-/uitgedrukt |
|  |  |
| 3: Gescheurde hoeken en verticale scheuren in het lijf van de ligger | C3: Conus ontbreekt (deels) |
|  |  |
| 4: Afgesprongen delen van de hoeken en in het lijf van de ligger | C4 Conus met corrosiesporen |
|  |  |
| 5: Afgesprongen delen en/of scheuren tot voorbij de oplegging | C5: Conus met corrosiesporen + staafkop zichtbaar |

Figure A.7: Examples of different damage classes for both the beam heads and cones. [49]

# B

# Measurement plans

| Steunpunt | Inspectiedatum | Voeg | Staven per ligger | | 1 | 2 | 3 | 4 | 5 | 6 | 7 | 8 | 9 | 10 | 11 | 12 | 13 | 14 | 15 | 16 | 17 | 18 | 19 | 20 | 21 | 22 | 23 | 24 | 25 |
|---|---|---|---|---|---|---|---|---|---|---|---|---|---|---|---|---|---|---|---|---|---|---|---|---|---|---|---|---|---|
| STP 4(5) | 8 maart 2022 | Bituum | 5 | Liggerkop | 2 | | 2 | | | | | | | | | | 2 | | | | | | | | | | | | |
| | | | | Conusvulling | | | | | | | | | | | | | | | | | | | C3 | | | | | C2 | |
| | | | | Risicoklasse | | | | | | | | | | | | | | | | | | | R1 | | | | | R1 | |
| STP 5(4) | 19 januari 2022 | Voeg | 5 | Liggerkop | | | | | | | | | 1 | | | | | | | KB | KB | KB | | | | | 1 | | |
| | | | | Conusvulling | | C2 | | | | | | | | | | | | | | KB | KB | KB | | | | | | | |
| | | | | Risicoklasse | | R1 | | | | | | | | | | | | | | | | | | | | | | | |

| Schadeklasse liggerkoppen | | Schade conusvulling | | Risisco runctieverlies voorspanstaven | |
|---|---|---|---|---|---|
| 1 | Gescheurde hoeken van ligger | C1 | Conus gescheurd | R1 | Op lange termijn (binnen 10 jaar) is functieverlies te verwachten |
| 2 | Afgesprongen delen van de hoeken van de ligger | C2 | Conus los-.uitgedrukt | R2 | Op korte termijn (binnen 5 jaar) is functieverlies te verwachten |
| 3 | Gescheurde hoeken en verticale scheuren in het lijf van de ligger | C3 | Conus ontbreekt (deels) | R3 | Per direct (binnen 1 jaar) is functieverlies te verwachten |
| 4 | Afgesprongen delen van de hoeken en in het lijf van de ligger | C4 | Conus met corrosiesporen | | |
| 5 | Afgesprongen delen en/of scheuren tot voorbij de oplegging | C5 | Conus met corrosiesporen + staafkop zichtbaar | KB | Liggerkop voorzien van kathodische bescherming |

| Steunpunt | Ligger | Zone | Risico | Schade | Bijzonderheden |
|---|---|---|---|---|---|
| **STP 5** | L2 | II: Schade zonder KB | R1: Binnen 10 jaar functieverlies | C2: Conus los- of uitgedrukt | Hoge chloride metingen 2019 |
| | L9 | II: Schade zonder KB | | 1: Gescheurde hoeken ligger | |
| | L13 | I: Geen schade | | - | Controle meting |
| | L17 | III: Schade met KB | | KB: Kathodische bescherming | |
| | L23 | II: Schade zonder KB | | 1: Gescheurde hoeken ligger | |
| **STP 4** | L1 | II: Schade zonder KB | | C2: Conus los- of uitgedrukt | |
| | L3 | II: Schade zonder KB | | C2: Conus los- of uitgedrukt | Nieuwe corrosie schade aan steunpuntligger 5-6 |
| | L9 | I: Geen schade | | - | Controle meting |
| | L13 | II: Schade zonder KB | | C2: Conus los- of uitgedrukt | |
| | L19 | II: Schade zonder KB | R1: Binnen 10 jaar functieverlies | C3: Conus ontbreekt | |
| | L24 | II: Schade zonder KB | R1: Binnen 10 jaar functieverlies | C2: Conus los- of uitgedrukt | |

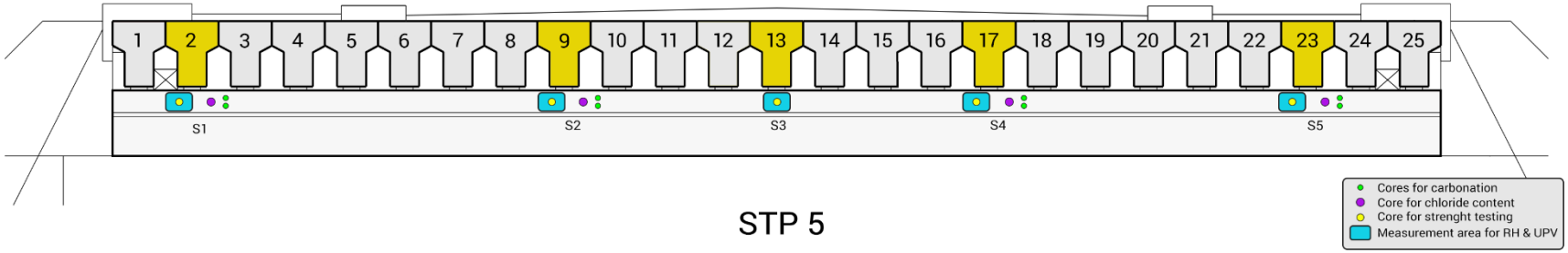


*Figuur 1: Dwarsdoorsnede van STP 5 met locaties voor metingen*

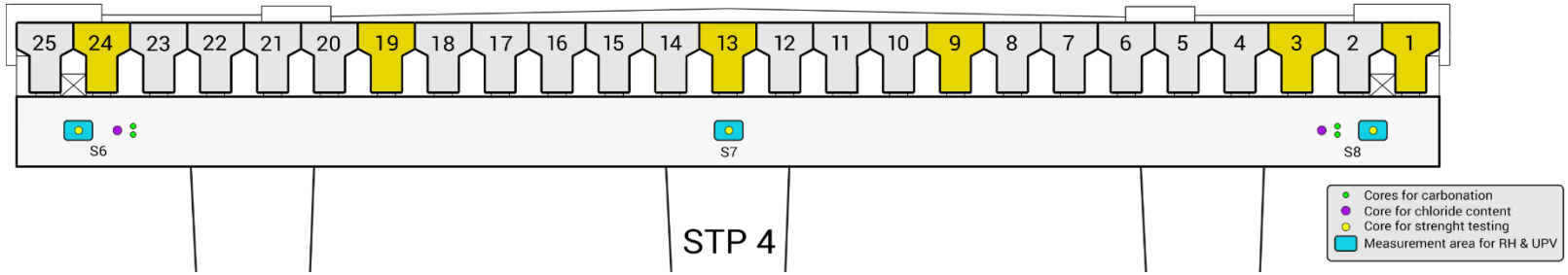


*Figuur 2: Dwarsdoorsnede van STP 4 met locaties voor metingen*

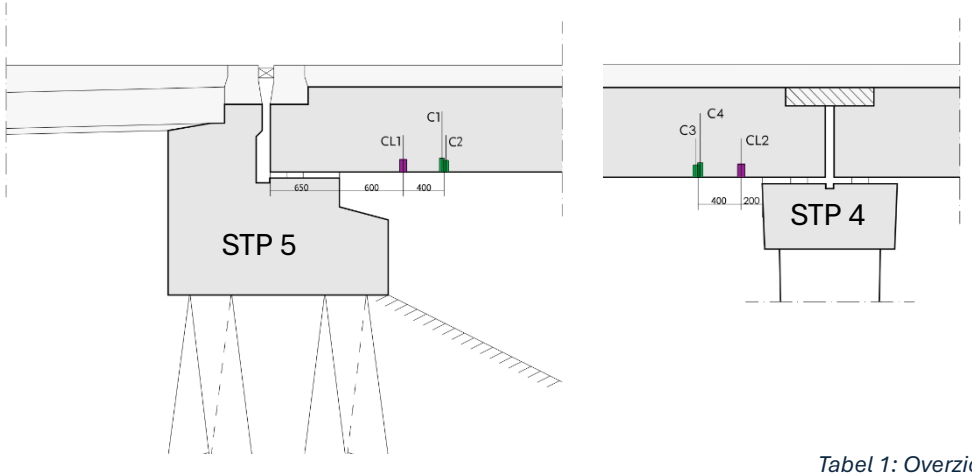


| Steunpunt | Locatie | Druksterkte | Chloride | Carbonatie | Totaal |
|---|---|---|---|---|---|
| **STP 5** | Steunpuntligger<br>S1, S2, S3*, S4, S5 | 5 | 4 | 8 | **17** |
| **STP 5** | Liggerkoppen<br>L2, L9, L13*, L17, L23 | - | 4 | 8 | **12** |
| **STP 4** | Steunpuntligger<br>S6, S7*, S8 | 3 | 2 | 4 | **9** |
| **STP 4** | Liggerkoppen<br>L3, L24 | - | 2 | 4 | **6** |
| *= Geen chloride en carbonatie metingen | | 8 | 12 | 24 | **44** |

*Tabel 1: Overzicht van aantal kernen*

*Figuur 3: Dwarsdoorsnede van de steunpunten voor metingen chloride (paars) en carbonatie (groen)*

| **Maandag 24 Juni** | | | |
|---|---|---|---|
| **Tijd** | **Wat** | **Wie** | **Notities** |
| **8:00** | Begin dag bij Ardeweg<br>- Bespreking planning<br>- Controleren equipment | Iedereen | - Aanwezigen:<br>- Giatec<br>- Bryan<br>- Penny<br>- Gert<br>- Zhi |
| **8:30** | Naar Ardeweg viaduct<br>- Visuele inspectie<br>- Weersverwachting checken<br>- Schoonmaken/voorbereiden meetlocaties | Iedereen | - Gereedschap meenemen voor verwijdering KB |
| | [STP 4] **GPR** metingen<br>- Locaties markeren voor kernen boren en andere metingen | - Penny, Bryan, Gert, Zhi | - Steunpunt: S6, S7, en S8<br>- Liggers: L3, L13 en L24 |
| | [STP 4] **ICOR en Resipod** metingen | - Giatec, Penny, Bryan, Gert, Zhi | - Steunpunt: S6, S7, en S8<br>- Liggers: L3, L13 en L24<br>- Resipod op zelfde locaties als de ICOR |
| | [STP 4] **RH** metingen<br>- Over hele Steunpuntligger | - Penny, Bryan, Gert, Zhi | - Tenminste 12 metingen doen met beide R- en Q-type hamers<br>- Metingen doen aan de onderkant v/d liggers |
| | [STP 4] **UPV** metingen<br>- Steunpuntligger<br>- Liggerkoppen | - Penny, Bryan, Gert, Zhi | - Op locaties S6, S7 en S8<br>- Semi-directe methode voor steunpunt ligger (40cm afstand)<br>- Directe methode zijkanten van liggerkop |
| **12:00** | **Break** | | |
| **13:00** | Verwachte eindtijd opstellen taludsteiger STP 5 | -Heijmans | |
| | [STP 5] Start **GPR** metingen<br>- Steunpuntligger<br>- Tussen de liggers<br>- Liggerkoppen | - Penny, Bryan, Gert, Zhi | - Wapening vinden en markeren |
| | [STP 5] Locaties markeren voor kernen boren<br>- Raster uitzetten voor metingen<br>- 5 locaties steunpuntligger | - Penny, Zhi | - Steunpunt: S1, S2, S3, S4 en S5<br>- Liggers: 2, 9, 13, 17 en 23 |
| | [STP 5] Visuele inspectie conus corrosie | - Gert, Bryan | - Foto's maken met spiegel |

| | | | |
|---|---|---|---|
| | [STP 5] **ICOR en Resipod** metingen | - Giatec, Penny, Bryan, Gert, Zhi | - Steunpunt: S1, S2, S3, S4<br>- Liggers: L2, L9, L17 en L23<br>- Resipod over de hele lengte steunpuntligger |
| | [STP 5] **UPV** metingen<br>- Steunpuntligger<br>- Liggerkoppen | - Penny, Bryan, Gert, Zhi | - Semi-directe methode voor steunpunt ligger (15cm afstand)<br>- Directe methode zijkanten van liggerkop |
| | [STP 5] **RH** metingen<br>- Zelfde locatie als UPV | - Penny, Bryan, Gert, Zhi | - Tenminste 12 metingen doen met beide R- en Q-type hamers<br>- Metingen doen aan de onderkant v/d liggers |
| **16:30** | **Einde dag** | | |

| **Dinsdag 25 Juni** | | | |
|---|---|---|---|
| **Tijd** | **Wat** | **Wie** | **Notities** |
| **8.00** | Begin dag bij Ardeweg<br>- Bespreking planning<br>- Controleren equipment<br>- Weersverwachting checken<br>- Visuele inspectie<br>- (Kathodische bescherming verwijderen) | Iedereen | - Aanwezigen:<br>- SGS Intron<br>- Ivo<br>- Dikkerboom<br>- Bryan<br>- Penny<br>- Zhi |
| | [STP 5] Wapening blootleggen voor corrosie metingen | - Dikkerboom, Zhi | - Steunpunt: S1, S2, S3, S4 en S5<br>- Liggers: 2, 9, 13, 17 en 23 |
| | [STP 4] **UPE** metingen<br>- Gebruik **GPR** vooraf voor het in kaart brengen voorspankanaal<br>- Voorspankanaal liggers<br>- Boringen n.a.v. resultaat | - SGS Intron, Ivo | - Onderzoek naar voorspanningskanaal (defecten in grouting)<br>- Wie neemt boor mee?(diameter) |
| | [STP 5] Vervolg corrosie metingen<br>- Continuïteitsmetingen<br>- **Half cell potential (profometer)** | - Penny, Ivo, Zhi | - Steunpunt: hele breedte<br>- Liggers: 2, 9, 13, 17 en 23 |
| | [STP 4] Wapening blootleggen voor corrosie metingen | - Dikkerboom | - Steunpunt: S6 en S8<br>- Liggers: L3 en L24 |
| **12:30** | **Break** | | |
| **13:00** | [STP 4] **Half cell potential (profometer)** Metingen | - Penny, Ivo, Zhi | - Steunpunt: hele breedte (of S6 en S8 gezien de tijd)<br>- Liggers: L3 en L24 |

| | | | |
|---|---|---|---|
| **14:00** | [STP 4] **Kernen boren** voor Druksterkte, chloride en carbonatie onderzoek | - Dikkerboom | - Druksterkte: S6, S7 en S8<br>- Corrosie:<br>- Steunpunt: S6 en S8<br>- Liggers: L3 en L24 |
| **16:30** | **Einde dag** | | |

| **Woensdag 26 Juni** | | | |
|---|---|---|---|
| **Tijd** | **Wat** | **Wie** | **Notities** |
| **8:00** | [STP 5 ] Uitloop/ buffer voor metingen | - Iedereen | - Aanwezigen:<br>- Dikkerboom<br>- Zhi |
| | [STP 5] **Kernen boren** voor druksterke tests | - Dikkerboom | - Steunpunt: S1, S2, S3, S4 en S5 |
| | [STP 5] **Kernen boren** voor chloride en carbonatie onderzoek | - Dikkerboom | - Steunpunt: S1, S2, S3, S4 en S5<br>- Liggers: L2, L9, L13, L17 en L23 |
| | **Einde dag** | | |

- STP 5
    1. Chloride liggers 4x L2, L9, L17, L23 Ø60mm ↑ verticaal
    2. Carbonatie steunpunt 2x S2 en S4 Ø40mm → horizontaal
    3. Carbonatie liggers 4x L2, L9, L17, L23 Ø40mm ↑ verticaal
- STP 4
    1. Chloride steunpunt 2x S6 en S8 Ø60mm → horizontaal
    4. Chloride liggers 2x L3 en L24 Ø60mm ↑ verticaal
    2. Carbonatie steunpunt 2x S6 en S8 Ø40mm → horizontaal
    5. Carbonatie liggers 2x L3 en L24 Ø40mm ↑ verticaal

    **Totaal:** **18x**

| **Donderdag 11 Juli** | | | |
|---|---|---|---|
| **Tijd** | **Wat** | **Wie** | **Notities** |
| **7:00** | Begin dag bij Ardeweg<br>- Bespreking planning<br>- Controleren equipment | Iedereen | - Aanwezigen:<br>- Leo (Giatec)<br>- Dikkerboom<br>- Penny<br>- Ivo<br>- John<br>- Zhi |
| | - Visuele inspectie<br>- Weersverwachting checken<br>- Schoonmaken/voorbereiden meetlocaties | Iedereen | |
| | [STP 4] Gat maken voor corrosiemeting | Dikkerboom | - Linkerkant steunpunt |
| | [STP 5] Natspuiten Steunpunten en liggers | Iedereen | |
| | [STP 5] **GPR** metingen<br>- Locaties markeren voor kernen boren en corrosiemetingen | Zhi | - Steunpunt: linkerkant tussen L2 en L3 Area Scan<br>- Hele steunpunt voor wapening locaties<br>- L2, L9, L13, L17, L23 wapening locaties<br>- Kernen liggers markeren |

| | | | |
|---|---|---|---|
| | [STP 4] **GPR** metingen<br>- Locaties markeren voor kernen boren en corrosiemetingen | Zhi | - Steunpunt: linkerkant corrosie plek tussen L20 en L21<br>- S7 midden<br>- Kernen liggers markeren |
| | [STP 5] **Gecor en Resipod** metingen | - John, Zhi | - Beginnen resistiviteit + **Resipod**, potentiaal, en dan corrosion rate.<br>- Liggers L2, L9, L13, L17, L23<br>- 3 punten dichtbij liggerkop<br>- Hele steunpunt onder elke ligger |
| | [STP 4] **ICOR** metingen | - Leo, Penny | - Steunpunt: S6, S7<br>- Liggers: L20, L13 |
| | [STP 5] Kernen boren Liggers | - Dikkerboom | - Op 2 afstand van corrosiemeting |
| **11:00** | **Break** | | |
| | [STP 5] **ICOR** metingen | -Leo, Penny, Zhi | - Liggers L2, L9, L13, L17, L23<br>- 3 punten dichtbij liggerkop<br>- Hele steunpunt onder elke ligger |
| | [STP 5] Kernen boren Steunpunt carbonatie | - Dikkerboom | - S2 en S4<br>- evt kolommen als er tijd is |
| | [STP 4] **Gecor en Resipod** metingen | - John, Zhi | - Beginnen resistiviteit + **Resipod**, potentiaal, en dan corrosion rate.<br>- S6 en S7 |
| **14:00** | [STP 4] Kernen boren Steunpunt en liggers | - Dikkerboom | - Naast L20 en L13 |
| **Uitloop** | [STP 4] **Profometer** metingen | - Ivo, Zhi | - Alleen als er extra tijd is<br>- Rechterkant steunpunt |
| **15:00** | **Einde dag** | | |

# C

# Potential measurements on the beams

This chapter presents the July potential measurements performed on 5 spanning beams with the Profometer wheel electrode. An overview of the measurements can be seen in Table C.1. The determination of the used axis can be seen in Figure C.1. A point approximately 3 meters from the support beam was chosen and used as a starting point for the measurements. The x-axis corresponds with the longitudinal direction, while the y-axis corresponds with the lateral direction of the beam. Each face has been measured with 3 equally spaced lines.


Figure C.1: The local axis for the Profometer measurements.

Table C.1: Overview of performed potential measurements

| Beam | Measurements |
|---|---|
| L2 | Bottom face<br>West face<br>East face |
| L9 | Bottom face |
| L13 | Bottom face |
| L17 | Bottom face |
| L23 | Bottom face |

# L2

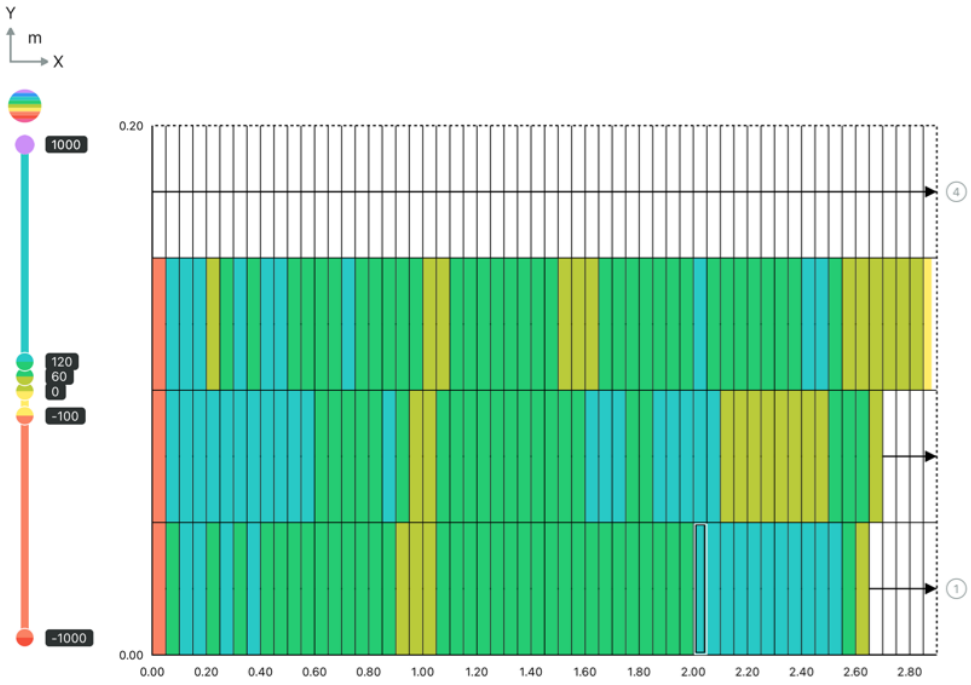


Figure C.2: Potential measurement of the L2 bottom face

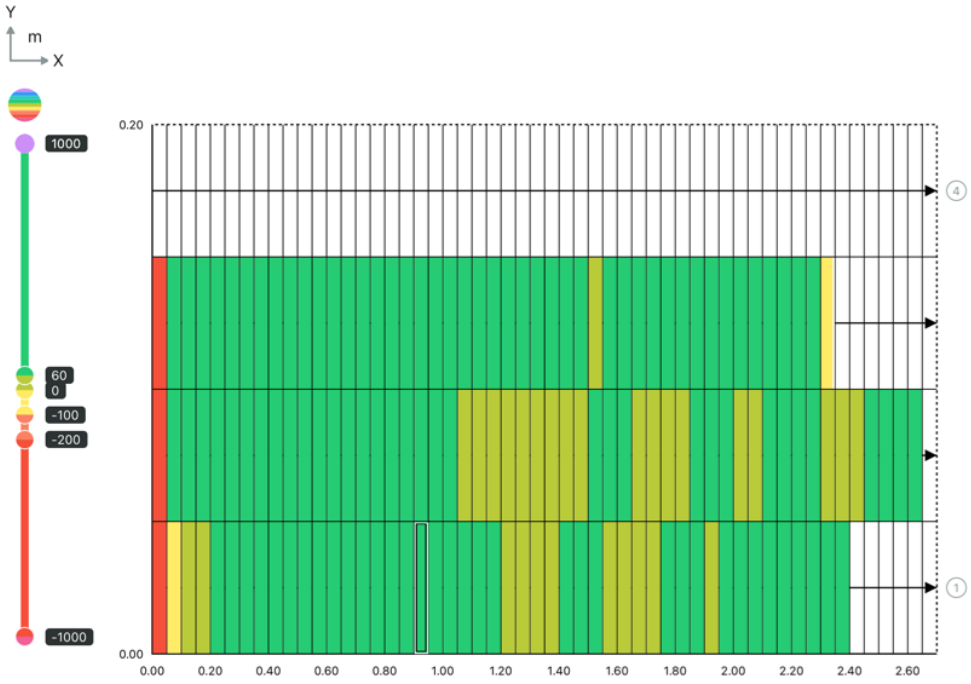


Figure C.3: Potential measurement of the L2 east face

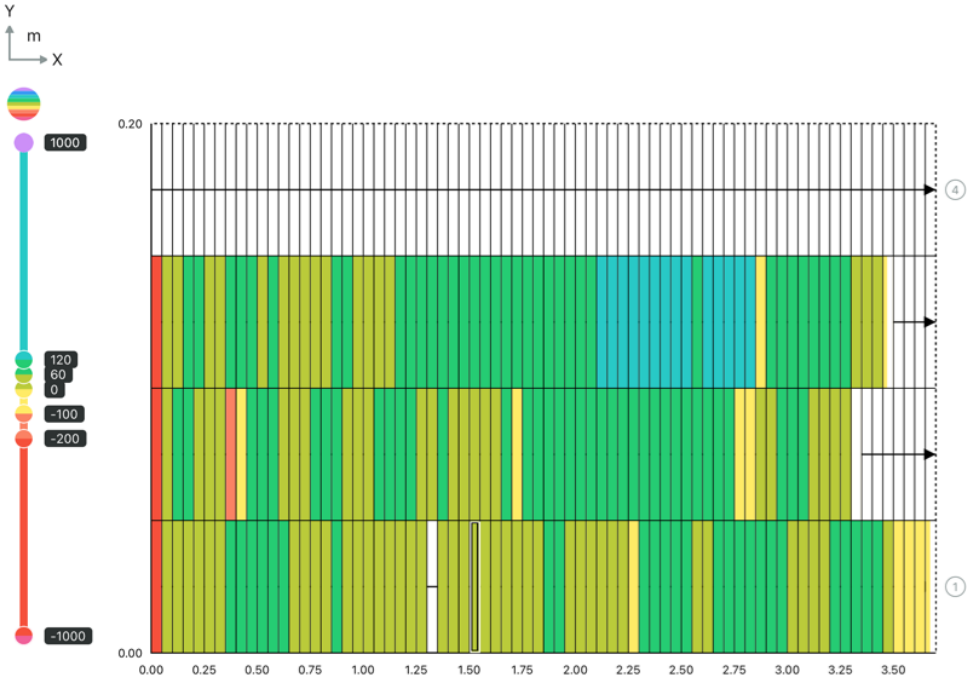


Figure C.4: Potential measurement of the L2 west face

# L9

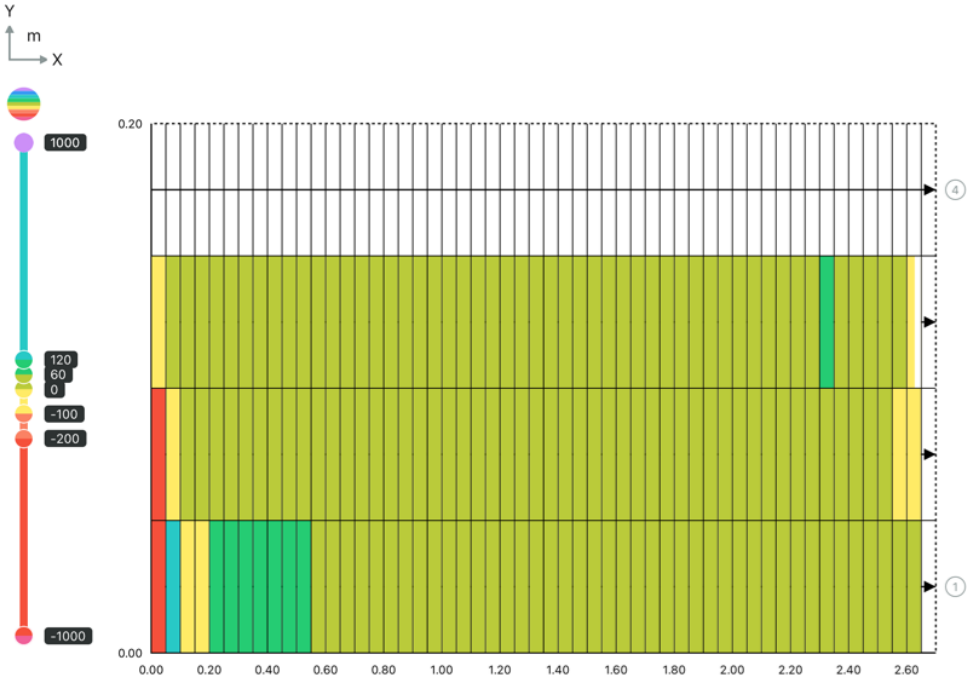


Figure C.5: Potential measurement of the L9 bottom face

## L13

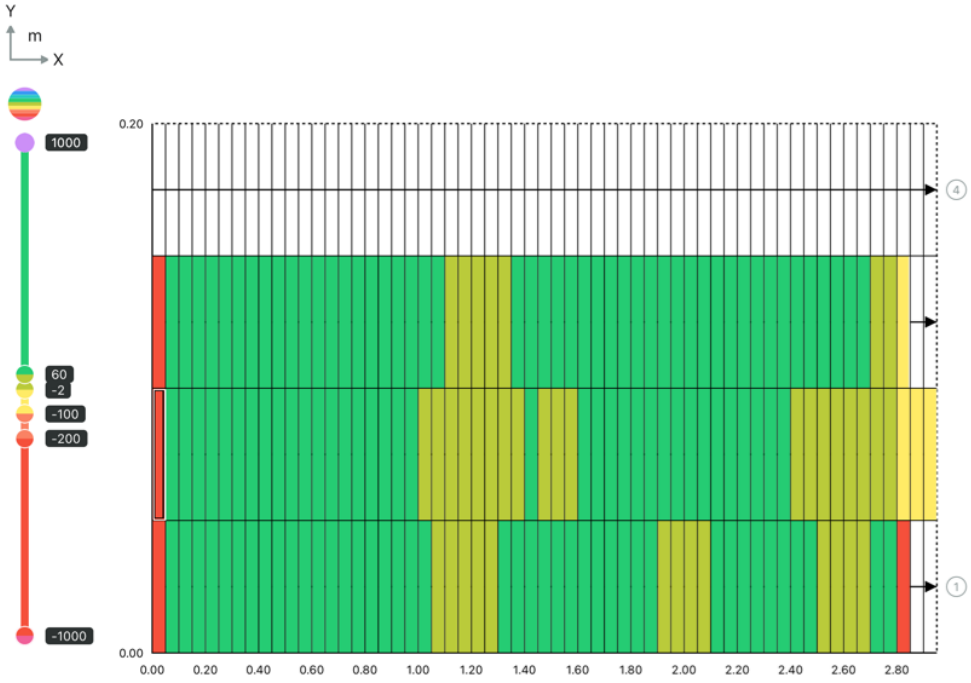


Figure C.6: Potential measurement of the L13 bottom face

## L17

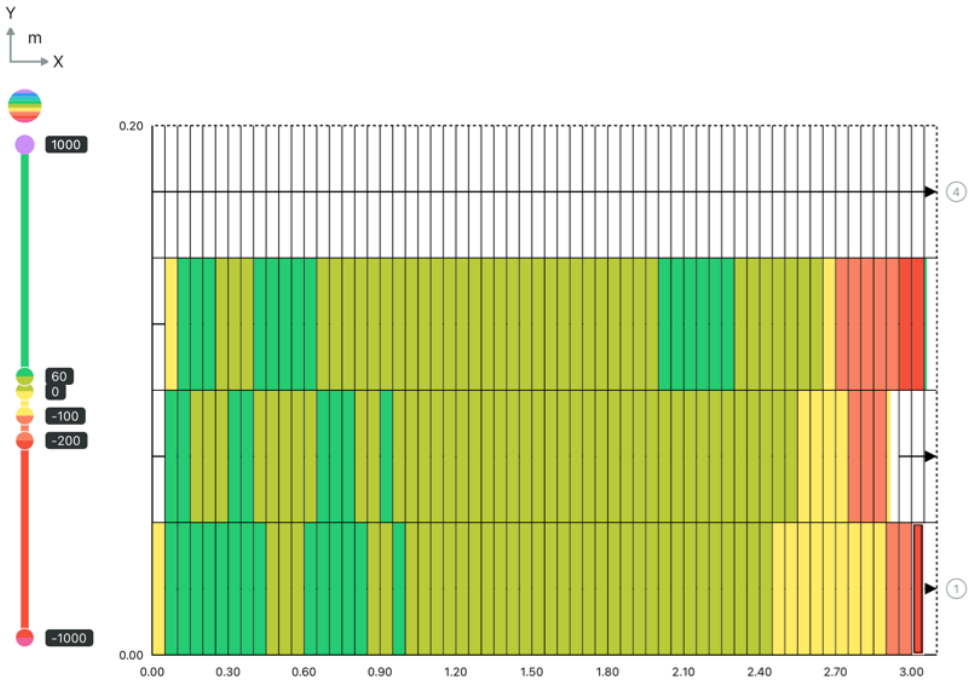


Figure C.7: Potential measurement of the L17 bottom face

# L23


Figure C.8: Potential measurement of the L23 bottom face

# D

# Results RH and UPV

| Location | coating | RQ | m1 | m2 | m3 | m4 | m5 | m6 | m7 | m8 | m9 | m10 | m11 | m12 | m13 | median | mean | stddev |
|---|---|---|---|---|---|---|---|---|---|---|---|---|---|---|---|---|---|---|
| k2-1 | Without coating | R | 52 | 65 | 66 | 62 | 66 | 64 | 58 | 59 | 62 | 62 | 64 | 68 | | 63.0 | 62.3 | 4.2 |
| k2-1 | Without coating | Q | 75 | 67 | 76 | 62 | 72 | 74 | 69 | 74 | 74 | 67 | 65 | 68 | | 70.5 | 70.3 | 4.3 |
| k2-1 | With coating | R | 27 | 50 | 35 | 29 | 59 | 58 | 35 | 31 | 48 | 32 | 50 | 48 | | 41.5 | 41.8 | 11.0 |
| k2-1 | With coating | Q | 38 | 61 | 64 | 29 | 37 | 57 | 26 | 62 | 67 | 31 | 63 | 70 | | 59.0 | 50.4 | 16.0 |
| k3-1 | Without coating | R | 64 | 61 | 65 | 51 | 55 | 58 | 60 | 62 | 62 | 64 | 67 | 65 | | 62.0 | 61.2 | 4.4 |
| k3-1 | Without coating | Q | 71 | 72 | 74 | 54 | 63 | 66 | 75 | 77 | 77 | 69 | 72 | 78 | | 72.0 | 70.7 | 6.6 |
| k3-1 | With coating | R | 38 | 36 | 44 | 51 | 59 | 46 | 45 | 49 | 49 | 52 | 56 | 46 | | 47.5 | 47.6 | 6.4 |
| k3-1 | With coating | Q | 32 | 55 | 63 | 29 | 42 | 66 | 38 | 47 | 72 | 21 | 56 | 70 | | 51.0 | 49.3 | 16.3 |
| k3-2 | Without coating | R | 63 | 62 | 66 | 58 | 52 | 59 | 58 | 63 | 52 | 59 | 58 | 64 | | 59.0 | 59.5 | 4.2 |
| k3-2 | Without coating | Q | 76 | 77 | 73 | 56 | 59 | 68 | 62 | 76 | 75 | 67 | 72 | 73 | | 72.5 | 69.5 | 6.8 |
| k3-2 | With coating | R | 29 | 54 | 60 | 29 | 37 | 54 | 27 | 42 | 50 | 20 | 39 | 55 | | 40.5 | 41.3 | 12.7 |
| k3-2 | With coating | Q | 31 | 45 | 70 | 42 | 40 | 53 | 21 | 50 | 65 | 39 | 50 | 61 | | 47.5 | 47.3 | 13.5 |
| S1 | Without coating | R | 52 | 51 | 44 | 48 | 50 | 40 | 45 | 51 | 45 | 39 | 44 | 38 | | 45.0 | 45.6 | 4.7 |
| S1 | Without coating | Q | 60 | 62 | 67 | 58 | 57 | 61 | 67 | 65 | 70 | 61 | 64 | 68 | | 63.0 | 63.3 | 4.0 |
| S1 | With coating | R | | | | | | | | | | | | | | | | |
| S1 | With coating | Q | 35 | 51 | 63 | 37 | 36 | 59 | 35 | 55 | 64 | 34 | 53 | 60 | | 52.0 | 48.5 | 11.6 |
| S2 | Without coating | R | 55 | 45 | 58 | 60 | 44 | 51 | 45 | 44 | 48 | 44 | 48 | 47 | | 47.5 | 49.1 | 5.4 |
| S2 | Without coating | Q | 60 | 68 | 72 | 68 | 52 | 60 | 66 | 57 | 57 | 58 | 59 | 60 | | 60.0 | 61.4 | 5.6 |
| S2 | With coating | R | 35 | 49 | 55 | 35 | 52 | 42 | 32 | 48 | 48 | 35 | 49 | 50 | | 48.0 | 44.2 | 7.6 |
| S2 | With coating | Q | 41 | 56 | 44 | 43 | 45 | 38 | 36 | 62 | 33 | 37 | 43 | 55 | | 43.0 | 44.4 | 8.5 |
| S3 | Without coating | R | 43 | 59 | 51 | 49 | 52 | 53 | 57 | 54 | 60 | 57 | 58 | 52 | | 53.5 | 53.8 | 4.6 |
| S3 | Without coating | Q | 67 | 69 | 71 | 65 | 62 | 72 | 74 | 61 | 67 | | | | | 67.0 | 67.6 | 4.2 |
| S3 | With coating | R | 29 | 55 | 52 | 45 | 42 | 52 | 47 | 52 | 56 | 39 | 51 | 52 | | 51.5 | 47.7 | 7.5 |
| S3 | With coating | Q | 46 | 68 | 51 | 41 | 44 | 50 | 59 | 46 | 58 | 63 | 38 | 60 | 68 | 51.0 | 52.0 | 9.7 |
| S4 | Without coating | R | 49 | 60 | 61 | 55 | 45 | 54 | 58 | 50 | 56 | 56 | 55 | 48 | | 55.0 | 53.9 | 4.7 |
| S4 | Without coating | Q | 71 | 73 | 69 | 68 | 68 | 75 | 65 | 73 | 75 | 72 | 76 | | | 72.0 | 71.4 | 3.3 |
| S4 | With coating | R | 32 | 36 | 32 | 52 | 44 | 36 | 32 | 39 | 42 | 50 | 31 | 46 | | 37.5 | 39.3 | 7.1 |
| S4 | With coating | Q | 44 | 70 | 69 | 37 | 36 | 44 | 30 | 56 | 62 | 41 | 62 | 64 | 48 | 48.0 | 51.3 | 13.0 |
| S5 | Without coating | R | 42 | 40 | 45 | 58 | 45 | 41 | 61 | 58 | 46 | 58 | 45 | 57 | | 45.5 | 49.7 | 7.6 |
| S5 | Without coating | Q | 55 | 67 | 66 | 66 | 72 | 61 | 62 | 61 | 61 | 62 | 64 | | | 62.0 | 63.4 | 4.2 |
| S5 | With coating | R | 34 | 49 | 54 | 58 | 53 | 56 | 52 | 58 | 48 | 48 | 58 | 55 | | 53.5 | 51.9 | 6.5 |
| S5 | With coating | Q | 36 | 45 | 63 | 31 | 51 | 63 | 44 | 60 | 60 | 41 | 43 | 65 | | 48.0 | 50.2 | 11.2 |
| L2 | Without coating | R | 65 | 60 | 64 | 60 | 70 | 68 | 64 | 58 | 65 | 65 | 62 | 59 | | 64 | 63.3 | 3.5 |
| L2 | Without coating | Q | 71 | 77 | 71 | 77 | 76 | 69 | 77 | 76 | 81 | 67 | 76 | 80 | | 76 | 74.8 | 4.2 |
| L9 | Without coating | R | 60 | 66 | 66 | 60 | 65 | 66 | 64 | 66 | 65 | 65 | 62 | 64 | | 65 | 64.1 | 2.1 |
| L9 | Without coating | Q | 75 | 74 | 74 | 73 | 72 | 82 | 73 | 71 | 72 | 70 | 75 | 77 | | 73.5 | 74.0 | 3.0 |
| L13 | Without coating | R | 61 | 60 | 62 | 63 | 58 | 60 | 62 | 54 | 56 | 64 | 61 | 62 | | 61 | 60.3 | 2.8 |
| L13 | Without coating | Q | 66 | 75 | 72 | 74 | 72 | 78 | 74 | 69 | 72 | 73 | 70 | 74 | | 72.5 | 72.4 | 3.0 |
| L17 | Without coating | R | 63 | 63 | 67 | 60 | 59 | 66 | 61 | 61 | 60 | 64 | 63 | 63 | | 63 | 62.5 | 2.3 |
| L17 | Without coating | Q | 75 | 69 | 74 | 75 | 76 | 76 | 73 | 70 | 72 | 74 | 74 | 74 | | 74 | 73.5 | 2.1 |
| L23 | Without coating | R | 58 | 66 | 69 | 64 | 70 | 66 | 66 | 71 | 64 | 58 | 62 | 68 | | 66 | 65.2 | 4.1 |
| L23 | Without coating | Q | 73 | 73 | 76 | 77 | 77 | 78 | 74 | 76 | 74 | 78 | 76 | 74 | | 76 | 75.5 | 1.8 |

| Name | Result | Date & Time | Time 1 (µs) | Gain (x) | Voltage (V) | Calib. Time Offset (µs) |
|---|---|---|---|---|---|---|
| L2.1 | 88 µs | 25/06/2024 10:11 | 88.5 | 100 | 150 | -2.9 |
| L2.2 | 79 µs | 25/06/2024 10:11 | 79.3 | 100 | 150 | -2.9 |
| | | | | | | |
| L9.1 | 77 µs | 25/06/2024 10:21 | 76.6 | 20 | 150 | -2.9 |
| L9.2 | 76 µs | 25/06/2024 10:21 | 76.3 | 20 | 150 | -2.9 |
| L9.3 | 76 µs | 25/06/2024 10:21 | 76.3 | 20 | 150 | -2.9 |
| | | | | | | |
| L13.1 | 78 µs | 25/06/2024 10:25 | 78.3 | 20 | 150 | -2.9 |
| L13.2 | 78 µs | 25/06/2024 10:25 | 77.8 | 20 | 150 | -2.9 |
| L13.3 | 87 µs | 25/06/2024 10:25 | 86.9 | 20 | 150 | -2.9 |
| | | | | | | |
| L17.1 | 87 µs | 25/06/2024 10:41 | 86.9 | 20 | 150 | -2.9 |
| L17.2 | 87 µs | 25/06/2024 10:41 | 86.5 | 20 | 150 | -2.9 |
| L17.3 | 87 µs | 25/06/2024 10:42 | 87.2 | 20 | 150 | -2.9 |
| | | | | | | |
| S1.1 | 65 µs | 26/06/2024 11:01 | 65.3 | 10000 | 100 | -3.1 |
| S1.2 | 64 µs | 26/06/2024 11:01 | 64.4 | 10000 | 100 | -3.1 |
| S1.3 | 64 µs | 26/06/2024 11:01 | 63.8 | 10000 | 100 | -3.1 |
| S1.4 | 64 µs | 26/06/2024 11:02 | 64.3 | 10000 | 100 | -3.1 |
| S1.5 | 65 µs | 26/06/2024 11:03 | 65 | 10000 | 100 | -3.1 |
| S1.6 | 63 µs | 26/06/2024 11:03 | 63.1 | 10000 | 100 | -3.1 |
| S1.7 | 54 µs | 26/06/2024 11:04 | 53.7 | 1000 | 50 | -3.1 |
| S1.8 | 54 µs | 26/06/2024 11:04 | 53.6 | 1000 | 50 | -3.1 |
| S1.9 | 55 µs | 26/06/2024 11:04 | 54.8 | 1000 | 50 | -3.1 |
| | | | | | | |
| S2.1 | 62 µs | 26/06/2024 11:04 | 62.5 | 1000 | 50 | -3.1 |
| S2.2 | 53 µs | 26/06/2024 11:04 | 53.2 | 1000 | 50 | -3.1 |
| S2.3 | 53 µs | 26/06/2024 11:04 | 52.8 | 1000 | 50 | -3.1 |
| | | | | | | |
| S3.1 | 56 µs | 26/06/2024 11:06 | 55.7 | 1000 | 100 | -3.1 |
| S3.2 | 55 µs | 26/06/2024 11:06 | 54.9 | 1000 | 100 | -3.1 |
| S3.3 | 54 µs | 26/06/2024 11:06 | 54.1 | 1000 | 100 | -3.1 |
| S3.4 | 56 µs | 26/06/2024 11:06 | 55.6 | 1000 | 100 | -3.1 |
| | | | | | | |
| S4.1 | 86 µs | 26/06/2024 11:07 | 86.5 | 1000 | 100 | -3.1 |
| S4.2 | 59 µs | 26/06/2024 11:07 | 58.9 | 1000 | 100 | -3.1 |
| S4.3 | 59 µs | 26/06/2024 11:07 | 58.5 | 1000 | 100 | -3.1 |
| S4.4 | 59 µs | 26/06/2024 11:07 | 59 | 1000 | 100 | -3.1 |
| | | | | | | |
| S5.1 | 58 µs | 26/06/2024 11:09 | 57.5 | 1000 | 100 | -3.1 |
| S5.2 | 57 µs | 26/06/2024 11:09 | 57.2 | 1000 | 100 | -3.1 |
| S5.3 | 58 µs | 26/06/2024 11:09 | 57.8 | 1000 | 100 | -3.1 |
| S5.4 | 49 µs | 26/06/2024 11:09 | 49.1 | 1000 | 200 | -3.1 |
| S5.5 | 49 µs | 26/06/2024 11:09 | 49.4 | 1000 | 200 | -3.1 |
| S5.6 | 49 µs | 26/06/2024 11:09 | 48.8 | 1000 | 200 | -3.1 |

# E

# Results Gecor-10 measurements

*Courtesy of John van den Berg*

## RESULTATEN CORROSIEMETINGEN MET GECOR 10; STP5 op locatie ARDEWEG viaduct

*donderdag 11 Juli 2024*

• diameter rebar = 28.0 mm; area rebar = 571.8 $cm^2$

| | **Resistivity** | | | **Potential** | | | | **CR** | | |
|---|---|---|---|---|---|---|---|---|---|---|
| | Resipod: | Sensor C: | Sensor A: | Sensor B: | Profometer | Sensor A: | Polarisation | Sensor A: | Sensor A: | Sensor A |
| Ligger no. | ρ (kΩ.m) | ρ (kΩ.m) | ρ (kΩ.m) | OCP (mV) | OCP (mV) | $E_{corr}$ (mV) | time | $I_{corr}$ (µA/$cm^2$) | $R_{Ohm}$ (kΩ) | $E_{pol}$ (mV) |
| 1 | 0.45 | 0.02 | 0.21 | -236 | -230.3 | -224.3 | 30 | 0.396 | 3.49 | 21.7 |
| 2 | 0.18 | 0.42 | 0.13 | -260 | -217.0 | -359.6 | 30 | 0.876 | 2.23 | 12.4 |
| 3 | 0.23 | 0.66 | 0.60 | -200 | -187.7 | -188.8 | 30 | 0.285 | 10.07 | 30.3 |
| 3 | - | - | 0.87 | - | - | -195.7 | 100 | 0.153 | 14.42 | 35.4 |
| 4 | 0.93 | 1.27 | 1.50 | -110 | -112.7 | -91.0 | 100 | 0.067 | 25.05 | 61.2 |
| 5 | 0.83 | 1.15 | 0.88 | -50 | -39.3 | -44.8 | 100 | 0.130 | 14.62 | 52.3 |
| 6 | 0.88 | 1.39 | 0.76 | -38 | -46.7 | -40.6 | 100 | 0.167 | 12.59 | 46.3 |
| 7 | 0.69 | 1.25 | 0.84 | -59 | -38.0 | -39.1 | 100 | 0.135 | 13.98 | 50.4 |
| 8 | 1.32 | 0.79 | 1.74 | -84 | -40.7 | -88.4 | 100 | 0.057 | 29.02 | 48.0 |
| 9 | 1.69 | 2.33 | 1.82 | -81 | -65.3 | -86.9 | 100 | 0.067 | 30.26 | 67.3 |
| 10 | 1.51 | 2.19 | 1.07 | -88 | -64.3 | -74.9 | 100 | 0.126 | 17.85 | 46.7 |
| 11 | 1.49 | 1.98 | 1.29 | -40 | -63.7 | -81.0 | 100 | 0.077 | 21.57 | 53.3 |
| 12 | 1.10 | 1.30 | 1.36 | -48 | -66.7 | -62.4 | 100 | 0.076 | 22.66 | 59.6 |
| 13 | 1.20 | 1.23 | 0.82 | -62 | -44.0 | -63.8 | 100 | 0.166 | 13.64 | 40.8 |
| 14 | 1.71 | 1.75 | 1.18 | -51 | -113.7 | -67.7 | 100 | 0.110 | 19.67 | 49.6 |
| 15 | 1.51 | 1.97 | 1.20 | -46 | -83.0 | -68.1 | 100 | 0.107 | 19.94 | 51.0 |
| 16 | 0.96 | 1.46 | 1.72 | -49 | -77.7 | -89.7 | 100 | 0.057 | 28.68 | 47.4 |
| 17 | 0.74 | 1.26 | 0.38 | -97 | -54.7 | -104.4 | 30 | 0.344 | 6.26 | 16.9 |
| 17 | - | - | 0.39 | - | - | -106.8 | 100 | 0.294 | 6.48 | 24.5 |
| 18 | 1.14 | 1.44 | 0.62 | -102 | -57.0 | -81.4 | 100 | 0.154 | 10.25 | 44.0 |
| 19 | 1.05 | 1.34 | 0.49 | -67 | -81.3 | -67.8 | 100 | 0.321 | 8.11 | 18.3 |
| 20 | 0.84 | 0.94 | 0.69 | -67 | -38.7 | -71.1 | 100 | 0.271 | 11.52 | 26.7 |
| 21 | 0.95 | 1.44 | 0.48 | -58 | -51.0 | -69.0 | 100 | 0.162 | 8.00 | 24.8 |
| 22 | 1.35 | 1.69 | 0.87 | -57 | -65.0 | -64.5 | 100 | 0.158 | 14.54 | 40.3 |
| 23 | 1.10 | 1.59 | 0.76 | -65 | -51.0 | -84.8 | 100 | 0.176 | 12.71 | 38.6 |
| 24 | 1.13 | 1.43 | 0.54 | -85 | -37.7 | -70.6 | 100 | 0.159 | 9.07 | 48.7 |
| 25 | 1.53 | 1.96 | 0.69 | -70 | -60.0 | -67.3 | 100 | 0.123 | 11.58 | 36.7 |

## RESULTATEN CORROSIEMETINGEN MET GECOR 10; T-Liggers op locatie ARDEWEG viaduct

*donderdag 11 Juli 2024*

• diameter rebar = 8.0 mm; area rebar = 16.3 $cm^2$

| | **Resistivity** | | | **Potential** | | | **CR** | | |
|---|---|---|---|---|---|---|---|---|---|
| | Resipod: | Sensor C: | Sensor A: | Sensor B: | Sensor A: | Polarisation | Sensor A: | Sensor A: | Sensor A |
| Ligger no. | ρ (kΩ.m) | ρ (kΩ.m) | ρ (kΩ.m) | OCP (mV) | $E_{corr}$ (mV) | time | $I_{corr}$ (µA/$cm^2$) | $R_{Ohm}$ (kΩ) | $E_{pol}$ (mV) |
| L2 | 0.91 | 0.73 | *2.63 | 53 | *54.6 | 100 | *0.039 | *43.90 | *202.4 |
| L13 | 1.35 | 1.20 | 0.46 | 30 | 47.4 | 100 | 0.395 | 7.66 | 24.3 |
| L17 | 1.05 | 1.57 | 0.51 | -10 | -16.3 | 100 | 0.315 | 8.53 | 35.5 |
| L23 | 2.34 | 1.51 | 0.29 | 36 | 35.4 | 100 | 0.694 | 4.81 | 13.8 |

* = Mogelijk foutieve meting

**RESULTATEN CORROSIEMETINGEN MET GECOR 10; LIGGER(koppen) ARDEWEG viaduct in WOLFHEZE** *dinsdag 29 Oktober 2024*

• diameter rebar = 8.0 mm; area rebar = 16.3 $cm^2$ & **polarisation time = 30 sec.**

Corr.risk*: v = verwaarloosbaar, l = laag, m = matig, h = hoog

| Ligger no. | Resipod: ρ (kΩ.m) | Sensor C: ρ (kΩ.m) | Sensor A: ρ (kΩ.m) | Sensor B: OCP (mV) | Profometer OCP (mV) | Sensor A: $E_{corr}$ (mV) | Corr. risk*: | Sensor A: $I_{corr}$ (µA/$cm^2$) | Sensor A: $R_{Ohm}$ (kΩ) | Sensor A $E_{pol}$ (mV) |
|---|---|---|---|---|---|---|---|---|---|---|
| Ligger 4L1: | | | | | | | | | | |
| 25 cm | 0.38 | 0.19 | 0.2112 | –222 | –321 | | m | 0.560 | 3.52 | 14.2 |
| 50 cm | 1.74 | 1.50 | 0.8562 | –190 | | –115.7 | l | 0.188 | 14.27 | 42.6 |
| 75 cm | 0.75 | 0.58 | | –220 | –292 | | l/m | schade | | |
| 100 cm | 1.33 | 1.33 | | –205 | –285 | | v/l/m | 0.390 | 2.75 | 20.5 |
| 125 cm | 1.24 | 0.68 | 0.3864 | –169 | | – 98.7 | l/m | 0.504 | 6.44 | 15.9 |
| 150 cm | 1.97 | 1.07 | | –180 | | – 83.1 | v/l | 0.487 | 6.60 | 16.4 |
| Ligger 17: | | | | | | | | | | |
| 25 cm | 0.36 | 0.20 | 0.2508 | –278 | –259 | –237.0 | l/m | 0.411 | 4.18 | 19.4 |
| 50 cm | 0.08 | KB coating | | –243 | –205 | | m/h | KB coating | | |
| 75 cm | 0.15 | KB coating | | –320 | –373 | | m/h | KB coating | | |
| 100 cm | 0.50 | 0.55 | | –199 | –181 | –133.5 | l/h ? | 1.088 | 4.12 | 7.3 |
| 125 cm | 1.13 | 1.30 | | –105 | – 81 | – 85.7 | v/l/m | 0.891 | 3.62 | 8.9 |
| 150 cm | | 0.79 | 0.8898 | – 67 | – 57 | – 65.2 | l | 0.116 | 14.83 | 68.8 |
| Ligger 13: | | | | | | | | | | |
| 25 cm | 0.48 | 0.25 | 0.2640 | –161 | –169 | –136.2 | l/m | 0.499 | 4.40 | 16.0 |
| 50 cm | 0.55 | | 0.7086 | – 92 | – 96 | – 86.5 | l | 0.154 | 11.81 | 51.9 |
| 75 cm | 0.38 | 0.27 | | –123 | –118 | –112.2 | l/m | 0.192 | 10.35 | 41.6 |
| 100 cm | 0.78 | 0.57 | | – 84 | – 80 | –117.7 | v/l | 0.080 | 32.29 | 100.1 |
| 125 cm | | 0.79 | 0.8274 | –124 | –117 | –106.6 | l | 0.173 | 13.79 | 46.3 |
| 150 cm | 0.90 | 0.41 | 0.4572 | –133 | –130 | –155.3 | l/m | 0.355 | 7.62 | 22.5 |
| Ligger 2: | | | | | | | | | | |
| 25 cm | 0.30 | 0.13 | 0.2874 | –214 | | –211.9 | l/m | 0.452 | 4.79 | 21.2 |
| 50 cm | 0.64 | 0.64 | | – 96 | – 99 | –105.2 | l/m | 0.699 | 1.84 | 11.4 |
| 75 cm | 0.52 | 0.43 | 0.1902 | – 66 | –154 | – 83.7 | l/m | 0.243 | 3.17 | 32.8 |
| 100 cm | 0.72 | 0.42 | 0.1890 | – 83 | –104 | – 79.7 | l/m | 0.403 | 3.15 | 19.8 |
| 125 cm | 0.95 | 0.60 | 0.5214 | – 91 | –114 | –105.9 | l | 0.336 | 8.69 | 23.7 |
| 150 cm | 1.06 | 0.27 | 0.4518 | – 96 | –111 | –106.7 | l/m | 0.326 | 7.53 | 24.4 |

• diameter rebar = 8.0 mm; area rebar = 16.3 $cm^2$ & **polarisation time = 100 sec.**

Corr.risk*: v = verwaarloosbaar, l = laag, m = matig, h = hoog

| Ligger no. | Resipod: ρ (kΩ.m) | Sensor C: ρ (kΩ.m) | Sensor A: ρ (kΩ.m) | Sensor B: OCP (mV) | Profometer OCP (mV) | Sensor A: $E_{corr}$ (mV) | Corr. risk*: | Sensor A: $I_{corr}$ (µA/$cm^2$) | Sensor A: $R_{Ohm}$ (kΩ) | Sensor A: $E_{pol}$ (mV) |
|---|---|---|---|---|---|---|---|---|---|---|
| Ligger 4L1: | | | | | | | | | | |
| 25 cm | 0.38 | 0.19 | 0.3030 | –222 | –321 | | l/m | 0.426 | 5.05 | 18.7 |
| 50 cm | 1.74 | 1.50 | 3.7542 | –190 | | –122.5 | v/l | 0.035 | 62.57 | 228.3 |
| 50 cm repeat | | | 3.4128 | | | –100.8 | v/l | 0.036 | 56.88 | 223.1 |
| 75 cm | 0.75 | 0.58 | | –220 | –292 | | l/m | schade | | |
| 100 cm | 1.33 | 1.33 | | –205 | –285 | | v/l/m | 0.390 | 12.48 | 61.8 |
| 125 cm | | 0.68 | | –169 | | –106.1 | l | 0.302 | 7.17 | 26.4 |
| 150 cm | 1.97 | 1.07 | 0.5598 | –180 | | – 91.9 | v/l | 0.248 | 9.33 | 32.1 |
| Ligger 17: | | | | | | | | | | |
| 25 cm | 0.36 | 0.20 | 0.3240 | –278 | –259 | | l/m | 0.283 | 5.40 | 28.2 |
| 50 cm | | KB | 0.4494 | –243 | –205 | | l/m | 0.225 | 7.49 | 35.4 |
| 75 cm | 0.15 | KB | | –320 | –373 | | m/h | KB coating | | |
| 100 cm | 0.50 | 0.55 | | –199 | –181 | | l | KB coating | | |
| 125 cm repeat | | 0.79 | 0.5424 | –124 | –117 | – 91.2 | l | 0.185 | 9.04 | 43.2 |
| 150 cm | | 0.79 | 0.9690 | – 67 | – 57 | – 79.5 | v/l | 0.085 | 16.15 | 93.5 |
| Ligger 13: | | | | | | | | | | |
| 25 cm | 0.48 | 0.25 | | –161 | –169 | –137.9 | l/m | 0.177 | 12.60 | 45.0 |
| 50 cm | 0.55 | 0.40 | | – 92 | – 96 | – 96.9 | l/m/h | 1.350 | 1.54 | 5.9 |
| 50 cm repeat | | | 0.2760 | | | – 90.3 | l/m | 0.440 | 4.60 | 18.1 |
| 75 cm | 0.38 | 0.27 | 0.4386 | –123 | –118 | –113.9 | l/m | 0.231 | 7.31 | 34.5 |
| 100 cm | 0.78 | 0.57 | 1.4136 | – 84 | – 80 | –111.9 | v/l | 0.092 | 23.56 | 87.0 |
| 125 cm | | 0.79 | 0.5814 | –124 | –117 | –109.9 | l | 0.207 | 9.69 | 38.4 |
| 150 cm | 0.90 | 0.41 | 0.3450 | –133 | –130 | –131.1 | l/m | 0.254 | 5.75 | 31.4 |
| Ligger 2: | | | | | | | | | | |
| 25 cm | 0.30 | 0.13 | 0.2646 | –214 | | –205.8 | l/m | 0.348 | 4.41 | 22.9 |
| 50 cm | 0.64 | 0.64 | 0.5580 | – 96 | – 99 | –107.8 | l | 0.192 | 9.30 | 41.7 |
| 75 cm | 0.52 | 0.43 | 0.3156 | – 66 | –154 | –101.4 | l/m | 0.400 | 5.26 | 19.9 |
| 100 cm | 0.72 | | 0.5730 | – 83 | –104 | – 86.4 | l | 0.269 | 9.55 | 29.6 |
| 125 cm | 0.95 | 0.60 | 0.5172 | – 91 | –114 | – 95.2 | l | 0.282 | 8.62 | 28.2 |
| 150 cm | 1.06 | | 0.6072 | – 96 | –111 | – 98.9 | v/l | 0.216 | 10.12 | 36.8 |

*CR values at different polarization times (30 & 100 seconds)*

| Ligger no. | Sensor A: $I_{corr}$ (µA/cm$^2$) Polarization time 30 sec. | Sensor A: $I_{corr}$ (µA/cm$^2$) Polarization time 100 sec. |
|---|---|---|
| Ligger 4L1: | | |
| 25 cm | 0.560 | 0.426 |
| 50 cm | 0.188 | 0.035 |
| 50 cm repeat | | 0.036 |
| 75 cm | schade | schade |
| 100 cm | 0.390 | 0.390 |
| 125 cm | 0.504 | 0.302 |
| 150 cm | 0.487 | 0.248 |
| Ligger 17: | | |
| 25 cm | 0.411 | 0.283 |
| 50 cm | KB coating | 0.225 |
| 75 cm | KB coating | KB coating |
| 100 cm | 1.088 | KB coating |
| 125 cm | 0.891 | 0.185 |
| 150 cm | 0.116 | 0.085 |
| Ligger 13: | | |
| 25 cm | 0.499 | 0.177 |
| 50 cm | 0.154 | 1.350 |
| 50 cm repeat | | 0.440 |
| 75 cm | 0.192 | 0.231 |
| 100 cm | 0.080 | 0.092 |
| 125 cm | 0.173 | 0.207 |
| 150 cm | 0.355 | 0.254 |
| Ligger 2: | | |
| 25 cm | 0.452 | 0.348 |
| 50 cm | 0.699 | 0.192 |
| 75 cm | 0.243 | 0.400 |
| 100 cm | 0.403 | 0.269 |
| 125 cm | 0.336 | 0.282 |
| 150 cm | 0.326 | 0.216 |

**Guidelines for corrosion risk assessment**

| Concrete resistivity ρ (kΩ.m) | Corrosion current density $I_{corr}$ (µA/cm$^2$) | Corrosion risk: |
|---|---|---|
| < 0.1 | > 1 | High/Hoog |
| 0.1 to 0.5 | 0.5 to 1 | Moderate/Matig |
| 0.5 to 1 | 0.1 to 0.5 | Low/Laag |
| > 1 | < 0.1 | Negligible/ Verwaarloosbaar |

| Half-cell potential vs CSE $E_{corr}$ (mV) | Corrosion risk: | Risk % |
|---|---|---|
| < -500 | Severe | > 90 |
| -500 to -350 | High/Hoog | 90 |
| -350 to -200 | Moderate/Matig | 50 |
| > -200 | Low/Laag | 10 |

*JvdB; 17-12-2024*

# F

# Carbonation

This chapter presents the carbonated cores. Photos of each core were taken just after the phenolphthalein indicator solution was applied to the fresh concrete surface. The results are summarized in table F.1.

Table F.1: carbonation depth of the concrete cores

| Location | Max depth [mm] |
|---|---|
| S1-CL1 | 24 |
| S2-CL1 | 16 |
| S4-CL1 | 5 |
| S5-CL1 | 8 |
| | |
| L2-CL1 | 0 |
| L13-CL1 | 11 |
| L17-CL1 | 5 |
| L23-CL1 | 11 |
| | |
| S6-CL1 | 9 |
| S8-CL1 | 8 |


Figure F.1: Overview of all the tested cores


Figure F.2: Carbonation of core S1-CL1


Figure F.3: Carbonation of core S2-CL1

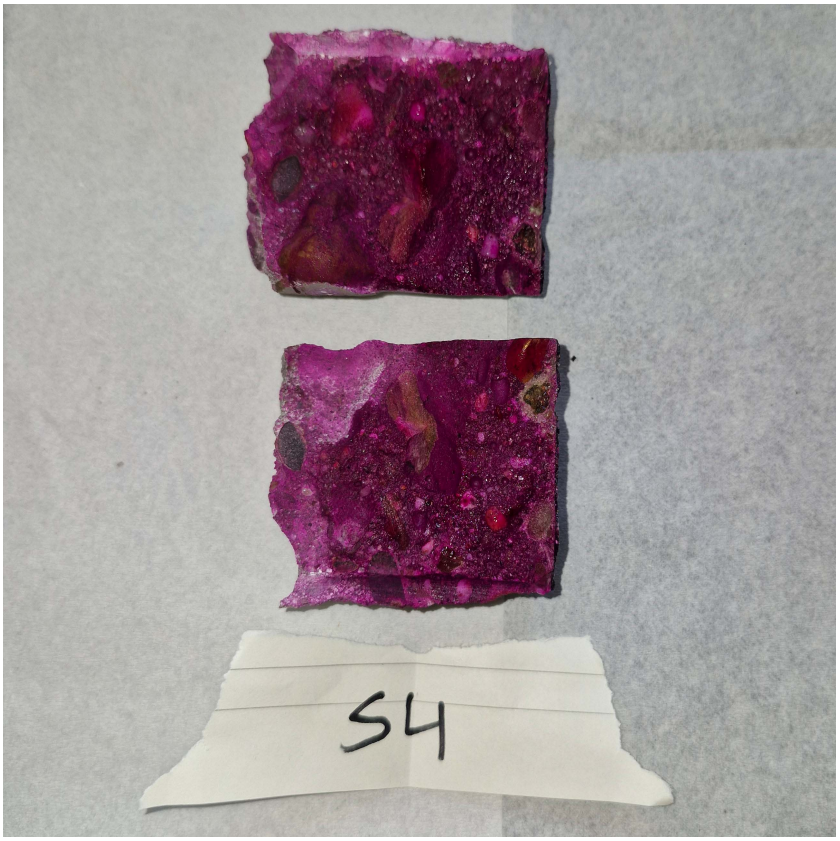


Figure F.4: Carbonation of core S4-CL1


Figure F.5: Carbonation of core S5-CL1


Figure F.6: Carbonation of core L2-CL1

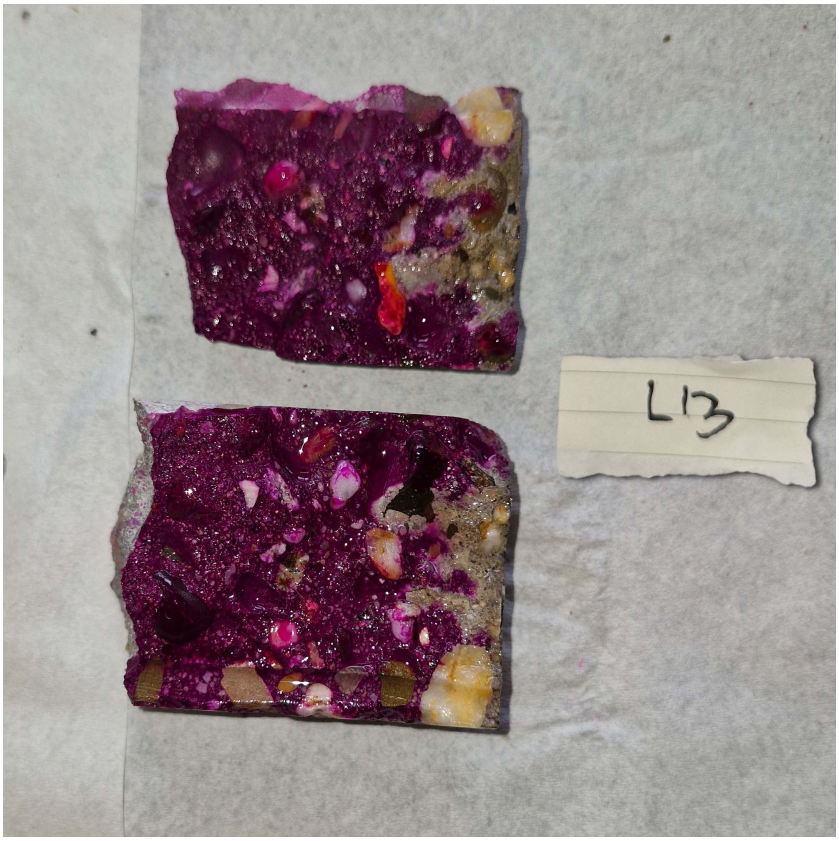


Figure F.7: Carbonation of core L13-CL1

Figure F.8: Carbonation of core L17-CL1

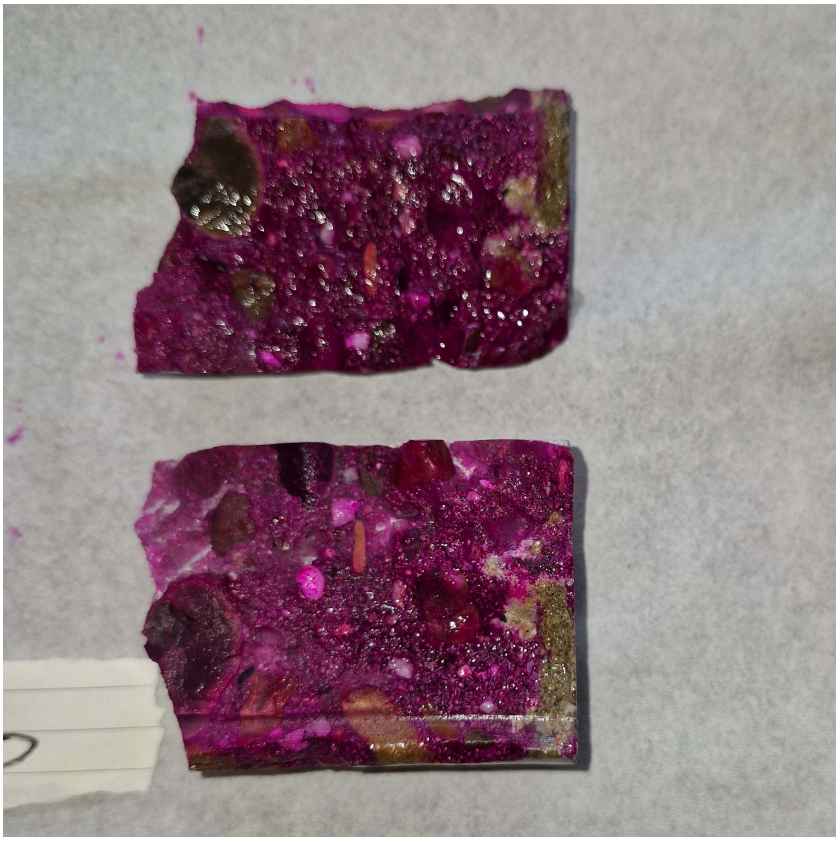

Figure F.9: Carbonation of core L23-CL1

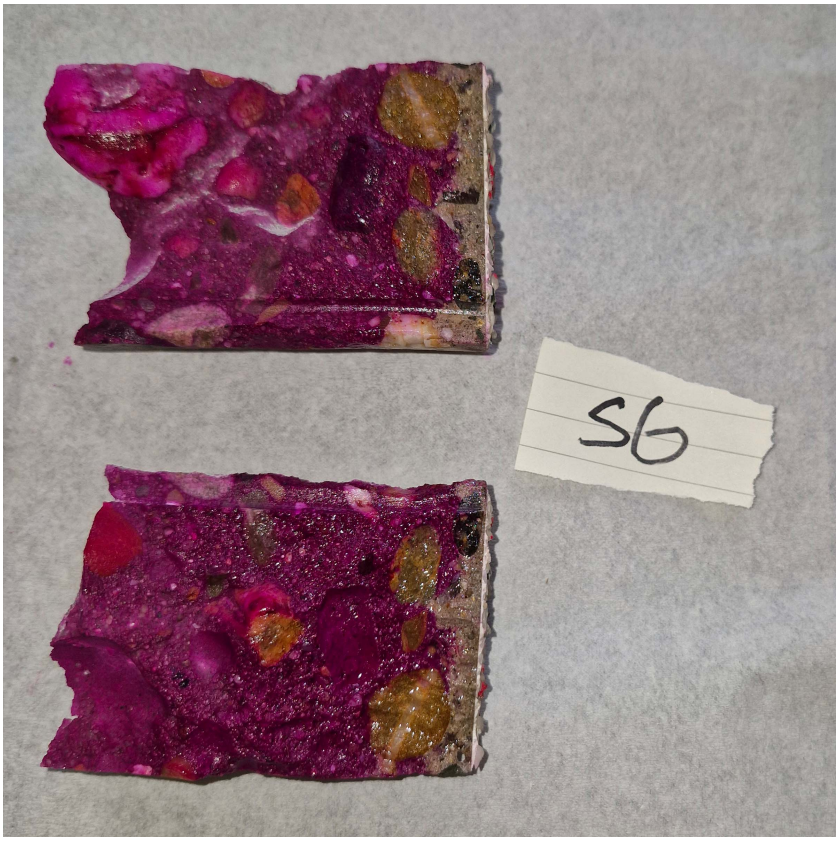


Figure F.10: Carbonation of core S6-CL1

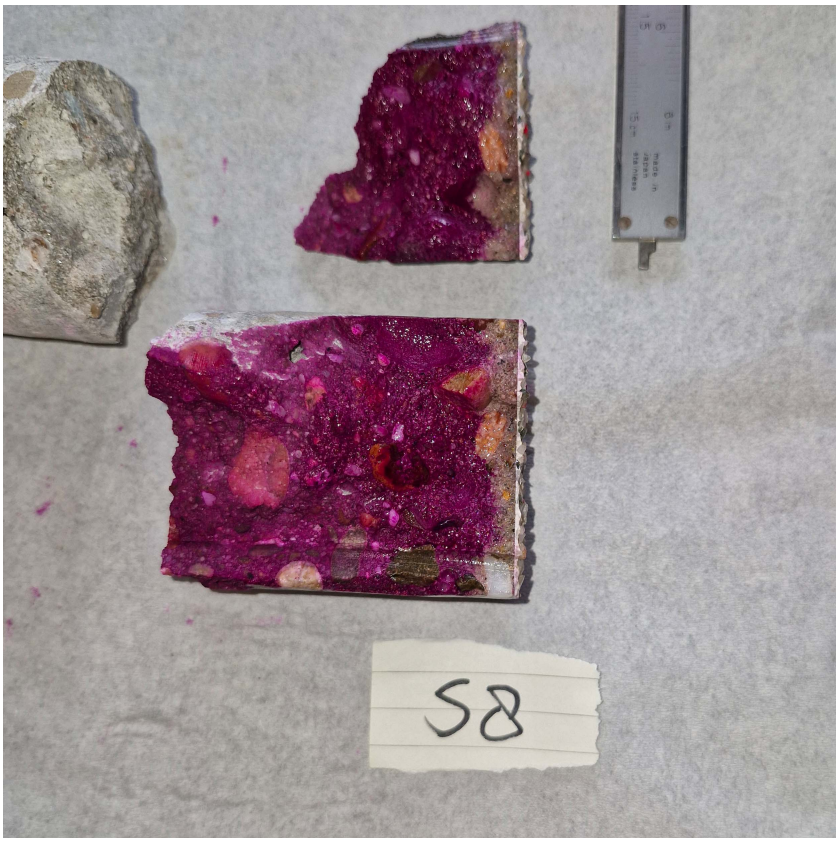


Figure F.11: Carbonation of core S8-CL1

# G

# Overview chloride titrations

# Chloride content calculated with Volhard method

| Date | Sample number | Sample weight [g] | Pertrischaal weight [g] | Filter weight [g] | Dried sample [g] | Cement weight [g] | Cement % | Total solution [ml] | Pipetted solution [ml] | Added AgNO3 [ml] | Titration: NH4SCN [ml] | Chloride content [%] | |
|---|---|---|---|---|---|---|---|---|---|---|---|---|---|
| 07/08/2024 | Blanco | | | | | | | | 100 | 10 | 9.92 | | |
| 07/08/2024 | S1-1 (1) | 21.995 | 79.173 | 0.503 | 93.997 | 7.674 | 34.9 | 500 | 100 | 10 | 9.64 | 0.06 | 0.07 |
| 07/08/2024 | S1-1 (2) | 25.029 | 70.321 | 0.498 | 88.442 | 7.406 | 29.6 | 500 | 100 | 10 | 9.60 | 0.08 | |
| 07/08/2024 | S1-2 (1) | 22.267 | 72.750 | 0.500 | 93.148 | 2.369 | 10.6 | 500 | 100 | 10 | 9.20 | 0.54 | 0.52 |
| 07/08/2024 | S1-2 (2) | 19.780 | 48.188 | 0.486 | 65.084 | 3.370 | 17.0 | 500 | 100 | 10 | 8.96 | 0.50 | |
| 08/08/2024 | S1-3 (1) | 16.880 | 72.750 | 0.497 | 86.951 | 3.176 | 18.8 | 500 | 100 | 10 | 9.10 | 0.46 | 0.42 |
| 08/08/2024 | S1-3 (2) | 23.360 | 49.552 | 0.499 | 69.376 | 4.035 | 17.3 | 500 | 100 | 10 | 9.06 | 0.38 | |
| 28/08/2024 | S1-4 (1) | 29.086 | 43.174 | 0.503 | 66.251 | 6.512 | 22.4 | 500 | 100 | 10 | 8.74 | 0.32 | 0.32 |
| 28/08/2024 | S1-4 (2) | 29.086 | 43.174 | 0.503 | 66.251 | 6.512 | 22.4 | 500 | 100 | 10 | 8.76 | 0.32 | |
| 28/08/2024 | S1-5 (1) | 31.683 | 70.343 | 0.501 | 96.048 | 6.479 | 20.4 | 500 | 100 | 10 | 9.38 | 0.15 | 0.15 |
| 28/08/2024 | S1-5 (2) | 31.683 | 70.343 | 0.501 | 96.048 | 6.479 | 20.4 | 500 | 100 | 10 | 9.34 | 0.16 | |
| 19/09/2024 | S1*-1 (1) | 25.532 | 121.340 | 0.495 | 142.850 | 4.517 | 17.7 | 500 | 100 | 10 | 9.68 | 0.09 | 0.10 |
| 19/09/2024 | S1*-1 (2) | 25.532 | 121.340 | 0.495 | 142.850 | 4.517 | 17.7 | 500 | 100 | 10 | 9.66 | 0.10 | |
| 19/09/2024 | S1*-2 (1) | 26.916 | 127.564 | 0.488 | 150.827 | 4.141 | 15.4 | 500 | 100 | 10 | 9.60 | 0.14 | 0.13 |
| 19/09/2024 | S1*-2 (2) | 26.916 | 127.564 | 0.488 | 150.827 | 4.141 | 15.4 | 500 | 100 | 10 | 9.62 | 0.13 | |
| 19/09/2024 | S1*-3 (1) | 24.407 | 47.590 | 0.501 | 67.621 | 4.877 | 20.0 | 500 | 100 | 10 | 8.58 | 0.49 | 0.49 |
| 19/09/2024 | S1*-3 (2) | 24.407 | 47.590 | 0.501 | 67.621 | 4.877 | 20.0 | 500 | 100 | 10 | 8.56 | 0.49 | |
| 20/09/2024 | S1*-4 (1) | 22.562 | 121.358 | 0.499 | 138.143 | 6.276 | 27.8 | 500 | 100 | 10 | 7.96 | 0.55 | 0.56 |
| 20/09/2024 | S1*-4 (2) | 22.562 | 121.358 | 0.499 | 138.143 | 6.276 | 27.8 | 500 | 100 | 10 | 7.94 | 0.56 | |
| 20/09/2024 | S1*-5 (1) | 27.336 | 127.570 | 0.491 | 147.968 | 7.429 | 27.2 | 500 | 100 | 10 | 7.60 | 0.55 | 0.55 |
| 20/09/2024 | S1*-5 (2) | 27.336 | 127.570 | 0.491 | 147.968 | 7.429 | 27.2 | 500 | 100 | 10 | 7.64 | 0.54 | |
| 20/09/2024 | S1*-6 (1) | 21.689 | 47.590 | 0.495 | 65.975 | 3.799 | 17.5 | 500 | 100 | 10 | 8.58 | 0.63 | 0.62 |
| 20/09/2024 | S1*-6 (2) | 21.689 | 47.590 | 0.495 | 65.975 | 3.799 | 17.5 | 500 | 100 | 10 | 8.60 | 0.62 | |
| 20/09/2024 | S1*-7 (1) | 14.092 | 49.587 | 0.499 | 61.362 | 2.816 | 20.0 | 500 | 100 | 10 | 8.96 | 0.60 | 0.60 |
| 20/09/2024 | S1*-7(2) | 14.092 | 49.587 | 0.499 | 61.362 | 2.816 | 20.0 | 500 | 100 | 10 | 8.98 | 0.59 | |

| | | | | | | | | | | | | |
|---|---|---|---|---|---|---|---|---|---|---|---|---|
| 23/09/2024 S1*-8 (1) | 15.056 | 47.590 | 0.495 | 60.636 | 2.505 | 16.6 | 500 | 100 | 10 | 9.14 | 0.55 | 0.56 |
| 23/09/2024 S1*-8 (2) | 15.056 | 47.590 | 0.495 | 60.636 | 2.505 | 16.6 | 500 | 100 | 10 | 9.12 | 0.57 | |
| | | | | | | | | | | | | |
| 07/08/2024 S2-1 (1) | 18.627 | 49.551 | 0.491 | 64.682 | 3.987 | 21.4 | 500 | 100 | 10 | 9.66 | 0.12 | 0.12 |
| 07/08/2024 S2-1 (2) | 32.280 | 48.367 | 0.500 | 77.492 | 3.655 | 11.3 | 500 | 100 | 10 | 9.68 | 0.12 | |
| | | | | | | | | | | | | |
| 28/08/2024 S2-2 (1) | 22.470 | 47.386 | 0.498 | 65.520 | 4.834 | 21.5 | 500 | 100 | 10 | 9.80 | 0.04 | 0.05 |
| 28/08/2024 S2-2 (2) | 22.470 | 47.386 | 0.498 | 65.520 | 4.834 | 21.5 | 500 | 100 | 10 | 9.78 | 0.05 | |
| | | | | | | | | | | | | |
| 08/08/2024 S4-1 (1) | 29.827 | 48.188 | 0.493 | 74.407 | 4.101 | 13.7 | 500 | 100 | 10 | 9.60 | 0.14 | 0.23 |
| 08/08/2024 S4-1 (2) | 16.379 | 48.361 | 0.505 | 61.987 | 3.258 | 19.9 | 500 | 100 | 10 | 9.34 | 0.32 | |
| | | | | | | | | | | | | |
| 29/08/2024 S4-2 (1) | 19.292 | 70.323 | 0.501 | 85.238 | 4.878 | 25.3 | 500 | 100 | 10 | 9.74 | 0.07 | 0.06 |
| 29/08/2024 S4-2 (2) | 19.292 | 70.323 | 0.501 | 85.238 | 4.878 | 25.3 | 500 | 100 | 10 | 9.78 | 0.05 | |
| | | | | | | | | | | | | |
| 08/08/2024 S5-1 (1) | 21.591 | 47.584 | 0.500 | 63.750 | 5.925 | 27.4 | 500 | 100 | 10 | 9.32 | 0.18 | 0.20 |
| 08/08/2024 S5-1 (2) | 21.591 | 47.584 | 0.500 | 63.750 | 5.925 | 27.4 | 500 | 100 | 10 | 9.16 | 0.23 | |
| | | | | | | | | | | | | |
| 29/08/2024 S5-2 (1) | 24.158 | 47.590 | 0.500 | 67.204 | 5.044 | 20.9 | 500 | 100 | 10 | 9.68 | 0.08 | 0.08 |
| 29/08/2024 S5-2 (2) | 24.158 | 47.590 | 0.500 | 67.204 | 5.044 | 20.9 | 500 | 100 | 10 | 9.68 | 0.08 | |
| | | | | | | | | | | | | |
| 04/09/2024 L2-1 (1) | 27.778 | 70.331 | 0.502 | 95.327 | 3.284 | 11.8 | 500 | 100 | 10 | 9.82 | 0.05 | 0.04 |
| 04/09/2024 L2-1 (2) | 27.778 | 70.331 | 0.502 | 95.327 | 3.284 | 11.8 | 500 | 100 | 10 | 9.86 | 0.03 | |
| | | | | | | | | | | | | |
| 04/09/2024 L2-2 (1) | 27.019 | 47.589 | 0.503 | 71.539 | 3.572 | 13.2 | 500 | 100 | 10 | 9.88 | 0.02 | 0.01 |
| 04/09/2024 L2-2 (2) | 27.019 | 47.589 | 0.503 | 71.539 | 3.572 | 13.2 | 500 | 100 | 10 | 9.90 | 0.01 | |
| | | | | | | | | | | | | |
| 04/09/2024 L13-1 (1) | 26.652 | 49.588 | 0.496 | 71.092 | 5.644 | 21.2 | 500 | 100 | 10 | 9.88 | 0.01 | 0.02 |
| 04/09/2024 L13-1 (2) | 26.652 | 49.588 | 0.496 | 71.092 | 5.644 | 21.2 | 500 | 100 | 10 | 9.86 | 0.02 | |
| | | | | | | | | | | | | |
| 04/09/2024 L13-2 (1) | 28.087 | 127.560 | 0.506 | 151.572 | 4.581 | 16.3 | 500 | 100 | 10 | 9.86 | 0.02 | 0.02 |
| 04/09/2024 L13-2 (2) | 28.087 | 127.560 | 0.506 | 151.572 | 4.581 | 16.3 | 500 | 100 | 10 | 9.86 | 0.02 | |
| | | | | | | | | | | | | |
| 04/09/2024 L17-1 (1) | 28.649 | 121.334 | 0.498 | 145.900 | 4.581 | 16.0 | 500 | 100 | 10 | 9.86 | 0.02 | 0.02 |
| 04/09/2024 L17-1 (2) | 28.649 | 121.334 | 0.498 | 145.900 | 4.581 | 16.0 | 500 | 100 | 10 | 9.90 | 0.01 | |
| | | | | | | | | | | | | |
| 04/09/2024 L17-2 (1) | 24.787 | 70.322 | 0.498 | 92.080 | 3.527 | 14.2 | 500 | 100 | 10 | 9.92 | 0.00 | 0.00 |
| 04/09/2024 L17-2 (2) | 24.787 | 70.322 | 0.498 | 92.080 | 3.527 | 14.2 | 500 | 100 | 10 | 9.92 | 0.00 | |
| | | | | | | | | | | | | |
| 10/09/2024 L23-1 (1) | 30.612 | 47.590 | 0.498 | 75.788 | 2.912 | 9.5 | 500 | 100 | 10 | 9.86 | 0.04 | 0.02 |

| | | | | | | | | | | | | |
|---|---|---|---|---|---|---|---|---|---|---|---|---|
| 10/09/2024 L23-1 (2) | 30.612 | 47.590 | 0.498 | 75.788 | 2.912 | 9.5 | 500 | 100 | 10 | 9.90 | 0.01 | |
| 10/09/2024 L23-2 (1) | 25.415 | 49.586 | 0.495 | 71.462 | 4.034 | 15.9 | 500 | 100 | 10 | 9.92 | 0.00 | 0.00 |
| 10/09/2024 L23-2 (2) | 25.415 | 49.586 | 0.495 | 71.462 | 4.034 | 15.9 | 500 | 100 | 10 | 9.90 | 0.01 | |
| | | | | | | | | | | | | |
| 10/09/2024 S6-1 (1) | 28.214 | 121.334 | 0.496 | 146.409 | 3.635 | 12.9 | 500 | 100 | 10 | 9.46 | 0.22 | 0.22 |
| 10/09/2024 S6-1 (2) | 28.214 | 121.334 | 0.496 | 146.409 | 3.635 | 12.9 | 500 | 100 | 10 | 9.48 | 0.21 | |
| 11/09/2024 S6-2 (1) | 26.233 | 70.324 | 0.498 | 93.323 | 3.732 | 14.2 | 500 | 100 | 10 | 8.90 | 0.48 | 0.48 |
| 11/09/2024 S6-2 (2) | 26.233 | 70.324 | 0.498 | 93.323 | 3.732 | 14.2 | 500 | 100 | 10 | 8.92 | 0.47 | |
| | | | | | | | | | | | | |
| 11/09/2024 S8-1 (1) | 28.889 | 66.684 | 0.491 | 91.625 | 4.439 | 15.4 | 500 | 100 | 10 | 9.30 | 0.25 | 0.25 |
| 11/09/2024 S8-1 (2) | 28.889 | 66.684 | 0.491 | 91.625 | 4.439 | 15.4 | 500 | 100 | 10 | 9.28 | 0.26 | |
| 11/09/2024 S8-2 (1) | 23.950 | 121.350 | 0.502 | 140.895 | 4.907 | 20.5 | 500 | 100 | 10 | 9.28 | 0.23 | 0.23 |
| 11/09/2024 S8-2 (2) | 23.950 | 121.350 | 0.502 | 140.895 | 4.907 | 20.5 | 500 | 100 | 10 | 9.26 | 0.24 | |
| | | | | | | | | | | | | |
| 14/11/2024 Blanco | | | | | | | | 100 | 10 | 4.94 | | |
| | | | | | | | | | | | | |
| 14/11/2024 L2-1-1 (1) | 23.630 | 66.682 | 0.501 | 87.199 | 3.614 | 15.2941 | 500 | 100 | 10 | 9.26 | 0.33 | 0.3237 |
| 14/11/2024 L2-1-1 (2) | 23.630 | 66.682 | 0.501 | 87.199 | 3.614 | 15.2941 | 500 | 100 | 10 | 9.3 | 0.31 | |
| 14/11/2024 L2-1-2 (1) | 23.827 | 73.959 | 0.503 | 95.591 | 2.698 | 11.3233 | 500 | 100 | 5 | 4.56 | 0.25 | 0.2431 |
| 14/11/2024 L2-1-2 (2) | 23.827 | 73.959 | 0.503 | 95.591 | 2.698 | 11.3233 | 500 | 100 | 5 | 4.58 | 0.24 | |
| 15/11/2024 L2-2-1 (1) | 24.744 | 66.683 | 0.499 | 88.351 | 3.575 | 14.4479 | 500 | 100 | 5 | 4.82 | 0.06 | 0.0645 |
| 15/11/2024 L2-2-1 (2) | 24.744 | 66.683 | 0.499 | 88.351 | 3.575 | 14.4479 | 500 | 100 | 5 | 4.8 | 0.07 | |
| 15/11/2024 L2-2-2 (1) | 23.015 | 73.957 | 0.515 | 94.194 | 3.293 | 14.3081 | 500 | 100 | 5 | 4.9 | 0.02 | 0.0215 |
| 15/11/2024 L2-2-2 (2) | 23.015 | 73.957 | 0.515 | 94.194 | 3.293 | 14.3081 | 500 | 100 | 5 | 4.9 | 0.02 | |
| 19/11/2024 L2-3-1 (1) | 27.596 | 61.565 | 0.517 | 83.578 | 6.1 | 22.1047 | 500 | 100 | 5 | 4.84 | 0.03 | 0.0291 |
| 19/11/2024 L2-3-1 (2) | 27.596 | 61.565 | 0.517 | 83.578 | 6.1 | 22.1047 | 500 | 100 | 5 | 4.84 | 0.03 | |
| 19/11/2024 L2-3-2 (1) | 23.675 | 47.588 | 0.512 | 66.460 | 5.315 | 22.4498 | 500 | 100 | 5 | 4.92 | 0.01 | 0.0133 |
| 19/11/2024 L2-3-2 (2) | 23.675 | 47.588 | 0.512 | 66.460 | 5.315 | 22.4498 | 500 | 100 | 5 | 4.88 | 0.02 | |
| | | | | avg | 4.0991667 | 16.6547 | | | | | | |
| 14/11/2024 L17-1-1 (1) | 27.144 | 47.386 | 0.498 | 69.655 | 5.373 | 19.7944 | 500 | 100 | 5 | 4.64 | 0.10 | 0.0924 |
| 14/11/2024 L17-1-1 (2) | 27.144 | 47.386 | 0.498 | 69.655 | 5.373 | 19.7944 | 500 | 100 | 5 | 4.68 | 0.09 | |
| 15/11/2024 L17-1-2 (1) | 25.275 | 51.711 | 0.499 | 72.851 | 4.634 | 18.3343 | 500 | 100 | 5 | 4.8 | 0.05 | 0.0497 |

| | | | | | | | | | | | | |
|---|---|---|---|---|---|---|---|---|---|---|---|---|
| 15/11/2024 L17-1-2 (2) | 25.275 | 51.711 | 0.499 | 72.851 | 4.634 | 18.3343 | 500 | 100 | 5 | 4.82 | 0.05 | |
| | | | | | | | | | | | | |
| 19/11/2024 L17-2-1 (1) | 24.531 | 73.966 | 0.519 | 94.377 | 4.639 | 18.9108 | 500 | 100 | 5 | 4.84 | 0.04 | 0.0344 |
| 19/11/2024 L17-2-1 (2) | 24.531 | 73.966 | 0.519 | 94.377 | 4.639 | 18.9108 | 500 | 100 | 5 | 4.86 | 0.03 | |
| | | | | | | | | | | | | |
| 20/11/2024 L17-2-2 (1) | 23.257 | 66.683 | 0.514 | 86.435 | 4.019 | 17.2808 | 500 | 100 | 5 | 4.88 | 0.03 | 0.0265 |
| 20/11/2024 L17-2-2 (2) | 23.257 | 66.683 | 0.514 | 86.435 | 4.019 | 17.2808 | 500 | 100 | 5 | 4.88 | 0.03 | |
| | | | | | | | | | | | | |
| 20/11/2024 L17-3-1 (1) | 31.310 | 51.711 | 0.513 | 77.827 | 5.707 | 18.2274 | 500 | 100 | 5 | 4.86 | 0.02 | 0.0248 |
| 20/11/2024 L17-3-1 (2) | 31.310 | 51.711 | 0.513 | 77.827 | 5.707 | 18.2274 | 500 | 100 | 5 | 4.86 | 0.02 | |
| | | | | | | | | | | | | |
| 20/11/2024 L17-3-2(1) | 27.990 | 49.586 | 0.513 | 71.285 | 6.804 | 24.3087 | 500 | 100 | 5 | 4.92 | 0.01 | 0.0026 |
| 20/11/2024 L17-3-2 (2) | 27.990 | 49.586 | 0.513 | 71.285 | 6.804 | 24.3087 | 500 | 100 | 5 | 4.94 | 0.00 | |
| | | | | avg | 5.196 | 19.4761 | | | | | | |

# H

# GPR 3D scans T-beams

This chapter presents the 3D scans of the harvested beams.

## H.1. Beam L2

Figure H.1: Beam L2

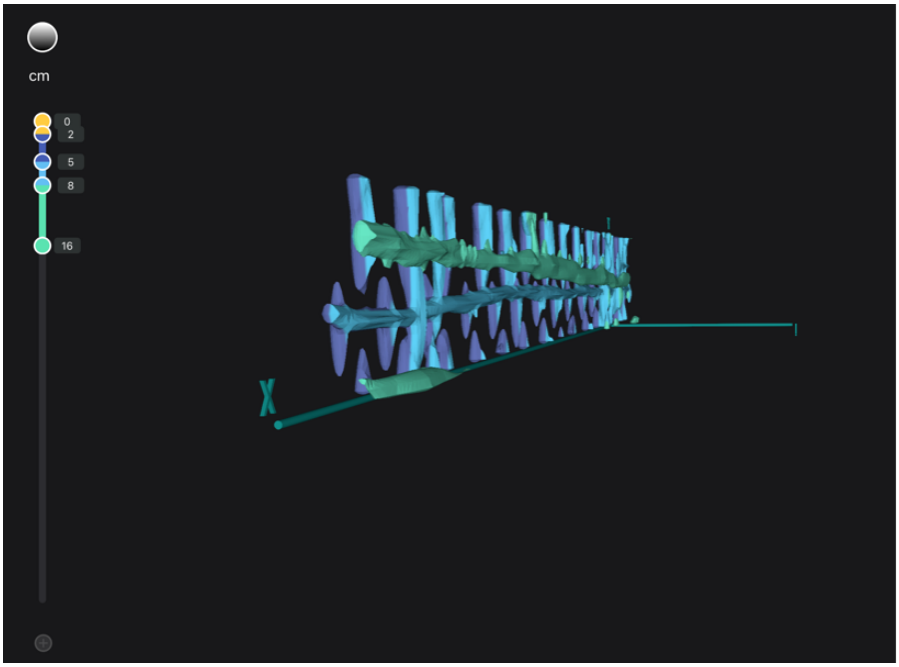


Figure H.2: 3D scan of Beam L2

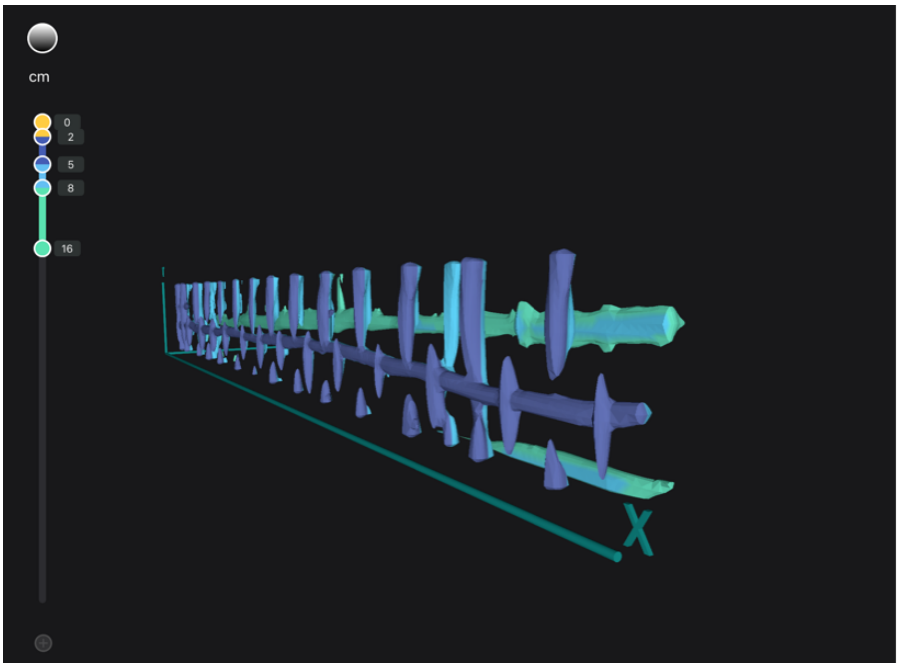


Figure H.3: 3D scan of Beam L2

## H.2. Beam L13

Figure H.4: Beam L13

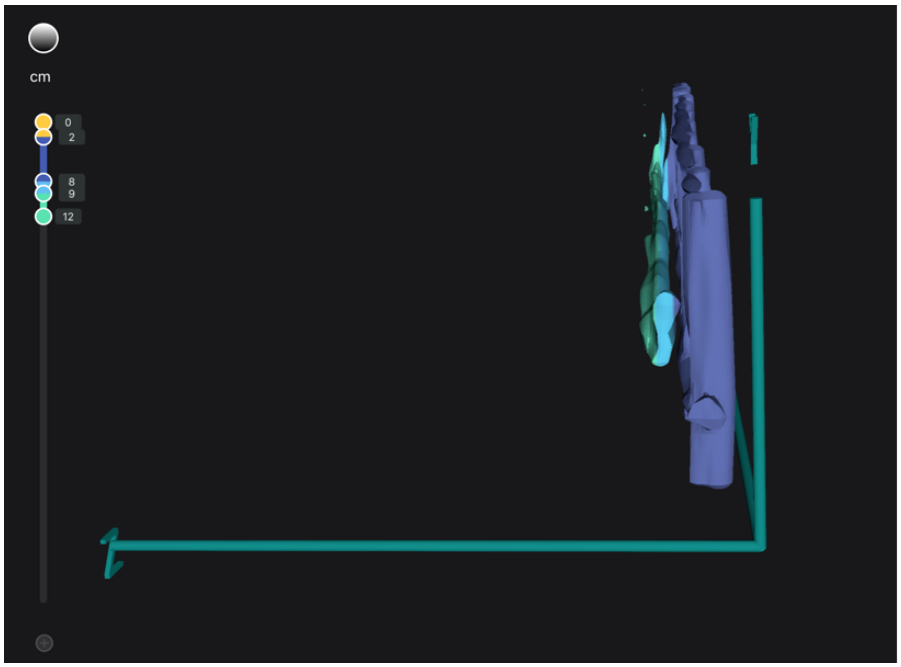


Figure H.5: 3D scan of Beam L13

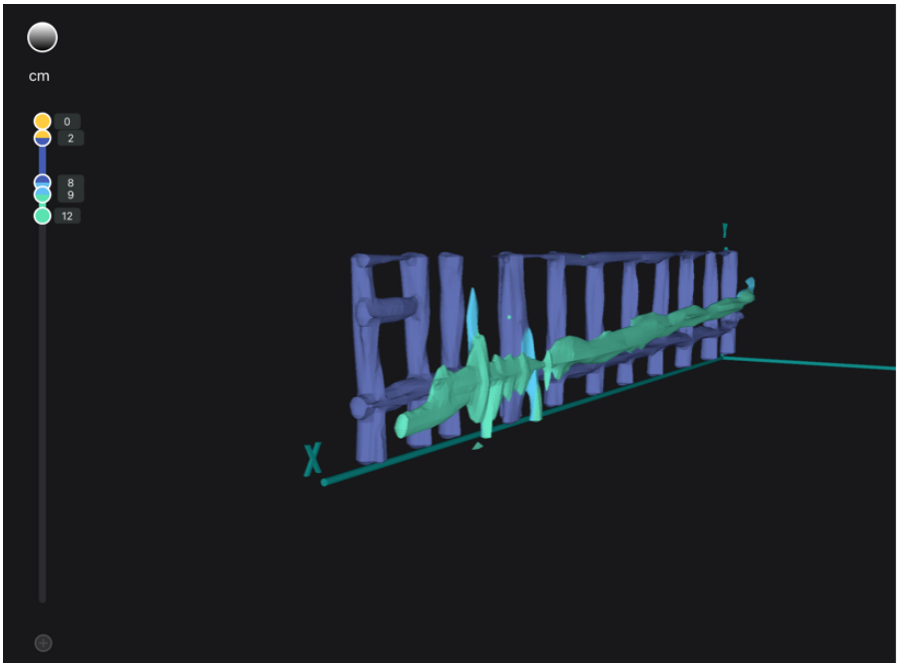


Figure H.6: 3D scan of Beam L13

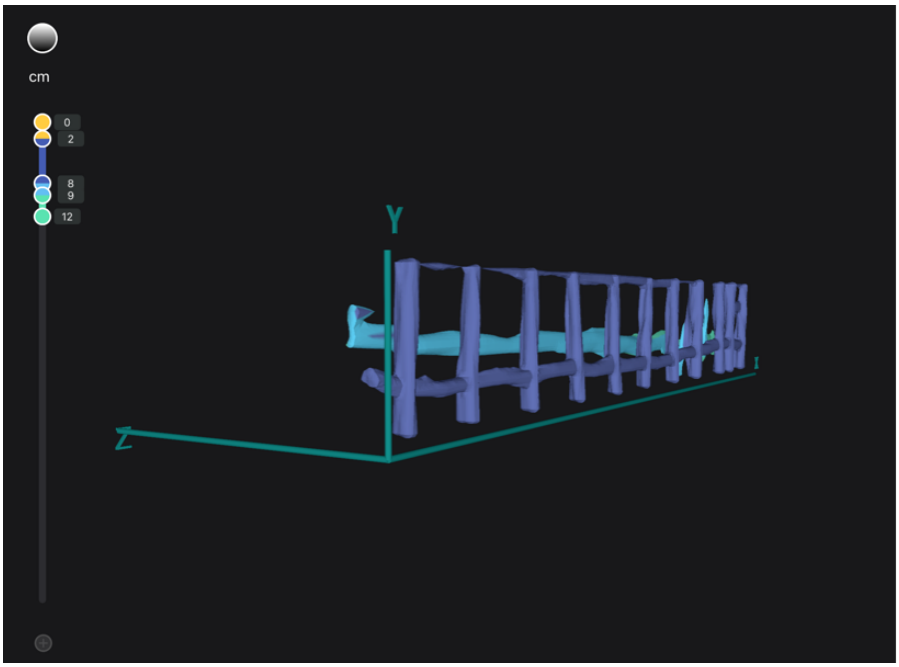


Figure H.7: 3D scan of Beam L13

## H.3. Beam L17

Figure H.8: Beam L17

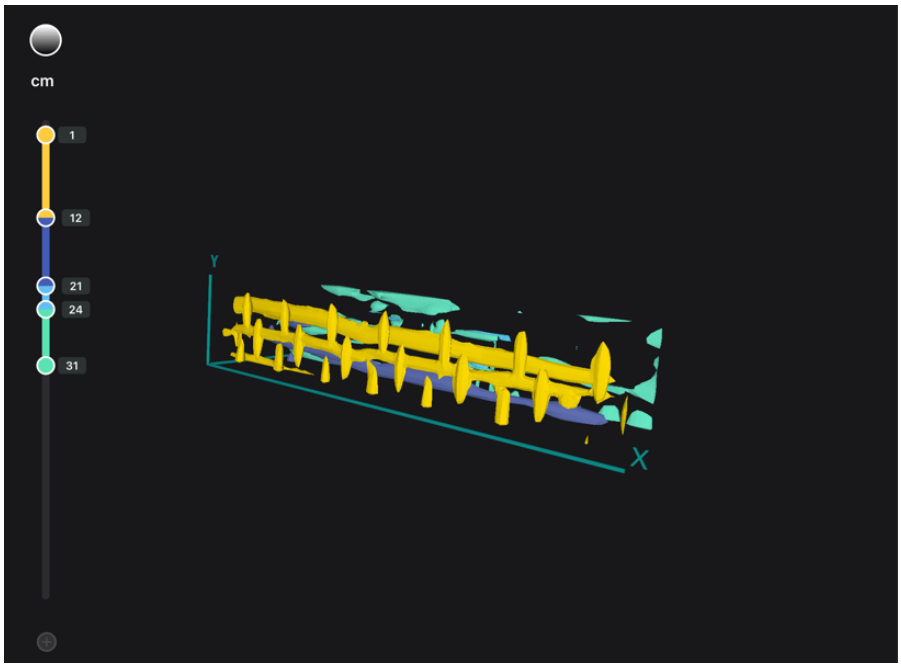


Figure H.9: 3D scan of Beam L17

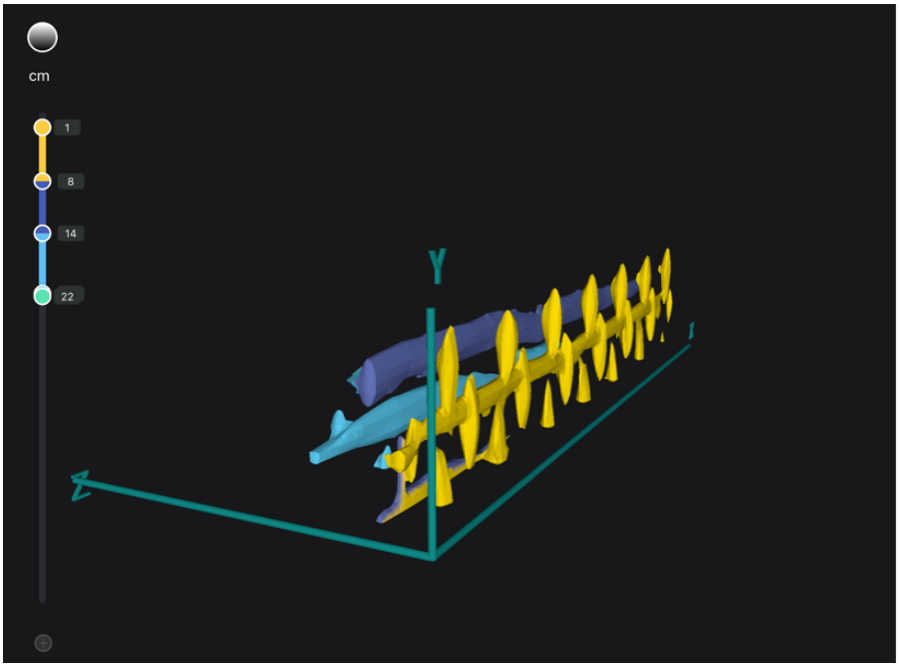


Figure H.10: 3D scan of Beam L17

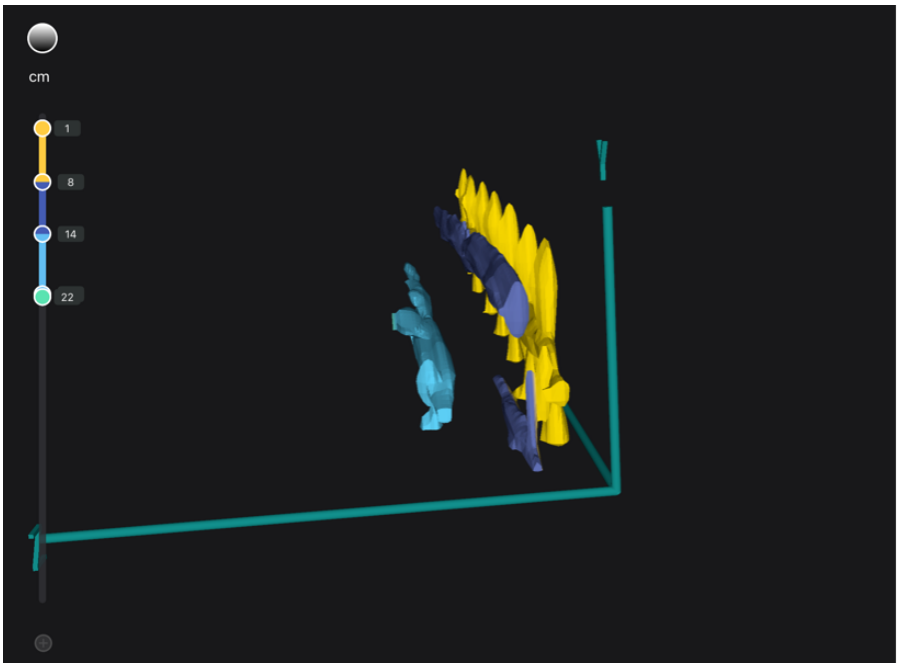


Figure H.11: 3D scan of Beam L17

# H.4. Beam L23

Figure H.12: Beam L23

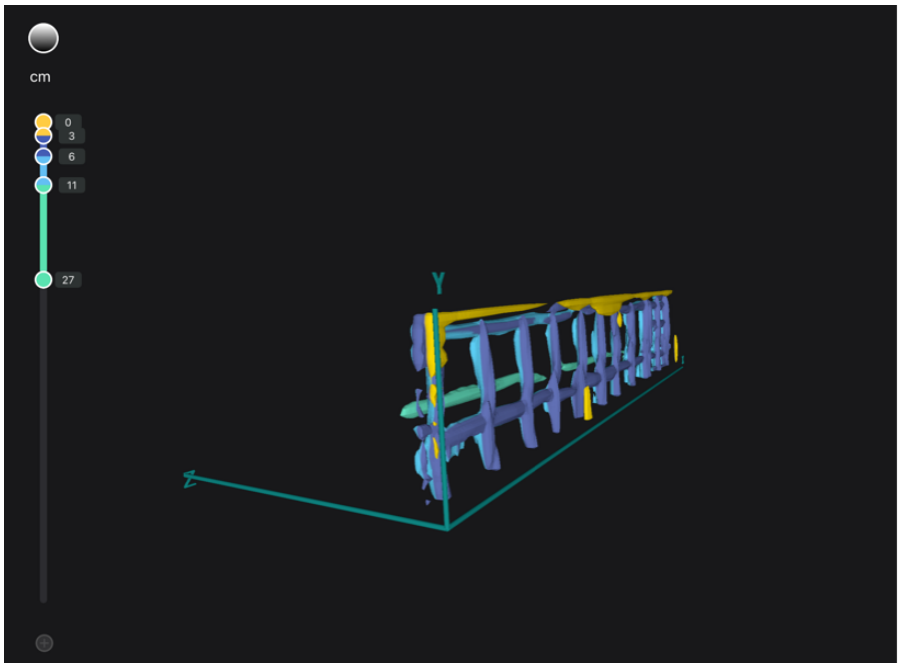


Figure H.13: 3D scan of Beam L23

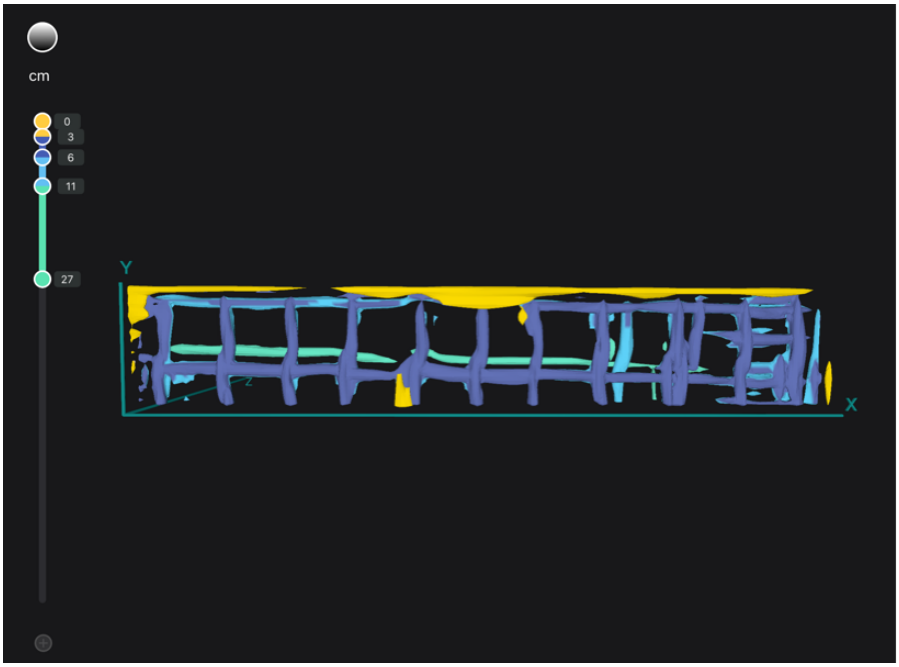


Figure H.14: 3D scan of Beam L23